



Swansea University
Prifysgol Abertawe



Swansea University E-Theses

The characterization and prevention of UV photodegradation of dye-sensitized solar cells.

Carnie, Matthew John

How to cite:

Carnie, Matthew John (2011) *The characterization and prevention of UV photodegradation of dye-sensitized solar cells.* thesis, Swansea University.

<http://cronfa.swan.ac.uk/Record/cronfa42960>

Use policy:

This item is brought to you by Swansea University. Any person downloading material is agreeing to abide by the terms of the repository licence: copies of full text items may be used or reproduced in any format or medium, without prior permission for personal research or study, educational or non-commercial purposes only. The copyright for any work remains with the original author unless otherwise specified. The full-text must not be sold in any format or medium without the formal permission of the copyright holder. Permission for multiple reproductions should be obtained from the original author.

Authors are personally responsible for adhering to copyright and publisher restrictions when uploading content to the repository.

Please link to the metadata record in the Swansea University repository, Cronfa (link given in the citation reference above.)

<http://www.swansea.ac.uk/library/researchsupport/ris-support/>

The Characterization and Prevention of UV Photodegradation of Dye-Sensitized Solar Cells

Matthew John Carnie

**Thesis submitted to Swansea University in fulfilment of the
requirements for the degree of Engineering Doctorate**

**EPSRC Engineering Doctorate Centre for Steel Technology
Swansea University**

College of Engineering- Materials Research Centre

2011

ProQuest Number: 10821350

All rights reserved

INFORMATION TO ALL USERS

The quality of this reproduction is dependent upon the quality of the copy submitted.

In the unlikely event that the author did not send a complete manuscript and there are missing pages, these will be noted. Also, if material had to be removed, a note will indicate the deletion.



ProQuest 10821350

Published by ProQuest LLC (2018). Copyright of the Dissertation is held by the Author.

All rights reserved.

This work is protected against unauthorized copying under Title 17, United States Code
Microform Edition © ProQuest LLC.

ProQuest LLC.
789 East Eisenhower Parkway
P.O. Box 1346
Ann Arbor, MI 48106 – 1346

SUMMARY

The initial focus of this thesis is a full characterization study of the UV photodegradation of dye-sensitized solar cells (DSCs). This has been achieved by exposing cells to UV light and measuring the change in their properties with I-V measurements, EIS and UV-Vis spectrophotometry. Insights into the photodegradation mechanisms of DSCs were gained and it was found that the principle cause of cell failure is the consumption of I_3^- by reaction with oxidative holes that arise from direct excitation of the TiO_2 semiconductor. Changes to the cell properties, particularly the change to the V_{OC} , were used to assess the effectiveness of different levels of UV filtering. It was subsequently found that filtering was required at greater than 385 nm but no more than 400 nm. The effects of filtering upon the performance of DSCs was also investigated by applying filters at various wavelength cut-offs. It was shown that the further into the visible region the cut-off moves, the greater the reduction in cell efficiency and it was estimated that a 400 nm filter should not reduce relative cell efficiency by more than 10% in a forward illuminated cell and should be much less than a 2% relative reduction in a reverse illuminated cell. Furthermore it was shown that dyes with broader photocurrent action spectra, such as N749, suffer less reduction in $\% \eta$ due to UV filtering than dyes with narrower action spectra, emphasising the need for sensitizers or co-sensitizers to absorb more red and near infra red radiation. Finally, during the characterization study it was found that the depleted I_3^- could be restored by application of a reverse bias. The consequence of this upon the long term stability of DSCs was investigated by periodic application of the reverse bias during UV exposure.

The photostability of clear polymer films was also investigated. These films could be used for counter electrode materials, and/or encapsulation materials for flexible dye-sensitized solar cells (DSCs) built upon a steel substrate. This was achieved by conducting accelerated weathering experiments on various polymer films. The extent of photodegradation in these films was measured using spectroscopic techniques and it was found that the rate of photodegradation could be reduced significantly by the application of a comparatively thin layer (20 μm) of a commercially available, polyurethane clear lacquer containing UV absorber and Hindered Amine Light Stabilizer additions. As well as preventing photodegradation in the polymer film, the application of a UV absorbing clearcoat was also considered necessary to filter UV light in order to prevent direct band gap excitation of the TiO_2 semi-conductor, which is known to photocatalyse the breakdown of organic chemicals adsorbed onto, or in the vicinity of TiO_2 particles. The UV cut-offs of various films, lacquers and additives were investigated and a number of possible solutions were put forward.

Acknowledgements

First of all I would like to thank EPSRC and TATA Steel Colours for their funding of this work and for their support of the doctorate training scheme. I feel extremely privileged to have received the sponsorship of both organisations and I hope that this document lives up to their expectations. There are a great number of individuals from TATA who have given up their time along the way. There are too many to thank individually, but special thanks must go to Paul Jones, Dr. Maarten Wijdekop, Dr. Jon Elvins and Rodney Rice. I would also like to thank Graham Swanston from BASF for his help with the work presented in *chapter 8* of this thesis.

This work would not have been possible without the guidance of Prof. Dave Worsley. I am extremely grateful for his continuing supervision and support. This project was fantastic to work on and was made all the more fun because of my colleagues at Swansea University, I say colleagues but what I really mean is: friends. I regret that I cannot thank you all individually but I must thank Dr. Trystan Watson especially for his support and interesting discussions. Thanks also (in no particular order) to Beverly Williams, Dr. Ian Mabbett, Dr. Bruce Philip, Dr. Jim Sullivan, Dr. Dave Penney, Martyn Cherrington, Dr. Andrew Robinson, Dr. Peter Douglas, Khalil Khan, Dr. Geraint Williams, Prof. Neil McMurray and Daniel Bryant.

Between submitting this thesis and sitting my viva voce I went to Nantucket, MA and married. Jay Doyle. Thank you for being you. I am luckiest man alive.

This is dedicated to my parents, Robert and Carol. If I ever become half as good as a parent as either of you, I will have achieved a lot in life.

Matthew John Carnie
05/03/2012

| | | |
|-------------|--|-----------|
| 1. | INTRODUCTION | 1 |
| 1.1 | Energy from the Sun | 1 |
| 1.2 | Semiconductors | 2 |
| 1.3 | Solar Cell Technologies | 3 |
| 1.4 | Excitonic Solar Cells | 4 |
| 1.5 | Dye-Sensitized Solar Cells | 7 |
| 1.5.1 | Basic Operating Principles | 7 |
| 1.6 | Metal Oxide Semi Conductors as Photoelectrodes | 11 |
| 1.6.1 | TiO ₂ | 11 |
| 1.6.2 | ZnO | 14 |
| 1.6.3 | Other Metal Oxides | 14 |
| 1.7 | The Sensitizing Dye | 14 |
| 1.7.1 | Metal Complexes | 15 |
| 1.7.2 | Porphyrins and Pthlocyanines | 18 |
| 1.7.3 | Organic Sensitizers | 20 |
| 1.7.4 | Quantum Dot Sensitized Solar Cells | 21 |
| 1.8 | The Redox Electrolyte | 21 |
| 1.8.1 | Gel Electrolytes and Hole Conductors | 22 |
| 1.9 | Electron Transfer Processes in Dye Sensitized Solar Cells | 24 |
| 1.10 | Industrialisation and Scale-Up of DSC Technology | 25 |
| 1.11 | DSC Measurement Techniques | 26 |
| 1.11.1 | IV Measurements | 26 |
| 1.11.2 | IPCE Measurements | 28 |
| 1.11.3 | Impedance Spectroscopy | 29 |
| 1.11.3.1 | Impedance Spectroscopy of DSCs | 33 |
| 1.11.3.2 | Modelling using the Transmission Line Element | 36 |
| 1.12 | DSC Stability | 38 |
| 1.12.1 | Sensitizer Stability | 40 |
| 1.12.2 | Loss of Triiodide Electrolyte | 40 |
| 1.12.3 | H ₂ O and CO ₂ Ingress | 40 |
| 1.12.4 | Counter Electrode Degradation | 41 |
| 1.12.5 | Visible and UV Light Soaking | 41 |
| 1.13 | Photodegradation of Polymer Films | 42 |
| 1.13.1 | Mechanisms of Photodegradation | 42 |
| 1.13.1.1 | Homogeneous Excitation | 43 |
| 1.13.1.2 | Activation of TiO ₂ | 44 |
| 1.13.2 | Mechanisms of Photodegradation of Polymers | 45 |
| 1.13.3 | Protection from Ultra Violet Radiation | 49 |
| 1.13.3.1 | UV absorbers | 50 |
| 1.13.3.2 | Hindered Amine Light Stabilisers (HALS) | 51 |
| 1.14 | Weathering and Accelerated Testing | 52 |
| 1.14.1 | Natural Exposure | 53 |
| 1.14.2 | Artificial Exposure Methods | 53 |
| 1.14.2.1 | Carbon Arc | 54 |
| 1.14.2.2 | Xenon Arc Sources | 54 |
| 1.14.2.3 | Fluorescent Tube Lamps | 55 |
| 1.15 | Aims and Objectives | 55 |
| 1.16 | References | 56 |

| | | |
|------------|--|------------|
| 2. | EXPERIMENTAL PROCEDURES | 65 |
| 2.1 | Fabrication of DSC Test Cells | 65 |
| 2.1.1 | Manufacture of the Working Electrode | 65 |
| 2.1.2 | Manufacture of the Counter Electrode | 66 |
| 2.1.3 | Filling and Sealing | 66 |
| 2.2 | Cell Measurements | 67 |
| 2.2.1 | IV Measurements | 67 |
| 2.2.2 | EIS Measurements | 68 |
| 2.2.3 | IPCE Measurements | 69 |
| 2.3 | UV-Vis Measurements | 69 |
| 2.4 | FTIR Spectrophotometry and ATR accessory | 70 |
| 2.5 | Accelerated Weathering | 70 |
| 2.5.1 | QUV Accelerated Weathering | 70 |
| 2.5.2 | UV Exposure of DSC Test Cells | 71 |
| 2.5.3 | Visible Light Soaking of DSC Test Cells | 72 |
| 2.6 | Spectral Emission Measurements | 72 |
| 2.7 | UV Exposure of DSCs under a N₂ Atmosphere | 73 |
| 2.8 | References | 73 |
| 3. | CHARACTERISATION OF UV PHOTODEGRADATION IN DYE-SENSITIZED SOLAR CELLS | 74 |
| 3.1 | Initial Experiment | 74 |
| 3.1.1 | Cell Characteristics at 120 Hours Exposure | 75 |
| 3.1.2 | Changes in Cell Properties during the Exposure Period | 77 |
| 3.2 | Reverse Illumination and Cells Exposed under Electrical Load | 82 |
| 3.3 | Photobleaching of the Electrolyte | 86 |
| 3.4 | Dye Stability | 87 |
| 3.5 | Irradiation of Cells under a Nitrogen Atmosphere | 89 |
| 3.6 | Conclusion | 92 |
| 3.7 | References | 93 |
| 4. | MEASUREMENT OF PHOTBLEACHING USING LARGER AREA CELLS | 94 |
| 4.1 | IV Data for Larger Area Cells | 95 |
| 4.1.1 | Issues Relating to the IV Measurements of the Larger Area Cells | 97 |
| 4.1.2 | Long Term IV Trends in UV Exposed Larger Area Cells | 97 |
| 4.2 | Impedance Data for Larger Area Cells | 100 |
| 4.2.1 | Issues Relating to EIS Measurements of Larger Area Cells | 100 |
| 4.2.2 | Long Term Trends in R _{BR} of Larger Area Cells | 102 |
| 4.2.3 | Qualitative Analysis of Nyquist Plots | 103 |
| 4.3 | Colour Change Measured with UV-Vis Spectroscopy | 105 |
| 4.4 | Conclusion | 110 |
| 4.5 | References | 111 |
| 5. | VISIBLE LIGHT SOAKING VS. UV IRRADIATION | 112 |
| 5.1 | IV Data | 113 |
| 5.2 | EIS Data | 116 |
| 5.3 | Conclusion | 117 |

| | | |
|------------|--|------------|
| 5.4 | References | 118 |
| 6. | UV FILTERING OF DYE-SENSITIZED SOLAR CELLS | 120 |
| 6.1 | The Effects of UV Filtering upon DSC Stability | 120 |
| 6.2 | The Effect of UV Filtering on Cell Performance and Efficiency | 123 |
| 6.2.1 | The Dyes | 123 |
| 6.2.2 | The Filters | 126 |
| 6.3 | The Effect of Filtering on Cell Performance – Forward Illumination | 128 |
| 6.3.1 | Filtering of Cells Made with N719 Dye | 129 |
| 6.3.2 | Filtering of Cells Made with N3 Dye | 132 |
| 6.3.3 | Filtering of Cells Made with Z907 Dye | 132 |
| 6.3.4 | Filtering of Cells Made with N749 Dye | 133 |
| 6.3.5 | Forward Illumination Summary | 134 |
| 6.4 | The Effect of Filtering on Cell Performance – Reverse Illumination | 135 |
| 6.5 | Conclusion | 141 |
| 6.6 | References | 142 |
| 7. | ELECTROLYTE REGENERATION AND PHOTOCURRENT RECOVERY IN UV PHOTODEGRADED DYE-SENSITIZED SOLAR CELLS. | 143 |
| 7.1 | Electrolyte Regeneration by Application of a Reverse Bias | 145 |
| 7.2 | Period Electrolyte Regeneration | 146 |
| 7.2.1 | Case Studies | 146 |
| 7.2.2 | Systematic Study of Periodic Cell Regeneration | 149 |
| 7.3 | Conclusion | 153 |
| 8. | UV PHOTODEGRADATION OF POLYMER FILMS INTENDED FOR USE AS COUNTER ELECTRODE MATERIALS IN FLEXIBLE DYE-SENSITIZED SOLAR CELLS | 155 |
| 8.2 | The Topsheet as a UV Filter | 155 |
| 8.2.1 | The UV Cut-Off | 156 |
| 8.2.1.1 | Original Samples | 157 |
| 8.2.1.2 | The use of Added UV Absorbers – Tinuvin 477 | 159 |
| 8.2.1.3 | Inorganic and Yellow Pigments | 159 |
| 8.2.1.4 | Kimoto Films | 162 |
| 8.2.1.5 | UV Absorbers in a UV Cured Adhesive | 159 |
| 8.2.1.6 | UV Filtering by the Electrolyte | 163 |
| 8.3 | UV Stability of the Topsheet | 165 |
| 8.3.1 | UV Protection with Polyurethane Clearcoat Lacquers | 165 |
| 8.3.2 | Colaminates and other Films | 167 |
| 8.3.3 | Accelerated Weathering of PU Clearcoats and Colaminated Films | 168 |
| 8.3.3.1 | Photodegradation Observed with UV-Vis Spectroscopy | 168 |
| 8.3.3.2 | Quantifying Photodegradation using UV-Vis – The Yellowness Index | 171 |
| 8.3.4 | FTIR spectroscopy | 172 |
| 8.3.5 | ATR-FTIR Spectroscopy | 177 |

| | | |
|-------------|---|------------|
| 8.3.5.1 | Uncoated Melinex ST505 (PET) | 178 |
| 8.3.5.2 | ATR spectra of BASF LP and BASF HP Lacquers at 3517 Hours QUV | 180 |
| 8.3.5.3 | ATR spectra of Melinex Coated with the Beckers Lacquer | 183 |
| 8.3.5.4 | ATR spectra of T2754 and St Gobain Co-laminates | 183 |
| 8.3.5.5 | ATR spectra of Icosolar T2823 | 185 |
| 8.4 | Conclusions of Work on Original Film Samples | 186 |
| 8.5 | UV Cured Lacquers from Bayer | 187 |
| 8.5.1 | Action of the Lacquers | 187 |
| 8.5.2 | Yellowness Index of the Bayer Lacquers | 188 |
| 8.5.3 | FTIR Spectroscopy | 189 |
| 8.5.4 | Disappearance of the NCO Cross Linker Peak at 2265cm ⁻¹ | 191 |
| 8.5.5 | ATR Spectroscopy of Bayer UV Cured Lacquers | 192 |
| 8.5.6 | Conclusions to Work on Bayer UV Cured Clearcoats | 143 |
| 8.6 | PET vs. PEN as the Topsheet Material | 194 |
| 8.6.1 | PET vs. PEN – Yellowness Index | 196 |
| 8.6.2 | FTIR and ATR Analysis of PEN | 196 |
| 8.6.3 | Measuring Photodegradation of PEN with FTIR and ATR Spectroscopy | 199 |
| 8.6.4 | PEN vs. PET – Conclusion | 200 |
| 8.7 | The Effect of Coating Weight on the Efficacy of the Lacquer | 201 |
| 8.8 | The Effect of Increasing Additives on the Coating Performance | 202 |
| 8.9 | Curing of the BASF lacquers | 203 |
| 8.9.1 | Spray Coating and Curing the Lacquers on the PV Accelerator Pilot Line | 205 |
| 8.10 | Chapter 8. Conclusion | 209 |
| 8.11 | References | 209 |
| 9. | CONCLUSIONS AND FUTURE WORK | 210 |

Chapter

1.

Introduction

1. INTRODUCTION

When Michael Grätzel and Brian O' Regan published their seminal paper in 1991 [1], photoelectrochemical solar cells were already a well studied subject [25]. Grätzel and O' Regan's break-through came when they used colloidal dispersions of TiO_2 , which when applied to a conducting glass substrate and after a heat treatment, formed large surface area photoelectrodes and when used in conjunction with efficient sensitizers, vastly increased the efficiency of the photoelectrochemical cell. Further developments of screen printable polymer-organic TiO_2 pastes [6] and high efficiency cells built on metal substrates [7] has lead to the realisation that it may be possible to produce Dye Sensitized Solar Cells (DSCs) utilising a roll-to-roll process. This high-throughput method of manufacturing has the potential to reduce the cost of DSCs considerably, meaning that even low efficiency modules could be produced on such a scale as to contribute a significant proportion of electricity production for a given country. In 2006 TATA Steel Colors (then Corus Colors) became interested in DSC technology and after initial feasibility studies, it was announced in February 2007 that Dyesol, the Australian manufacturer of DSC materials, and Corus Colors would initiate a collaborative program aimed at integrating DSC technology into Corus Colors' metal building products [8].

One of the biggest challenges facing the commercialisation of DSCs is their stability and in particular their susceptibility to photodegradation by UV light. The main body of work in this thesis is a study of UV photodegradation of DSCs, in particular how the degradation can be characterised and what measures can be taken to limit it. A flexible metal based DSC will almost certainly have a transparent polymer counter-electrode. This thesis will also look at the photodegradation of materials likely to be considered for use as the counter-electrode.

1.1 Energy from the Sun

The Earth's atmosphere receives energy from the sun at an average rate of 5.445×10^{24} J or 1.5125×10^{18} kWh per year [9]. According to the International Energy Agency, total human consumption of energy in 2008 was 8428 Mtoe [10]. A Mtoe is a unit measure of energy in

millions of tonnes of oil equivalents. 8428 Mtoe is equal to 3.5×10^{20} J or 9.8×10^{13} kWh or in other words our energy consumption is less than one-hundredth of a percent of the energy the earth receives from the sun. If it were possible to harness just one-tenth of a percent of the total energy received from the sun, there would be virtually limitless amounts of energy available for as long as the sun continues to radiate towards earth. The supply of energy from the sun is abundant, cost-free and inexhaustible, yet it is thinly distributed over a wide area and at ground level and the supply is highly variable [9]. Harnessing energy from the sun efficiently, is a challenge that has been facing scientists ever since Daryl Chapin, Calvin Fuller, and Gerald Pearson developed the first modern silicon photovoltaic cell at Bell Laboratories in 1954 [11].

1.2 Semiconductors

Electrons in isolated atoms can exist only at discrete or quantized energy levels and due to the Pauli Exclusion Principle, the number of electrons that can exist at any particular energy level is strictly limited. When atoms are brought close together, as in a crystal lattice, their potential functions overlap, the exclusion principle still holds and the energy level must split and form a cluster of acceptable energy levels. These clusters or bands consist of a large number of closely packed, discrete energy levels or bands. The energy of the electrons in the material can be represented on a one-dimensional energy diagram showing various ranges of energies that electrons are allowed to have and the ranges in between the allowed bands where electrons are forbidden to exist (figure 1.1).

The distribution in the outermost or highest energy bands determines most of the electrical and thermal properties of the material. This is similar to the outermost electrons in an atom. These are called the valence electrons, which determine the atom's chemical characteristics. The highest occupied ground state band is known as the valence band. In electrical insulators the valence band is full and the energy gap between the valence band and the next allowed band (the conduction band) is so large that no energy applied can excite a valence electron to the conduction band as there are no empty allowed states available.

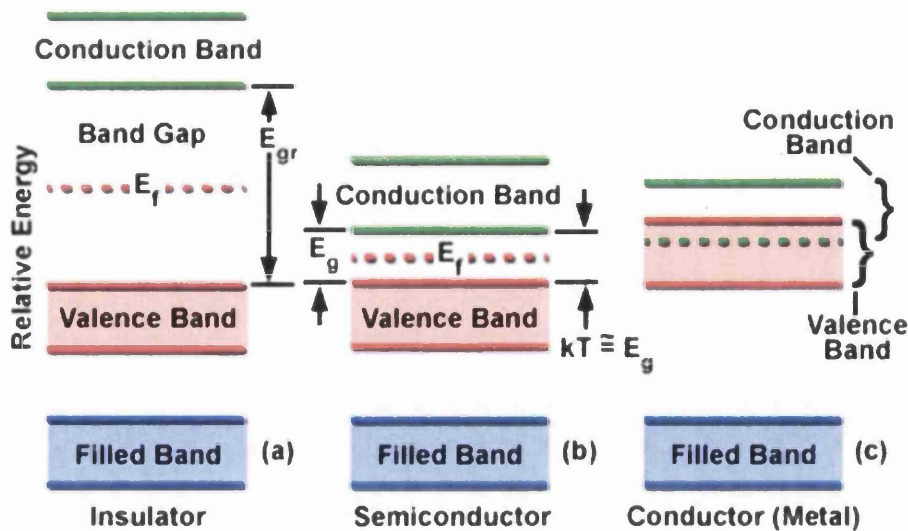


Figure 1.1 Energy band gaps in electrical insulators, conductors and semiconductors

Semiconductors are similar to insulators except that the forbidden gap between the valence and conduction bands is much smaller. Electrons in the valence band can receive energy, in the form of photons or thermal energy which allows them to jump the band gap to the conduction band. These electrons are now free to accept electrical energy from an applied field and to move through the crystal generating electrical current. In addition to this, the sites or “holes” left vacant in the valence band can become charge carriers themselves. An electron near a hole can jump in and fill it, leaving a new hole in its place; another electron can jump into this hole and so on. Although current is carried by moving electrons travelling in one direction it can also be viewed as a flow of positively charged holes moving in the opposite direction. Thus conduction is done by both holes and electrons. When the conduction of current is due only to those electrons excited from the valence band to the conduction band the material is called an intrinsic semiconductor [12].

1.3 Solar Cell Technologies

Figure 1.2 below shows a timeline of the evolution of different photovoltaic technologies. Table 1.1 below shows the latest figures for the best known efficiencies as published in

Progress in Photovoltaics in January 2011 [13]. At the time of writing in early 2011 there are many competing photovoltaic technologies.

1.4 Excitonic Solar Cells

The p-n junction of the silicon solar cell is the archetype of conventional solar cells whereby light absorption produces free electron-hole pairs and charge carrier separation is driven by a built in electrical field. Excitonic solar cells, which include Dye-Sensitized Solar Cells (DSCs) and Organic Solar Cells (OPV), differ in that excitons (mobile excited states) are generated upon light absorption, and if not created directly at the heterointerface as in DSCs, they must diffuse to it in order to photogenerate charge carriers [14]. The generation of excitons and charge transport in DSCs will be described in detail in the following chapters.

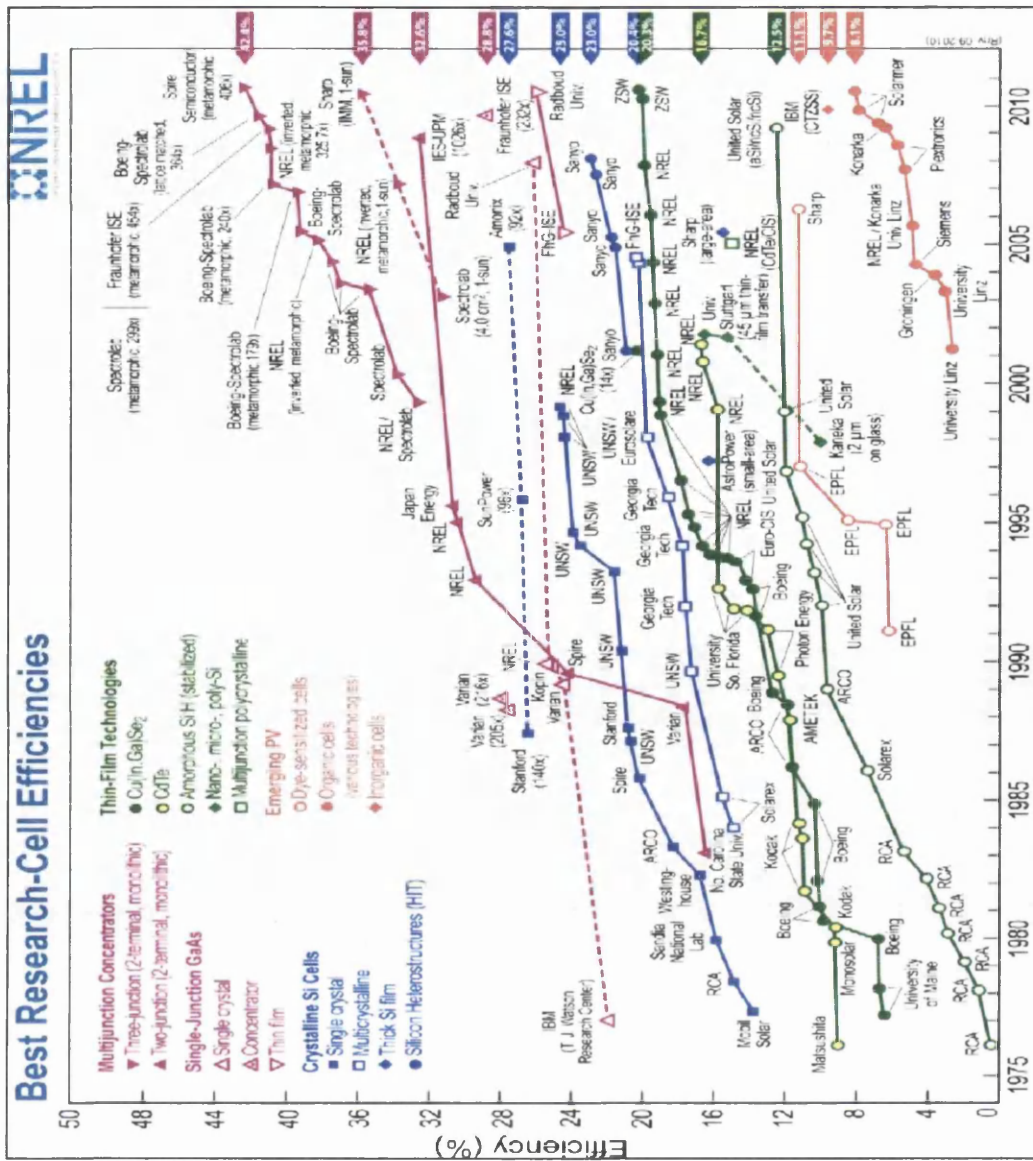


Figure 1.2 "Best Research-Cell Efficiencies" for experimental photovoltaics for lab scale cells, certified by NREL [15]

Table 1.1 Confirmed terrestrial cell and submodule efficiencies measured under the global AM1.5 spectrum (1000 Wm^{-2}) at 25°C - adapted from [13]. For an explanation the various parameters, refer to chapter 1.11.1

| Classification | η (%) | Area (cm^2) | Voc (V) | Jsc (mA/cm^2) | FF (%) | Test Centre (and Date) |
|--|------------|------------------------|---------|--------------------------|--------|------------------------|
| <u>Silicon</u> | | | | | | |
| Si (crystalline) | 25.0 | 4.0 | 0.706 | 42.7 | 82.8 | Sandia (3/99) |
| Si (multicrystalline) | 20.4 | 1.0 | 0.664 | 38.0 | 80.9 | NREL (5/04) |
| Si (thin film transfer) | 16.7 | 4.0 | 0.645 | 33.0 | 78.2 | FhG-ISE (7/01) |
| Si (thin film submodule) | 10.5 | 94.0 | 0.492 | 29.7 | 72.1 | FhG-ISE (8/07) |
| <u>III-V cells</u> | | | | | | |
| GaAs (thin film) | 27.6 | 1.0 | 1.107 | 29.6 | 84.1 | NREL (11/10) |
| GaAs (multicrystalline) | 18.4 | 4.0 | 0.994 | 23.2 | 79.7 | NREL (11/95) |
| InP (crystalline) | 22.1 | 4.0 | 0.878 | 29.5 | 85.4 | NREL (4/90) |
| <u>Thin Film Chalcogenide</u> | | | | | | |
| CIGS (cell) | 19.6 | 1.0 | 0.713 | 34.8 | 79.2 | NREL (4/09) |
| CIGS (submodule) | 16.7 | 16.0 | 0.661 | 33.6 | 75.1 | FhG-ISE (3/00) |
| CdTe (cell) | 16.7 | 1.0 | 0.845 | 26.1 | 75.5 | NREL (9/01) |
| CdTe (submodule) | 12.5 | 35.0 | 0.838 | 21.2 | 70.5 | NREL (9/10) |
| <u>Amorphous/nanocrystalline Si</u> | | | | | | |
| Si (amorphous) | 10.1 | 1.0 | 0.886 | 16.75 | 67 | NREL (7/09) |
| Si (nanocrystalline) | 10.1 | 1.2 | 0.539 | 24.4 | 76.6 | JQA (12/97) |
| <u>Photochemical</u> | | | | | | |
| Dye sensitised | 10.4 | 1.0 | 0.729 | 22 | 65.2 | AIST (8/05) |
| Dye sensitized (submodule) | 9.9 | 17.1 | 0.719 | 19.4 | 71.4 | AIST (8/10) |
| <u>Organic</u> | | | | | | |
| Organic polymer | 8.3 | 1.0 | 0.816 | 14.46 | 70.2 | NREL(11/10) |
| Organic (submodule) | 3.5 | 208.4 | 8.62 | 0.847 | 48.3 | NREL (7/09) |
| <u>Multijunction devices</u> | | | | | | |
| GaInP/GaAs/Ge | 32.0 | 4.0 | 2.622 | 14.37 | 85 | NREL (1/03) |
| GaAs/CIS (thin film) | 25.8 | 4.0 | — | — | — | NREL (11/89) |
| a-Si/ $\mu\text{c-Si}$ (thin film cell) | 11.9 | 1.2 | 1.346 | 12.92 | 68.5 | NREL (8/10) |
| a-Si/ $\mu\text{c-Si}$ (thin film submodule) | 11.7 | 14.2 | 5.462 | 2.99 | 71.3 | AIST (9/04) |
| Organic (2-cell tandem) | 8.3 | 1.1 | 1.733 | 8.03 | 59.5 | FhG-ISE (10/10) |

1.5 Dye-Sensitized Solar Cells

The advantages often stated of DSCs over other PV technologies are their (relatively) low cost, their ability to work well in diffuse and low level light conditions, their aesthetic value, in that they can be made transparent and in a variety of colours, and their potential for flexible roll-to-roll processing. The basic operating principles of the DSC, such as the photoexcitation of the dye, charge injection into and transport through the semi-conductor and the redox processes that occur, can be understood by most and have ignited interest from scientists of many disciplines as well as engineers and industrialists. The seeming simplicity of DSC devices has also caught the public attention and one can buy DIY DSC kits for school children. There is even a video on YouTube explaining how to make a DSC device using TiO_2 harvested from the icing sugar of powdered donuts which is then dyed using Starbuck's Passion Tea! [16] This seeming simplicity of DSC operation belies an inherent complexity of DSC devices which when studied in great detail, become irresistible to researchers. From a scientist's point of view DSCs are superbly fascinating and the complexity of the interactions between the different components of DSCs has led to an almost exponential increase in research publications. From 1991 when Grätzel and O' Regan published their now famous paper in Nature, the number of DSC research publications per year has gone from 1 in 1993 to almost 600 in 2009. Industrial interest is also growing with large multinational companies such as BASF and Bosch in Europe and Toyota, Sharp, Panasonic, Sony, Fujikura, and Samsung in Asia [17]. Tata Steel and G24i both have pilot lines here in Wales and both companies are capable of producing modules using roll-to-roll processes.

1.5.1 Basic Operating Principles

The semiconductor most often employed in DSCs is a mesoporous layer of sintered TiO_2 nanoparticles [18]. Other oxides have been investigated such as Nb_2O_5 [19], ZnO and SnO_2 [20; 21]. Adsorbed onto the metal oxide film is a dye, which when photoexcited can inject an electron from its LUMO into the conduction band of the oxide. Injected electrons can then percolate through the network of interconnected nanoparticles until they reach a

conductive contact and are then exported to an external circuit to do work. The dye, having donated its electron, finds itself oxidised and is subsequently reduced to its original state via electron donation from a redox electrolyte, the basis of which is frequently a I^-/I_3^- redox couple dissolved in an organic solvent. It is highly important that this process occurs quickly in order to prevent the oxidised dye from recapturing an injected electron from the conduction band of the oxide. Having sacrificed their electrical potential to do work, the electrons flowing in the external circuit return to the counter electrode whereby they reduce the I_3^- of the redox couple that was oxidised in the restoration of dye, thus completing the circuit [18; 22; 23]. Figure 1.3 shows the energy level diagram describing the energetics of the basic processes. Important factors here are that the LUMO of the dye must be higher than the oxide conduction band in order to achieve efficient electron injection and the V_{OC} of the cell is derived from the energy difference between the electron Fermi level in the semiconductor and the redox potential of the electrolyte.

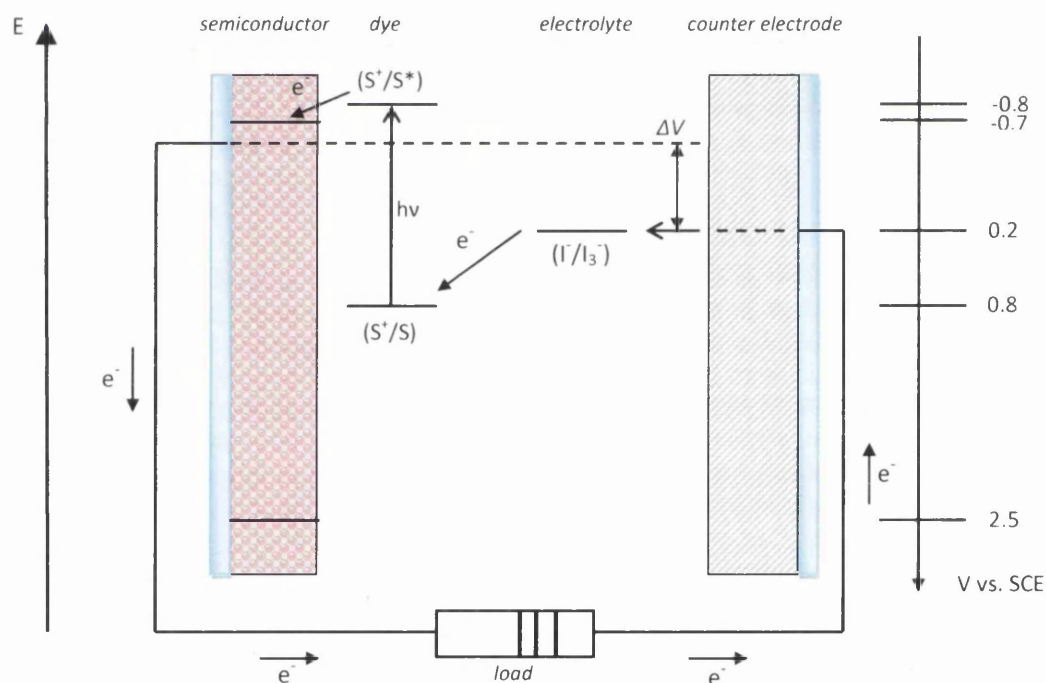


Figure 1.3 Energy level diagram outlining the basic operating principles of a DSC device - reproduced from [24]

In order to visualise the basic principles outlined above, it is helpful to visualise the general DSC architecture (see figure 1.4 below). From sunward (top) side to the back contact, this usually consists of:

1. A transparent layer or topsheet (glass or polymer film)
2. A transparent conductive oxide (TCO), normally indium or fluorine doped tin oxide, coated onto 1.
3. A layer of wide band gap oxide semiconductor, sintered onto 1 & 2
4. A monolayer of sensitising dye adsorbed onto 3
5. An electrolyte, normally containing an iodine/tri-iodide redox couple
6. A thin platinum catalytic layer deposited onto 7.
7. A rear electrode (or counter electrode), usually TCO, coated onto 8.
8. Substrate, often glass.

Elements 1-4 form the working electrode, or photoanode, of the cell whilst elements 6-8 form the counter electrode with the electrolyte in between. Often both electrode substrates are glass and so DSCs are often transparent. In a flexible DSC based on metal substrates the working electrode is sintered onto the metal substrate and the counter electrode forms the topsheet, meaning that light has to travel through the electrolyte.

Figure 1.3 perhaps presents a simplistic version of the electron transfer processes and only shows those processes that are beneficial to photocurrent generation. There are however loss mechanisms. Firstly there is the possibility of direct recombination of the excited state dye whereby the electron returns to its ground state, there is also recombination of electrons in the oxide conduction band with the oxidised dye or with acceptors in the electrolyte. The electron transfer processes and loss mechanisms will be discussed more thoroughly in *chapter 1.9*, the following chapters will discuss the various components that make up the DSC device.

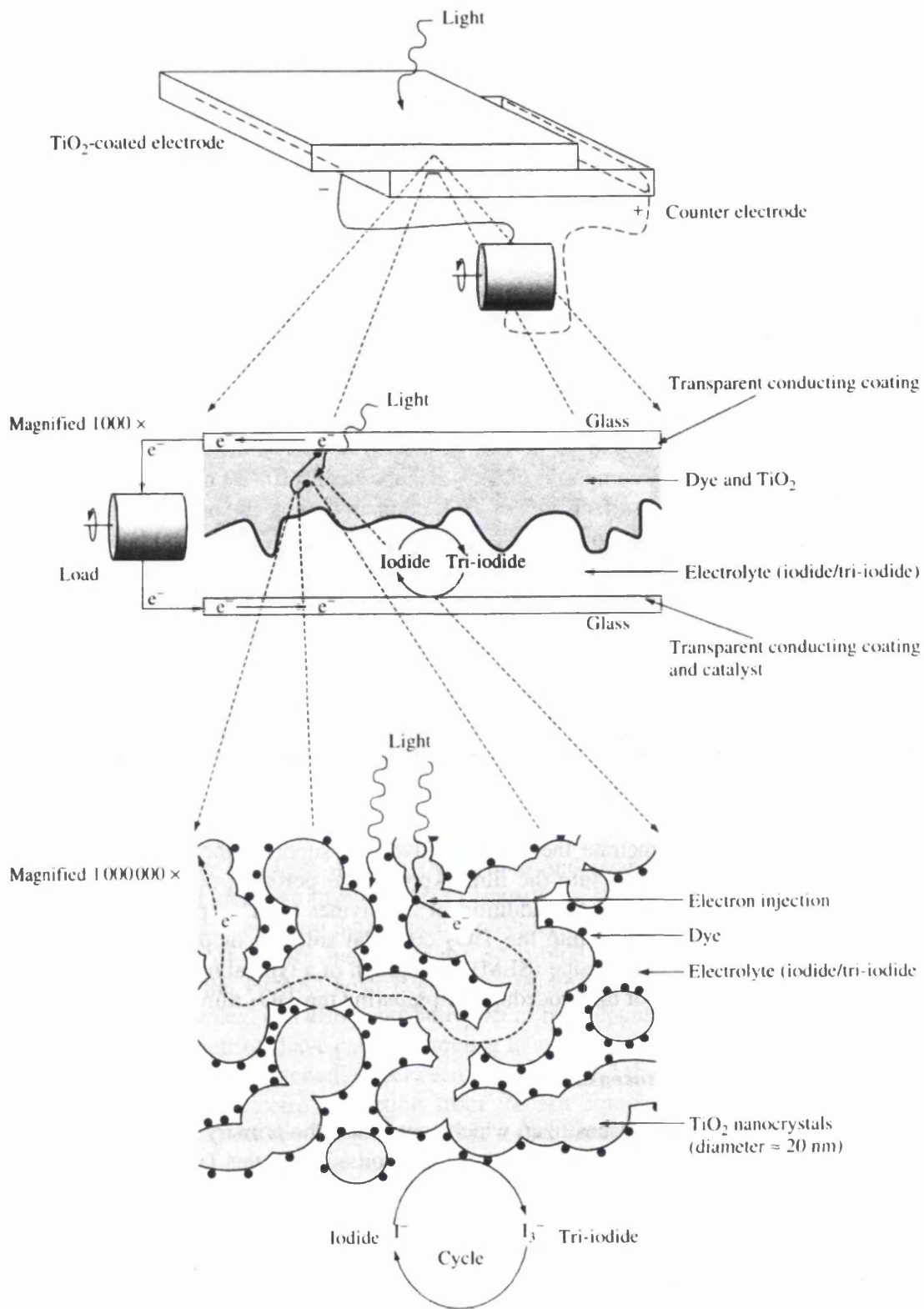


Figure 1.4 Schematic of DSC cell architecture at varying magnifications – reproduced from [25]

1.6 Metal Oxide Semi Conductors as Photoelectrodes

Figure 1.5 below shows the position of valence and conduction band edges of several semiconductors and their corresponding band gaps. The band gaps of the metal oxide semiconductors are around 3.2 eV for TiO₂ (anatase), WO₃ and ZnO and 3.8 eV for SnO₂. The values of the band gaps mean that the semiconductors absorb UV light and so dye-sensitization is essential in order to increase the light harvesting range of photovoltaic devices built upon these semiconductors.

A good photoelectrode will facilitate light harvesting, electron injection and electron collection. In order to maximize light harvesting the unsensitized semiconductor framework should be transparent and of sufficiently high surface area to enable maximum dye adsorption. Electron injection efficiency can be maximised by having a large density of unpopulated states in the semiconductor at lower absolute energies than that of the excited state of the dye (S^+/S^* - see figure 1.3). The electron collection efficiency is determined by the kinetic competition between the effective rate of electron diffusion and electron lifetimes, (τ_n) which are governed by rates of interception and recombination [26].

The metal oxide semi conductors listed in figure 1.5 as well as others not listed have been investigated for use in DSCs but TiO₂ still remains the dominant semiconductor in both academic research and industry.

1.6.1 TiO₂

TiO₂ is perhaps the most versatile of the metal oxides, delivering the highest solar-conversion efficiencies. TiO₂ is readily available in vast quantities, chemically stable and non-toxic and is already produced in large quantities [27]. As of May 2011 the price of TiO₂ is \$3300-3500 per tonne [28] compared to indium, which is used in transparent conducting films such as ITO and costs over \$900000 per tonne [29], hence it can be seen that TiO₂ is a relatively low-cost material.

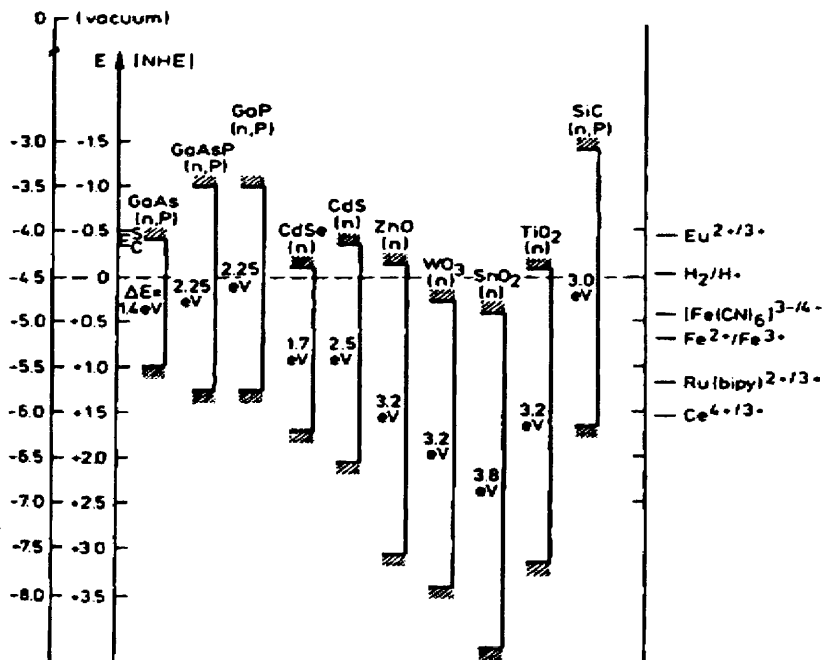


Figure 1.5 Position of valence and conduction band edges of several semiconductors in contact with an aqueous electrolyte at pH = 1.0 – reproduced from [24]

For TiO₂, the band gaps of rutile (3.02 eV) and anatase (3.2 eV) mean that the most common, room temperature stable, crystalline forms of TiO₂ are photoactive from 387 nm to 411 nm. Upon absorption of a photon of sufficient energy, an electron-hole pair is created and when TiO₂ is in contact with an electrolyte solution, a space-charge layer is formed underneath the TiO₂ surface. The resulting electric field transports electrons to the bulk and holes to the surface where a photoanodic reaction, such as the oxidation of water can set in. This process can be remarkably efficient at certain wavelengths with IPCE values as high as 80% at 300 nm [30]. The photoactivity of TiO₂ is also responsible for its role as a photocatalyst for the degradation of organic compounds [31] which will be discussed further in *chapter 1.13.1.2* below.

Sensitization of TiO₂ was discovered by Clark and Sutin in 1977 where they used single crystals of rutile TiO₂ sensitized with aqueous Ru(bpy)₃²⁺ [2] and, by 1985 Grätzel and co-workers were using colloidal TiO₂ particles [32]. Colloidal dispersions of TiO₂ nano-particles still form the basis of most TiO₂ pastes used in research and manufacture of DSCs but research is ongoing into alternative nanometre sized structures such as nano-wires [33] and

nano-tubes [34]. Figure 1.6 shows the nano-structure of a typical mesoporous TiO_2 film consisting of nano-particles of around 20 nm. TiO_2 film morphology is a major factor in DSC performance and nanoparticles are essential to increase the electrode surface area and therefore amount of dye adsorbed. Conversely, large particles are required to enhance light absorption through light scattering. This is often achieved through the addition of a layer of larger TiO_2 particles (ca. 500 nm sized particles) which are deposited onto the mesoporous film in order to scatter photons back into the transparent film and enhance red and near-IR light harvesting [35]. The porosity of the TiO_2 film is also important and can be controlled by changing the amount of binder in the paste (ideally about 50-60%). Higher porosities lead to higher incidences of termination particles (dead ends), meaning less interconnects between the particles and a decrease in charge collection efficiency [36]. Other modifications to the TiO_2 architecture include the addition of a TiO_2 blocking layer which is sometimes added to prevent recombination between the TCO and the electrolyte. This usually consists of a layer of particles ca. 50 nm thick deposited by spray pyrolysis [37]. Another type of modification is TiCl_4 treatment [38] which forms an ultrapure TiO_2 shell on the photoelectrode, the resulting increased roughness leads to greater adsorption of the sensitizer and improvements in J_{sc} and IPCE [39].

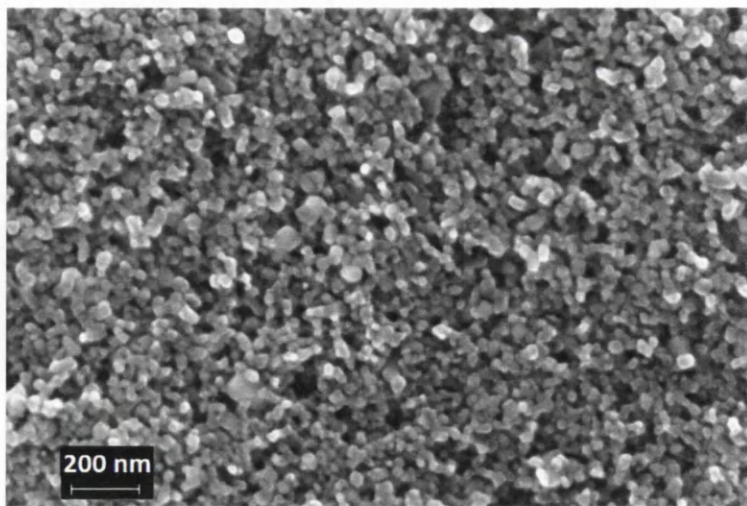


Figure 1.6 A typical mesoporous TiO_2 film consisting of 20 nm sized nano-particles – reproduced from [40]

1.6.2 ZnO

Having a similar band gap and conduction band edge to TiO_2 , ZnO has been extensively studied as a photoelectrode for DSCs. ZnO is less chemically stable than TiO_2 , amphoteric and so dissolves readily in both acidic and basic conditions. The attractiveness of ZnO to DSC researchers can be attributed to the relative ease of synthesizing highly crystalline ZnO with different morphologies, such as nanoparticles, nanowires, nanorods, nanotubes, tetrapods, nanoflowers, nanosheets, and branched nanostructures [17]. Despite showing great promise, ZnO DSCs have not yet matched up to the performance of TiO_2 based devices. One possible reason for the lower overall efficiency of ZnO is its stability, which has shown to be compromised in solvent-rich or acidic environments [41]. There is also evidence that irreversible dye agglomeration occurs in the ZnO electrodes due to the dissolution of Zn^{2+} ions from ZnO which may be caused by interactions with the carboxylic acid groups of the dye [42]. The dissolution can lead to precipitation of dye- Zn^{2+} complexes [43].

1.6.3 Other Metal Oxides

A study of the following metal oxides: TiO_2 , Nb_2O_5 , ZnO, SnO_2 , In_2O_3 , WO_3 , Ta_2O_5 , and ZrO_2 , was conducted by Sayama, Sugihara, and Arakawa [19] and they found that TiO_2 cells showed the highest short-circuit photocurrent (I_{sc}). Nb_2O_5 cells showed the highest V_{oc} and this can be attributed the higher band gap of 3.49 eV [44] compared to anatase at 3.2 eV. Of the oxides listed above, a literature survey seems to suggest that (apart from ZnO) SnO_2 is attracting the most recent research interest [45; 46].

1.7 The Sensitizing Dye

In their comprehensive review of 2010 [17], Hagfeldt *et al* listed some of the essential criteria that an effective photosensitizer should possess. These are listed below.

1. The absorption spectrum of the photosensitizer should be as wide as possible, preferably absorbing into the near-infrared (NIR) region.
2. The photosensitizer should have anchoring groups ($-\text{COOH}$, $-\text{H}_2\text{PO}_3$, $-\text{SO}_3\text{H}$, etc.) to strongly bind the dye onto the semiconductor surface.
3. The excited state level of the photosensitizer should be higher in energy than the conduction band edge of the semiconductor to achieve sufficient electron injection efficiency (see figure 1.3). This is true for n-type semiconductors such as TiO_2 but for p-type DSCs, the HOMO level of the photosensitizer should be at more positive potential than the valence band of the semiconductor.
4. The oxidized-state potential of the photosensitizer must be more positive than the redox potential of electrolyte for effective dye regeneration
5. Dye aggregation on the semiconductor surface should be avoided through optimization of the molecular structure of the dye or by addition of coadsorbents that prevent aggregation.
6. The sensitizer should be photo-, electrochemically and thermally stable.

Furthermore Nazeerudin and Yum in their chapter in *Dye-Sensitized Solar Cells* (EPFL Press) [47], also emphasise the need for directionality when the sensitizer is in the excited state. This directionality refers to the stereochemistry of the sensitizer because for efficient electron transfer to occur there is a need for effective coupling of the LUMO of the sensitizer to the Ti 3d orbital in the TiO_2 film.

1.7.1 Metal Complexes

Photosensitizers based on ruthenium bipyridyl complexes have been thoroughly investigated as sensitizers for water splitting and for photoelectrochemical solar cells [2; 32; 48; 49]. To date, photosensitizers of polypyridyl complexes of ruthenium and osmium [38; 50] give the best performance in terms of conversion yield and stability. The most promising of these have the general structure $\text{ML}_2(\text{X})_2$ where M stands for Ru or Os. L is 2,2'-bipyridyl-4,4'-dicarboxylic acid and X represents a halide, cyanide, thiocyanate or water [51]. In general, metal complex sensitizers have anchoring ligands for adsorption onto the semiconductor surface. These ligands can also be chromophoric groups. Ancillary

ligands which are not directly attached onto the semiconductor surface can be used for tuning the overall properties of the complexes [52]. Efficient energy conversion has been observed using bis-(4,4'-dicarboxylic acid-2,2'-bipyridine) as anchoring ligands, these complexes have become well studied and in 1993, Nazeeruddin achieved $\eta > 10\%$ using $\text{Ru}(2,2'\text{-bipyridyl-4,4'-dicarboxylic acid})_2(\text{NCS})_2$, more commonly known as N3 dye [38]. Some efficient and commonly used Ru-complex sensitizers are shown in figure 1.7 below.

For efficient electron injection to occur good dye adsorption is essential. On exposure of the semiconductor to the dye solution, the anchor groups result in the formation of a monolayer of dye being adsorbed onto its surface, giving near complete coverage. Figure 1.8 shows a dye with hydroxamic acid anchoring group complexes, adsorbed to the TiO_2 particle surface. Photoexcitation initiates a metal-to-ligand charge transfer (MLCT) whereby excitation causes electron transfer from a d-orbital of the metal to the π^* orbital of the ligand anchoring group, which forms the LUMO. The NCS ligand used in the N3 and black dyes causes the HOMO level of the dye to shift negatively, resulting in a red shift of the absorption property of the complex and a reduction in the energetic losses involved in regeneration of the dye by the redox electrolyte. Good electrical interaction between the ligand anchor and the conduction band of the TiO_2 results in effective electron injection from the Ru complex into the TiO_2 and once charge transfer has occurred, electron lifetime (τ_n) may be enhanced by using self-assembly assisting agents to improve the organisation of the sensitizer monolayer. This helps shield conduction band electrons from recapture by the oxidised mediator.

Many different ruthenium complexes comprising a variety of ligand groups have been, and continue to be researched. Complexes with different metal centres, e.g. Fe, Os, Re and Pt have been investigated. However, none of these can rival the performance of the Ru complexes. It is thought that this is as a result of the HOMO level of the Ru complexes being best matched to the redox potential of the iodine based electrolytes most commonly used in DSC fabrication. In all cases, development of efficient photosensitizers requires close matching of the LUMO level to the semiconductor conduction band to effectively inject electrons into the conduction band of the semiconductor and of the HOMO level to accept electrons from the electrolyte ions. With further development of the ruthenium dye structure it is believed that an increase in light harvesting in the 700-900nm region may be

achieved. The ultimate goal is to produce a dye that has a near vertical rise in photoresponse in the 920nm region that could lead to high efficiencies.

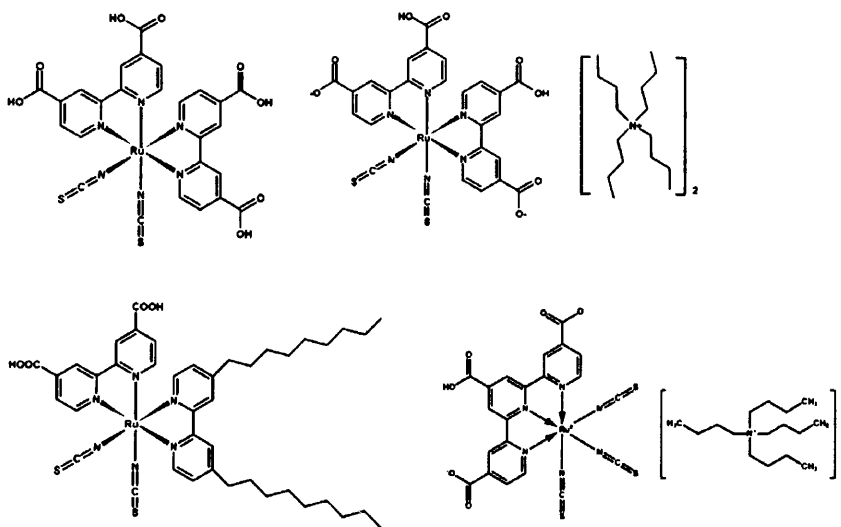


Figure 1.7 Structures of the dyes used in this chapter. Clockwise from top- left: N3, N719, N749 and Z907

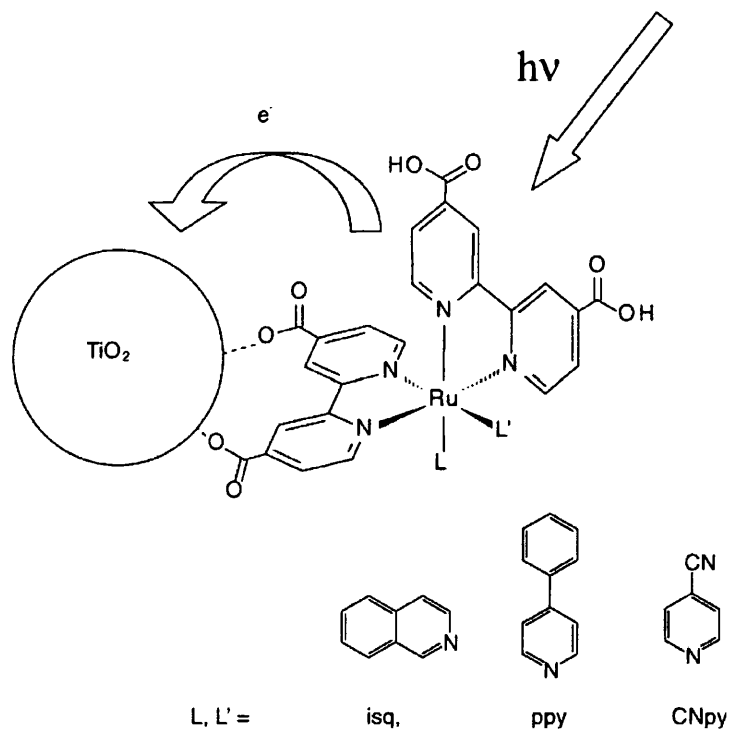


Figure 1.8 Showing dye anchorage to a TiO_2 particle of a dye involving a carboxylic acid anchoring group – reproduced from [52]

1.7.2 Porphyrins and Phthalocyanines

One of the drawbacks of ruthenium complexes is the limited absorption in the near-infrared region of the solar spectrum. Porphyrin and phthalocyanine systems exhibit intense spectral response bands in the near-IR region and possess good chemical, photo-, and thermal stability, providing good potential candidates for photovoltaic applications [17].

Porphyrins are ubiquitous in nature and in fact the haem- group in our own haemoglobin is a porphyrin. Chlorophylls are based on reduced porphyrin structure which is probably why they were among the first porphyrin related compounds investigated as DSC sensitizers [53]. Porphyrins synthesised for DSC sensitization have an appropriate LUMO level that resides above the conduction band of the TiO_2 and a HOMO level that lies below the redox couple in the electrolyte solution [54]. These are important factors for charge injection and separation. Figure 1.9 shows novel porphyrin sensitizers, in which the aryl groups act as electron donors and the malonic acid binding group as an acceptor. The figure is taken from reference [55] where a multinational collaboration led by David Officer produced a DSC of $\% \eta = 7.1$ using dye number 2. As of 2010 efficiencies of 11% have been achieved by a group led by Grätzel [56].

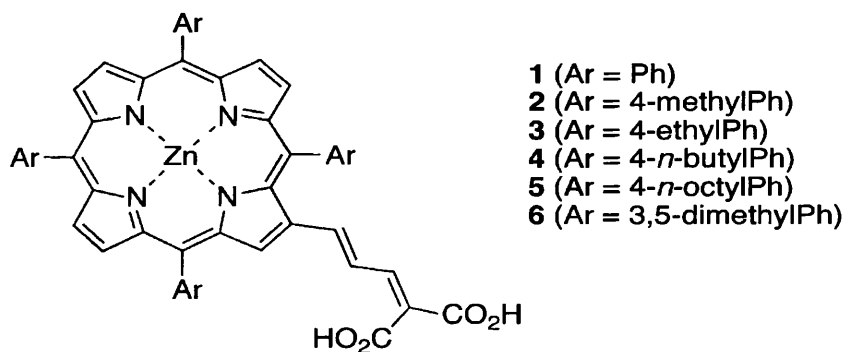


Figure 1.9 Porphyrin sensitizers, dye No 2 achieved $\% \eta = 7.1$ in 2007 – reproduced from [55]

Phthalocyanines are well known for their intense absorption in the red and NIR regions (they are often intensely blue or green in colour). They also show electrochemical, photochemical and thermal stability. Because of this, they have become an excellent option to explore for solar cell applications and have been the focus of intense research for the development of efficient NIR absorbers [57]. Efficiencies for phthalocyanines are generally lower than the other dye species mentioned so far with $\eta = 5.3\%$ achieved in 2012 [58]. Despite this they still attract attention for their use as co-sensitizers in conjunction with lower wavelength absorbers. Figure 1.10 shows the absorbance spectrum of a phthalocyanine dye overlain with that of N719 (both in solution). It can be observed that there is hardly any spectral overlap in the NIR region. Co-sensitization of dyes like this has the potential to increase cell efficiency by increasing the range of photons that can be captured by the DSC device [59; 60].

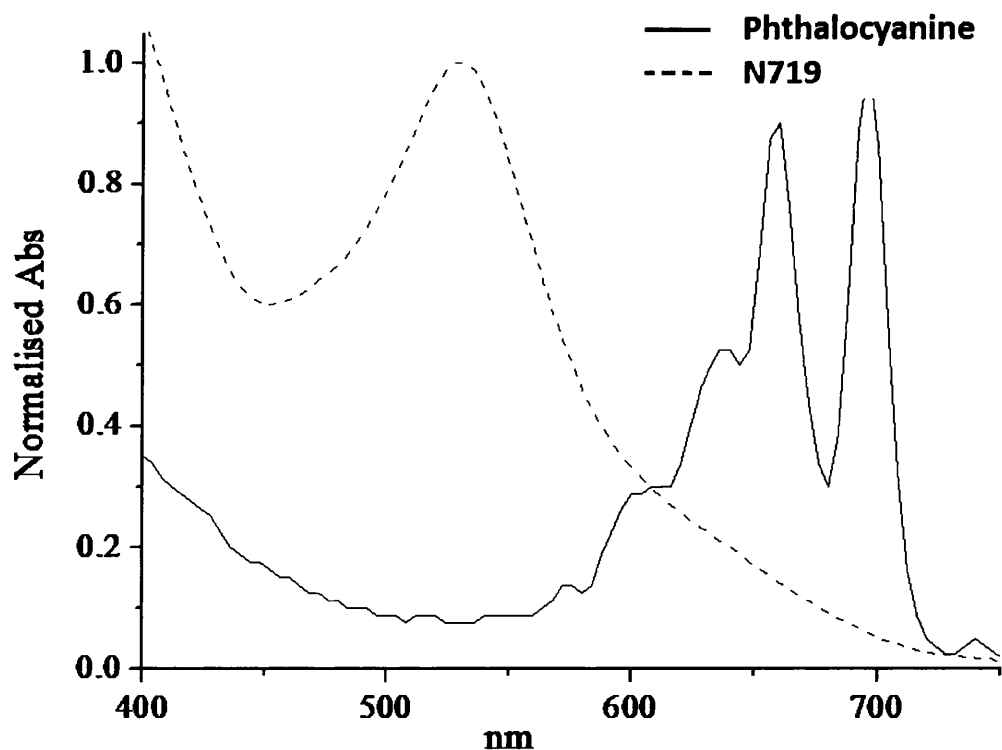


Figure 1.10 Absorbance spectrum of a phthalocyanine dye overlain with that of N719 (both in solution) showing the potential of co-sensitization to achieve more comprehensive capture of photons across the visible and toward the NIR spectrum – courtesy of [61]

1.7.3 Organic Sensitizers

Metal-free organic dyes have attracted increasing attention due to their high structural flexibility and low toxicity. In contrast to Ru (II) complexes, different light absorbing groups can be incorporated into the organic framework to tune the absorption over a broad spectral range and to achieve high molar extinction coefficients [62; 63].

Recent progress has been made in the field of highly absorbing metal-free organic dyes and organic dyes featuring an electron donor and acceptor moiety connected by a π -conjugation bridge have reached over 10% efficiency [64]. Two high performing organic sensitizers are shown in figure 1.11 below

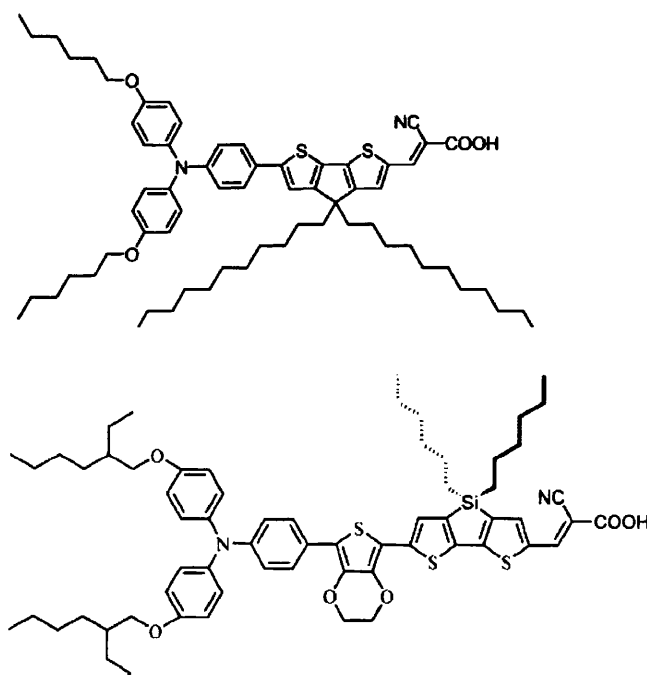


Figure 1.11 C220 (top) and C219 (bottom), two high performing organic sensitizers – reproduced from [62] and [64] respectively

1.7.4 Quantum Dot Sensitized Solar Cells

Quantum dots are small particles of semiconductors such as CdS, CdSe, CdTe, CuInS₂, Cu₂S and PbS. They are of the right size to produce a quantum confinement of the exciton in the absorber material leading to a size-dependent absorption spectrum. Depending on their particle size, these materials can absorb photons over a broad spectral range or within a confined window of the solar spectrum [65]. The replacement of the light harvesting material in a standard DSC involves modification of other components to preserve the favourable band alignment for charge separation, charge transfer processes, and stability. For example, the I⁻/I₃⁻ redox couple employed in standard DSCs is not chemically compatible with quantum dots leading to fast degradation of the nanocrystals [66]. As of 2012 cell efficiencies of 5.4% have been achieved [67].

1.8 The Redox Electrolyte

The function of the redox couple in the electrolyte is to reduce the dye cation after electron injection as well as to carry charge between the electrodes. The redox couple most often employed is the I⁻/I₃⁻ couple and in this case the oxidised dye is reduced by the I⁻ ion, which is in turn oxidized to I₃⁻. The I₃⁻ ions must then diffuse towards the platinised counter electrode where they can be reduced by electrons from the external circuit. The I⁻ created at the counter electrode must then diffuse towards the photoanode [68]. In order to achieve rapid regeneration of the oxidized dye, I⁻ should be present in high concentration or diffusion of I⁻ should be fast. In non viscous electrolytes such as acetonitrile, an iodide concentration of 0.3 M is sufficient, while in viscous ionic liquids a higher concentration may be necessary [69].

The cations of the I⁻/I₃⁻ couple and the solvents used to dissolve them, both have influence on electrolyte properties. Different cations such as H⁺, Li⁺, K⁺ or Mg²⁺ alter the conduction band energy of the TiO₂ by adsorption onto the surface [70]. Faster dye regeneration is observed when using electrolytes containing cations that adsorb at the TiO₂ surface which has been attributed to a higher local concentration of the iodide anion near the

TiO₂/electrolyte interface [71]. Organic solvents are used to dissolve the mediators and any additives that might be included. Dipolar aprotic solvents are generally preferred due to the electrochemical stability and the solubility of the redox mediators and additives within them. The type of solvent employed can influence the flat band potential (V_{fb}) of the cell and therefore V_{OC} and due to the current being carried by mobile charge carriers, the viscosity and polarity of the solvent will also have an effect on J_{SC} [68].

Additives are often employed such as imidazolium derivatives like 1-propyl-3-methylimidazolium iodide (PMMI) to improve cell performance by decreasing the resistance of the electrolyte [72]. *Tertiary*-butylpyridine (*t*-BP) additions can improve the open circuit voltage by causing a negative shift of the TiO₂ conduction band. The increase in the open-circuit voltage and fill factor caused by *t*-BP additions is due to the suppression of the dark current at the semiconductor electrolyte interface [38].

Other redox couples have been investigated and the other halides (and pseudohalides) behave similarly. Br^-/Br_3^- [73], $SCN^-/(SCN)_3^-$ [74] and $SeCN^-/(SeCN)_3^-$ [75] redox couples have been tested with some success, as have Co^{3+}/Co^{2+} redox couples [76]. Faster redox couples such as ferrocene/ferrocenium have been employed, but these are sometimes in danger of eliminating the photovoltaic effect due to the rapid recombination of photoinjected electrons with the oxidized half of the redox couple [77].

Air and water stable room temperature ionic liquids (RTILs) are attractive as an alternative to organic solvents due to their unique characteristics such as chemical and thermal stability, negligible vapour pressure, nonflammability, high ionic conductivity and wide electrochemical window [78].

1.8.1 Gel Electrolytes and Hole Conductors

The solvents used in the electrolyte are volatile and often aggressive. Because of this, aspects such as cell sealing can become an issue as the electrolyte can leach out of the seal over time. Even if less aggressive solvents were used, a liquid electrolyte is not ideal and for ultra long term cell stability is likely that solid-state or quasi solid-state DSCs need be

developed. Electrolytes based on both organic solvents and ionic liquids can be gelled, polymerized, or dispersed with polymeric materials using gelling agents to transform the liquid electrolyte into a quasi-solid electrolyte [17]. These quasi-solid-state cells however tend to be lower in efficiency than their liquid electrolyte analogues primarily due to the lower mobility of the iodide species through the solid or quasi-solid medium and imperfect wetting of pores with the electrolyte [79]. Some interesting work was recently presented at the HOPV 2011 conference in Valencia by Satoshi Uchida in which he showed the use of hydrotalcite clay nanoparticles as a gelling agent. Uchida achieved $\eta = 10.1\%$ and good photocurrents at $J_{sc} = 18.2 \text{ mA cm}^{-2}$ due to the high ionic conductivity of the clay-gelled electrolyte [80].

Hole transport mediums such as spiro-OMeTAD have been investigated for use in DSCs since at least 1998 [81]. Spiro-OMeTAD refers to: 2,2',7,7'-tetrakis-(N,N-dimethoxyphenylamine)9,9'-spirobifluorene and is shown in figure 1.12 below. The method of charge transport differs from standard DSCs in that the transfer of charge is electronic (electron hopping – see figure 1.12) rather than ionic diffusion.

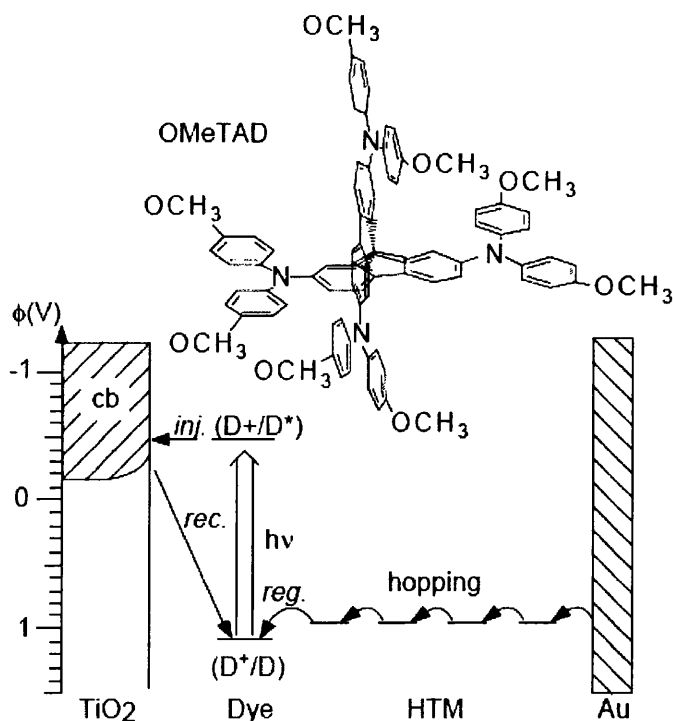


Figure 1.12 Chemical structure of spiro-OMeTAD and electron-transfer scheme showing electron hopping through the HTM – reproduced from [81]

The basic DSC electron transfer processes, the cell architecture and the materials used have now been described. This chapter will now describe the electron transfer processes in greater detail.

The electron transfer processes described so far have mostly concentrated on beneficial processes i.e. those processes that contribute towards generating photocurrent. There are however, loss mechanisms which compete with the beneficial transfer processes.

Figure 1.13 describes an overview of the electron transfer processes with the beneficial transfers in green and detrimental transfers in red. The time constants for these transfer is also shown which is important as in high efficiency cells, the detrimental processes must occur much more slowly relatively to the beneficial processes.

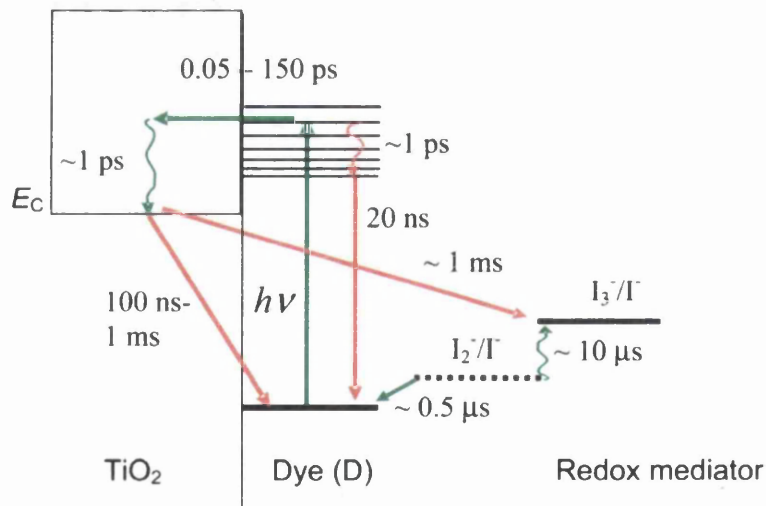


Figure 1.13 Overview of the electron transfer processes in a DSC with the time constants of the beneficial processes in green and detrimental processes in red – reproduced from [71]

Electronic injection is extremely fast with charge transfer to the TiO_2 conduction band from ruthenium sensitizers being achieved in as little as 20 fs [82]. This is fast enough to compete with the excited state decay of S^* which has a half life of as much as 2 μs when measured in

a model system using transient absorption spectroscopy [83]. In a complete DSC however, S^* decay may be as fast as 150 ± 50 ps [84]. Electron injection is also much faster than recombination of conduction band electrons with the electrolyte or oxidised dye which occur in the μ s to ms domain.

Regeneration of the oxidized dye can be summarised in two steps (equations 1.1 and 1.2 below), where in the first step an intermediate, $[\text{dye}^+, \text{I}^-]$, is formed. Equation 1.1 is fast (ca. 500 ns) whilst equation 1.2 is at least an order of magnitude slower and so it is the rate determining step and occurs usually in the μ s domain [85].



In order to achieve an efficient as possible reduction at the Pt counter electrode, the charge transfer resistance should be less than $1 \Omega \text{ cm}^2$.

1.10 Industrialisation and Scale-Up of DSC Technology

The manufacture of DSC test cells in the laboratory can take almost 24 hours due to various heat treatments and an overnight dyeing step. This is not however compatible with the industrialisation and scale up of DSC modules, especially if considering roll-to-roll manufacturing processes. Fortunately work has been carried out to try and speed up the “rate limiting steps” in the manufacturing processes of large area DSC modules.

The first step to be considered is the sintering of the TiO_2 , which in the laboratory involves a heat treatment that takes around 30 minutes (plus cooling time). This is obviously an impossibly slow step to be directly translated onto a roll-to-roll process. Work in Swansea University has offered a solution to this problem by rapidly sintering the TiO_2 photoelectrode by the application of near infra-red radiation (NIR) [86]. It has been shown that sintering is achievable in just 12.5 s and that the cells were virtually identical in performance to those produced using the conventional heating method. This is promising

for the fast processing of DSCs on a metal substrate but it should be noted that this method will not work on glass as it is transparent to NIR.

The next step, dyeing of the TiO₂ which is usually carried out overnight in the laboratory, is another step which cannot translate to the production line. Faster dyeing has been achieved by Hinsch [87] and Sommeling [88] in which they achieved dyeing in 30-60 minutes but recent work has reduced the dyeing time to 5 minutes using a pumping procedure [59]. Using this method, co-sensitization has been achieved with resulting efficiencies greater than that of either dye individually. Collaborations between Swansea University and Bangor University have also resulted in the development of a technique to monitor dye uptake in-situ [86]. This is something which will be of interest to process engineers setting up manufacturing pilot lines.

1.11 DSC Measurement Techniques

There is an obvious need for the development of suitable measurement techniques for the characterisation of DSCs, not just to measure basic cell operating parameters, but also to delve, with great precision and detail into the processes that occur within the cell so that a greater understanding of the mechanisms involved in photocurrent generation can be achieved. Some of these techniques are the same as those used to characterise older PV technologies such as IV and IPCE measurements but they often have to be adapted, usually by slowing scan rates, due to the photoelectrochemical nature of DSC devices. Other techniques come from electrochemistry such as EIS and from photochemistry and physics such as transient absorption spectroscopy and intensity modulated photocurrent spectroscopy (IMPS).

1.11.1 IV Measurements

Standard IV measurements are conducted under a light intensity of 1 Sun (1000 W m⁻²) with spectral matching to ASTM G173-03 [89] or Air Mass 1.5 (AM 1.5) as it is more commonly

referred to. DSCs are often measured at lower light levels as efficiency can increase at lower light intensity. Figure 1.14 shows a typical IV curve. The IV scan can be carried out in the direction of I_{SC} to V_{OC} or *vice versa* but the scan rate must be slower than Si-PV cells to allow for the diffusional processes that occur within a DSC device. The important points on the IV curve are therefore:

1. I_{SC} is the short circuit current, at this point the voltage of the cell is zero and therefore, the power output is also zero.
2. V_{OC} is the open circuit voltage at this point the current (and power output) is zero.
3. P_{MAX} is the maximum power point and is the product of V_{MAX} (maximum voltage) and I_{MAX} (maximum current)

The solar to electrical energy conversion efficiency ($\% \eta$) can be calculated from the short circuit photocurrent density (J_{SC}) measured in $A\ m^{-2}$, the fill factor (FF), V_{OC} and the intensity of incident light (P_{in}). The fill factor is the quotient of the actual maximum power point and the theoretical maximum power point. The theoretical maximum power point is the product of J_{SC} and V_{OC} and so FF is given by:

$$FF = \frac{J_{MAX} \cdot V_{MAX}}{J_{SC} \cdot V_{OC}} \quad (1.3)$$

The $\% \eta$ is therefore given by:

$$\% \eta = \frac{J_{SC} \cdot V_{OC} \cdot FF}{P_{in}} \quad (1.4)$$

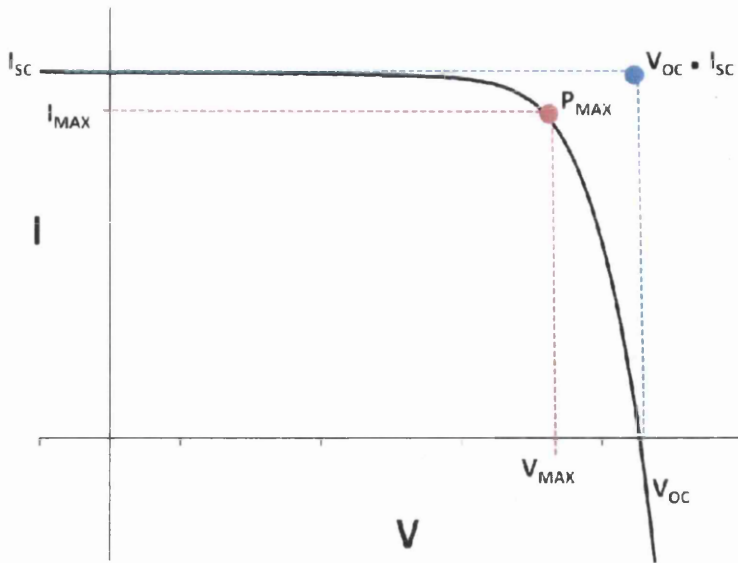


Figure 1.14 Typical DSC IV curve showing important values for calculating cell parameters

1.11.2 IPCE Measurements

The incident-photon to current conversion efficiency (IPCE) is a measure of the spectral responsiveness of a photovoltaic device. The J_{sc} of a device is measured at differing wavelengths by a monochromatic light source and divided by the incident photon flux at that wavelength. The resulting IPCE values can be plotted against wavelength to give a plot such as the normalised IPCE plot of an N719-dyed cell shown in figure 1.15 below.

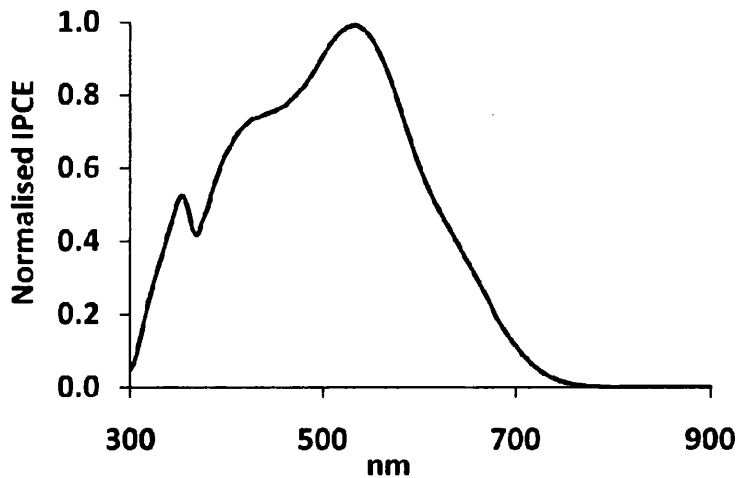


Figure 1.15 Normalised IPCE spectrum of an N719-dyed DSC device

1.11.3 Impedance Spectroscopy

The electrochemical impedance spectroscopy (EIS) of DSCs is research topic in itself and there have been many papers written on EIS characterization of DSC devices. For a more detailed description, refer to the recent works by Bisquert, Fabregat-Santiago and Halme [90-97]. The advantages of impedance spectroscopy is that it allows an understanding of the electron transfer and transport processes in complete DSC devices.

In EIS a bias potential is applied to a system which is perturbed by a small sine wave modulation, usually $\pm 5-10$ mV relative to the bias potential, the resulting sinusoidal current response is then measured as a function of modulation frequency. The sinusoidal bias perturbation and consequent current response is shown in figure 1.16 below.

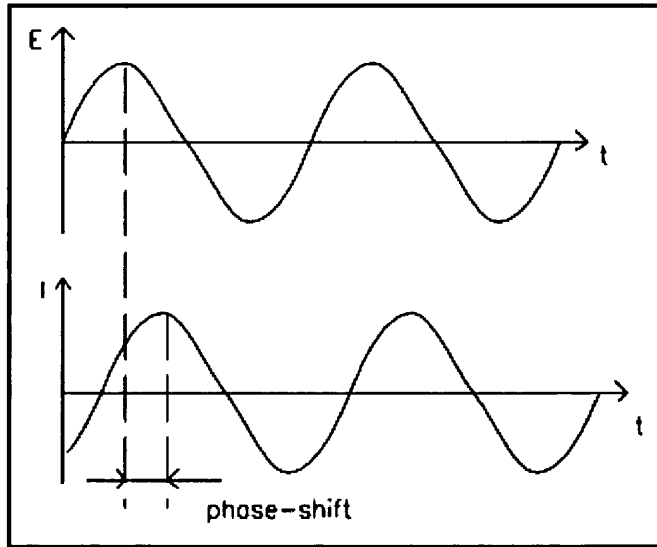


Figure 1.16 Sinusoidal bias perturbation and consequent current response in a system being measured by EIS

The modulation signal as a function of time can be expressed as:

$$E_t = E_0 \sin(\omega t) \quad (1.5)$$

Where E_t is the potential at time t , E_0 is the amplitude of the signal and ω is the radial frequency. In a linear system the response signal is phase shifted by magnitude, ϕ and has amplitude I_0 and so, current response, I_t , is given by:

$$I_t = I_0 \sin(\omega t + \phi) \quad (1.6)$$

Analogously to Ohms law, the impedance, $Z = E_t/I_t$ and so can be expressed as:

$$Z = \frac{E_t}{I_t} = \frac{E_0 \sin(\omega t)}{I_0 \sin(\omega t + \phi)} = Z_0 \frac{\sin(\omega t)}{\sin(\omega t + \phi)} \quad (1.7)$$

The impedance is therefore expressed in terms of magnitude, Z_0 and a phase shift ϕ .

It is possible, using Euler's formula (equation 1.8) to express impedance as a complex function.

$$e^{j\phi} = \cos\phi + j\sin\phi \quad (1.8)$$

Where j is the imaginary unit, so that the potential is given by:

$$E_t = E_0 e^{j\omega t} \quad (1.9)$$

And the current response given by:

$$I_t = I_0 e^{(j\omega t - \phi)} \quad (1.10)$$

The impedance therefore becomes the complex number described by:

$$Z(\omega) = \frac{E}{I} = Z_0 e^{j\phi} = Z_0(\cos\phi - j\sin\phi) \quad (1.11)$$

Impedance therefore, has a real part and an imaginary part and if the real part is plotted on the x-axis and the imaginary part on the y-axis then the result is the Nyquist plot. Figure 1.17 shows a typical Nyquist plot that would be gained from a resistor/capacitor pair wired in parallel (shown inset in figure 1.17). Every point on the plot represents the impedance at a particular frequency with higher frequencies on the left hand side of the plot and lower frequencies on the right hand side. The impedance can be represented by a vector of length $|Z|$ (shown as blue arrow in figure 1.17).

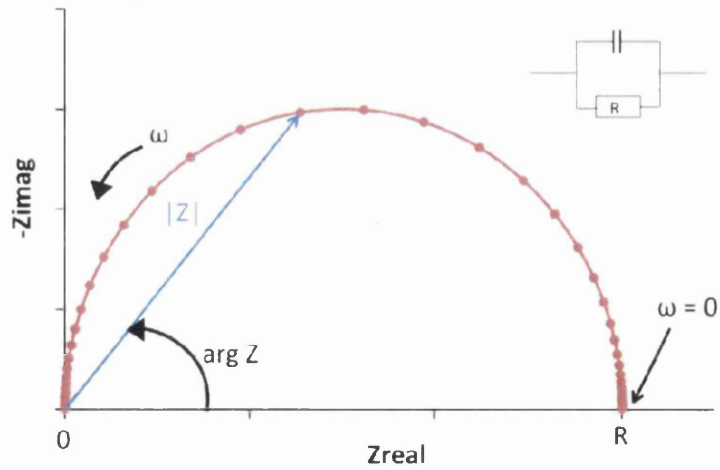


Figure 1.17 Nyquist plot of a resistor/capacitor in parallel, showing impedance vector

Other ways of presenting impedance data are the Bode phase and magnitude plots. For both plots, the impedance is plotted with $\log \omega$ on the x-axis. For the phase plot, the phase shift is plotted on the y-axis and for the magnitude plot, the absolute impedance, $|Z|$ is plotted on the y-axis.

Figure 1.18 below shows the Bode magnitude and phase plots of the same resistor/capacitor pair described in figure 1.17 but unlike the Nyquist plots, Bode plots show frequency information.

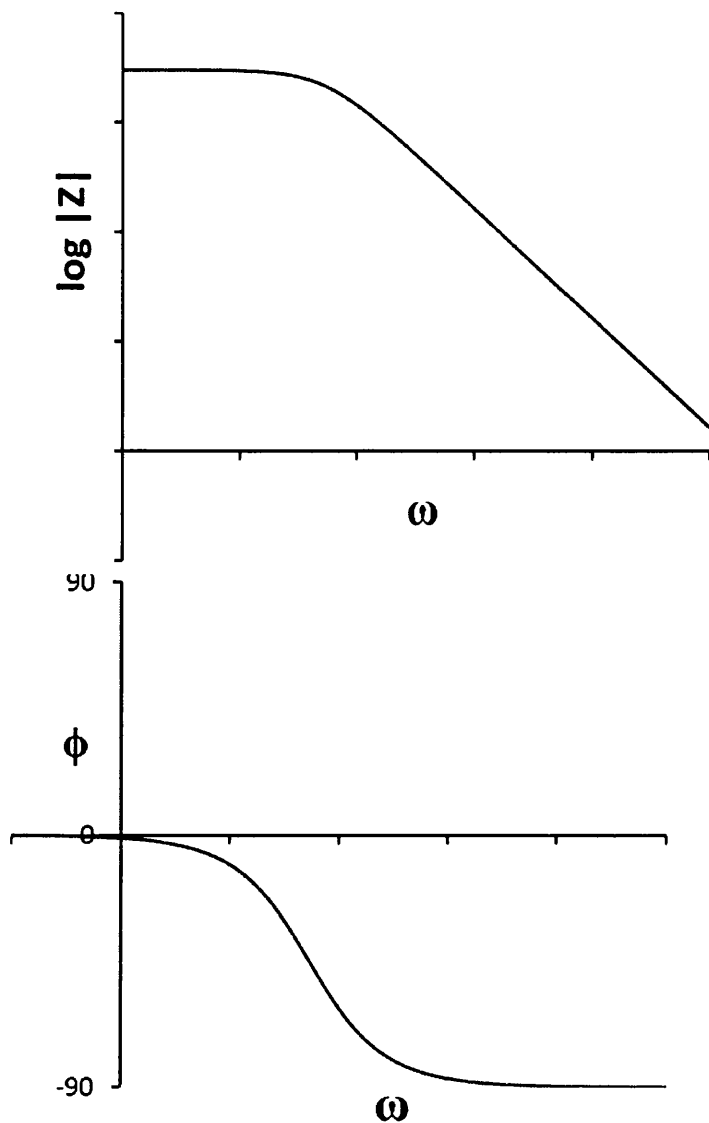


Figure 1.18 Bode magnitude plot (above) and Bode phase plot (below) of resistor/capacitor pair in parallel

1.11.3.1 Impedance Spectroscopy of DSCs

A typical Nyquist plot of a DSC device measured with a bias potential near V_{MAX} will look similar to that which can be observed in figure 1.19 below. The smaller of the two arcs is representative of the resistance at the counter electrode/electrode interface, R_{ce} whilst the larger of the arcs is representative of a charge transfer resistance related to recombination of electrons at the TiO_2 /electrode interface and is denoted by R_r . There also may be a third

arc at the lower frequency end which is representative of the Nernst diffusion impedance. This is often hidden by the R_r arc, and in fact it can be seen that there is a small distortion of the R_r arc on the right hand side which is caused by the Nernst diffusion arc. The spans of the arcs on the x-axis give the values for that particular resistance. The length along the x-axis from $Z_{real} = 0 \Omega$ to the start of the R_{ce} arc gives the series resistance, R_s which is the resistance across the TCO and electrical contacts.

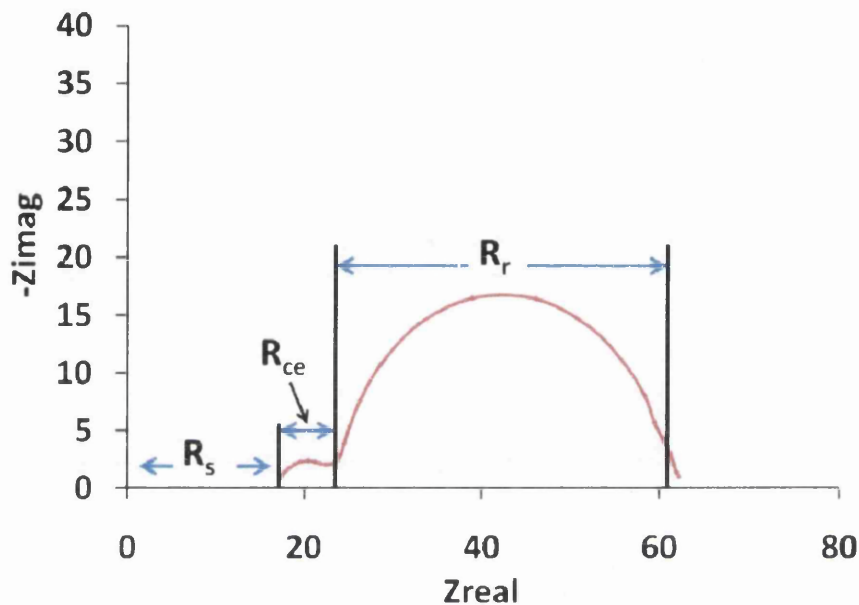


Figure 1.19 Typical Nyquist plot of a DSC device held at a bias potential near V_{MAX} with the corresponding resistances shown

In order to interpret the data more effectively, a model is often used to try and explain the resistive, capacitive and diffusional electronic processes that are occurring within the cell. The models describe the internal distribution of electrochemical potential in response to the modulated perturbation of the external electrical potential at steady state [94]. So where there may be some capacitance at one of the interfaces in the cell, the model will have an element relating to the impedance of a capacitor (equation 1.12) to describe it.

$$Z = \frac{1}{j\omega C} \quad (1.12)$$

An easier way to model impedance data is to use equivalent circuit models. Most impedance data analysis packages have a model editor where the operator can fit a circuit

element such as a capacitor to a graphical representation of an equivalent circuit. Figure 1.20 shows a simple equivalent circuit which can be used to model the data in figure 1.19.

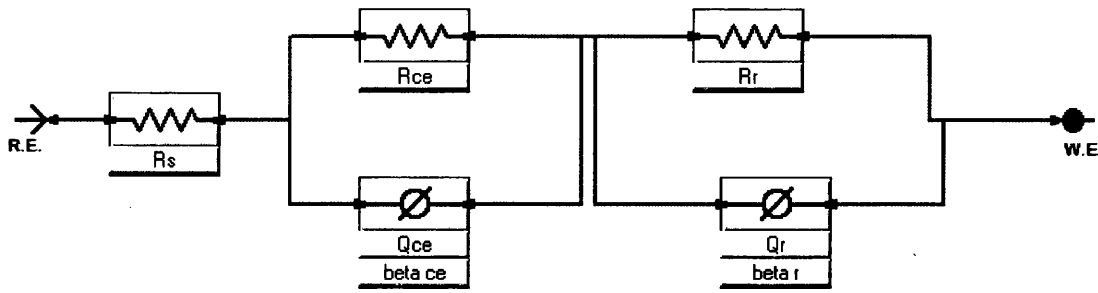


Figure 1.20 Equivalent circuit, as modelled with Gamry's Echem Analyst software

In the model above the series resistance is represented by a single resistor, R_s . The counter electrode/electrolyte interface is represented by a resistor, R_{ce} and a constant phase element which models capacitance in a non-ideal capacitor, this is represented by two values, Q_{ce} and β_{ce} . The TiO_2 /electrolyte interface is modelled by another resistor, R_r and another constant phase element with parameters, Q_r and β_r .

As mentioned, the constant phase element (CPE) represents the capacitance in a non-ideal capacitor. Mathematically the impedance of a CPE is given as:

$$\frac{1}{Z} = Q^\circ (j\omega)^\beta \quad (1.13)$$

Numerically Q° has the same value as admittance ($1/|Z|$) when $\omega = 1 \text{ rad s}^{-1}$. The units of Q° are $S \cdot s^\beta$ where S = Siemens and s = seconds. The β value is a factor describing the ideality of the CPE with respect to capacitance so if $\beta = 1$, then the impedance is equal to that of a capacitor i.e. $Q^\circ = C$ (see equation 1.12). In some cases the equivalent capacitance, C_{eq} can be calculated from the CPE parameters and the impedance of its resistor partner using the following equation:

$$C_{eq} = \frac{(R \times Q^\circ)^{1/\beta}}{R} \quad (1.14)$$

The equivalent circuit model shown in figure 1.20 usually makes a good fit, especially when fitting the double-arc Nyquist plot seen in figure 1.19. It is however obvious that there is no element that describes the Nernstian diffusion of ions in the electrolyte, so care should be taken then when using this model, to only fit it to data points which correspond to the impedance at the TiO_2 /electrolyte interface and the counter electrode/electrolyte interface.

1.11.3.2 Modelling using the Transmission Line Element

In the previous section it was stated that the larger impedance arc of the Nyquist plot shown in section 1.19 is representative of the TiO_2 /electrolyte recombination resistance, R_r . This however, is not strictly true as this complex impedance arc is also influenced by the resistance of electron transport through the film, R_t . This is perhaps easier to visualise when looking at the transmission line model (figure 1.21). In figure 1.21, the lighter grey area represents filling by the electrolyte into a TiO_2 pore (the TiO_2 is shown as a dark grey area). It can be seen that at any point where the electrolyte is in contact with the TiO_2 , there is a chance of recombination and the impedance across that interface is represented by a resistance, r_r and a (chemical) capacitance c_μ . This is just as it was in the simplified model (figure 1.20 above). However in the in the transmission line model there is also the transport resistance though the film, r_t . The number of these repeating units depends on the film thickness, L and so because r_t is in series, the total transport resistance, R_t is defined as $R_t = r_t L$. Conversely as c_μ and r_r are in parallel, total recombination resistance, $R_r = r_r / L$ and total chemical capacitance, $C_\mu = c_\mu L$.

To summarise, the elements in this model are: $C_\mu (=c_\mu L)$, the chemical capacitance that stands for the change of electron density as a function of the Fermi level. $R_t (=r_t L)$, the electron transport resistance. $R_r (=r_r / L)$, a charge-transfer resistance related to recombination of electrons at the TiO_2 /electrolyte interface. R_s , a series resistance accounting for the transport resistance across the TCO. R_{TCO} is a charge-transfer resistance for electron recombination from the uncovered layer of the TCO to the electrolyte. C_{TCO} is the capacitance at the triple contact TCO/ TiO_2 /electrolyte interface. $Z_{d(\text{sol})}$ is the impedance of diffusion of redox species in the electrolyte. R_{Pt} is the charge-transfer resistance at the

counter electrode/electrolyte interface and C_{Pt} is the interfacial capacitance at the counter electrode/electrolyte interface [94].

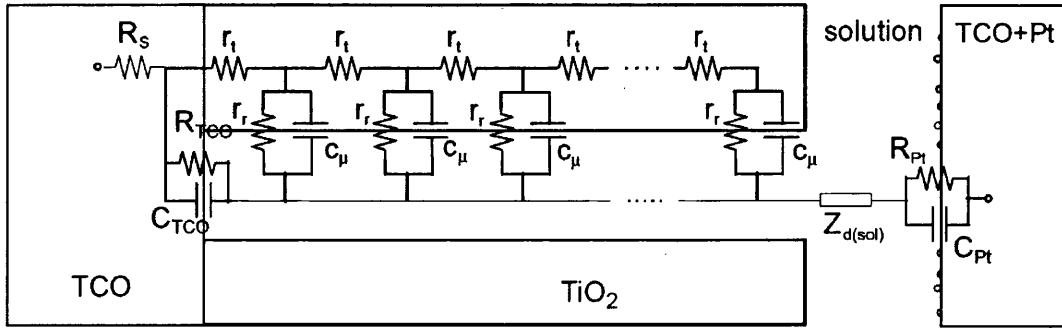


Figure 1.21 Transmission line model of DSC – reproduced from [94]

The impedance of the transmission line model can be described as:

$$Z = \left(\frac{R_t R_r}{1 + i\omega/\omega_k} \right)^{1/2} \coth \left[(\omega_k/\omega_d)^{1/2} (1 + i\omega/\omega_d)^{1/2} \right] \quad (1.15)$$

Where $\omega_d = D_n/L^2 = 1/R_t C_\mu$ and is the characteristic frequency of diffusion in a finite layer (D_n being the electron chemical diffusion coefficient), $\omega_k = 1/R_r C_\mu$ is the rate constant for recombination, ω is the angular frequency and $i = \sqrt{-1}$ [94].

Fortunately the transmission line model is incorporated into some model editing software. For example, Gamry's Echem Analyst package incorporates it in to three different elements:

- Bisquert Open (BTO), which models L , r_t , r_r , Q_r and β_r , measured under open circuit conditions
- Bisquert Short (BTS), which models the same as above but under short circuit conditions
- Unified (UTL), which models the above plus $Z_{d(sol)}$ and the triple contact TCO/TiO₂/electrolyte interface.

The principles of the transmission line model and its theoretical basis has been explained figure 1.22 shows how the transmission line model manifests itself in the raw data. Figure

1.22 shows a Nyquist plot of a device and it can be seen that there is a short straight line of 45° slope between the R_r and R_{ce} arcs. This is a characteristic of $R_t < R_r$ and the length of the straight line along the x-axis is equal to $R_t/3$. This feature is shown in Figure 1.22 below.

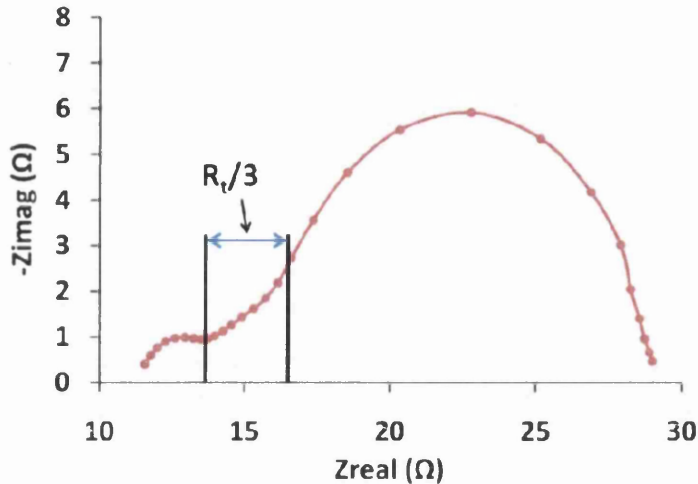


Figure 1.22 Nyquist plot showing 45° line between the R_r and R_{ce} arcs which is a characteristic of $R_t < R_r$. The length of this line along the Z_{real} axis is equal to $R_t/3$

It has been shown that EIS can be used to monitor photodegradation in DSCs. Reported trends include a reduction in R_r and an increase in C_{μ} during light soaking tests [98].

1.12 DSC Stability

For anyone working towards the industrialisation of DSC, stability is perhaps one of the greatest challenges faced. Looking at the cell architecture and components described so far, a number of potential stability issues can be postulated.

First of all the semiconductor is a potent photocatalyst and the photocatalytic properties of TiO_2 are well documented [99101]. The photocatalytic reactions may proceed *via* several steps [102], the most important of which is the production of electron-hole pairs by direct excitation of the TiO_2 with UV light. This results in a redox process, creating radicals which

can ultimately result in degradative attack on organic molecules in the vicinity of the TiO_2 [31]. The dye can be organometallic or organic, as are components of the electrolyte. All organic compounds within the cell either adsorb or have the potential to adsorb onto the TiO_2 surface meaning that all these components will be susceptible to UV photocatalytic degradation. The I^-/I_3^- redox couple may also be susceptible to UV catalysed photodegradation. In DSCs however the hole in the TiO_2 conduction band is said to be quenched by the iodide ion in the electrolyte, but it has been reported this still leaves the possibility of side reactions occurring with residual oxygen leading to attack on the dye surface groups [87].

The seal most of often used to seal the cell is a thermoplastic such as Surlyn or Bynel, both from DuPont. Two potential problems could be foreseen here. Firstly the electrolyte often contains some fairly aggressive and volatile solvents which have the potential to leach or evaporate out through the seal. Secondly, the transmission rates of the seals may not be good enough to prevent solvent evaporation out of the cell or indeed to stop the ingress of H_2O and O_2 into the cell. For long term stability a water vapour transmission rate (WVTR) of less than 10^{-6} $\text{g}/\text{cm}^2/\text{day}$ is probably needed. One approach to solve the sealing issues has been investigated by Andreas Hirsch where he has shown the sealing of cell modules using glass frit [103].

One of the problems of studying DSC stability is that there seems to be no defined test methods or indeed any well defined measure of stability. Is a cell considered stable if it loses 5% relative η over the test period, or is it 10% or indeed 20%? Which cell parameters are measured to assess stability? It seems efficiency decreases alone are not enough and that other parameters such as J_{SC} , V_{OC} and FF should also be measured to try and gain a better understanding of degradation processes [104]. Impedance data also can be used as it has been shown that the resistive and capacitive properties of the cell interfaces change under ageing tests [98]. Although there are no defined tests, there are some common tests employed such as heat cycling stability tests in the dark, visible light soaking at 1 sun with or without elevated temperatures, UV stability tests and humidity tests [104].

1.12.1 Sensitizer Stability

As the sensitizing dye is attached to the TiO_2 *via* an organic moiety it is perhaps understandable why DSC stability studies focussed initially on the stability of the sensitizer. As early as 1997, work was being conducted by Grätzel's group in which they ascertained that certain Ru sensitizers would be stable for 10^7 to 10^8 redox cycles giving a predicted lifetime of over 20 years [105] but it has been shown using photocurrent mapping techniques that localised degradation occurs in unmasked parts of a partially masked cell when exposed to light soaking conditions [106]. Another aspect of sensitizer stability work is focused on stability at elevated temperatures which has been linked to dye desorption [87; 88], this is important for BIPV applications as roof temperatures in summer (even in the UK!) can reach 80°C .

1.12.2 Loss of Triiodide from the Electrolyte

Depletion of I_3^- has been observed in DSC cells subjected to outdoor testing as evidenced by an increase in the Nernst diffusion impedance, and changes to the cell's Raman spectra [107] and it has been shown that in extreme cases decreased I_3^- can cause a reduction in J_{sc} by diffusion limitation [108]. The mechanism of I_3^- consumption has been suggested as either the sublimation of iodine [109], or perhaps the formation of iodate by reactions with water or other impurities in the electrolyte [110]. It appears however that I_3^- depletion could be as a result of a photoreactions as in a study by Sommeling *et al* it was found that electrolyte bleaching occurred rapidly in illuminated cells held at 85° but did not occur in cells held at 85°C and kept in the dark [88].

1.12.3 H_2O and O_2 Ingress

Water can have a serious negative impact upon the chemical stability of a DSC as the ester linkages of the carboxylic acid groups adsorbed onto the TiO_2 surface can be hydrolyzed.

Because of this, hydrophobic dyes such as Z907 can be employed which have aliphatic chains which prevent water adsorption onto the TiO_2 surface [111].

It is thought that oxygen present inside the DSCs can oxidize the organic components of the DSCs. It has also been suggested that I_3^- can be irreversibly oxidized to IO_3^- due to oxidative surface states. Many hypotheses regarding degradation of DSCs involve the presence of water or oxygen [104]. There exists the possibility that trying to keep oxygen and water out of the cell may make DSCs economically unviable due to the costs of special materials and processes. Instead of trying to keep water and oxygen out of the cell, the solution may be to live with water in the cell, and so some research groups are investigating water stable dyes and aqueous electrolytes [112].

1.12.4 Counter Electrode Degradation

It has been shown that Pt can be prone to dissolution or anodic corrosion in the presence of iodide, with obvious consequences for long-term stability [113]. The degradation of the counter electrode may be due to a poor contact between the Pt and the TCO or impurities which could lead to detachment of the Pt particles. Counter electrode performance can be monitored with EIS [104].

1.12.5 Visible and UV Light Soaking

Although there are no standard tests for DSC stability, a common accelerated ageing test often performed is visible light soaking. DSC cells perform remarkably well under visible light soaking conditions and in 2008, Dyesol reported cells remaining efficient after 20000 hours visible light soaking [114]. However, care should be taken when using visible light soaking results to infer outdoor stability. For instance, the emission spectra of the two leading suppliers of light soaking cabinets do not emit significantly in the UV region compared to the AM 1.5 spectrum and in a system where a potent UV activated photocatalyst that is surrounded by organic chemicals is unwise to exclude UV light from

simulated tests. Furthermore, it has been shown that DSCs can degrade quickly under UV illumination [115] and that filtering at $\lambda < 384$ nm improves the stability of a DSC cell [116]. This suggests that the photo-catalytic properties of the TiO_2 contribute at least in part to the degradation of the DSC. UV filtering has not been the only method employed, in 2001, Hinsch showed that MgI_2 additions to the electrolyte improved UV stability. It was found that as well as increasing UV stability, the MgI_2 additions lowered the photovoltage of the cell suggesting that the TiO_2 surface polarity might play a role in UV stability of the cell and the photoreactivity of the TiO_2 [87]

A number of trends have been reported during long term and accelerated tests. These include an increase in J_{SC} and a decrease in V_{OC} [117]. Electrochemical impedance spectroscopy (EIS) has also been used to monitor degradation and it has been shown that the modelled resistance of the recombination resistance decreases concurrently with the increase in J_{SC} and that the drop in V_{OC} is due to a positive shift in the TiO_2 conduction band [98]. Impedance spectroscopy has also shown that the Nernst diffusion impedance of triiodide (I_3^-) increases as a result of the change of the components of the electrolyte during long term outdoor testing [107].

1.13 Photodegradation of Polymer Films

Part of this project is to look at the photostability of clear polymer films intended for use as the counter electrode and topsheet (encapsulation) materials. The following chapters will look at the photodegradation in general and specifically that of polymers.

1.13.1 Mechanisms of Photodegradation

Photodegradation in polymers arises from photochemical excitations which occur in one of two ways: *Homogeneous excitation* occurs in organic molecules containing chromophores (conjugated π -systems, azo compounds, etc) whereby a chromophore will absorb photons in the UV spectrum leading to a breakdown in structure. *Heterogeneous excitation* occurs

where semi-conducting materials such as TiO_2 absorb photons to produce high energy excited states which can destroy surrounding polymer matrices [118; 119].

1.13.1.1 Homogeneous Excitation

The basis of photodegradation by homogeneous excitation occurs when ground state electrons in the valence band of a chromophore become excited through the absorption of a photon and become promoted to the conduction band. This excited state is referred to as an excited singlet state (S^*) and for this to occur the photon must have an energy equivalent or greater than the band gap.

The electron is unstable in its excited state and will seek to lose its absorbed energy as quickly as possible to return to the ground state. The excited electron can achieve this in a number of ways (see the Jablonski diagram, figure 1.23). The most common deactivation route is through internal conversion (IC) back to the ground state which occurs where energy is lost thermally. Energy can also be lost through inter-system crossing (ISC) which creates excited triplet states which are much longer lived and can undergo bond cleavage.

The relative importance of the different deactivation pathways depends upon the absorbing chromophore; aromatics usually undergo fluorescence whilst carbonyls tend to undergo inter system crossing and create a triplet excited state (T). It is the bond cleavage reaction that is of interest since it is this process that generates the free radicals, which ultimately lead to degradation.

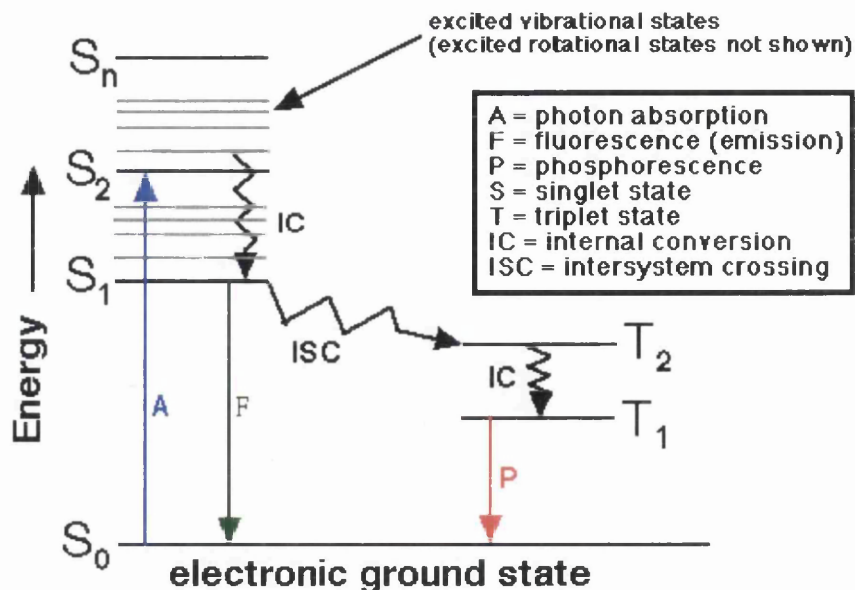


Figure 1.23 The Jablonski diagram illustrating the pathways to deactivation of the excited singlet state (S^*) [120]

1.13.1.2 Activation of TiO_2

TiO_2 is largely chemically inert and is commonly found as a pigment in paints or even toothpaste but in the presence of UV light it is a potent photocatalyst for many reactions including those which will eventually lead to degradation of organic chemicals adsorbed to or in the vicinity of TiO_2 particles. There are three proposed mechanisms all involving photosensitized oxidation of surrounding polymer/organics. One theory involves the formation of oxygen radical anions through electron transfer from the excited titanium dioxide (equation 1.16). Further to this it has been suggested that singlet state oxygen (1O_2) could be formed by ion annihilation (equation 1.17). The ion radicals or the singlet oxygen then react with water to form hydroxyl and perhydroxyl radicals (equation 1.18), these are highly reactive species that cause the degradation of surrounding polymers [121]

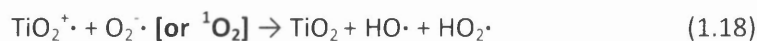


Figure 1.24 below gives a graphic representation of the above reactions. Note that the oxygen radical is formed by reduction by excited electrons in the conduction band. This goes on to form the perhydroxyl radical that attacks the organic coating. The hydroxyl radicals are formed by oxidation at the positive gap left by excited electrons in the valence band. The HO· radicals attack the coating producing measurable by-products such as CO₂ and HCl.

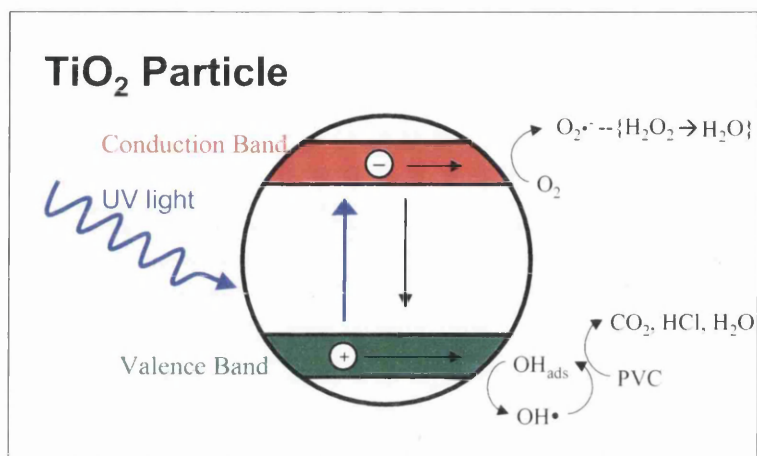


Figure 1.24 Graphical representation of TiO₂ photosensitized-oxidation of polymers

1.13.2 Mechanisms of Photodegradation of Polymers

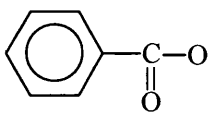
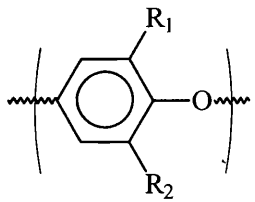
Polymers in general are fairly stable materials, although when exposed to the physical effects of the environment, some chemical and/or physical changes will gradually occur. The occurrence and rate of these changes is primarily dependent on the intensity and wavelength of any UV irradiation [122; 123]. These changes can be induced either homogeneously or heterogeneously and the distinction between these two routes lies in the presence and classification of any chromophore. These chromophores can be either organic or inorganic and are present as pigments, part of the structure or act as external impurities. When considering the absorption and emission properties of manmade polymers they can be classified as one of two types (table 1.2 below). Type A polymers absorb and emit light through isolated chromophores situated as in-chain or end-chain groups. Type B polymers

absorb and emit chromophores present in the repeating units of the backbone structure of the polymer [124].

Figure 1.25 below shows the absorption spectra of many common polymers. It is clear that Type A polymers, with the exception of polystyrene, do not absorb light below 290nm. This value is critical as this is the lower limit of sunlight reaching the earth's surface. It would not therefore be expected that these polymers should degrade under normal UV light conditions, but they do degrade and this is due to a number of factors. The absorption spectra in figure 1.25 are for pure polymers, it doesn't take into account the light scattering abilities of crystallites, particularly at shorter wavelengths. Processing, manufacture and fabrication leave polymers susceptible to thermal degradation and oxidation, operations which can significantly increase the light absorbing capacity of the polymer by introducing chromophores such as extended saturation and carbonyl groups. It is now accepted that impurities introduced during polymerisation and processing are responsible for the absorption of Type A polymers above 290nm. Type B polymers as shown in figure 1.25 clearly absorb in the visible and near-UV regions of the spectrum and so are susceptible to photodegradation with no impurities present [121].

Table 1.2 Type A and Type B polymers

| Type A Polymers | |
|---|-------------------------|
| <u>Typical chromophoric groups</u> | <u>Typical polymers</u> |
| ---C=C---C=C--- | Poly(vinyl halides) |
| $\begin{array}{c} \text{---C---} \\ \parallel \\ \text{O} \end{array} \text{---} \text{---C=C---} \begin{array}{c} \text{---C---} \\ \parallel \\ \text{O} \end{array}$ | Polyacrylics |
| $\text{R}_1\text{OOH} \quad \text{Ti}^{+4}, \text{Al}^{+3}, \text{Fe}^{+3}$ | Poly(vinyl alcohols) |
| $[\text{R}_1\text{---H}^+\text{---O}_2^-]$ | Aliphatic esters |
| $\left[\begin{array}{c} \text{---C=C---} \\ \vdots \\ \text{O}_2 \end{array} \right]$ | Polyurethanes |

| Type B Polymers | |
|--|--|
| <u>Typical chromophoric groups</u> | <u>Typical polymers</u> |
|  | Polyethylene terephthalate |
|  | Poly(2,6-dialkyl-1,4-phenylene ether) Poly(ethersulphone) |

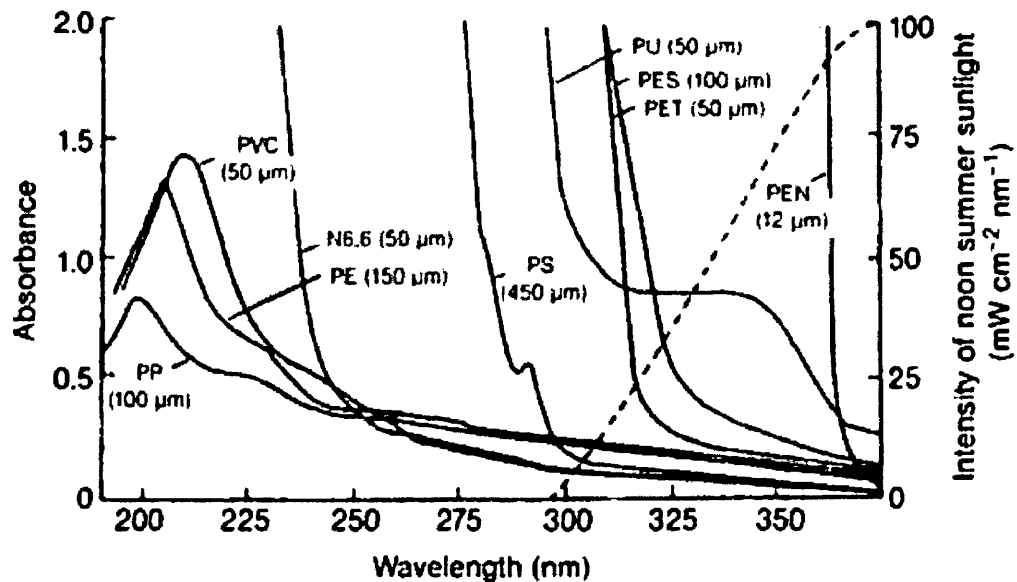


Figure 1.25 UV absorption spectra of films of type A polymers: polypropylene (PP), polyethylene (PE), polyvinyl chloride (PVC), nylon 6,6 (N6,6), and polystyrene (PS); and type B polymers: polyethersulfone (PES), polyethylene terephthalate (PET), polyethylene naphthalate (PEN,) and polyurethane (PU). The spectral emission of sunlight is shown as a dotted black line. – reproduced from [125]

Degradation mechanisms include photodegradation, photo-thermal degradation (oxidation), photo-oxidation, photolysis and photo-hydrolysis. However regardless of which degradation mechanism takes place it is widely believed that all the mechanisms involve free radical processes [125]. It is also accurate to say that for most cases the degradation processes are similar to those found in thermal degradation with the only significant difference being the initiation step and the nature of the degradation products. Figure 1.26 shows the three major steps of initiation, propagation and termination involved in the free radical process.

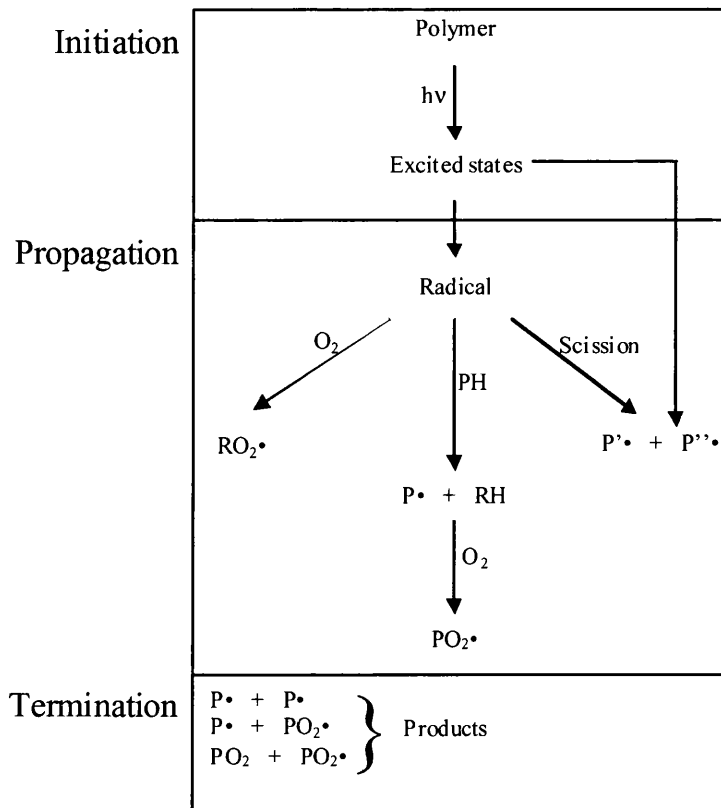


Figure 1.26 Initiation, propagation and termination of the free radical photodegradation of polymers

1.13.3 Protection from Ultra Violet Radiation

A number of ways exist, both chemical and physical to minimize the degrading effects of UV light upon polymers. There are four main mechanisms: UV screening, UV absorption, excited state quenching and free radical scavenging. The latter two of these methods are the most effective. Excited state quenching is the acceleration in some way, of the decay, of the initial excited state in order to reduce the chances of intersystem crossing and the creation of excited triplet states. Free radical scavenging involves the addition of chemical stabilisers to neutralise free radicals before they have a chance to interact with the coating, these usually have anti-oxidant properties [126]. The most commonly used method for use in commercial coatings is UV absorption.

When choosing a suitable UV absorber it is necessary to consider its compatibility. UV absorbers are organic or inorganic compounds which absorb in the best case all UV light < 400 nm, are transparent for all visible light > 400 nm, and convert the excitation energy entirely into heat [127].

There are two main types of commercial UV absorber: hydroxybenzophenones and hydroxyphenylbenzotriazoles. Hydroxybenzophenones absorb UV light to form excited states, but then release heat to return to the original ground state. This functional mechanism is characterized by an intra-molecular hydrogen transfer [128] during a keto-enol tautomerisation reaction. This reversible reaction of UV absorption and heat dissipation leaves the absorber unchanged and thus it can undergo many cycles of UV absorbance so long as no other process interferes with the reaction (figure 1.27).

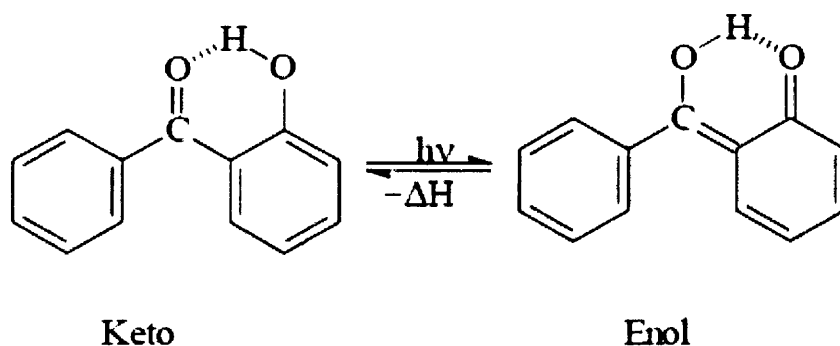


Figure 1.27 Keto-enol tautomer energy-dissipation in hydroxybenzophenones

Benzotriazoles dissipate energy by a proton transfer reaction (figure 1.28).

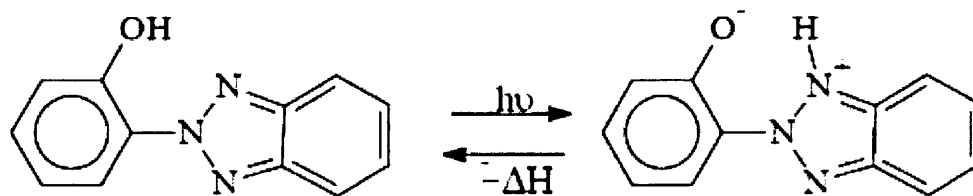


Figure 1.28 Benzotriazole stabilization mechanism in hydroxyphenyl benzotriazole

1.13.3.2 Hindered Amine Light Stabilisers (HALS)

These are relatively new components in the UV stabiliser market and are particularly effective in polymer applications. The majority of studies ascribe the function of HALS to radical scavenging by the nitroxide that can be formed by the oxidation of the HALS. The main function of HALS are to prevent radical initiation by quenching the initiating excited states [129]. HALS such as 2,2,6,6-tetramethylpiperidines (figure 1.29) inhibit oxidation by transformation of the parent amines to *N*-oxyl radicals, either by reaction with peroxy radicals or occasionally by reaction with singlet oxygen, which stops oxidative degradation by the coupling of alkyl radicals [130] (figure 1.30). HALS differ from UV absorbers in that they do not rely solely on the physical absorption of UV light, therefore their efficiency is not dependent upon them being at a high concentration on the surface of the coating.

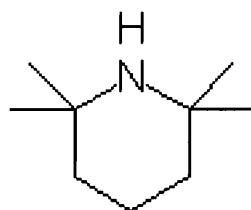


Figure 1.29 2,2,6,6-tetramethylpiperidine

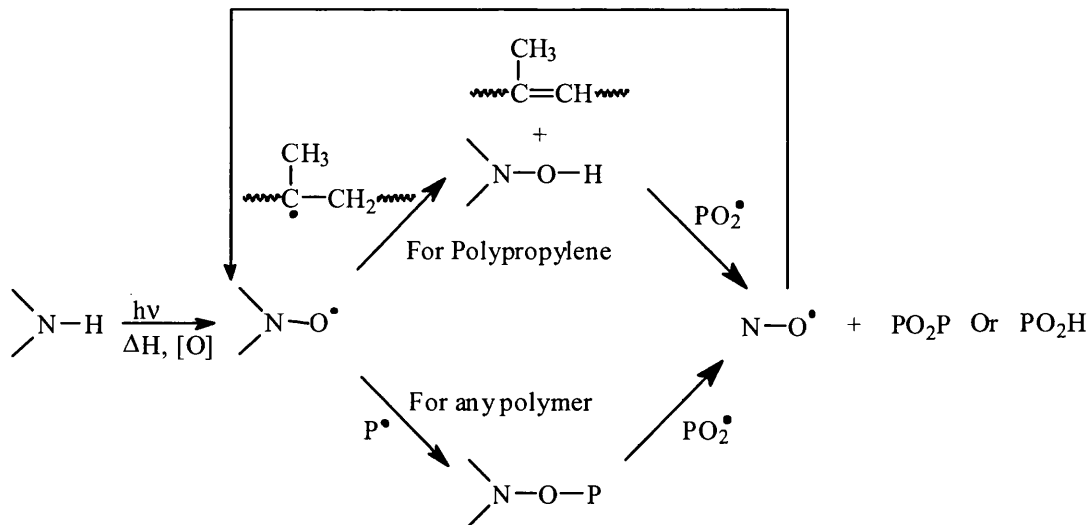


Figure 1.30 Initiation, propagation and termination of HAL stabilisation [131]

1.14 Weathering and Accelerated Testing

In order to assess the stability of the polymer films intended for use as counter electrode materials, there is an obvious need for accelerated testing to try and estimate how the films will perform in a real world environment. Ideally a test should be rapid and be accurately reflect real world performance. The most ideal method available would be to test the candidate films in the expected environment in real time. However given that materials are expected to perform for 15 years plus, this is type of testing is impracticable. Therefore it is necessary to have accelerated tests to give an accurate idea of the degradation results over a much shorter time period.

As described previously, the major influences of the environment on degradation tend to be sunlight (UV), temperature, oxygen, water and other pollutants. These factors can act either on their own or in combination and can also combine with other environmental factors such as wind and hail etc to result in coating degradation. The rate at which polymer films degrade is predominantly governed by the exposure site, temperature, rainfall and the strength of ultra violet radiation. The rate can also be accelerated by certain cycle patterns of some of the above factors. Thus it is very difficult to create an accelerated test, which mimics the varying real life environments faced by the polymer film. Current

methods used for assessing performance combine both accelerated and natural weathering tests. Accelerated tests involve the following two steps:

- 1) **The use of more extreme conditions than those expected during its service** i.e. the use of lower wavelength radiation from either xenon arc or carbon arc lamps, or through higher intensity incident radiation. However, it should be noted that this provides an unnatural environment and can lead to different chemical processes occurring within the film and thus different degradation processes being promoted than would be otherwise expected.
- 2) **Evaluation of chemical changes that are occurring within the film prior to physical manifestations of degradation.** Certain techniques such as UV-Vis are, capable of picking up on minute changes that are occurring within the polymer that can be extrapolated out to give a more rapid but accurate idea of long term performance.

1.14.1 Natural Exposure

When the environment in which the product is going to be used is known, it is possible to use one of the many testing sites around the world which gives a similar environmental effect. Typically weathering sites are situated in locations where there are climatic extremes, around the world. This allows for natural exposure but under more extreme conditions than would normally be experienced in service. This combined with novel test rigs leads to an accelerated or harsher test than would be necessary for service conditions whilst still using the forces nature. Some of the more popular climatic weathering stations around the world are: Florida, which provides a sub-tropical climate with high UV exposure, high temperature and high humidity, which gives a realistic reproducible acceleration of European climates. Arizona has a very low rainfall a hot dry climate and Hoek van Holland provides an environment that is both industrial and marine in nature.

1.14.2 Artificial Exposure Methods

The main advantage of using a completely artificial exposure technique is that it is fully controllable, defined and reproducible. However it can only be useful if all the degradation processes that occur are accelerated at the same rate. The use of radiation of a higher energy than that of natural exposure (figure 1.31) has the added complication of introducing new higher energy photochemistry's that do not occur under normal conditions. The commercial accelerated techniques available usually use one of a relatively small number of light sources, these being carbon arc, xenon arc and fluorescent tubes.

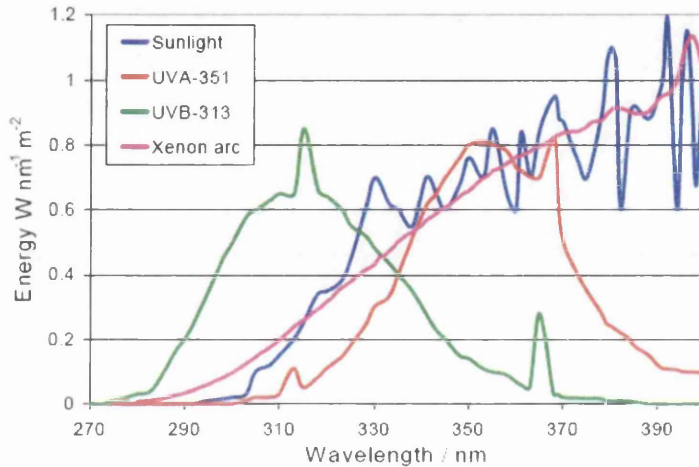


Figure 1.31 Emission spectra of natural sunlight and UV-A, UV-B and Xenon arc lamps.

1.14.2.1 Carbon Arc

The spectral output of the carbon arc lamp has very little in common with that of natural sunlight, mainly consisting of three intense peaks between 250 and 450 nm. It is currently being phased out of the test standards for metals and plastics although it is still commonly used for textile evaluation.

1.14.2.2 Xenon Arc Sources

These provide a better simulation of sunlight than the carbon arc, although filters are required to remove UV radiation shorter than that experienced naturally. Emitted radiation also contains a high intensity of infrared radiation and so overheating of the samples must be prevented. The close simulation of natural sunlight and the ability to control the source automatically combine to make xenon arc sources a useful alternative.

1.14.2.3 Fluorescent Tube Lamps

Available most commonly as UVA and UVB spectral outputs, they produce very little infrared radiation and are much cheaper to maintain and run than xenon arc lamps. The UVB lamps contain radiation of high intensity below that of the solar cut off, and as such they provide a high degree of acceleration which may not be representative of natural weathering conditions due to the involvement of higher energy photons.

1.15 Aims and Objectives

This thesis will first set out the results of systematic study to characterize the UV photodegradation of DSCs so that the mechanisms can be further understood in order to apply effective UV protection measures. It is hoped that this can be achieved by exposing DSC test cells to UV light and measuring the changes to their properties periodically using various analytical techniques. This data will then be used to try and determine the minimum level of UV filtering required to ensure long term DSC stability.

UV filtering will have an obvious affect on DSC performance so this will be investigated. As UV filtering will block UV and possibly some blue photons, alternative dyes with broader action spectra that absorb more in the red end of the spectrum will be investigated to see if

these suffer less from efficiency losses due to UV filtering, than dyes with narrower action spectra.

Finally an investigation of the photostability of clear polymer films intended for use as counter electrode materials, and/or encapsulation materials for flexible Dye-Sensitized Solar Cells (DSCs), built upon a steel substrate. Accelerated weathering experiments will be conducted on various polymer films and the extent of photodegradation of these films will be measured using spectroscopic techniques. An investigation of polyurethane clear lacquer topcoats will also be investigated as well as the addition of UV absorbers and Hindered Amine Light Stabilizers to improve the photostability of these films.

1.16 References

1. B. O'Regan and M. Grätzel, "A Low-Cost, High-Efficiency Solar Cell Based on Dye-Sensitized Colloidal TiO₂ Films," *Nature*, vol.353, no.6346, pp.737-740, 1991
2. W.D.K. Clark and N. Sutin, "Spectral Sensitization of N-Type Titanium Dioxide Electrodes by Polypyridineruthenium(ii) Complexes," *Journal of the American Chemical Society*, vol.99, no.14, pp.4676-4682, 1977
3. H. Gerischer, "The Impact of Semiconductors on the Concepts of Electrochemistry* 1," *Electrochimica Acta*, vol.35, no.11-12, pp.1677-1699, 1990
4. S. Licht, G. Hodes, R. Tenne and J. Manassen, "A Light-Variation Insensitive High Efficiency Solar Cell," *Nature*, vol.326, no.6116, pp.863-864, 1987
5. A. Nozik, "Photoelectrochemical Cells," *Philosophical Transactions of the Royal Society of London. Series A, Mathematical and Physical Sciences*, vol.295, no.1414, pp.453, 1980
6. T. Ma, T. Kida, M. Akiyama, K. Inoue, S. Tsunematsu, K. Yao, H. Noma and E. Abe, "Preparation and Properties of Nanostructured TiO₂ Electrode by a Polymer Organic-Medium Screen-Printing Technique," *Electrochemistry Communications*, vol.5, no.4, pp.369-372, 2003
7. S. Ito, N. Ha, G. Rothenberger, P. Liska, P. Comte, S. Zakeeruddin, P. Péchy, M. Nazeeruddin and M. Grätzel, "High-Efficiency (7.2%) Flexible Dye-Sensitized Solar Cells with Ti-Metal Substrate for Nanocrystalline-TiO₂ Photoanode," *Chemical communications*, vol.2006, no.38, pp.4004-4006, 2006
8. Dyesol press release (2007). "Dyesol and Corus Metal Building Products Development Program Accelerated ". Retrieved 11.01.2011, from http://www.dyesol.com/index.php?element=DYE070213+-+Dyesol_and_Corus.
9. M.P. Thekaekara, "Solar Irradiance, Total and Spectral," *Solar energy engineering.(A78-27852 10-44) New York, Academic Press, Inc., 1977, p. 37-59., 1977*
10. International Energy Agency (2010, 12.01.2011). "Key World Energy Statistics." from http://www.iea.org/textbase/nppdf/free/2010/key_stats_2010.pdf.

11. D.M. Chapin, C.S. Fuller and G.L. Pearson, "A New Silicon P-N Junction Photocell for Converting Solar Radiation into Electrical Power," *Journal of Applied Physics*, vol.25, pp.676, 1954
12. A.A.M. Sayigh and C.E. Backus (1977). Solar Energy Engineering, Academic Press New York.
13. M.A. Green, K. Emery, Y. Hishikawa and W. Warta, "Solar Cell Efficiency Tables (Version 37)," *Progress in Photovoltaics: Research and Applications*, vol.19, no.1, pp.84-92, 2011
14. B.A. Gregg, "Excitonic Solar Cells," *The Journal of Physical Chemistry B*, vol.107, no.20, pp.4688-4698, 2003
15. G.J.M. Fechine, M.S. Rabello and R.M. Souto-Maior, "The Effect of Ultraviolet Stabilizers on the Photodegradation of Poly(Ethylene Terephthalate)," *Polymer Degradation and Stability*, vol.75, no.1, pp.153-159, 2002
16. http://www.youtube.com/watch?v=bVwzJEhMmD8&feature=player_embedded.
17. A. Hagfeldt, G. Boschloo, L. Sun, L. Kloo and H. Pettersson, "Dye-Sensitized Solar Cells," *Chemical Reviews*, vol.110, no.11, pp.6595-6663, 2010
18. M. Grätzel, "Dye-Sensitized Solar Cells," *Journal of Photochemistry and Photobiology C: Photochemistry Reviews*, vol.4, no.2, pp.145-153, 2003
19. K. Sayama, H. Sugihara and H. Arakawa, "Photoelectrochemical Properties of a Porous Nb₂O₅ Electrode Sensitized by a Ruthenium Dye," *Chemistry of Materials*, vol.10, no.12, pp.3825-3832, 1998
20. W.E. Ford, J.M. Wessels and M.A.J. Rodgers, "Time-Resolved Luminescence Investigation of the Adsorption of Ru(Bpy)₃²⁺ onto Antimony-Doped SnO₂ Colloidal Particles," *Langmuir*, vol.12, no.14, pp.3449-3453, 1996
21. K. Tennakone, G. R. R. A. Kumara, I. R. M. Kottegoda and V. P. S. Perera, "An Efficient Dye-Sensitized Photoelectrochemical Solar Cell Made from Oxides of Tin and Zinc," *Chemical Communications*, no.1, pp.15-16, 1999
22. J. Bisquert, D. Cahen, G. Hodes, S. Rühle and A. Zaban, "Physical Chemical Principles of Photovoltaic Conversion with Nanoparticulate, Mesoporous Dye-Sensitized Solar Cells," *The Journal of Physical Chemistry B*, vol.108, no.24, pp.8106-8118, 2004
23. M. Grätzel, "Solar Energy Conversion by Dye-Sensitized Photovoltaic Cells," *Inorganic Chemistry*, vol.44, no.20, pp.6841-6851, 2005
24. A. Hagfeldt and M. Grätzel, "Light-Induced Redox Reactions in Nanocrystalline Systems," *Chemical Reviews*, vol.95, no.1, pp.49-68, 1995
25. G.P. Smestad, "Education and Solar Conversion::: Demonstrating Electron Transfer," *Solar Energy Materials and Solar Cells*, vol.55, no.1-2, pp.157-178, 1998
26. T.W. Hamann, R.A. Jensen, A.B.F. Martinson, H. Van Ryswyk and J.T. Hupp, "Advancing Beyond Current Generation Dye-Sensitized Solar Cells," *Energy Environ. Sci.*, vol.1, no.1, pp.66-78, 2008
27. K. Kalyanasundaram (2010). Photochemical and Photoelectrochemical Approaches to Energy Conversion. Dye-Sensitized Solar Cells. K. Kalyanasundaram. Lausanne, EPFL Press: 23.
28. <http://www.icis.com/v2/chemicals/9076545/titanium-dioxide/pricing.html>
Accessed 07/08/2011
29. <http://www.metal-pages.com/metalprices/indium/> Accessed 07/08/2011,
30. Ladislav Kavan (2010). Titania in Diverse Forms as Substrates Dye-Sensitized Solar Cells. K. Kalyanasundaram. Lausanne, EPFL Press: 49.
31. A. Robinson, J. Searle and D. Worsley, "Novel Flat Panel Reactor for Monitoring Photodegradation," *Materials Science and Technology*, vol.20, no.8, pp.1041-1048, 2004

32. J. Desilvestro, M. Grätzel, L. Kavan, J. Moser and J. Augustynski, "Highly Efficient Sensitization of Titanium Dioxide," *Journal of the American Chemical Society*, vol.107, no.10, pp.2988-2990, 1985
33. M. Adachi, Y. Murata, J. Takao, J. Jiu, M. Sakamoto and F. Wang, "Highly Efficient Dye-Sensitized Solar Cells with a Titania Thin-Film Electrode Composed of a Network Structure of Single-Crystal-Like TiO₂ Nanowires Made by the "Oriented Attachment" Mechanism," *Journal of the American Chemical Society*, vol.126, no.45, pp.14943-14949, 2004
34. G.K. Mor, K. Shankar, M. Paulose, O.K. Varghese and C.A. Grimes, "Use of Highly-Ordered TiO₂ Nanotube Arrays in Dye-Sensitized Solar Cells," *Nano Letters*, vol.6, no.2, pp.215-218, 2005
35. S. Hore, C. Vetter, R. Kern, H. Smit and A. Hinsch, "Influence of Scattering Layers on Efficiency of Dye-Sensitized Solar Cells," *Solar Energy Materials and Solar Cells*, vol.90, no.9, pp.1176-1188, 2006
36. K.D. Benkstein, N. Kopidakis, J. van de Lagemaat and A.J. Frank, "Influence of the Percolation Network Geometry on Electron Transport in Dye-Sensitized Titanium Dioxide Solar Cells," *The Journal of Physical Chemistry B*, vol.107, no.31, pp.7759-7767, 2003
37. S. Ito, P. Liska, P. Comte, R. Charvet, P. Pechy, U. Bach, L. Schmidt-Mende, S.M. Zakeeruddin, A. Kay, M.K. Nazeeruddin and M. Grätzel, "Control of Dark Current in Photoelectrochemical (TiO₂/I⁻, I₃⁻) and Dye-Sensitized Solar Cells," *Chemical Communications*, no.34, pp.4351-4353, 2005
38. M. Nazeeruddin, A. Kay, I. Rodicio, R. Humphry-Baker, E. Müller, P. Liska, N. Vlachopoulos and M. Grätzel, "Conversion of Light to Electricity by Cis-X2bis (2, 2'-Bipyridyl-4, 4'-Dicarboxylate) Ruthenium (II) Charge-Transfer Sensitizers (X= Cl-, Br-, I-, Cn-, and Scn-) on Nanocrystalline Titanium Dioxide Electrodes," *Journal of the American Chemical Society*, vol.115, no.14, pp.6382-6390, 1993
39. P.M. Sommeling, B.C. O'Regan, R.R. Haswell, H.J.P. Smit, N.J. Bakker, J.J.T. Smits, J.M. Kroon and J.A.M. van Roosmalen, "Influence of a TiCl₄ Post-Treatment on Nanocrystalline TiO₂ Films in Dye-Sensitized Solar Cells," *The Journal of Physical Chemistry B*, vol.110, no.39, pp.19191-19197, 2006
40. J. Bisquert (2008). "Dye-Sensitized Solar Cells." Retrieved 08/08/2011, from http://www.elpl.uji.es/juan_home/research/solar_cells.htm.
41. T.P. Chou, Q. Zhang and G. Cao, "Effects of Dye Loading Conditions on the Energy Conversion Efficiency of ZnO and TiO₂ Dye-Sensitized Solar Cells," *The Journal of Physical Chemistry C*, vol.111, no.50, pp.18804-18811, 2007
42. K. Keis, J. Lindgren, S.-E. Lindquist and A. Hagfeldt, "Studies of the Adsorption Process of Ru Complexes in Nanoporous ZnO Electrodes," *Langmuir*, vol.16, no.10, pp.4688-4694, 2000
43. M. Quintana, T. Edvinsson, A. Hagfeldt and G. Boschloo, "Comparison of Dye-Sensitized ZnO and TiO₂ Solar Cells: Studies of Charge Transport and Carrier Lifetime," *The Journal of Physical Chemistry C*, vol.111, no.2, pp.1035-1041, 2006
44. J. Sancho-Parramon, V. Janicki and H. Zorc, "Compositional Dependence of Absorption Coefficient and Band-Gap for Nb₂O₅-SiO₂ Mixture Thin Films," *Thin Solid Films*, vol.516, no.16, pp.5478-5482, 2008
45. P. Docampo and H.J. Snaith, "Obviating the Requirement for Oxygen in SnO₂-Based Solid-State Dye-Sensitized Solar Cells," *Nanotechnology*, vol.22, pp.225403, 2011
46. S.H. J and D. C, "SnO₂ -Based Dye-Sensitized Hybrid Solar Cells Exhibiting near Unity Absorbed Photon-to-Electron Conversion Efficiency," *Nano Lett.*, vol.10, no.4, pp.1259, 2010

47. J.-h. Yum and M.K. Nazeeruddin (2010). Molecular Engineering of Sensitizers for Conversion of Solar Energy into Electricity. Dye-Sensitized Solar Cells. K. Kalyanasundaram. Lausanne, EPFL Press: 23.
48. N. Serpone, E. Pelizzetti and M. Grätzel, "Photosensitization of Semiconductors with Transition Metal Complexes - a Route to the Photoassisted Cleavage of Water," *Coordination Chemistry Reviews*, vol.64, pp.225-245, 1985
49. D. THEWISSEN, M. EEUWHORST-REINTEN, K. TIMMER, A. TINNEMANS and A. MACKOR (1982). Development of a Practical Process for the Production of Hydrogen by Photo-Chemical Cleavage of Water with Visible Light and Homogeneous and/or Hetero-Genic Catalysts, Springer.
50. M. Alebbi, C.A. Bignozzi, T.A. Heimer, G.M. Hasselmann and G.J. Meyer, "The Limiting Role of Iodide Oxidation in Cis-Os(Dcb)₂ (CN)₂/TiO₂ Photoelectrochemical Cells," *The Journal of Physical Chemistry B*, vol.102, no.39, pp.7577-7581, 1998
51. A. Hagfeldt and M. Grätzel, "Molecular Photovoltaics," *Accounts of chemical research*, vol.33, no.5, pp.269-277, 2000
52. A.S. Polo, M.K. Itokazu and N.Y. Murakami Iha, "Metal Complex Sensitizers in Dye-Sensitized Solar Cells," *Coordination Chemistry Reviews*, vol.248, no.13-14, pp.1343-1361, 2004
53. A. Kay and M. Grätzel, "Artificial Photosynthesis. 1. Photosensitization of Titania Solar Cells with Chlorophyll Derivatives and Related Natural Porphyrins," *The Journal of Physical Chemistry*, vol.97, no.23, pp.6272-6277, 1993
54. W.M. Campbell, A.K. Burrell, D.L. Officer and K.W. Jolley, "Porphyrins as Light Harvesters in the Dye-Sensitized TiO₂ Solar Cell," *Coordination Chemistry Reviews*, vol.248, no.13-14, pp.1363-1379, 2004
55. W.M. Campbell, K.W. Jolley, P. Wagner, K. Wagner, P.J. Walsh, K.C. Gordon, L. Schmidt-Mende, M.K. Nazeeruddin, Q. Wang, M. Grätzel and D.L. Officer, "Highly Efficient Porphyrin Sensitizers for Dye-Sensitized Solar Cells," *The Journal of Physical Chemistry C*, vol.111, no.32, pp.11760-11762, 2007
56. T. Bessho, S.M. Zakeeruddin, C.-Y. Yeh, E.W.-G. Diau and M. Grätzel, "Highly Efficient Mesoscopic Dye-Sensitized Solar Cells Based on Donor-Acceptor-Substituted Porphyrins," *Angewandte Chemie International Edition*, vol.49, no.37, pp.6646-6649, 2010
57. M. Garcia-Iglesias, J.-H. Yum, R. Humphry-Baker, S.M. Zakeeruddin, P. Pechy, P. Vazquez, E. Palomares, M. Grätzel, M.K. Nazeeruddin and T. Torres, "Effect of Anchoring Groups in Zinc Phthalocyanine on the Dye-Sensitized Solar Cell Performance and Stability," *Chemical Science*, vol.2, no.6, pp.1145-1150, 2011
58. M. Kimura, H. Nomoto, N. Masaki and S. Mori, "Dye Molecules for Simple Co-Sensitization Process: Fabrication of Mixed-Dye-Sensitized Solar Cells," *Angewandte Chemie*, pp.n/a-n/a, 2012
59. P.J. Holliman, M.L. Davies, A. Connell, B.V. Velasco and T.M. Watson, "Ultra-Fast Dye Sensitisation and Co-Sensitisation for Dye Sensitized Solar Cells," *Chemical Communications*, vol.46, no.38, pp.7256-7258, 2010
60. N. Robertson, "Catching the Rainbow: Light Harvesting in Dye-Sensitized Solar Cells," *Angewandte Chemie International Edition*, vol.47, no.6, pp.1012-1014, 2008
61. "Image Courtesy of Dr. Matthew L. Davies - Bangor University,"
62. N. Cai, S.-J. Moon, L. Cevey-Ha, T. Moehl, R. Humphry-Baker, P. Wang, S.M. Zakeeruddin and M. Grätzel, "An Organic D-π-A Dye for Record Efficiency Solid-State Sensitized Heterojunction Solar Cells," *Nano Letters*, vol.11, no.4, pp.1452-1456,

63. A. Mishra, M.K.R. Fischer and P. Bäuerle, "Metal Free Organic Dyes for Dye Sensitized Solar Cells: From Structure: Property Relationships to Design Rules," *Angewandte Chemie International Edition*, vol.48, no.14, pp.2474-2499, 2009
64. W. Zeng, Y. Cao, Y. Bai, Y. Wang, Y. Shi, M. Zhang, F. Wang, C. Pan and P. Wang, "Efficient Dye-Sensitized Solar Cells with an Organic Photosensitizer Featuring Orderly Conjugated Ethylenedioxythiophene and Dithienosilole Blocks," *Chemistry of Materials*, vol.22, no.5, pp.1915-1925,
65. S. Rühle, M. Shalom and A. Zaban, "Quantum Dot Sensitized Solar Cells," *ChemPhysChem*, vol.11, no.11, pp.2290-2304,
66. E.M. Barea, M. Shalom, S. Gime nez, I. Hod, I. Mora-Sero, A. Zaban and J. Bisquert, "Design of Injection and Recombination in Quantum Dot Sensitized Solar Cells," *Journal of the American Chemical Society*, vol.132, no.19, pp.6834-6839,
67. P.K. Santra and P.V. Kamat, "Mn-Doped Quantum Dot Sensitized Solar Cells: A Strategy to Boost Efficiency over 5%," *Journal of the American Chemical Society*, vol.134, no.5, pp.2508- 2511, 2012
68. K.-j. Jiang and Shozo Yanagida (2010). Optimization of Redox Mediators and Electrolytes. Dye-Sensitized Solar Cells
K. Kalyanasundaram. Lausanne, EPFL Press.
69. P. Wang, B. Wenger, R. Humphry-Baker, J.-E. Moser, J. Teuscher, W. Kantlehner, J. Mezger, E.V. Stoyanov, S.M. Zakeeruddin and M. Grätzel, "Charge Separation and Efficient Light Energy Conversion in Sensitized Mesoscopic Solar Cells Based on Binary Ionic Liquids," *Journal of the American Chemical Society*, vol.127, no.18, pp.6850-6856, 2005
70. S. Pelet, J.-E. Moser and M. Grätzel, "Cooperative Effect of Adsorbed Cations and Iodide on the Interception of Back Electron Transfer in the Dye Sensitization of Nanocrystalline TiO₂," *The Journal of Physical Chemistry B*, vol.104, no.8, pp.1791-1795, 2000
71. G. Boschloo and A. Hagfeldt, "Characteristics of the Iodide/Triiodide Redox Mediator in Dye-Sensitized Solar Cells," *Accounts of chemical research*, vol.42, no.11, pp.1819-1826, 2009
72. P. Bonhôte, A.-P. Dias, N. Papageorgiou, K. Kalyanasundaram and M. Grätzel, "Hydrophobic, Highly Conductive Ambient-Temperature Molten Saltst," *Inorganic Chemistry*, vol.35, no.5, pp.1168-1178, 1996
73. S. Ferrere, A. Zaban and B.A. Gregg, "Dye Sensitization of Nanocrystalline Tin Oxide by Perylene Derivatives," *The Journal of Physical Chemistry B*, vol.101, no.23, pp.4490-4493, 1997
74. G. Oskam, B.V. Bergeron, G.J. Meyer and P.C. Searson, "Pseudohalogens for Dye-Sensitized TiO₂ Photoelectrochemical Cells," *The Journal of Physical Chemistry B*, vol.105, no.29, pp.6867-6873, 2001
75. P. Wang, S.M. Zakeeruddin, J.-E. Moser, R. Humphry-Baker and M. Grätzel, "A Solvent-Free, SeCN⁻/(SeCN)₃⁻ Based Ionic Liquid Electrolyte for High-Efficiency Dye-Sensitized Nanocrystalline Solar Cells," *Journal of the American Chemical Society*, vol.126, no.23, pp.7164-7165, 2004
76. P.J. Cameron, L.M. Peter, S.M. Zakeeruddin and M. Grätzel, "Electrochemical Studies of the Co(iii)/Co(ii)(Dbbip)₂ Redox Couple as a Mediator for Dye-Sensitized Nanocrystalline Solar Cells," *Coordination Chemistry Reviews*, vol.248, no.13-14, pp.1447-1453, 2004
77. B.A. Gregg, F. Pichot, S. Ferrere and C.L. Fields, "Interfacial Recombination Processes in Dye-Sensitized Solar Cells and Methods to Passivate the Interfaces," *The Journal of Physical Chemistry B*, vol.105, no.7, pp.1422-1429, 2001

78. L. Guo, X. Pan, M. Wang, C. Zhang, X. Fang, S. Chen and S. Dai, "Novel Hydrophobic Ionic Liquids Electrolyte Based on Cyclic Sulfonium Used in Dye-Sensitized Solar Cells," *Solar Energy*, vol.85, no.1, pp.7-11, 2011
79. O.A. Ieperuma, G.R. Asoka Kumara, H.-S. Yang and K. Murakami, "Quasi-Solid Electrolyte Based on Polyacrylonitrile for Dye-Sensitized Solar Cells," *Journal of Photochemistry and Photobiology A: Chemistry*, vol.217, no.2-3, pp.308-312,
80. S. Uchida High Performance Nano-Clay Electrolyte for Dye-Sensitized Solar Cells. HOPV 2011. Valencia.
81. U. Bach, D. Lupo, P. Comte, J.E. Moser, F. Weissörtel, J. Salbeck, H. Spreitzer and M. Grätzel, "Solid-State Dye-Sensitized Mesoporous TiO₂ Solar Cells with High Photon-to-Electron Conversion Efficiencies," *Nature*, vol.395, no.6702, pp.583-585, 1998
82. D. Kuang, S. Ito, B. Wenger, C. Klein, J.-E. Moser, R. Humphry-Baker, S.M. Zakeeruddin and M. Grätzel, "High Molar Extinction Coefficient Heteroleptic Ruthenium Complexes for Thin Film Dye-Sensitized Solar Cells," *Journal of the American Chemical Society*, vol.128, no.12, pp.4146-4154, 2006
83. P. Wang, S.M. Zakeeruddin, J.E. Moser, R. Humphry-Baker, P. Comte, V. Aranyos, A. Hagfeldt, M.K. Nazeeruddin and M. Grätzel, "Stable New Sensitizer with Improved Light Harvesting for Nanocrystalline Dye-Sensitized Solar Cells," *Advanced Materials*, vol.16, no.20, pp.1806-1811, 2004
84. S.E. Koops, B.C. O'Regan, P.R.F. Barnes and J.R. Durrant, "Parameters Influencing the Efficiency of Electron Injection in Dye-Sensitized Solar Cells," *Journal of the American Chemical Society*, vol.131, no.13, pp.4808-4818, 2009
85. J.N. Clifford, E. Palomares, M.K. Nazeeruddin, M. Grätzel and J.R. Durrant, "Dye Dependent Regeneration Dynamics in Dye Sensitized Nanocrystalline Solar Cells: Evidence for the Formation of a Ruthenium Bipyridyl Cation/Iodide Intermediate," *The Journal of Physical Chemistry C*, vol.111, no.17, pp.6561-6567, 2007
86. T. Watson, P. Holliman and D. Worsley, "Rapid, Continuous in Situ Monitoring of Dye Sensitisation in Dye-Sensitized Solar Cells," *Journal of Materials Chemistry*, vol.21, no.12, pp.4321-4325, 2011
87. A. Hinsch, J.M. Kroon, R. Kern, I. Uhlendorf, J. Holzbock, A. Meyer and J. Ferber, "Long-Term Stability of Dye-Sensitised Solar Cells," *Progress in Photovoltaics: Research and Applications*, vol.9, no.6, pp.425-438, 2001
88. P.M. Sommeling, M. Späth, H.J.P. Smit, N.J. Bakker and J.M. Kroon, "Long-Term Stability Testing of Dye-Sensitized Solar Cells," *Journal of Photochemistry and Photobiology A: Chemistry*, vol.164, no.1-3, pp.137-144, 2004
89. ASTM International Astm G173-03 Standard Tables for Reference Solar Spectral Irradiances: Direct Normal and Hemispherical on 37° Tilted Surface.
90. J. Bisquert, "Theory of the Impedance of Charge Transfer Via Surface States in Dye-Sensitized Solar Cells," *Journal of Electroanalytical Chemistry*, vol.646, no.1-2, pp.43-51,
91. J. Bisquert and F. Fabregat-Santiago (2010). Impedance Spectroscopy: A General Introduction and Application to Dye-Sensitized Solar Cells. Dye-Sensitized Solar Cells K. Kalyanasundaram. Lausanne, EPFL Press.
92. J. Bisquert, F. Fabregat-Santiago, I.n. Mora-Seró, G. Garcia-Belmonte and S. Giménez, "Electron Lifetime in Dye-Sensitized Solar Cells: Theory and Interpretation of Measurements," *The Journal of Physical Chemistry C*, vol.113, no.40, pp.17278-17290, 2009
93. F. Fabregat-Santiago, J. Bisquert, L. Cevey, P. Chen, M. Wang, S.M. Zakeeruddin and M. Grätzel, "Electron Transport and Recombination in Solid-State Dye Solar Cell with Spiro-Ometad as Hole Conductor," *Journal of the American Chemical Society*, vol.131, no.2, pp.558-562, 2008

94. F. Fabregat-Santiago, J. Bisquert, G. Garcia-Belmonte, G. Boschloo and A. Hagfeldt, "Influence of Electrolyte in Transport and Recombination in Dye-Sensitized Solar Cells Studied by Impedance Spectroscopy," *Solar Energy Materials and Solar Cells*, vol.87, no.1-4, pp.117-131, 2005
95. J. Halme, P. Vahermaa, K. Miettunen and P. Lund, "Device Physics of Dye Solar Cells," *Advanced Materials*, vol.22, no.35, pp.E210-E234,
96. L. Han, N. Koide, Y. Chiba, A. Islam, R. Komiya, N. Fuke, A. Fukui and R. Yamanaka, "Improvement of Efficiency of Dye-Sensitized Solar Cells by Reduction of Internal Resistance," *Applied Physics Letters*, vol.86, no.21, pp.213501-213501-213503, 2005
97. M. Toivola, J. Halme, L. Peltokorpi and P. Lund, "Investigation of Temperature and Aging Effects in Nanostructured Dye Solar Cells Studied by Electrochemical Impedance Spectroscopy," *International Journal of Photoenergy*, 2009
98. H. Desilvestro, M. Bertoz, S. Tulloch and G. Tulloch (2010). Packaging, Scale-up and Commercialization of Dye Solar Cells. Dye-Sensitized Solar Cells K. Kalyanasundaram. Lausanne, EPFL Press.
99. J. Li, L.M. Peter and R. Potter, "Photoelectrochemical Response of TiO₂ Pigmented Membranes," *Journal of Applied Electrochemistry*, vol.14, no.4, pp.495-504, 1984
100. A. Mills, R. Davies and D. Worsley, "Water Purification by Semiconductor Photocatalysis," *Chemical Society Reviews*, vol.22, no.6, pp.417-434, 1993
101. A. Wold, "Photocatalytic Properties of Titanium Dioxide (TiO₂)," *Chemistry of Materials*, vol.5, no.3, pp.280-283, 1993
102. D. Ollis, E. Pelizzetti and N. Serpone, "Photocatalysis: Fundamentals and Applications," *Serpone and E. Pellizzetti (eds.) John Wiley and Sons, New York*, pp.603, 1989
103. R. Sastrawan, J. Beier, U. Belledin, S. Hemming, A. Hinsch, R. Kern, C. Vetter, F. Petrat, A. Prodi-Schwab and P. Lechner, "A Glass Frit-Sealed Dye Solar Cell Module with Integrated Series Connections," *Solar Energy Materials and Solar Cells*, vol.90, no.11, pp.1680-1691, 2006
104. M. Asghar, K. Miettunen, J. Halme, P. Vahermaa, M. Toivola, K. Aitola and P. Lund, "Review of Stability for Advanced Dye Solar Cells," *Energy & Environmental Science*, vol.3, no.4, pp.418-426, 2010
105. O. Kohle, M. Grätzel, A.F. Meyer and T.B. Meyer, "The Photovoltaic Stability of, Bis(Isothiocyanato)Ruthenium(II)-Bis-2, 2'-Bipyridine-4, 4'-Dicarboxylic Acid and Related Sensitizers," *Advanced Materials*, vol.9, no.11, pp.904-906, 1997
106. A. Barkschat, T. Moehl, B. Macht and H. Tributsch, "The Function of TiO₂ with Respect to Sensitizer Stability in Nanocrystalline Dye Solar Cells," *International Journal of Photoenergy*, vol.2008,
107. N. Kato, K. Higuchi, H. Tanaka, J. Nakajima, T. Sano and T. Toyoda, "Improvement in Long-Term Stability of Dye-Sensitized Solar Cell for Outdoor Use," *Solar Energy Materials and Solar Cells*, vol.95, no.1, pp.301-305, 2009
108. A. Hauch and A. Georg, "Diffusion in the Electrolyte and Charge-Transfer Reaction at the Platinum Electrode in Dye-Sensitized Solar Cells," *Electrochimica Acta*, vol.46, no.22, pp.3457-3466, 2001
109. H. Matsui, K. Okada, T. Kitamura and N. Tanabe, "Thermal Stability of Dye-Sensitized Solar Cells with Current Collecting Grid," *Solar Energy Materials and Solar Cells*, vol.93, no.6-7, pp.1110-1115, 2009
110. B. Macht, M. Turrión, A. Barkschat, P. Salvador, K. Ellmer and H. Tributsch, "Patterns of Efficiency and Degradation in Dye Sensitization Solar Cells Measured with Imaging Techniques," *Solar Energy Materials and Solar Cells*, vol.73, no.2, pp.163-173, 2002

111. P. Wang, S.M. Zakeeruddin, J.E. Moser, M.K. Nazeeruddin, T. Sekiguchi and M. Grätzel, "A Stable Quasi-Solid-State Dye-Sensitized Solar Cell with an Amphiphilic Ruthenium Sensitizer and Polymer Gel Electrolyte," *Nature Materials*, vol.2, no.6, pp.402-407, 2003
112. C. Law, S.C. Pathirana, X. Li, A.Y. Anderson, P.R.F. Barnes, A. Listorti, T.H. Ghaddar and B.C. O'Regan, "Water-Based Electrolytes for Dye-Sensitized Solar Cells," *Advanced Materials*, vol.22, no.40, pp.4505-4509, 2010
113. N. Papageorgiou, "Counter-Electrode Function in Nanocrystalline Photoelectrochemical Cell Configurations," *Coordination Chemistry Reviews*, vol.248, no.13-14, pp.1421-1446, 2004
114. Dyesol, "2008 Annual Report,"
115. H. Pettersson and T. Gruszecki, "Long-Term Stability of Low-Power Dye-Sensitized Solar Cells Prepared by Industrial Methods," *Solar Energy Materials and Solar Cells*, vol.70, no.2, pp.203-212, 2001
116. K. Tennakone, G. Kumara, I. Kottegoda, K. Wijayantha and V. Perera, "A Solid-State Photovoltaic Cell Sensitized with a Ruthenium Bipyridyl Complex," *Journal of Physics-London-D Applied Physics*, vol.31, pp.1492-1496, 1998
117. N. Kato, Y. Takeda, K. Higuchi, A. Takeichi, E. Sudo, H. Tanaka, T. Motohiro, T. Sano and T. Toyoda, "Degradation Analysis of Dye-Sensitized Solar Cell Module after Long-Term Stability Test under Outdoor Working Condition," *Solar Energy Materials and Solar Cells*, vol.93, no.6-7, pp.893-897, 2009
118. J.G. Calvert and J.N. Pitts (1966). Photochemistry, Wiley, New York.
119. D.O. Cowan and R.L. Drisko (1976). Elements of Organic Photochemistry, Plenum Press, New York.
120. T.G. Chasteen. "Jablonski Diagram - Relaxation Mechanism for Excited State Molecules." Retrieved 19/05/2008, from <http://www.shsu.edu/~chemistry/chemiluminescence/JABLONSKI.html>.
121. J.F. McKellar and N.S. Allen (1979). Photochemistry of Man-Made Polymers, Applied Science Publishers, London.
122. A.L. Andradý and N.D. Searle, "Photodegradation of Rigid Pvc Formulations .2. Spectral Sensitivity to Light-Induced Yellowing by Polychromatic-Light," *JOURNAL OF APPLIED POLYMER SCIENCE*, vol.37, no.10, pp.2789-2802, 1989
123. G. Kampf, K. Sommer and E. Zirngiebl, "Studies in Accelerated Weathering. I. Determination of the Activation Spectrum of Photodegradation in Polymers," *Progress in Organic Coatings*, vol.19, no.1, pp.69-77, 1991
124. A.C. Somersall and J.E. Guillet, "Photoluminescence of Synthetic Polymers," *Polymer Reviews*, vol.13, no.2, pp.135-187, 1975
125. N.S. Allen, "Sunlight Induced Degradation of Polymers," *ENG PLAST.*, vol.8, no.4, pp.247-286, 1995
126. J. Pospíšil and H.-J. Weideli, "Environmental Impacts Associated with the Application of Radical-Scavenging Stabilizers in Polymers," *Polymer Degradation and Stability*, vol.52, no.2, pp.109-117, 1996
127. B. Mahltig, H. Böttcher, K. Rauch, U. Dieckmann, R. Nitsche and T. Fritz, "Optimized UV Protecting Coatings by Combination of Organic and Inorganic Uv Absorbers," *Thin Solid Films*, vol.485, no.1-2, pp.108-114, 2005
128. Y. Dobashi, J.-i. Kondou and Y. Ohkatsu, "Photo-Antioxidant Abilities of 2-Hydroxybenzoyl Compounds," *Polymer Degradation and Stability*, vol.89, no.1, pp.140-144, 2005
129. P. Gijsman, "New Synergists for Hindered Amine Light Stabilizers," *Polymer*, vol.43, no.5, pp.1573-1579, 2002

130. V.B. Bojinov and I.P. Panova, "Photo-Stability of Yellow-Green Emitting 1,8-Naphthalimides Containing Built-in S-Triazine Uv Absorber and Hals Fragments and Their Acrylonitrile Copolymers," *Polymer Degradation and Stability*, vol.In Press, Corrected Proof,
131. G. Scott (1982). *Developments in Polymer Stabilisation-5* (G. Scott, Ed.), Applied Science Publishers, London.

Chapter

2.

**Experimental
Procedures**

2. EXPERIMENTAL PROCEDURES

2.1 Fabrication of DSC Test Cells

2.1.1 Manufacture of the Working Electrode

The photoanode was prepared by the doctor blading of a commercial TiO_2 paste (DSL 18NRT) onto Solaronix TCO22-15 fluorine doped SnO_2 glass followed by sintering at 500°C for 30 minutes. Strips of TCO coated glass were cut 2.5 cm wide using a glass cutter. The strips were cleaned first with hot water and detergent and then with IPA or ethanol. Tape guides were placed down either side of the strip and across the top using Scotch adhesive tape to allow draw down with a glass rod (see figure 2.1). A small amount of DSL NRT paste was placed onto the piece of tape running along the top edge of the glass. A glass rod was used to draw down the paste, pushing down firmly so that the Scotch tape acts as a height guide. The tape was then removed and the glass strip(s) placed in a Pyrex dish place and put first in an oven at 200°C for 10 minutes to remove binders from the paste. This was then placed in a high temperature oven at 500°C for 30 minutes.

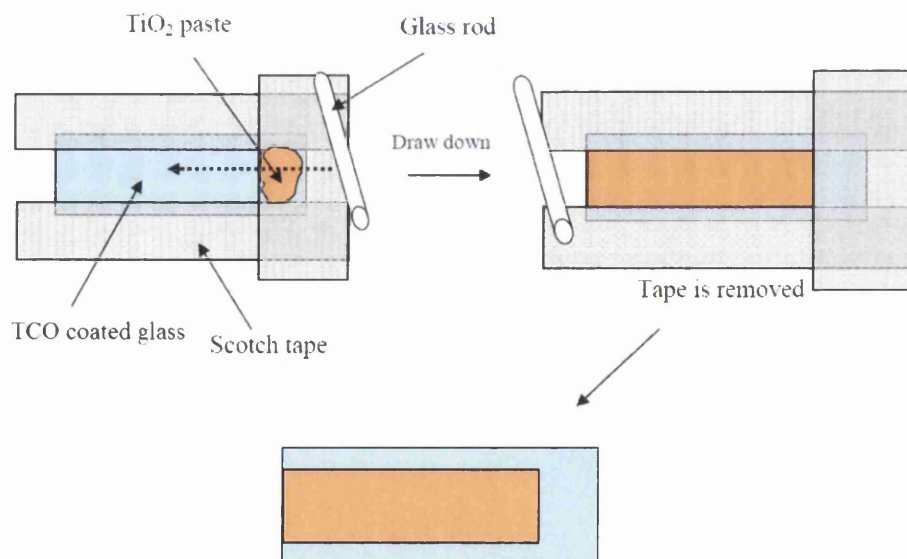


Figure 2.1 Draw-down of TiO_2 paste on TCO coated glass

The glass strips were removed from the oven and allowed cool. The strips were then cut into smaller strips 1.5 cm wide. The sintered TiO_2 was then scratched away using a

microscope cover-slip so that there remains a 1 cm x 1 cm square in the centre of the 2.5 cm x 1.5 cm strip, this is essentially the working electrode. Adsorption of the dye to the TiO₂ was achieved by immersion of the electrode in the dye solution over a period of 16-20 hours. N719 Dye was prepared at 0.3 mM in a 1:1 acetonitrile/T-Butanol solution.

2.1.2 Manufacture of the Counter Electrode

The counter electrodes were prepared by the deposition of 5 mM chloroplatinic acid and heat treated at 400 °C for 30 minutes. ITO coated glass is cut into strips 2.5 cm x 1.5 cm. Electrolyte back filling holes are drilled with 0.5 mm tungsten carbide drill bit. The counter electrode is then washed first, with water and detergent and then with ethanol or IPA. The counter electrodes are placed conductive side up (checked with the multimeter) and a thin layer of 5mM chloroplatinic acid is deposited using a capillary tube to coat the conductive glass. These are then placed in a high temperature oven at 400°C for 30 mins.

2.1.3 Filling and Sealing

The working electrodes were removed from the dye solution and rinsed with ethanol or IPA and air dried. Surlyn gaskets (50 µm) were used to seal the counter- and working-electrodes and act as a spacer between them. The two electrodes were placed together with the gasket and sealed, either with a t-shirt press or by using a hot plate and applying pressure carefully with a pestle. Once sealed, the cell was checked for short circuiting with a multi-meter and then placed in a vacuum desiccator. An 'O' ring is then placed around the back filling hole. An electrolyte solution (0.8 M 1-propyl-3-methylimidazolium iodide (PMII), 0.3 M benzimidazole, 0.1 M I₂ and 0.05 M guanidinium thiocyanate dissolved in N-methoxy propionitrile) was then introduced to the cell by vacuum injection whereby a drop of electrolyte was placed inside the ring and a vacuum is drawn using a vacuum pump. The electrolyte was then thoroughly cleaned from the cell surface with EtOH or IPA and the back filling hole was sealed with surlyn and a round microscope cover slip. Finally silver

contacts were painted on using silver, conductive paint and a cocktail stick. Figure 2.2 below shows a schematic of a completed test cell.

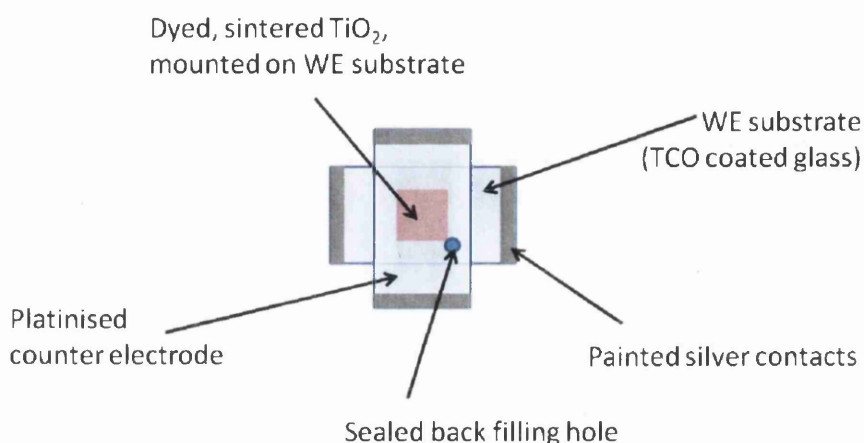


Figure 2.2 *schematic diagram of a typical glass-glass DSC test cell (active area = 1 cm x 1 cm)*

2.2 Cell Measurements

2.2.1 IV Measurements

Current-voltage (IV) measurements give all the important cell parameters described in chapter 1.11. Cell measurements were carried out using the Newport Oriel, Sol3A Class AAA Solar Simulator (figure 2.3) with a 450 Watt Xenon source. It is certified to IEC 60904-9 Edition 2 (2007), JIS C 8912, and ASTM E 927-05 standards for Spectral Match, Non-Uniformity of Irradiance, and Temporal Instability of Irradiance. Measurements were carried out at an irradiance of 1 Sun.

Before making any measurements, the light source is first calibrated to 1.00 ± 0.01 Sun using the NREL certified silicon reference cell. For most 1 cm^2 test cells made with the method described in section 2.1, the following settings apply: max reverse bias = -1.00 V, max forward bias = 0.8, Current limit = -50 mA, sample area = 1 cm^2 , No of sweep points = 200, pre-sweep delay = 1 s and dwell time = 200 ms, the power output of the lamp is also required, measured in Suns.

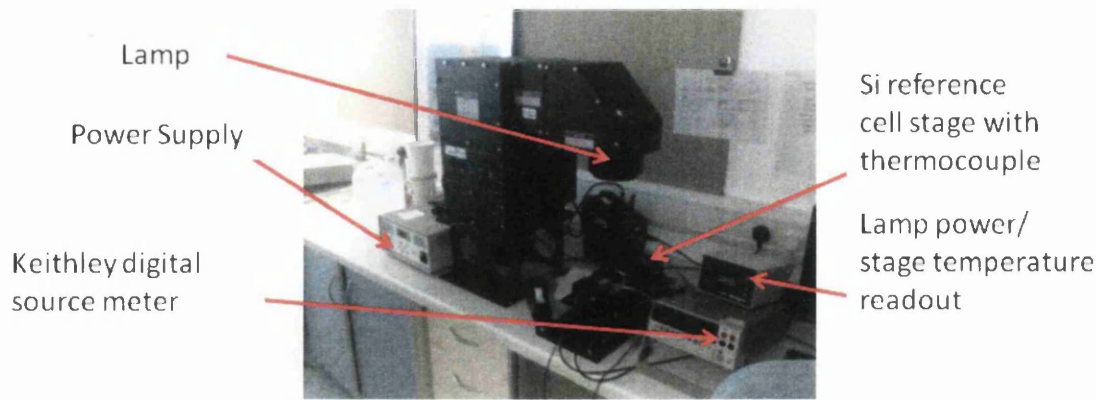


Figure 2.3 Newport Oriel Solar Simulator

2.2.2 EIS Measurements

For a discussion on the theoretical aspects of DSC EIS measurements, see *section 1.11.3*. Impedance measurements were originally carried out on a Solartron SI 1280 Electrochemical Measurement Unit using ZPlot software. Cells were measured in a two electrode set-up in the dark and held at a potential of -0.68 V. AC amplitude was ± 10 mV with a frequency range of 20 kHz to 0.1 Hz. Later measurements were carried out under the same conditions using a Gamry Reference 600 Potentiostat/Galvanostat/ZRA except in this case the upper frequency limit which was set at 50 kHz. The bias potential of -0.68 V was chosen as this is close to typical cell's max operating power point and so gives Nyquist plots that is easy to fit using the simple model described in *section 1.11.3*. Cells were measured in the dark which allowed a higher throughput, this was important as large numbers of measurements were made at any one time, the results are still valid but it is acknowledged that measuring the impedance of cells under illumination gives a better approximation to the cell's working conditions.

2.2.3 IPCE Measurements

IPCEs were measured on a Dyesol IPCE instrument between 300 nm and 1150 nm.

2.3 UV-Vis Measurements

UV-Vis %T measurements of both clear polymer films and DSC test cells were carried out using a Perkin Elmer Lambda 750s UV-VIS-NIR spectrophotometer (figure 2.4). UV-Vis identify early chemical indicators of the photodegradation of clear polymer films which is often characterised with a yellowing of the film and is evidenced by an increase in film absorbance at around 400 nm. The UV-Vis spectrophotometer was also used to monitor the electrolyte discolouration of DSC test cells.

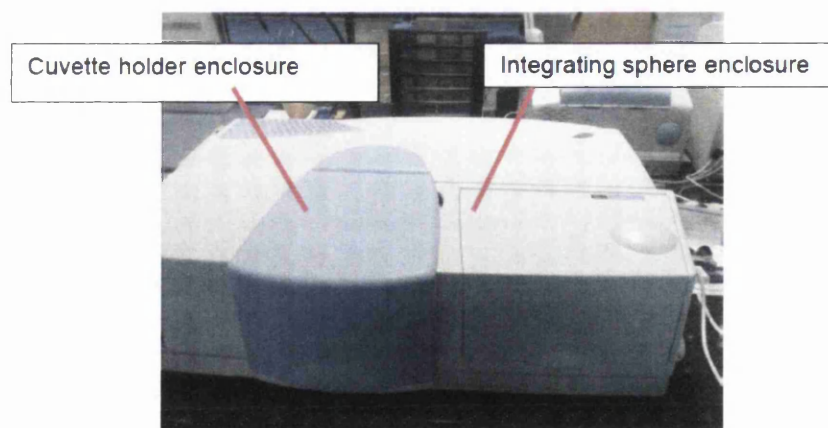


Figure 2.4 Perkin Elmer Lambda 750S

2.4 FTIR Spectrophotometry and ATR accessory

The spectrophotometer used was a Perkin Elmer Spectrum 100 (Figure 2.5). Spectra were measured from 4000 cm^{-1} to 450 cm^{-1} with a resolution of 4.00 cm^{-1} . ATR reflectance measurements were taken using the Perkin Elmer Universal ATR accessory.



Figure 2.5 *Perkin Elmer Spectrum 100 with Universal ATR Accessory fitted*

2.5 Accelerated Weathering

2.5.1 QUV Accelerated Weathering

Polymer film samples were cut to fit the Q panel sample holder and taped so that moisture would only form on the exposed side of the sample. The samples were then irradiated using a QUV Accelerated Weathering Cabinet (figure 2.6) which conforms to ISO 4892 (Methods of exposure to laboratory light sources). The lamps used were QUVA fluorescent tubes. The cabinets were operated continuously on an alternate 8 hour light cycle to 4 hours moisture cycle. The moisture cycle simulates the effect of rain followed by sunlight upon the panels. The cabinet achieves this by having a trough of water beneath the test panels which is heated during the period which the lamps are not operating.



Figure 2.6 QUV accelerated weathering cabinet

2.5.2 UV Exposure of DSC Test Cells

UV exposure was conducted using a custom made bank of 6 x 8 W UVA lamps held 5 cm above the test cells (figure 2.7). Measured intensity of the UV lamps was 0.64 W m^{-2} at a λ_{max} of 354 nm. This is of comparable UV intensity to ASTM G173-03(2008) which is given as 0.61 W m^{-2} at 354 nm [1].

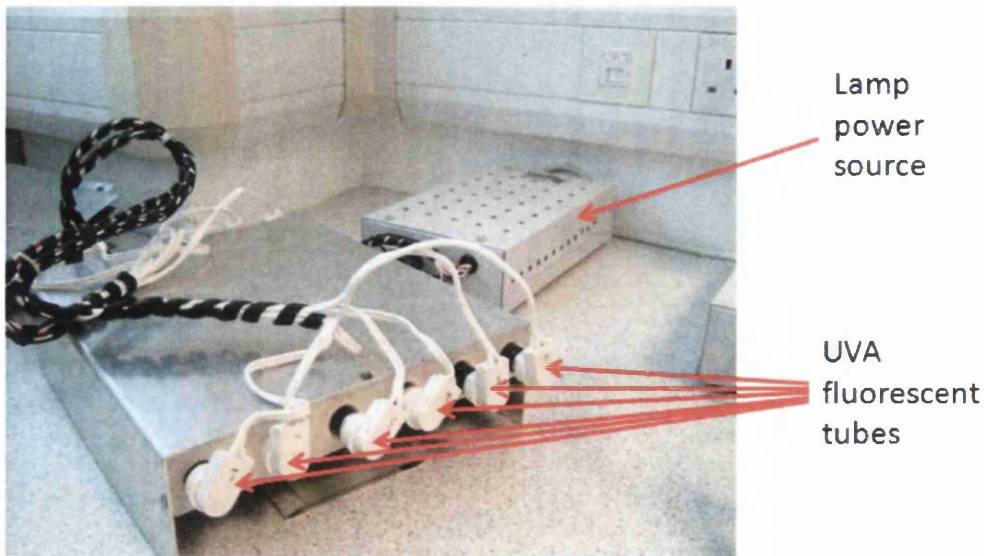


Figure 2.7 photograph showing the custom made bank of UVA lamps used for the UV exposure of DSC test cells

2.5.3 Visible Light Soaking of DSC Test Cells

Light soaking was carried out at in a Dyesol light soaking cabinet supplied with a 1000 W metal halide, high intensity discharge bulb. Intensity of illumination is controlled by adjusting the height of the lamp. As the lamp gets very hot and having the need to rule out temperature effects, the cells were light soaked at full lamp height which has been measured at 0.25 Sun using the NREL silicon reference cell.

2.6 Spectral Emission Measurements

Spectral emission measurements were carried using an Ocean Optics HR2000+ spectrometer which is a USB powered, fibre optic spectrophotometer consisting of a diffraction grating focussing spectra onto a CCD.

2.7 UV Exposure of DSCs under a N₂ Atmosphere

To expose cells to UV light under an inert atmosphere, hollow chambers were machined out of Al blocks (5 cm x 5 cm x 1 cm) and spigots were added to allow gas to flow through the chamber. The base of the chamber was electrically insulated with PTFE tape and DSC test cells were made with the same method described above. This time however, copper tape was used instead of silver paint as the contact so that wires could be soldered onto the contact to allow in-situ measurement without the need to break the seal. Test cells were then placed in the chamber, their connection wires were fed out through holes drilled into the side of the chamber which were then sealed with epoxy. A glass cover was sealed with epoxy to allow light to reach the cells. A schematic of the exposure chambers is shown in figure 2.8 below.

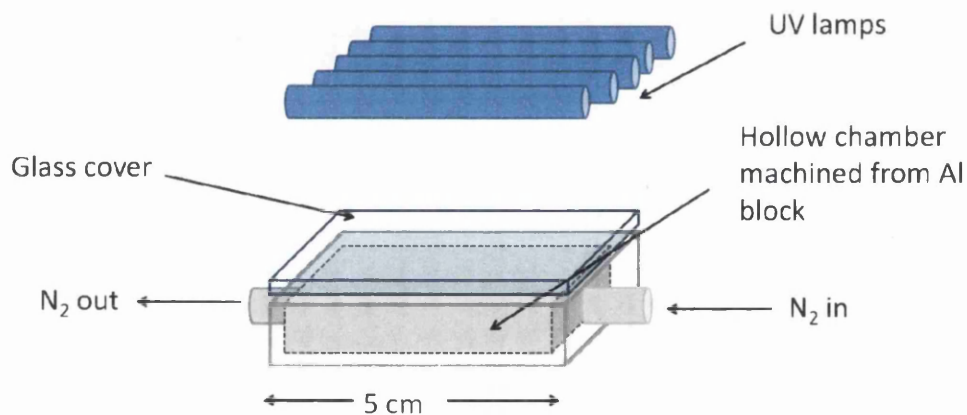


Figure 2.8 Schematic of inert atmosphere exposure chambers

2.8 References

1. ASTM International ASTM G173-03 Standard Tables for Reference Solar Spectral Irradiances: Direct Normal and Hemispherical on 37° Tilted Surface.

Chapter

3.

Characterisation of UV Photodegradation in Dye-Sensitized Solar Cells

3. CHARACTERISATION OF UV PHOTODEGRADATION IN DYE-SENSITIZED SOLAR CELLS

3.1 Initial Experiment

In order to assess UV protection measure for DSCs it was first necessary to fully understand what effects UV irradiation has upon the cell. It is well known that UV photodegradation leads to a loss in $\% \eta$. However, the aim of this experiment was to look at changes in the cell in more detail. This has been done initially with IV measurements and impedance spectroscopy. Eight cells were manufactured. Four were exposed using the bank of UV lamps described in *chapter 2.6.2*, the remaining four were kept in the dark.

The obvious method of measurement of the degree of photodegradation is to monitor changes in cell efficiency and indeed looking at Figure 3.1 below, it is clear that unprotected cells begin to fail at around 400 hours exposure and all have failed completely by around 800 hours exposure.

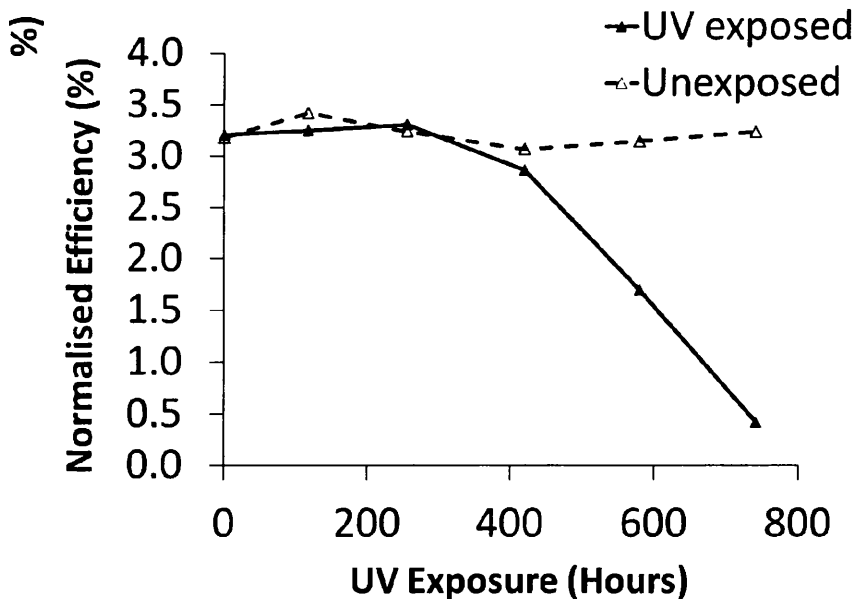


Figure 3.1 Effect of UV exposure upon the average efficiency of UV exposed and unexposed DSC test cells over the exposure period shown

3.1.1 Cell Characteristics at 120 Hours Exposure

It was found by looking at cell properties in more detail that signs of UV photodegradation occur much earlier than changes in $\% \eta$. Figure 3.2 shows the IV curves of a typical cell at 0 and 120 hours exposure.

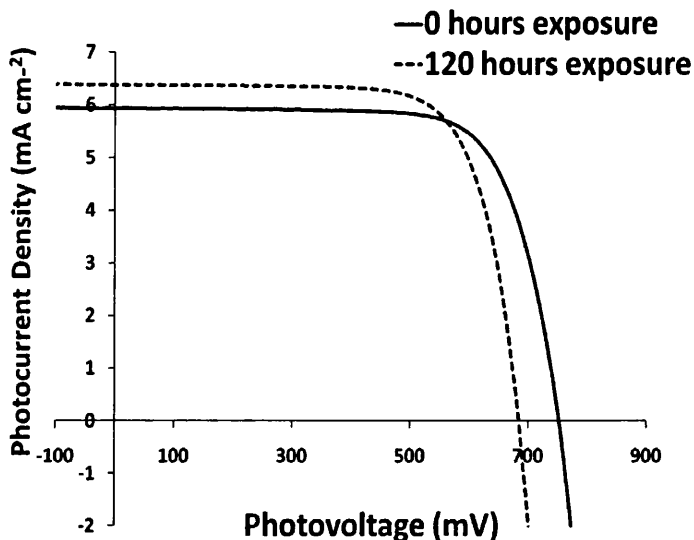


Figure 3.2 Typical IV curves of DSC test cells measured at one Sun, at 0 hours and 120 hours UV-exposure

Figure 3.2 shows that the V_{OC} has decreased whilst the J_{SC} has increased within just 120 hours of UV exposure. These changes can be attributed to UV exposure causing a positive shift in the TiO_2 conduction band (CB) possibly due to surface protonation [1]. This would explain the drop in V_{OC} as this is given by the energy difference between the TiO_2 quasi-Fermi level and that of the redox potential of the electrolyte [2] (see figure 1.5). The increase in J_{SC} could be due to an increase in electron injection efficiency caused by the increase in the energy gap between the excited state electrons in the LUMO of the dye and the TiO_2 conduction band [3].

Figure 3.3 shows the typical Nyquist plot and Figure 3.4, the Bode phase plot of cells at 0 and 120 hours exposure. The larger semi-circle of the Nyquist plot represents the resistance of electron transport within the TiO_2 film as well as the resistance TiO_2 /electrolyte back reaction (R_{BR}). It is clear from the Nyquist plot that the cell

experiences a large decrease in R_{BR} whilst the decrease in the phase angle at lower frequencies shown in the Bode phase plot suggests that electron lifetimes in the TiO_2 are reduced. Both of these results can be explained by an increase in the rate of the back reaction (equation 3.1) [1]. It is possible that the initial increased rate of reaction (3.1) could arise from dye ligand desorption (or desorption of another species) which exposes the TiO_2 surface.

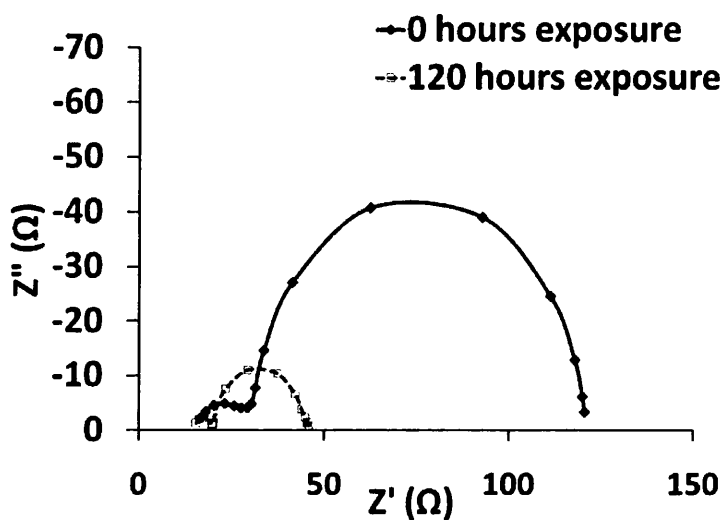
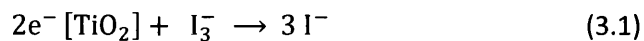


Figure 3.3 Typical Nyquist plot of cells at 0 and 120 hours exposure

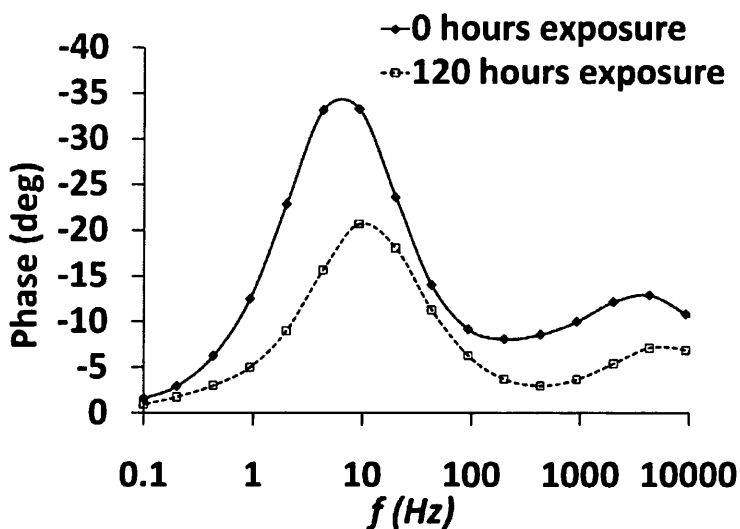


Figure 3.4 Typical Bode Phase plot of cells at 0 and 120 hours exposure.

3.1.2 Changes in Cell Properties during the Exposure Period

Figures 3.5 and 3.6 show the mean V_{OC} and J_{SC} respectively, of the cells tested over the 800 hour exposure period. The effect of UV exposure on V_{OC} is characterised by a large initial drop followed by a gentler decline. Despite J_{SC} initially increasing, at the point of failure J_{SC} decreases dramatically with a collapse in photocurrent which occurs at the point of cell failure.

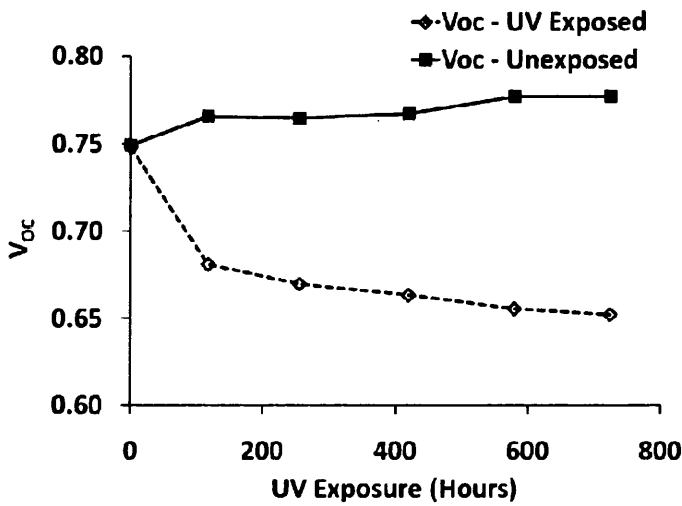


Figure 3.5 Mean V_{OC} of cells over the exposure period shown

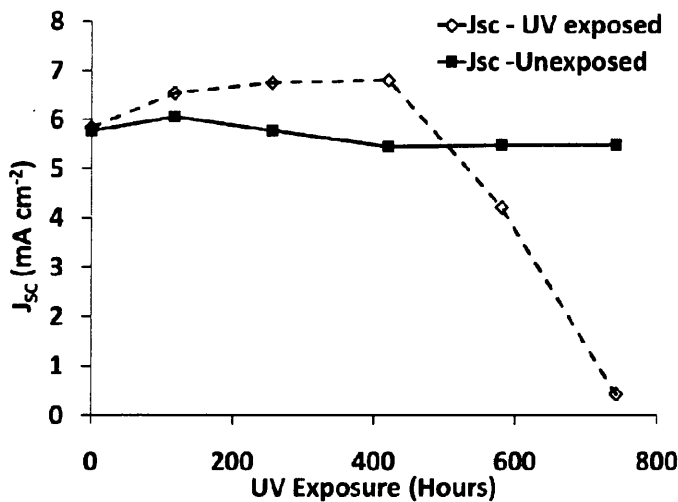


Figure 3.6 Mean J_{SC} of cells over the exposure period shown

Figure 3.7 shows the equivalent circuit used to model the EIS data in this chapter with R -Series representing the series resistance of the device, R -CE representing the charge transport resistance at the counter electrode (R_{CE}) and C -CE representing the platinum double layer capacitance (C_{CE}) at the counter electrode. R -BR represents the resistance of the electronic back reaction (R_{BR}) as well as electron transport within the TiO_2 film; CC -CPE (Q) and CC -CPE (n) are the constant phase element (CPE) parameters used to describe the chemical capacitance (C_{CC}) across the TiO_2 /electrolyte interface.

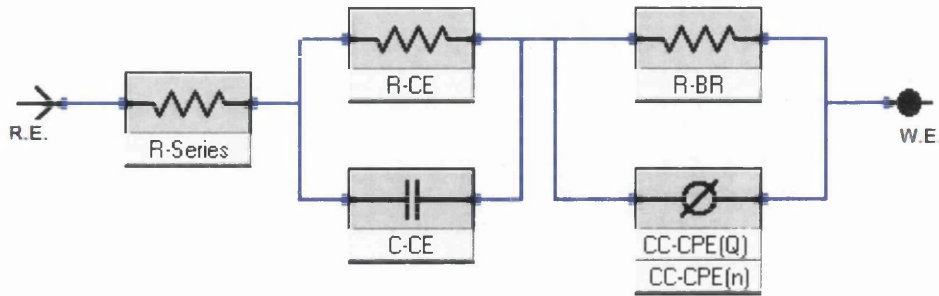


Figure 3.7 Equivalent circuit used to model EIS data

Figure 3.8 shows the trends in the all the modelled data, using the equivalent circuit in figure 3.7, over the exposure period. The equivalent chemical capacitance (C_{CC}) can be calculated from the CPE parameters and the value of R_{BR} with equation (3.2).

$$C_{CC} = \frac{(R_{BR} \times Q)^{1/n}}{R_{BR}} \quad (3.2)$$

There could be a number of reasons why the series resistances of cells kept in the dark increases whilst the resistances of those under illumination stay fairly constant (after a small initial decrease), it could simply be that the other resistances (R_{BR} and R_{CE}) in unexposed cells are increasing which could have an effect on the series resistance. The decreases in R_{BR} and R_{CE} of the irradiated cells seems to have a small effect on series resistance but this is unlikely to affect the R -Series a great deal as the series resistance is derived from the electrical contact resistances and resistances across the TCO electrodes.

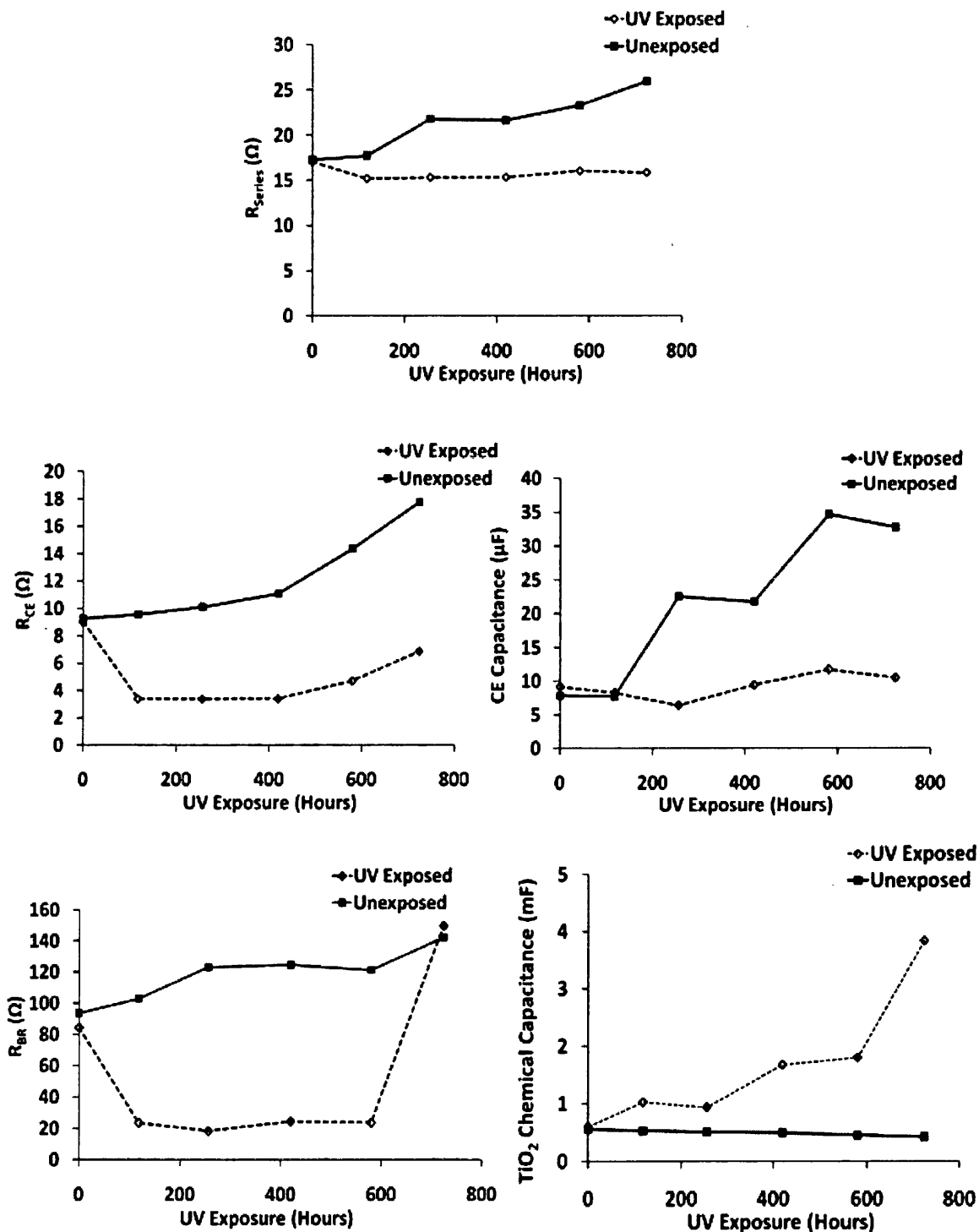


Figure 3.8 Trends in modelled cell properties over the exposure period. L-R from top: Series Resistance; R_{CE} (charge transport resistance at the counter electrode); C_{CE} (platinum double layer capacitance at the counter electrode); R_{BR} (resistance of chemical back reaction/ TiO_2 e^- diffusion); and Chemical Capacitance across the TiO_2 electrolyte interface. UV exposed cells are shown with a dashed line, unexposed cells are shown with a solid line

It has been shown by Hauch and Georg [4] that an increase in I_3^- concentration results in a decrease in R_{CE} (R_{CT} in figure 3.9), so the decrease in R_{CE} seen in irradiated cells is at first puzzling. The increase in the rate of the back reaction (equation 3.1), evidenced by a decrease in R_{BR} would suggest there should be a decrease in I_3^- concentration and therefore an increase in R_{CE} and not a decrease as is seen in figure 3.8.

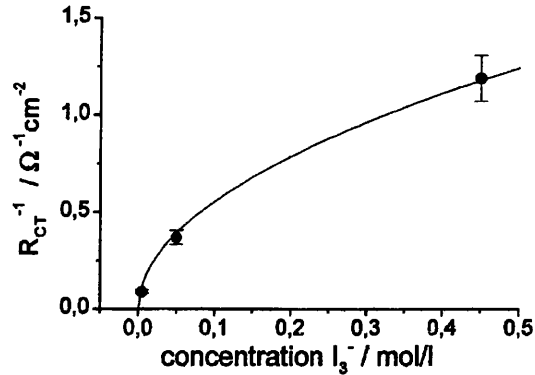


Figure 3.9 Dependence of the inverse of the charge-transfer resistance, R_{CT} [or R_{CE}] on the triiodide concentration, showing that $(1/R_{CE}) \propto \sqrt{[I_3^-]}$ – reproduced from [4].

It may be a possibility that, initially at least, there is an increase in the rate of reaction 3.3 at the photogenerated hole of the TiO_2 .



This would mean an initial increase in I_3^- concentration is possible in theory, which could explain the initial decrease in the resistance at the counter electrode. However, the collapse in photocurrent, the large increase in R_{BR} and the apparent bleaching of the electrolyte at the point of cell failure, all point to the removal of I_3^- from the electrolyte. If equation 3.3 was a dominant process then it would be expected that the yellow colour of the cell would darken and R_{CE} would reduce further as a result of increased I_3^- concentration. Instead, as the cells move towards failure, R_{CE} starts to increase slightly indicating the onset of the reduction in I_3^- concentration until the point of failure where the change in R_{BR} and other parameters show the near complete removal of I_3^- from the electrolyte. It is therefore necessary to propose a mechanism of I_3^- removal from the

electrolyte and it could be that I_3^- is being oxidised further at the TiO_2 photogenerated hole to a higher oxidation state such as I^+ , I^{3+} , I^{5+} (as IO_3^-) or perhaps I^{7+} (as IO_4^-).

Hauch and Georg [4] showed that I_3^- concentration has little effect on the C_{CE} so it is unclear why cells kept in the dark show an increase in capacitance at the counter electrode. Perhaps the increased capacitance has some relationship to the increase in V_{OC} seen in unexposed cells or maybe oxygen in the cell is poisoning the catalytic activity of the platinum, something which is not seen in UV exposed cells as the residual oxygen in the cell is being consumed by TiO_2 photoreactions. The reason however remains unclear and extensive literature searches have provided no clue as to the reason for the increase in C_{CE} for cells kept in the dark.

The initial drop in R_{BR} has already been explained above but it should be reiterated that at the point of failure, there is a large increase in R_{BR} . This along with the collapse in J_{SC} and the apparent photobleaching of the cell strongly suggest a removal of charge carriers, namely I_3^- , from the electrolyte. The steady increase in R_{BR} seen in unexposed cells occurs concurrently with the increase of V_{OC} and could be due to adsorption of species on the TiO_2 surface, causing a negative shift in the conduction band and blocking sites for the back reaction to occur resulting in increased I_3^- concentration. The increase in chemical capacitance is said to be as a result of the increase of the rate of equation 3.1 and the concurrent drop in V_{OC} [1].

It has been shown by Bisquert et al [5] that electron lifetimes (τ_n) in the TiO_2 film can be estimated from the product of R_{BR} and C_{CC} giving an RC time constant (equation 3.4). The estimated electron lifetime of cells over the exposure period is shown in figure 3.10 below.

$$\tau_n = R_{BR}C_{CC} \quad (3.4)$$

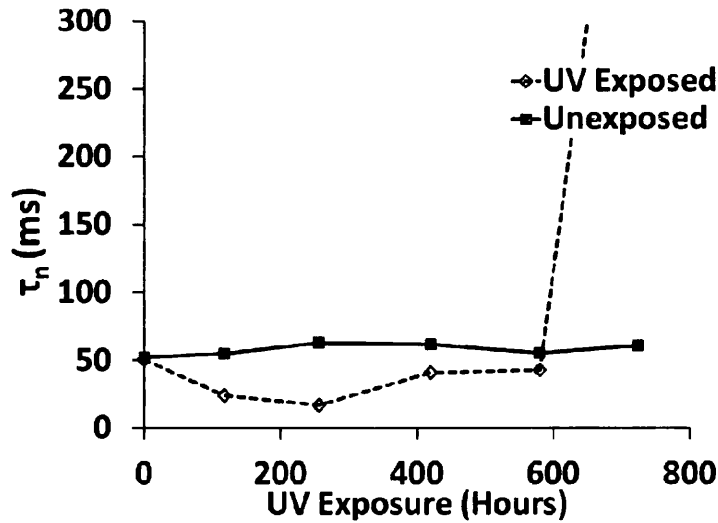


Figure 3.10 Estimated electron lifetime of the exposed and unexposed cells over the exposure period shown

The initial decrease in electron lifetime of exposed cells follows what one might expect if the rate of equation (3.1) was increasing due to UV exposure. It is interesting to note that between 300 and 400 hours exposure there is an increase in electron lifetime. This could indicate a slowing of the back reaction (equation 3.1) due to a reduction in I_3^- concentration. This is also the point where R_{CE} starts to increase which could also be due to decreasing I_3^- concentration; it is the point where J_{SC} starts to drop and it is the point at which $\% \eta$ starts to decline. These phenomena all indicate that during the exposure period the cell reaches a point, just before failure, where the level of charge carriers in the electrolyte drops to a critical level. After this point, cells undergo a rapid and catastrophic failure resulting in a collapsed J_{SC} and therefore $\% \eta$.

3.2 Reverse Illumination and Cells Exposed under Electrical Load

Figure 3.11 shows the mean efficiencies and the V_{OC} of the cells subjected to UV irradiation over the time period shown. Some cells were irradiated from the WE (Forward) side, some were illuminated from the CE (Reverse) side and some were irradiated under a load provided by 100 Ω resistor. These are compared to cells that were kept in the dark at 40°C as this was the measured temperature under the UV lamps.

In Figure 3.11 it is clear that there is a pattern in the relative rates of degradation of the cells tested. First to fail are the cells irradiated under load followed by cells irradiated from the WE side and cells irradiated from the CE side. Cells kept in the dark at 40°C show comparatively little sign of degradation, despite a gradual decline in efficiency. This pattern is repeated when looking at the drop in V_{OC} values but in this case the drop in V_{OC} manifests itself much quicker than the decline in efficiency.

Figure 3.12 shows the change in J_{SC} and the change in R_{BR} over the exposure period. Despite initially showing an initial increase of J_{SC} and a reduction of R_{BR} , cells that are continually exposed to UV irradiation suffer a collapse in photocurrent and a large increase in R_{BR} . At this point the failure of the cell coincides with a bleaching of the electrolyte which along with the collapse in J_{SC} and the large increase in R_{BR} strongly suggests that the cell degradation reaches a point where the I_3^- had been consumed until there are not enough charge carriers available to give the cell a viable photocurrent.

It is possible that apparent photo-bleaching of the electrolyte could be caused by TiO_2 catalysed reaction with the I^-/I_3^- redox couple. If this were the case then this could explain the relative rates of degradation seen in Figures 3.11 and 3.12. Cells exposed in reverse are filtered to a certain extent by the electrolyte. This slows degradation as filtering of the UV light decreases direct photo-excitation of the TiO_2 and thus decreases photodegradation. When under load there is less chance of recombination of the electron-hole pair created by direct photoexcitation as some of the electrons in the TiO_2 conduction band are removed via the external circuit.

This would result in a net increase in the number of oxidative holes which would increase the rate of photodegradation of the electrolyte and ultimately increase the rate of failure of the cell compared to those cells exposed without an external load.

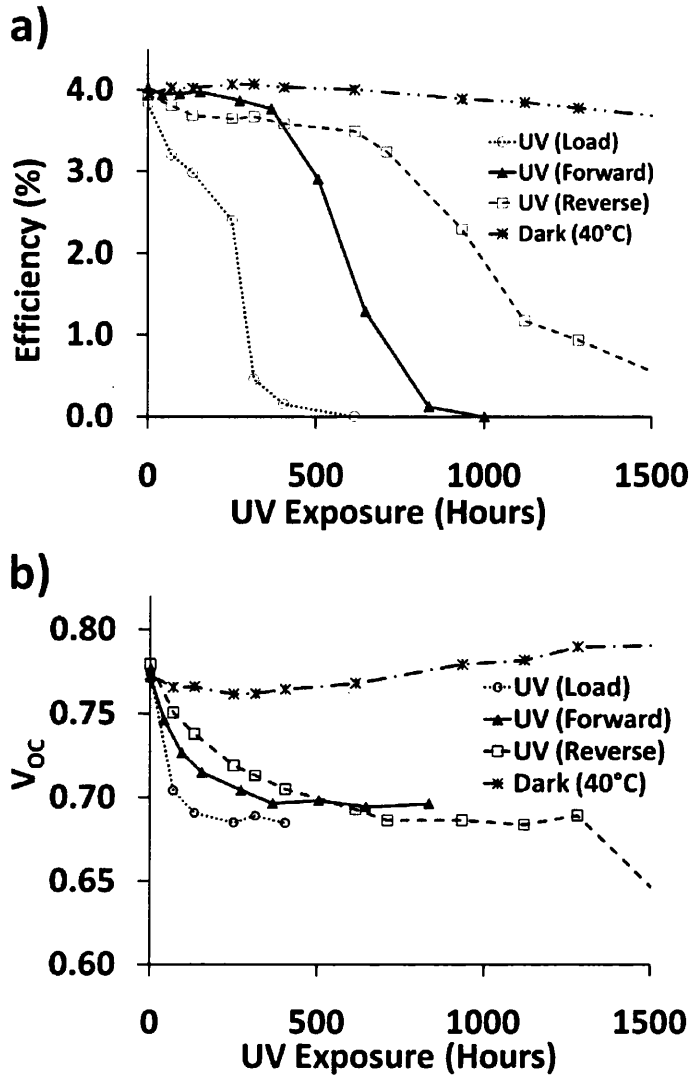


Figure 3.11 Mean efficiencies (a) and V_{OC} (b) of 1 cm x 1cm test cells subjected to UV irradiation over the time period shown. There are four cells in each set.

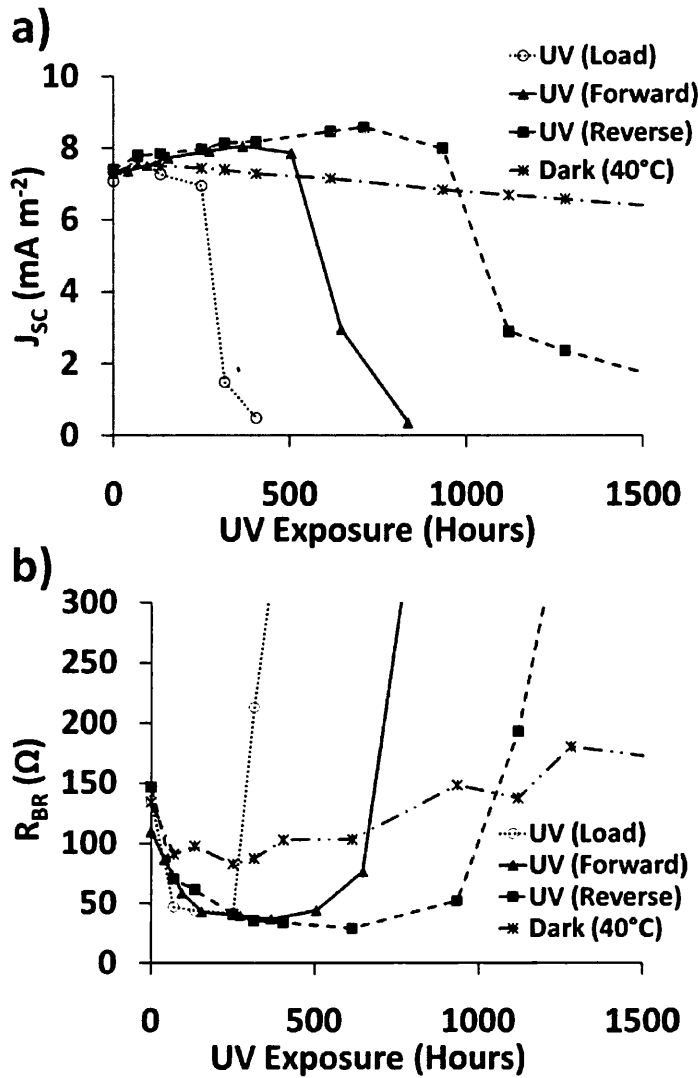


Figure 3.12 The change in J_{SC} (a) and the change in R_{BR} (b) over the exposure period

Figure 3.13 shows the estimated electron lifetimes of four sets of cells described in this chapter. In each case the electron lifetime is characterised by a decrease as the rate of the back reaction increases, followed by a gentle increase, which has been ascribed to the slowing of the back reaction, possibly due to I_3^- depletion, followed by a large increase attributed to passing the threshold of critical I_3^- concentration whereby photocurrent collapses and the back reaction virtually stops. The order this occurs in, with regards to the cell sets, matches the order of changes in all the other cell properties described in this chapter.

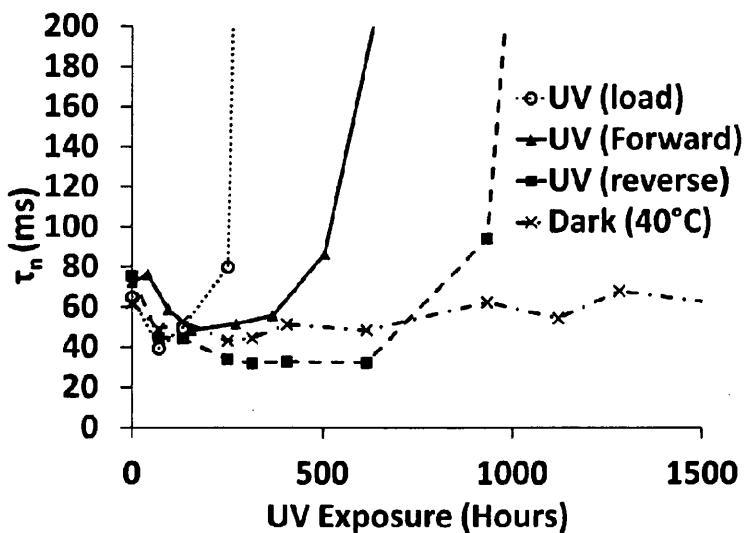


Figure 3.13 Estimated electron lifetimes over the exposure period

3.3 Photobleaching of the Electrolyte

During the initial experiment described in chapter 3.1 an attempt was made to measure the colour change in the cell as it was thought that the photobleaching of the electrolyte would be closely related to the other changes in the properties of the cell. Two methods were employed. The first was standard UV-Vis transmission measurements and the second was RGB colour analysis of photographs taken of the cells. Both methods were employed at the same intervals as the EIS and IV measurements. Unfortunately neither method produced reliable results.

It was difficult to maintain a consistent background light for the RGB photographs. The RGB value varied greatly for the same cells in pictures that were taken a few seconds apart. This could have been solved by using a light box or a deflected flash, however neither method was available at the time. The 1 cm² cells used in chapter 3.1 created alignment problems when using the UV-Vis spectrophotometer and so gave very unreliable results. It was decided that a new set of larger cells in order to cover the UV-Vis sample aperture and to get better results. The results of UV exposure of these larger cells will be described fully in chapter 4.

3.4 Dye Stability

Some work was briefly carried out upon dye stability in air. The samples used in this chapter consist of a titania film (Dyesol DSL18NRT) cast onto ITO glass and sintered, this was then dyed with N719 dye. Some samples were subjected to light soaking in the Dyesol light soaking unit, some were irradiated with UV light and some were kept in the dark in the light soaker to compare the effects of temperature. Dye degradation was measured by looking at a decrease in the absorption peak of the dye at 540 nm which can be seen in figure 3.14.

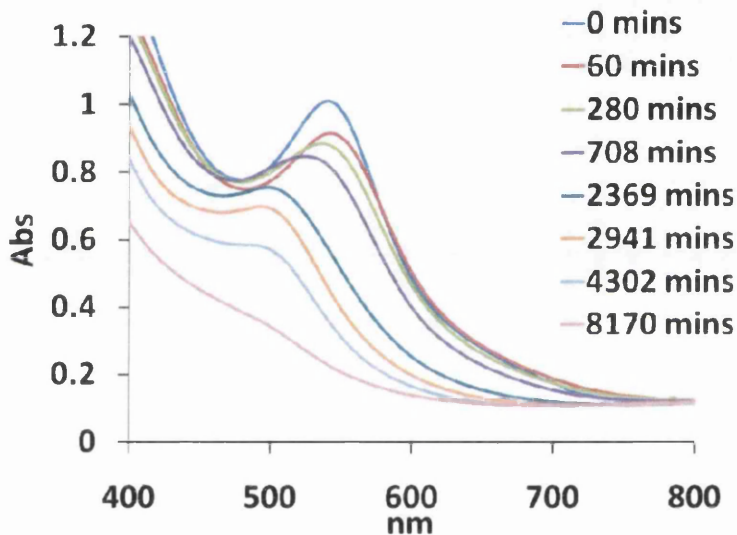


Figure 3.14 Decreases in absorbance of UV irradiated sample over 8200 minutes exposure

Figure 3.15 shows the decrease in absorbance at 540 nm of the samples over the course of 8500 minutes. These results should be looked at in conjunction with the emission spectra of the light sources in question (see *chapter 5*, in particular figure 5.1). It is clear from the output of the two light sources that they have very different emission spectra. There is only a small overlap at around 400 nm. Despite the light sources being very different, the samples behaviour under their respective sources of illumination is remarkably similar. The rate of degradation in the light soaked sample appears to be higher than the UV irradiated

sample at first but the rate relaxes after around 1000 minutes. The rate of degradation in the UV irradiated sample seems linear until around 3000 minutes where it too relaxes.

N719 has a λ max centred at 312 nm and is assigned as an intraligand (π - π^*) charge-transfer transition, but this unlikely to be the cause of degradation in the light soaked samples as the emission of the light soaker lamps at that wavelength is 0.01 W m^{-2} . N719 has another λ max at 386 nm assigned to the metal-to-ligand charge-transfer [6], this excitation is possible with the UV lamps used but the degradation under the UV lamps however, is likely to be caused by the photocatalytic activity of TiO_2 . Temperature effects can be ruled out as the samples kept in the dark were at similar temperatures to that under the UV lamps and in the light soaker. These unexposed cells show a very slow rate of degradation. Similarly, degradation in the light soaked sample must be due visible light absorption as the lamp emissions in the UV are low (around 0.01 W m^{-2} at 360 nm). N719 has a λ max at around 530 nm which is also due to the metal-to-ligand charge-transfer [6], so perhaps this is the origin of the mechanism of degradation.

The fast rate of degradation under the visible lamps may be due to charge injection from the excited dye into the TiO_2 conduction band. Where this occurs in an operating cell, the oxidised dye is quickly reduced by the I^- in the electrolyte. When the oxidised dye is exposed to air in this case, it may become unstable. It may be that the charge recombination from the TiO_2 to the dye or the relaxation of the excited state may be slow enough for the oxidised dye to react with air or moisture. This does not occur under UV illumination and the photodegradation is probably due to TiO_2 photocatalysis. As it seems that the degradation of the adsorbed dye in air occurs due to different mechanisms depending on the light source used, it may be unwise to compare relative rates without looking at the relative photon counts at the wavelengths in question for each light source. As work was continuing on the photostability of complete DSC test cells and it was seeming more likely that electrolyte degradation was more important, at least under UV illumination, no further work on dye stability was conducted.

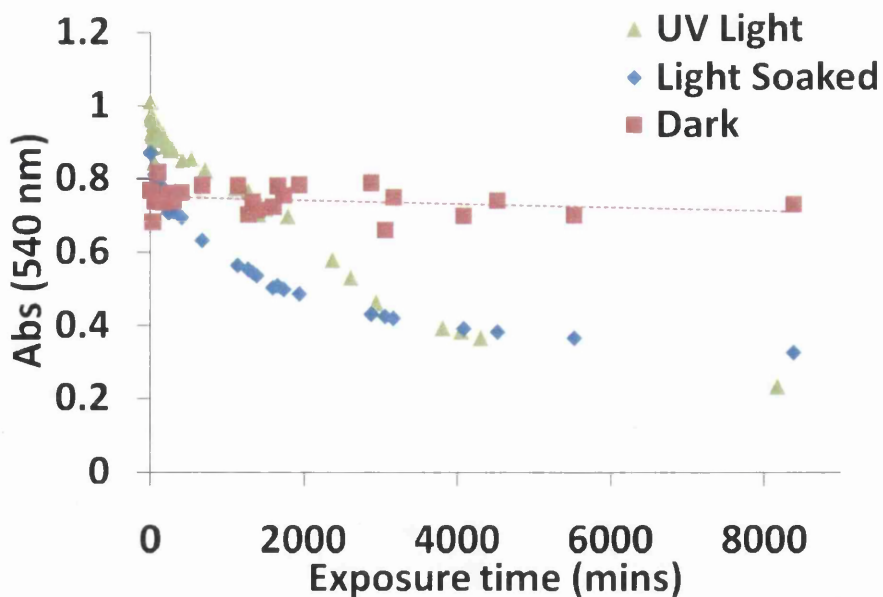


Figure 3.15 Decrease in absorbance at 540 nm of samples over 8500 minutes exposure

3.5 Irradiation of Cells under a Nitrogen Atmosphere

When this experiment was initially proposed it was thought the percolation of oxygen through the Surlyn seal may play a part in cell degradation. In order to assess this, the controlled atmosphere irradiation chambers described in *chapter 2.8* were used to irradiate cells in a N_2 atmosphere as it was thought that if the mechanism of DSC photodegradation under UV light is due to photo-oxidation of the electrolyte, then the rate of degradation may be slowed if no atmospheric oxygen is present, giving further insight into the mechanism. Cells were irradiated under open circuit conditions and under load. Figure 3.16 shows the IV characteristics of the cells over the exposure period shown it appears that cells fail faster under load when irradiated in air than when irradiated under N_2 , but when looking at the open circuit irradiated cells there seems to be no significant difference between the air and N_2 irradiated cells.

The reason for this could be that under load, the majority of the oxygen adsorbed onto the TiO_2 surface is consumed quickly *via* photoreactions. The rate of photodegradation then depends on the rate of oxygen percolation through the seal and in this case the rate of percolation through the seal is much slower when a nitrogen atmosphere is present. The

reason why this does not occur in cells exposed under open circuit could be that the overall rate of oxygen consumption within the cell is slower and so percolation through the seal is not an important factor in cell degradation. However, the drop in V_{OC} has so far been the best indicator of the onset photodegradation and there appears to be no significant difference in the rate of V_{OC} decrease between cells irradiated under a N_2 atmosphere and those irradiated in air. Nonetheless, as it is hypothesized that the mechanism of failure by accelerated UV exposure is the photooxidation of I_3^- , and that the I_3^- concentration is directly related to the diffusion limited current in the cell, then it could be inferred that the I_3^- in cells irradiated under load in air is undergoing a faster rate of photooxidation than the I_3^- in cells irradiated under load under an N_2 atmosphere.

The obvious next step would be to build cells in an inert atmosphere and to bubble nitrogen through the electrolyte prior to cell assembly as this would eliminate the majority of oxygen within the cell, although there is also the possibility of oxygen adsorbed to the TiO_2 surface being very difficult, if not impossible to remove. Unfortunately at the time these experiments were carried out, the facilities were not available to do this. At the time of writing however, an atmospheric chamber has become available and it would be recommended for use in future work to determine further, the photodegradation mechanism of DSCs.

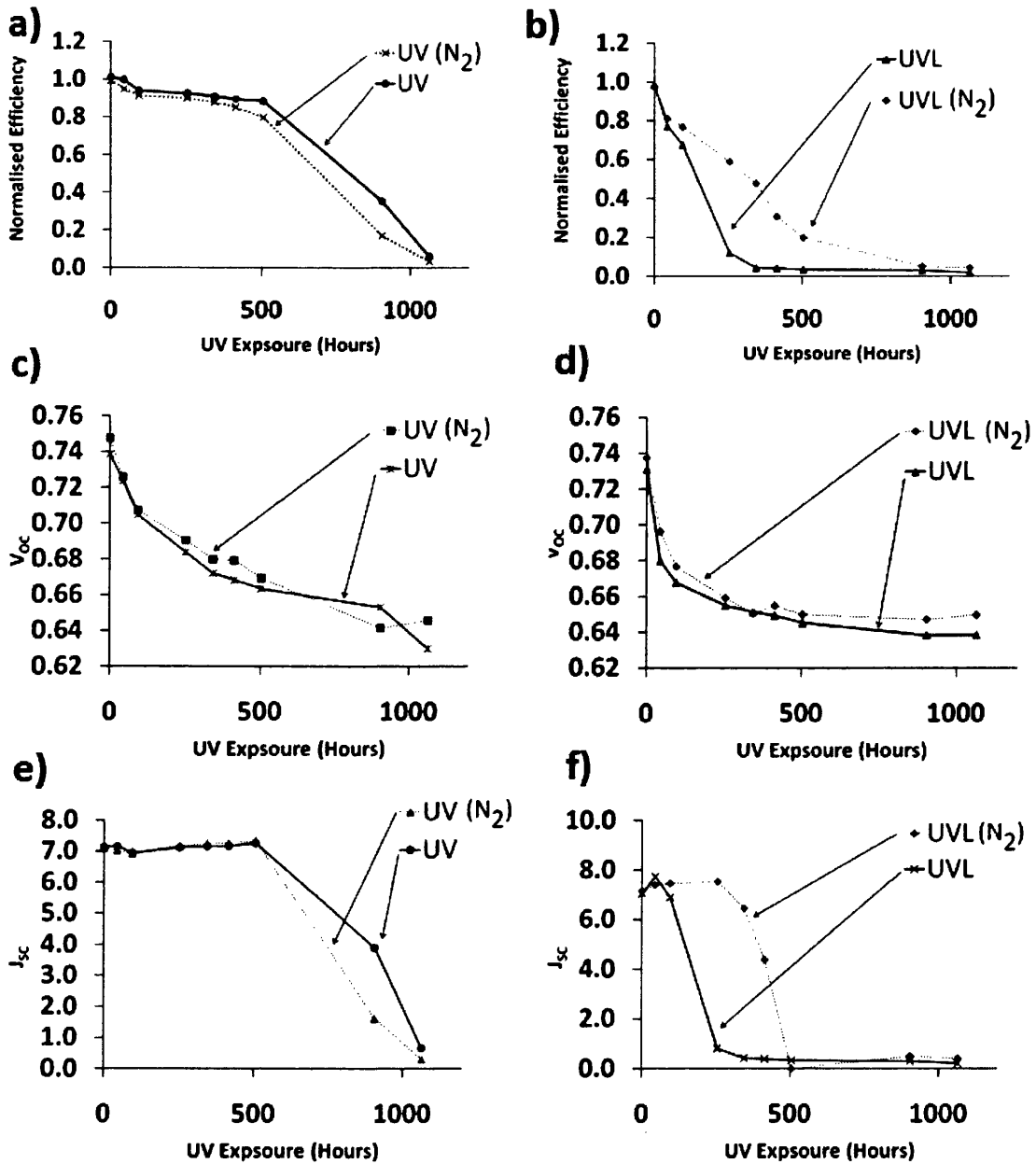


Figure 3.16 Changing IV characteristics of 1 cm x 1 cm test cells over the exposure period shown: a) normalised η of cells under open circuit; b) normalised η of cells under load; c) V_{oc} of cells under open circuit; d) V_{oc} of cells under load; e) J_{sc} of cells under open circuit; f) J_{sc} of cells under load. UV = UV exposed, open circuit; UVL = UV exposed, under load N_2 indicated the cell was exposed in a nitrogen atmosphere.

Figure 3.17 shows the change in R_{BR} of the cells over the exposure period and much like the IV data, it shows that the N_2 atmosphere makes a difference in cells irradiated under load but not in those exposed under open circuit conditions.

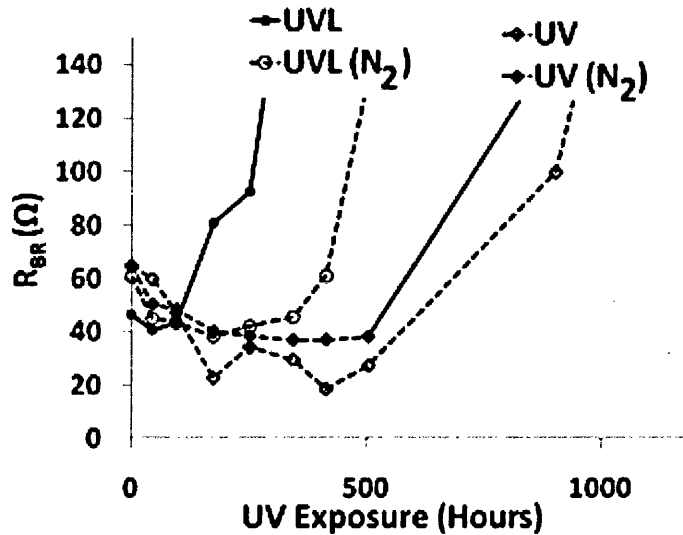


Figure 3.17 Change in R_{BR} for samples over the UV exposure period shown

3.6 Conclusion

UV irradiation is detrimental to dye sensitized solar cell performance. This chapter shows that there are subtle changes that occur within a few days of exposure that manifest themselves before changes in cell efficiency are detected. The open circuit voltage, short circuit current and back reaction resistance (V_{OC} , J_{SC} and R_{BR}) all change relatively rapidly and these are therefore potentially important indicators of cell degradation.

From the results in this chapter, the mechanism of degradation in cell performance seems to be through TiO_2 photo-catalysed attack on the electrolyte. This is evidenced by the collapse in J_{SC} seen at cell failure and the large increase in R_{BR} . This along with the photobleaching observed and modelled capacitive and resistive data from EIS measurements, suggests that I_3^- is being consumed by this process and that at some point

there are not enough charge carriers to carry a viable photocurrent or to facilitate the back reaction.

Further evidence of photo-catalytic action upon the electrolyte is given by the fact that cells degrade faster under electrical load. At open circuit electrons in the TiO₂ conduction band will quickly recombine with the photogenerated holes as there is no external transport mechanism. Holes in the valence band should be further stabilised by injection from the LUMO of the excited state dye. Under electrical load the electrons in the TiO₂ conduction band are exported to the external circuit with the result being a net increase in the number of photogenerated holes which in turn leads to a faster rate of photodegradation. Further evidence that the mechanism of photodegradation may be TiO₂ catalysed photooxidation comes from the fact that cells under load degrade marginally slower in an inert N₂ atmosphere. Cells degrade slower when irradiated from the CE side because photons have to travel through the electrolyte which has some UV filtering properties. The filtering properties of the electrolyte will be described further in *chapter 9*.

3.7 References

1. H. Desilvestro, M. Bertoz, S. Tulloch and G. Tulloch (2010). Packaging, Scale-Up and Commercialization of Dye Solar Cells, in Dye-Sensitized Solar Cells, K. Kalyanasundaram. Lausanne, EPFL Press.
2. M. Grätzel, Perspectives for dye-sensitized nanocrystalline solar cells, *Progress in Photovoltaics: Research and Applications* 2000 **8**(1) 171-185
3. S. Ferrere and B.A. Gregg, Large increases in photocurrents and solar conversion efficiencies by UV illumination of dye sensitized solar cells *Journal of Physical Chemistry B* 2001 **105**(32) 7602-7605
4. A. Hauch and A. Georg, Diffusion in the electrolyte and charge-transfer reaction at the platinum electrode in dye-sensitized solar cells *Electrochimica Acta* 2001 **46**(22) 3457-3466
5. J. Bisquert, F. Fabregat-Santiago, I. Mora-Seró, G. Garcia-Belmonte and S. Giménez, Electron Lifetime in Dye-Sensitized Solar Cells: Theory and Interpretation of Measurements, *The Journal of Physical Chemistry C* 2009 **113**(40) 17278-17290
6. Y. Zhang, H. Zhang, Y. Wang and W. F. Zhang, Efficient Visible Spectrum Sensitization of BaSnO₃ Nanoparticles with N719, *The Journal of Physical Chemistry C* 2008 **112**(23) 8553-8557

Chapter

4.

Measurement of Photobleaching using Larger Area Cells

4. MEASUREMENT OF PHOTBLEACHING USING LARGER AREA CELLS

Due to the problems described in the previous chapter with regards to measuring the colour change in DSCs as they undergo UV photodegradation, larger area cells were made using the same method as described in *chapter 2.1*, except that these cells had a WE electrode area of 6.25 cm^2 (i.e. $2.5 \text{ cm} \times 2.5 \text{ cm}$). At first an offset cell design (figure 4.2) was used as this would require less glass and would be simple to manufacture but the offset cells had poor fill factors due to the long electron transport distance to the electrical contact (figure 4.1).

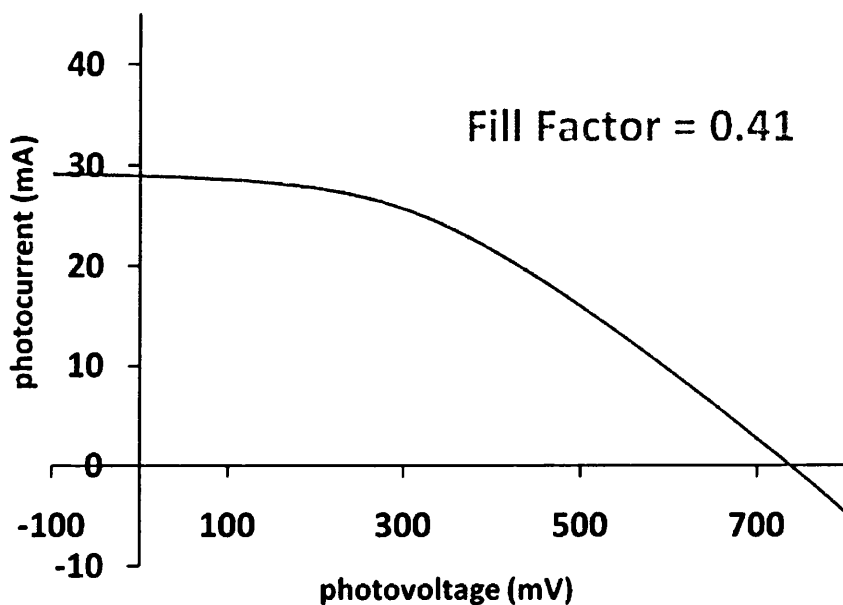


Figure 4.1 IV curve of larger area offset cell showing poor fill factor

The poor fill factor was partly solved by switching to the cross cell design, meaning that in effect these cells were a direct scale-up of the standard 1 cm^2 test cell design. Despite solving the poor fill factor problem the cross cells brought further issues which are explained in the following sections. Figure 4.2 shows the larger area cross cell along with the offset cell and 1 cm^2 test cell for comparison.

The larger area cells were subjected to UV exposure in the same manner described in *chapter 2.6.2* and the changes to IV and impedance properties were compared with cell colour changes measured with a UV-Vis spectrophotometer.

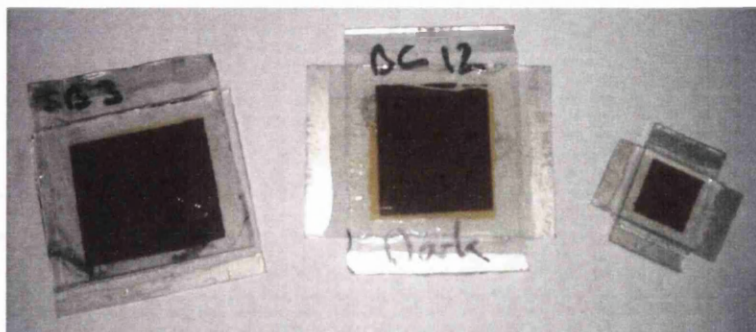


Figure 4.2 6.25 cm² offset cell (left), 6.25 cm² cross cell (middle) and 1 cm² test cell (right)

4.1 IV Data for Larger Area Cells

4.1.1 Issues Relating to the IV Measurements of the Larger Area Cells

Figure 4.3 shows the typical IV curve of a larger area cell. Apart from the increased photocurrent which is to be expected from a larger area device the most obvious difference between the larger cells and those described in *chapter 3* is that the IV curve has a considerable element of noise. In the case of figure 4.3 the curve has been smoothed using Microsoft Excel. The IV measurement software has an option to smooth the first 20% of the data points measured but it is not known if the software uses a similar algorithm to Excel. In any case, the data smoothing by Excel includes all data points and is just shown here for illustrative purposes. In this particular case the IV scan is in forward bias and started at higher voltage and scanned towards lower voltage, in effect scanning from just beyond V_{OC} to just after J_{SC} . It could be that the spikes seen at higher voltage are due to capacitive effects, possible due to charge build up at the CE-electrolyte double layer boundary. These effects are more severe at higher voltages and less so at lower voltages as seen by the relative smoothness of the curve.

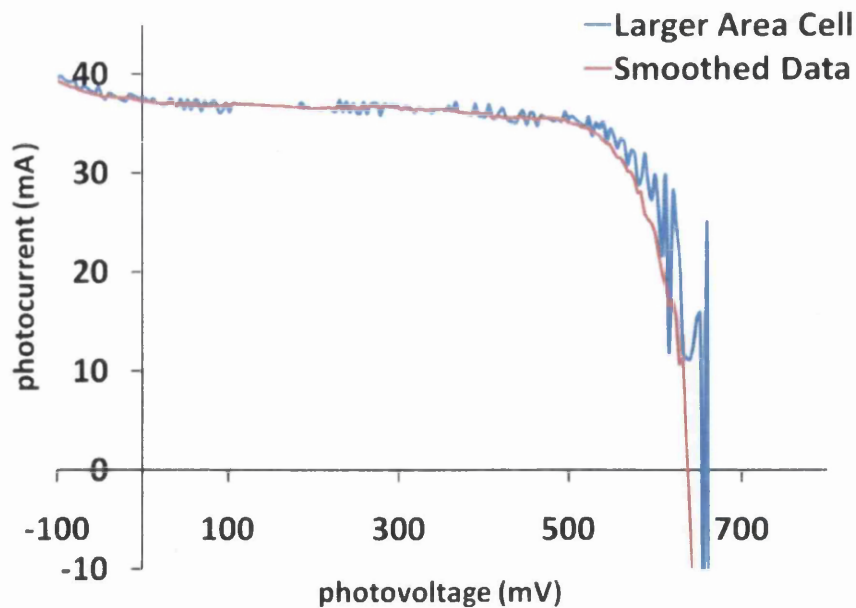


Figure 4.3 Typical IV curve of a larger area cell also showing smoothed data

The noise of the IV scans creates two problems for analysing the data from these cells. Firstly the fill factor seems to be artificially high. This seems to stem from the capacitive jumps from low to high current seen at around 680 mV. These appear to make the vertical part of the curve steeper than is to be expected and it could be that the solar simulator's software calculates the fill factor artificially high as a result of this. Secondly, as can be seen from the smoothed curve in figure 4.3 there may be some uncertainty in the calculation of the V_{OC} . The IV measurement software has an option to smooth the first 20% of received data points, which encompasses the vertical part of the curve; the V_{OC} is calculated from the smoothed data so there may be some uncertainty as to the accuracy of the value of V_{OC} .

There could be a number of reasons for the capacitive effect. Any effects related to short circuiting have been ruled out as all cells were tested for short circuits before back filling with the electrolyte and in any case the two cells in this set that were found to be shorting, exhibit the same level of noise in their IV curves. Other reasons could be poor platinisation of the CE leading to high double layer capacitances or insufficient binder removal in the TiO_2 film causing build up (and release) of charge in electronic traps. In any case, as this work is concerned with long term trends rather than basic cell properties, no further investigation was made into the reasons for the noise in seen in the vertical section of the

IV curve. The data calculated by the software was used but it was made sure that the points it used to calculate the V_{OC} were realistic.

4.1.2 Long Term IV Trends in UV Exposed Larger Area Cells

Figure 4.4 shows the trends in IV data for the four sets of cells tested. The same pattern of cell failure seen in chapter 3 is also observed here. There are however some differences between the larger area cells and the standard 1 cm^2 cells. Unexposed larger area cells appear to exhibit a large Nernst diffusional feature at lower frequencies (figure 4.6) which is not observed in their smaller analogues. Cell failure appears to be slower in these cells than the 1 cm^2 cells especially the cells exposed from the CE (reverse) side which were still giving good photocurrents at around 2000 hours exposure. The same drop in V_{OC} is observed although, in this case, there is no real difference between cells under load and cells under open-circuit. The same collapse in photocurrent is observed but again occurs much later in the larger area cell than in their smaller analogues.

Although the Surlyn seals used in the larger area cells are the same thickness as the seals used in the 1 cm^2 cells, due to their larger size, some warping of the seal occurred during the sealing process. This warping occurred along the plane of the seal and resulted in an electrolyte filling area larger than the 6.25 cm^2 area of the working electrode. This would mean that the larger area cells have a higher *electrolyte volume to working electrode area ratio*. This might explain the higher Nernst diffusion impedance exhibited and may also explain the noise of the IV curves as capacitive effects which have arisen from charge build up in the electrolyte. If the ratio of electrolyte volume to WE area is greater in the larger area cells then it appears that the higher volume of electrolyte in these larger cells has stabilised them somewhat against photodegradation compared to the smaller cells. It has been shown in *chapter 3* that UV exposure removes I_3^- from the electrolyte as evidenced by the photobleaching of the cell, the collapse in J_{SC} and the large increase in R_{BR} at the point of failure. It is thought that this is a reversible reaction as photodegraded cells, once put in dark, start to recover some of their photocurrent. Cell recovery will be fully discussed in *Chapter 8* but what this suggests is that UV exposure pushes the electrolyte far to one side

of an equilibrium consisting of photodegradation (I_3^- depletion) in one direction and recovery (I_3^- regeneration) in the other (see figure 4.5 below).

In the smaller cells, under constant UV illumination, the rate of photodegradation is much faster than the rate of recovery so the equilibrium is pushed far to the right. The higher volume of electrolyte in the larger cells means that there is more chance of recovery so it takes longer for UV exposure to push the equilibrium to the right hand side. This is seen especially in the CE (reverse) side exposed cells where due to filtering by the Pt electrode and the electrolyte, the rate of photodegradation is slower, both compared to the other cells in the data set and the reverse exposed 1 cm^2 cells in *chapter 3*. As mentioned, the recovery of photodegraded cells will be discussed in detail in *chapter 8* but it is worth mentioning here that once the equilibrium is pushed to the far right the rate of recovery is slow, even in degraded cells which are then kept in the dark. The larger area cells do however appear to recover faster in the dark than their smaller counterparts lending further evidence to the hypothesis that the larger volume of electrolyte stabilizes the cells somewhat against photodegradation.

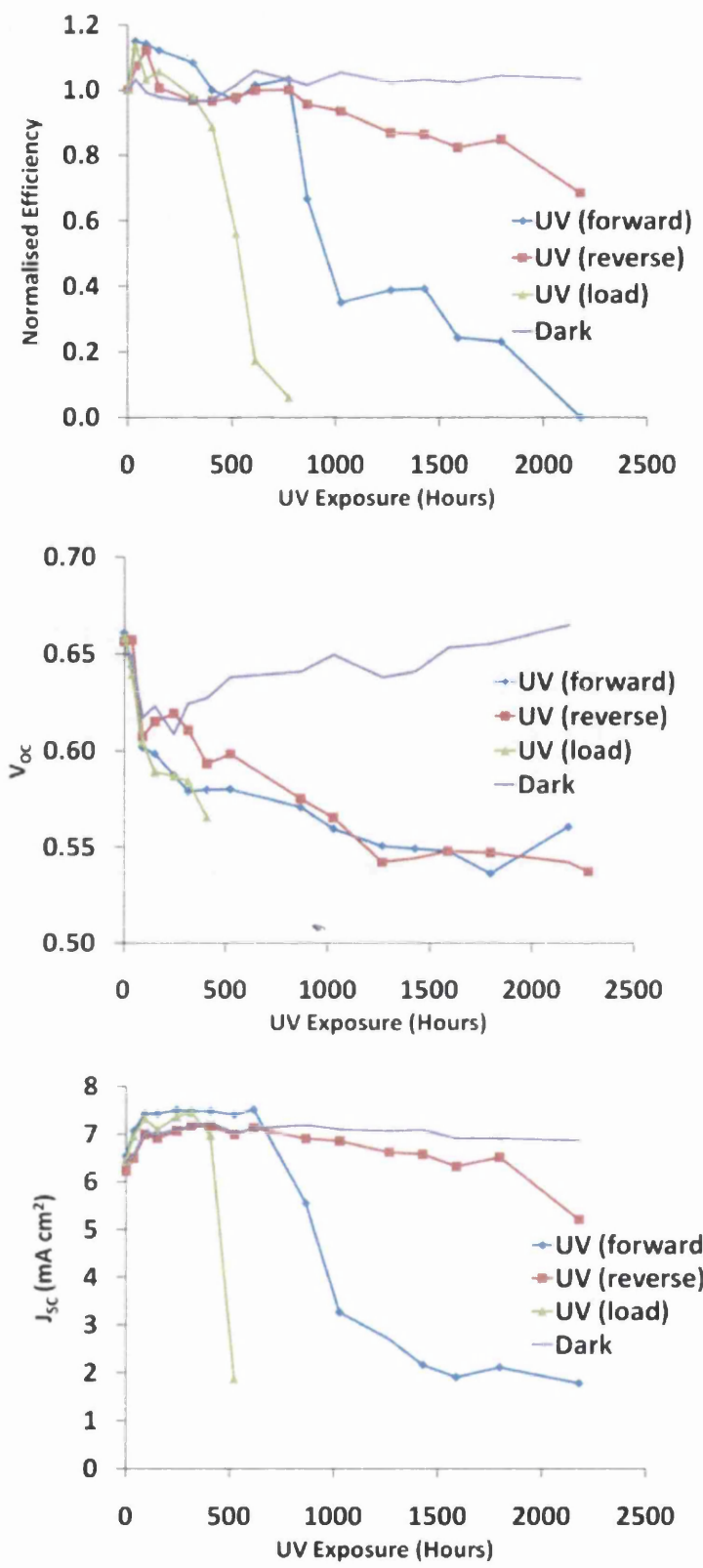


Figure 4.4

Long term IV trends for larger area (6.25 cm^2) test cells exposed to UV irradiation showing the decline in cell efficiency, the drop in V_{oc} and the reduction of J_{sc} which is typical of cells exposed to UV irradiation

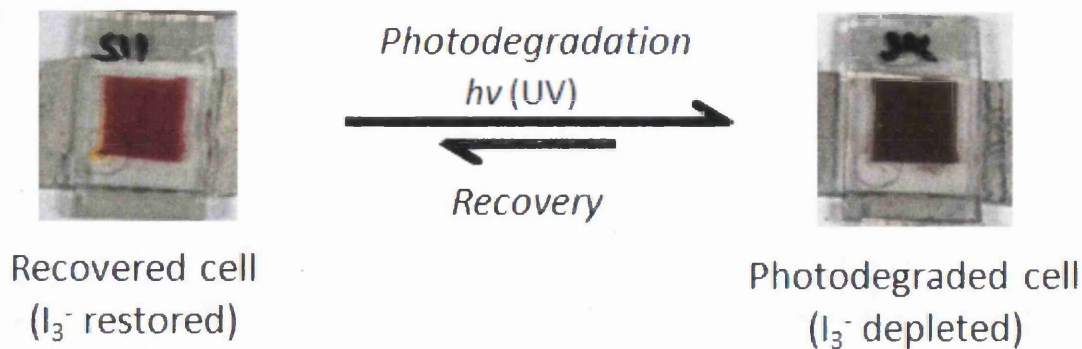


Figure 4.5 Photodegradation/recovery equilibrium of DSC test cells under UV irradiation

4.2 Impedance Data for Larger Area Cells

4.2.1 Issues Relating to EIS Measurements of Larger Area Cells

As with the IV measurements, EIS measurements of the larger cells brought some difficulties. Possibly due to the larger volume of the electrolyte, the Nernst diffusion resistance of the I_3^-/I^- was large with respect to R_{BR} . This creates a problem for modelling cell resistances as the model used to calculate resistance values does not include an element to represent the Nernst diffusion impedance of the electrolyte. In cells exposed to UV irradiation this was not a problem as although UV exposure causes a decrease in R_{BR} , it seems also to decrease the Nernst diffusion resistance of the cell, so that it becomes hidden by R_{BR} . As the majority of cells were being exposed to UV light, the model described in chapter 3, without a Nernst diffusion element was suitable for modelling these cells.

Figure 4.6 shows the Nyquist plot of a larger area cell before UV exposure and the model fit using the circuit model described in *chapter 3.1.2*. The feature due to Nernst diffusion is visible from around 50 Ω to 90 Ω (Z_{real}). In order to fit the model, which has no element to describe the Nernst diffusion, it was decided to only use those data points in the Nyquist plot that corresponded to the impedances at the CE/electrolyte interface and the TiO_2 /electrolyte interface. The model data is also shown in figure 4.6. The data points used to calculate the model plot are shown as “real data points” whilst those that were

calculated by the model are shown as “modelled data points”. The modelled Nyquist plot is typical of unexposed larger area cells that *do not* exhibit the Nernst diffusion feature at lower frequencies. The Nyquist plots are typical of Gerischer shaped photoelectrode plots which indicate that electron diffusion length in the TiO_2 film is greater than the film thickness resulting in large transport resistances and high recombination rates [1]. The decision to model the data this way was vindicated as, after around 2200 hours UV exposure, those cells kept in the dark exhibited an increase in R_{BR} which caused the Nernst diffusion feature to become more obscured within the R_{BR} arc and the measured Nyquist plot to become more like the modelled plot. This is illustrated in figure 4.7 below and it shows that the modelled data in figure 4.6 is an accurate representation of the Nyquist plot had the Nernst diffusion been hidden by R_{BR} in the first place.

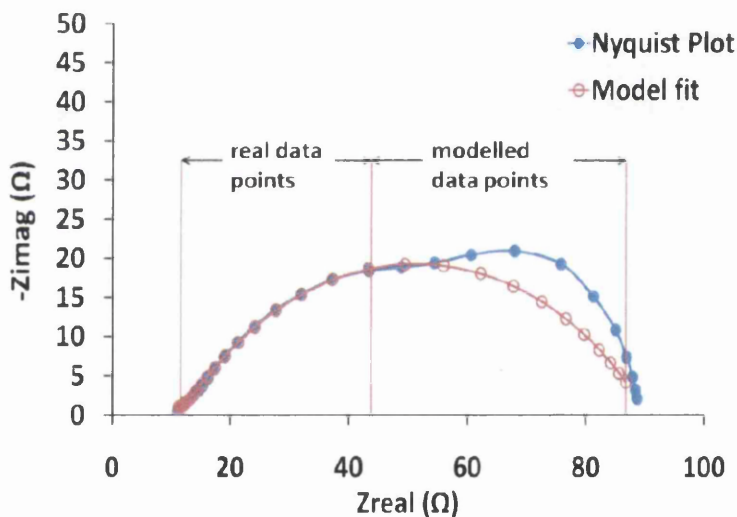


Figure 4.6 Nyquist plot of a larger area cell before UV exposure and the model fit using a similar circuit model as described in chapter 3.1.2, except this time C_{CE} is modelled with a constant phase element

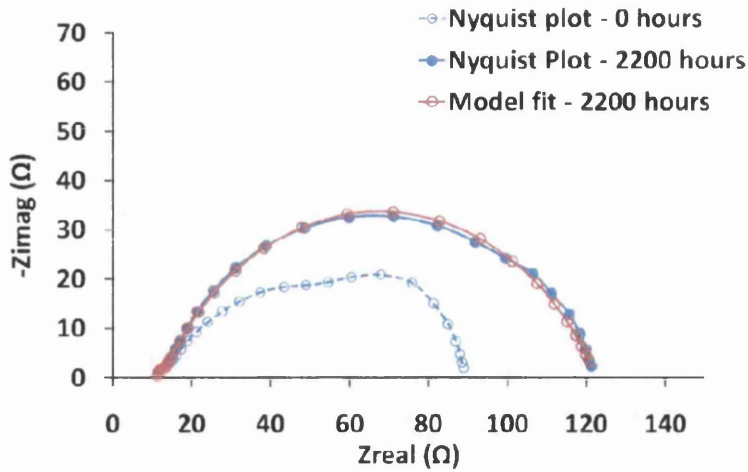


Figure 4.6 Nyquist plot of a larger area cell after 2200 hours in the dark and the model fit using the circuit model as in figure 4.6. The Nyquist plot at 0 hours from figure 4.6 is also shown.

4.2.2 Long Term Trends in R_{BR} of Larger Area Cells

Figure 4.7 shows the long term trend in the normalised R_{BR} of the test cells. The familiar pattern of initial drop in R_{BR} caused by the increase in recombination, followed by a large increase upon cell failure is observed. As with the IV data shown in figure 4.4 the CE (reverse) exposed cells survive remarkably well. There is however a sign at 2200 hours that the R_{BR} is about to increase, this coincides with a sign that J_{SC} is about to decrease indicating the possibility of imminent cell failure. Unfortunately the cells were not exposed further than 2200 hours so there is no way of knowing if this is the case.

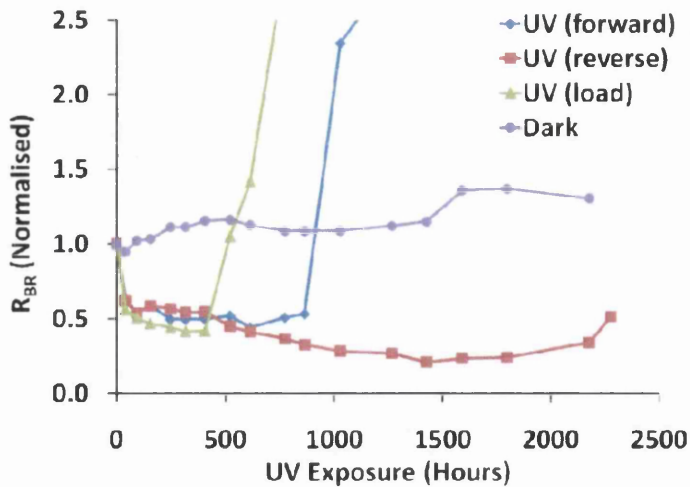


Figure 4.7 Long term trend in R_{BR} (normalised) of larger area cells

4.2.3 Qualitative Analysis of Nyquist Plots

In cells exposed to UV irradiation, the Gerischer shaped impedance curve gave way to the more familiar double arc representing CE and WE resistances and in most cases a short straight line of 45° was observed between the photo and counter electrode impedance arcs. This is said to be a characteristic of the electron transport resistance [1] and is often characterised using the transmission line model [2] (see chapter 1.11.3). Figure 4.8 shows a typical Nyquist curve before UV exposure, exhibiting the Gerischer type shape with a feature at lower frequencies that has been attributed to Nernst diffusion in chapter 4.3.1 and the typical curve after exposure exhibiting the more familiar double arc and transmission line. Figure 4.9 shows the transmission line feature in more detail. The transmission line feature is indicative of the charge transport resistance being greater than that of the recombination resistance (i.e. $R_t < R_{BR}$), this is in fact the opposite case of the Gerischer impedance described above where $R_t > R_{BR}$. The change from the Gerischer shape to the more familiar double arc transmission line feature is almost certainly due to the increased rate of the back reaction whereby the cell begins life under the condition $R_t > R_{BR}$ and so exhibits a Gerischer impedance. After UV exposure, R_{BR} decreases relative to the transport resistance so that $R_t < R_{BR}$ and so the cell exhibits the transmission line feature.

The opposite can be seen in cells kept in the dark whereby R_{BR} is seen to increase, maintaining the $R_t > R_{BR}$ relationship and so the Nyquist plot retains its Gerischer shape.

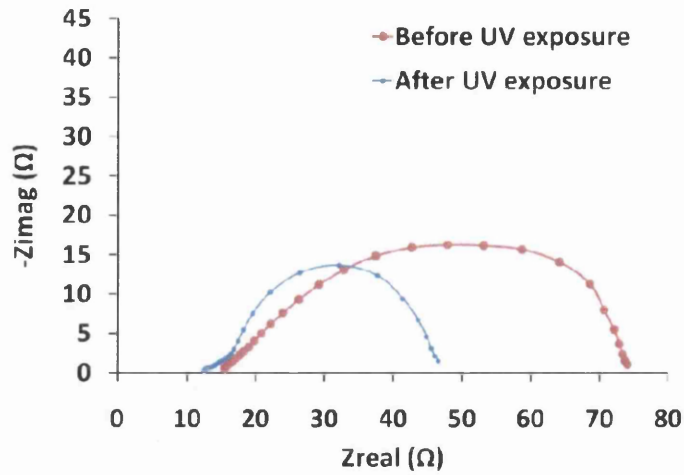


Figure 4.8 A typical Nyquist curve before UV exposure, exhibiting the Gerischer type shape and after UV exposure exhibiting the familiar double arc with transmission line feature

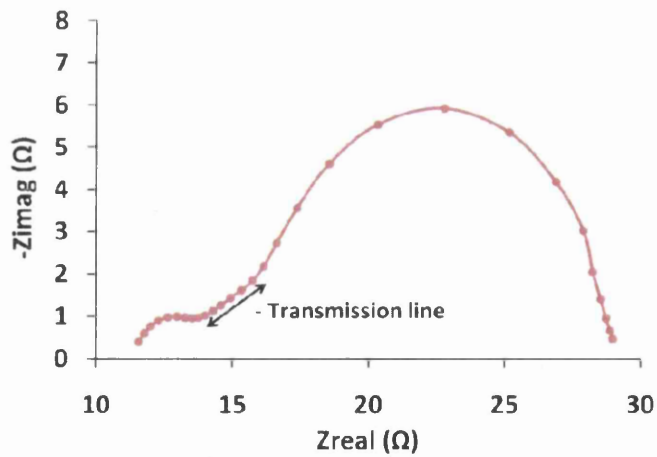


Figure 4.9 The transmission line feature of Figure 4.8 in more detail

The larger area cells with, a WE area of 6.25 cm^2 , were built in order to cover the sample aperture of the UV-Vis spectrophotometer which has a diameter of 3 cm. This was necessary to avoid the alignment issues experienced with the smaller cells. Figure 4.10 shows the UV-Vis spectra of a typical cell exposed from the WE side under open-circuit, at different stages of UV exposure. The two features of note are the λ_{max} of the dye (*ca* 530 nm) and the large absorbance at around 450 nm due to the yellow colouration of the electrolyte [3].

Figure 4.10 shows that the absorbance related to the adsorbed N719 dye remains relatively constant and the main colour shift is at much lower wavelengths where the electrolyte is absorbing. This adds weight to the suggestion that it is the failure of the electrolyte that is responsible for the failure of the cells. This is perhaps a little surprising given that the dye is adsorbed on the TiO_2 .

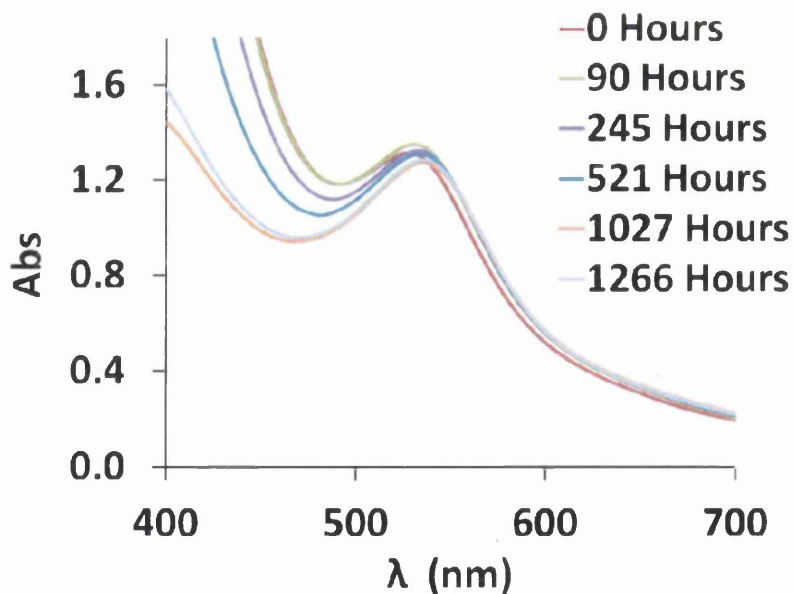


Figure 4.10 The UV-Vis spectra of a typical cell exposed from the WE side under open-circuit, at different stages of UV exposure

The relative colour changes are more clearly illustrated in Figure 4.11 where the absorbance of the cell at 531 nm (the λ_{\max} of the dye) and 450 nm (a representation of the electrolyte absorbance) are plotted as a function of time. 450 nm was chosen to represent electrolyte colouration as the λ_{\max} of the I^-/I_3^- redox couple is obscured by the large absorbance of the TiO_2 and also because the isosbestic point of I_2/I_3^- is around 460 nm [4]. Figure 4.11 shows that the electrolyte is clearly being degraded whilst dye absorbance remains fairly constant.

If the relative rates of colour change of the cells is compared (figure 4.12), the same pattern of degradation is seen as in the IV and Impedance data showing that colour change is a fundamental aspect of the UV photodegradation of DSCs and that the bleaching of the electrolyte is the dominant failure mechanism which leads to the collapse in photocurrent and the large increase in R_{BR} .

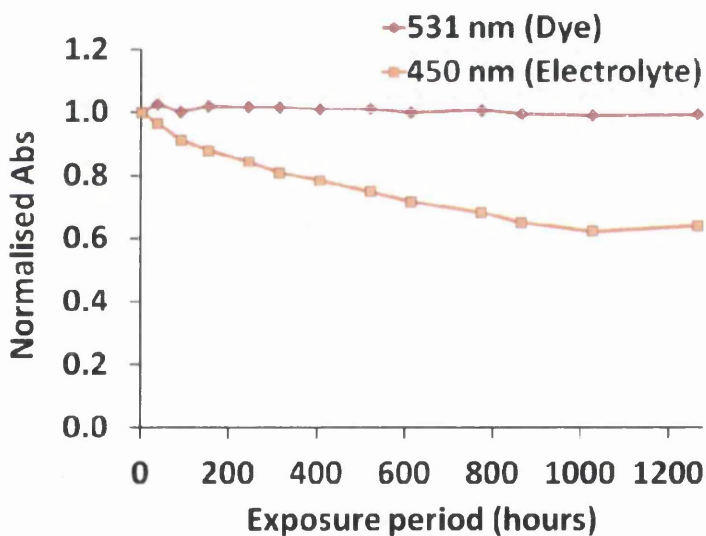


Figure 4.11 The changing absorbance of cells at 531 nm (representing dye colouration) and at 450 nm (representing electrolyte colouration) over the exposure period. The absorbance values were normalised to the absorbance value before exposure. All values were averaged from sets of four cells

Having observed that the electrolyte was being degraded it was desirable to work out the origin of the failure. It could be that the electrolyte is directly attacked or that it is related to TiO_2 photo-reactions. Figure 4.13 illustrates the changes in electrolyte absorbance at

450 nm as a function of UV exposure time for two model cells. The first model cell was assembled from two counter electrodes (to examine whether UV alone caused the failure). The second cell type was essentially a full DSC assembly but without any dyeing step.

It can be seen from the data in Figure 4.13 that the UV alone does not cause failure but that having a TiO_2 electrode causes very rapid failure. Indeed, comparing this data with that from figure 4.11 where the dye is included on the TiO_2 , the presence of the dye dramatically slows the rate of electrolyte failure. This is probably for two reasons. Firstly the dye will have taken up active sites on the TiO_2 and secondly it seems that at open circuit the dye is able to inject electrons into the TiO_2 (as evidenced by the accelerated failure under load). Hence it appears that it is the TiO_2 and photo-oxidation by photo-generated holes that is the primary reason for attack on the electrolyte.

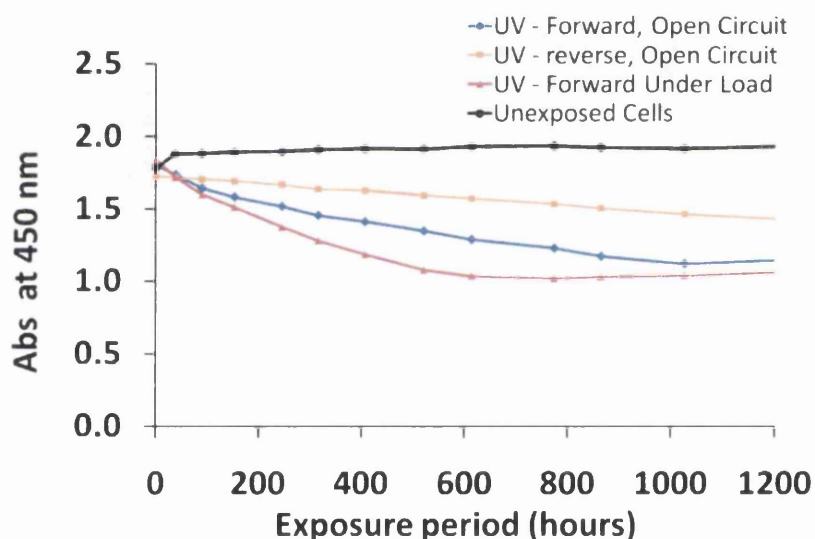


Figure 4.12 Relative rates of colour change (measured at 450 nm) of cells exposed to UV irradiation

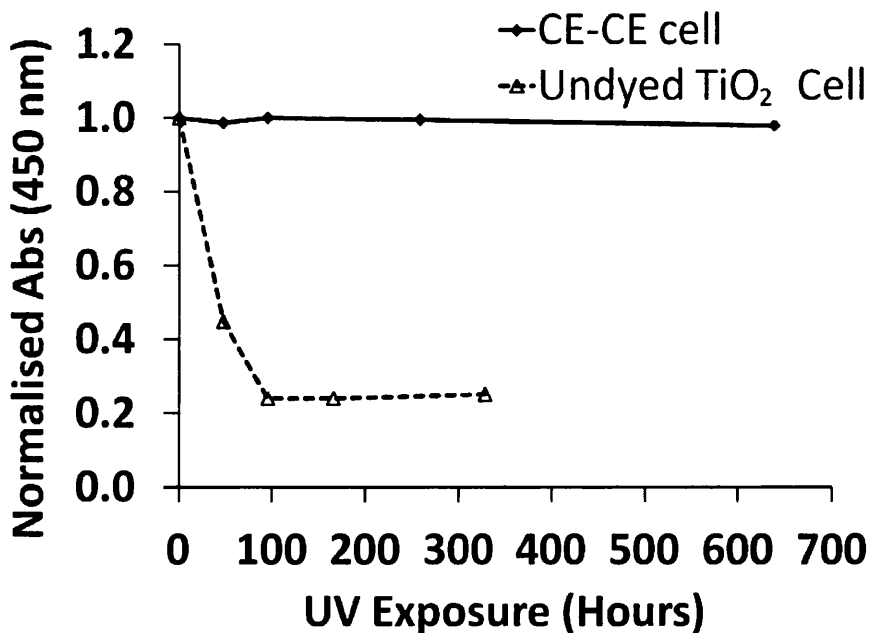


Figure 4.13 Change in absorbance of model cells. The undyed cell is essentially a complete DSC. The CE-CE cell consists of two counter electrodes and the electrolyte. This clearly shows that TiO₂ is required for electrolyte degradation under UV illumination.

The rapid bleaching observed in undyed cells is accompanied by impedance spectra (figure 4.14) which shows the typical initial reduction in R_{BR} of a DSC exposed to UV light. In this case where there is no dye the reduction in R_{BR} is very fast and is reduced considerably after just 48 hours exposure. This initial reduction is followed by a large increase in R_{BR} indicative of a very rapid consumption of charge carriers (I_3^-/I^-) within the electrolyte. The relative stability of the electrolyte without the presence of TiO₂ as indicated by the figure 4.13 is supplemented by the impedance data shown in figure 4.15 below. In figure 4.15 the smaller arc represents the Nernst diffusion resistance of the I_3^-/I^- redox couple, this is often hidden in DSCs and undyed cells by the much larger arc representing e^- diffusion in the TiO₂ and recombination resistance, referred to in his thesis as R_{BR} . It can be seen in figure 4.15 that although the series resistance of the cell has increased which is indicated by the shift of the Nyquist plot to higher Z_{real} between 0 and 639 hours exposure, the Nernst diffusion resistance of the electrolyte doesn't change indicating that there is no change to the composition of the electrolyte. This is of course also shown in figure 4.13 where the constant absorbance at 450 nm of the CE-CE cell indicates no change in the concentration of I_3^- despite a considerable amount of constant UV exposure.

All the evidence above points to the possibility that the TiO_2 surface in fresh cells initially has a greater coverage of adsorbents. These may be electrolyte components or some other residual material and their adsorption onto the surface makes recombination difficult and so results in larger R_{BR} values. UV exposure then initiates the removal of these adsorbed species allowing greater recombination and hence lowering R_{BR} . Once the I_3^- has been consumed to a critical level, R_{BR} then increases dramatically as the $\text{TiO}_2/\text{I}_3^-$ interfacial reaction is no longer possible. Perhaps most importantly, this occurs in cells where there is no dye present and also that it occurs rapidly in these undyed cells. In a normal DSC it might seem more probable that this initial exposure of the TiO_2 surface should be caused by desorbing dye ligands as these are the major adsorbents on the TiO_2 surface. The evidence here however, suggests that the initial increase in the recombination rate is due to the desorption of some component of the electrolyte and not desorption of the dye or one of its ligands.

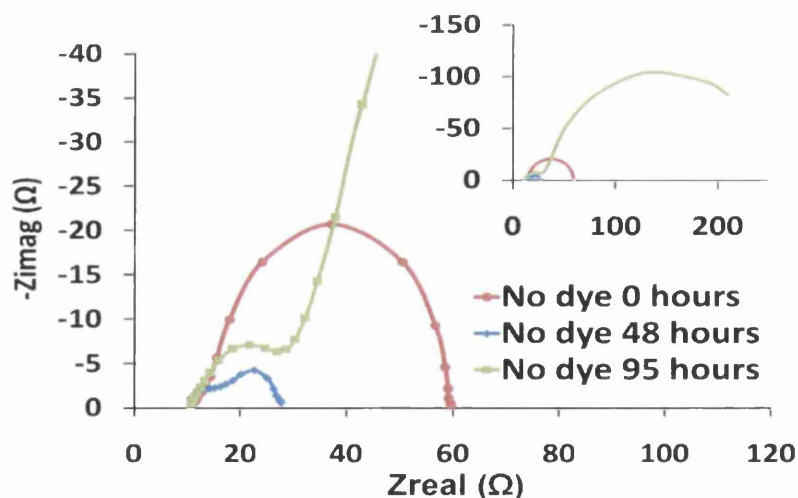


Figure 4.14 Change in Nyquist plots of undyed TiO_2 cells over the UV exposure period (inset is the same data expanded to a larger scale)

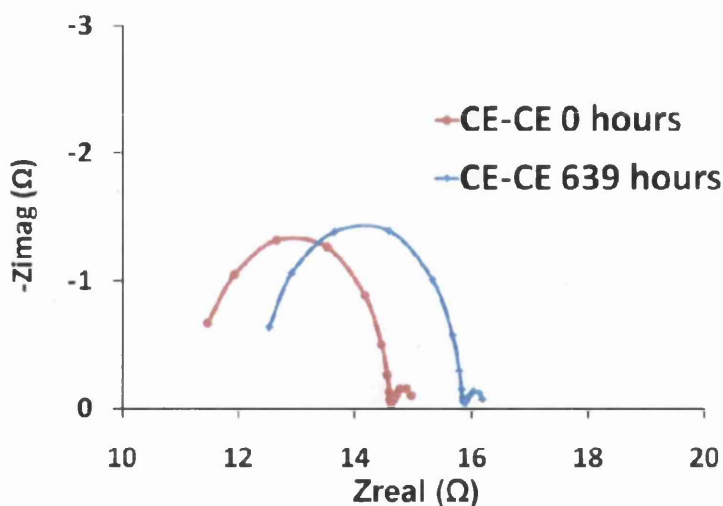


Figure 4.15 Nyquist plots showing Nernst diffusion resistance in CE-CE cells at 0 and 639 hours UV exposure.

4.4 Conclusion

The end of *chapter 3* concluded with the hypothesis that cell degradation under constant UV illumination occurs via a TiO_2 photo-catalysed attack on the electrolyte as evidenced by the collapse in J_{SC} seen at the point of cell failure and the large increase in R_{BR} . The photobleaching of the electrolyte has been characterised in this chapter and the relative rates of I_3^- consumption, as measured by a reduction in the absorbance of the cell at 450 nm, have been shown to follow the same pattern as other changes in cell properties such as V_{OC} , J_{SC} and R_{BR} , the pattern being that the rate of change of properties used to measure photodegradation always occurs fastest in cells irradiated from the WE side and under load and slowest when irradiated from the CE side and under open circuit. This is further evidence of a TiO_2 catalysed reaction and confirms that the electrolyte is undergoing a change in composition, along with, and in some cases *as a cause of* the other changes observed. The final observation that confirms TiO_2 as the cause of the cell failure is seen in figure 4.13. In a model cell with no TiO_2 the electrolyte does not change colour. Also in figure 4.13, the rapid change in colour seen in the undyed cell suggests that the dye helps stabilise the cell against photodegradation, probably by blocking active sites on the TiO_2 and by charge injection into the TiO_2 conduction band to increase the rate of recombination of the photogenerated electron-hole pair. Furthermore the evidence in this

chapter points to the fact that in accelerated UV exposure it appears that the electrolyte and not the dye is the most important factor in the initiation, propagation and termination of photodegradation in DSC test cell.

4.5 References

1. M. Toivola, J. Halme, L. Peltokorpi and P. Lund, Investigation of Temperature and Aging Effects in Nanostructured Dye Solar Cells Studied by Electrochemical Impedance Spectroscopy, *International Journal of Photoenergy* 2009
2. J. Bisquert and F. Fabregat-Santiago (2010). Impedance Spectroscopy: A General Introduction and Application to Dye-Sensitized Solar Cells, in Dye-Sensitized Solar Cells, K. Kalyanasundaram. Lausanne, EPFL Press.
3. X. Hong, Z. Wang, W. Cai, Feng Lu, J. Zhang, Y. Yang, N. Ma and Y. Liu, Visible-Light-Activated Nanoparticle Photocatalyst of Iodine-Doped Titanium Dioxide, *Chemistry of Materials* 2005 **17**(6) 1548-1552
4. C. R. Chinake and R. H. Simoyi, Kinetics and Mechanism of the Complex Bromate–Iodine Reaction¹, *The Journal of Physical Chemistry* 1996 **100**(5) 1643-1656

Chapter

5.

Visible Light Soaking vs. UV Irradiation

5. VISIBLE LIGHT SOAKING VS. UV IRRADIATION

Accelerated DSC stability testing is often carried out in a visible light soaking cabinet such as that described in *chapter 2.6.3*. In long term visible light-soaking tests, DSCs have shown remarkable stability [1]. However in some long term *outdoor* testing, DSCs have shown similar changes to those described in *chapters 3 and 4*, such as a change in electrolyte composition and an initial decrease in V_{OC} and increase in J_{SC} [2]. Figure 5.1 shows the emission spectra of the light soaker used in this chapter and the UVA lamps used in this and the previous two chapters. ASTM G173-03 – “Global Tilt” Solar Irradiance Spectrum [3], or AM 1.5 as it is more commonly known, is shown for comparison. The emission spectrum of the light soaker lamp is shown at 0.25 Sun as this was the level of intensity of the lamp during testing. The light soaker has a maximum power output of 0.9 Sun but this is only achievable when the lamp is virtually touching the test cells in the cabinet. The temperature of the cells exposed in this way is too high to rule out temperature effects on cell stability so it was decided to conduct the light soaking experiments at 0.25 Sun which gave a cell temperature of 40-50°C.

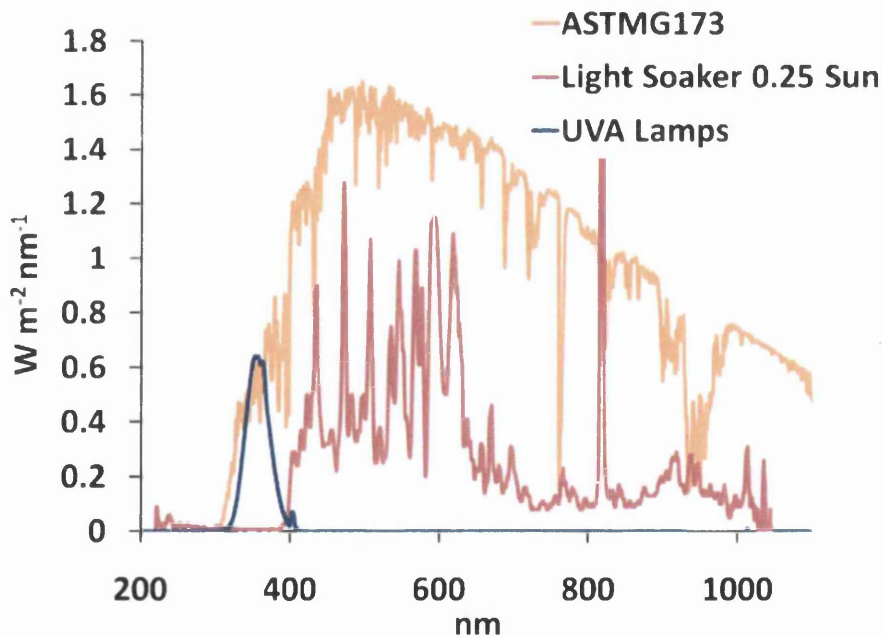


Figure 5.1 Emission spectra of light sources used in chapters 3, 4 and 5, compared to the emission spectrum given by AM 1.5

Two things are clear from Figure 5.1. The first is that there is a lack of intensity of UV light emitted by the lamp in the light soaking cabinet compared to that of the emission spectrum given by AM 1.5. The average intensity emitted by the light soaker between 300 nm and 400 nm is around 0.016 W m^{-2} with a maximum UV emission of 0.17 W m^{-2} at 399 nm. In contrast the maximum emission of the UVA lamps was measured at 0.64 W m^{-2} at around 354 nm with average emission intensity between 300 nm and 400 nm of around 0.25 W m^{-2} . The average intensity of AM 1.5 between 300 nm and 400 nm is 0.46 W m^{-2} with 0.61 W m^{-2} power density at 354 nm. The power of the UVA lamps is therefore reasonably consistent with respect to the emission spectrum of the sun between 300 nm and 400 nm.

The emission spectrum of the light soaking cabinet is not a good spectral match to that of the sun. The manufacturer of this cabinet is not alone however as a major competitor produces a light soaking unit which whilst having a good spectral match to AM 1.5 above 400 nm, misses out most of the solar spectrum from 300 nm to 390 nm as well. This is perhaps because these light soaking cabinets were originally designed for inorganic photovoltaics.

5.1 IV Data

Similarly to the experiments conducted in chapters 3 and 4, the cell sets consists of cells exposed from the WE side "LS (forward)", cells exposed from the CE side "LS (reverse)", cells exposed from the WE side under load "LS (load)" and cells kept in the light soaker in a light-tight container "Dark 40°C". Figure 5.2 shows the trends in $\% \eta$, V_{OC} and J_{SC} over the exposure period.

Looking at figure 5.2 at the cell efficiency it is striking how quickly cells exposed to UV light fail compared to those exposed under visible light soaking conditions. The order of $\% \eta$ decline follows the familiar pattern of cells under load failing faster than cells under open circuit which in turn fail faster than reverse illuminated cells under open circuit. However, in contrast to the cell sets tested in *chapters 3 and 4*, the cells kept in the dark fail faster than those under illumination as if visible light somehow stabilises the cell.

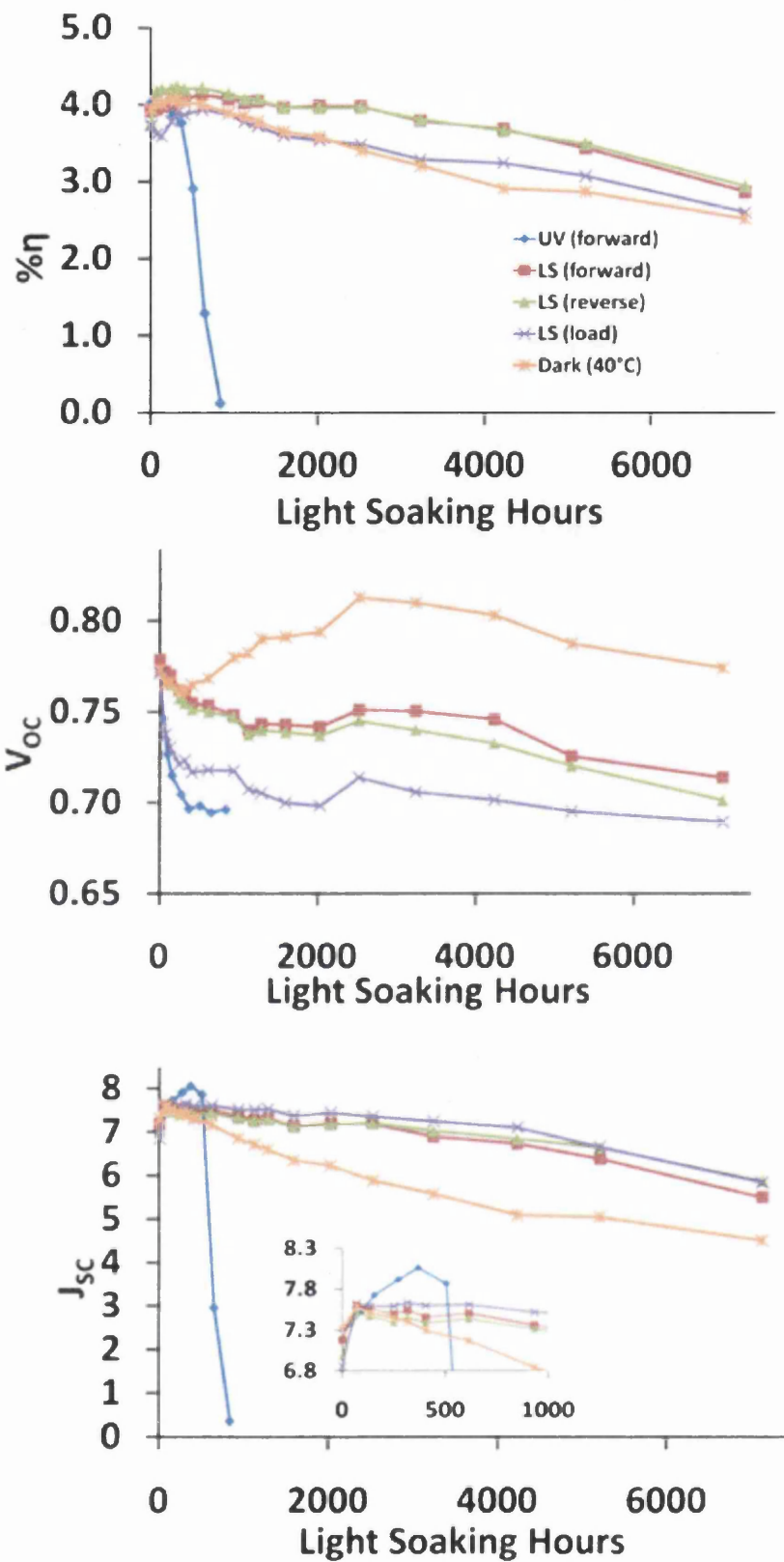


Figure 5.2 Trends in $\% \eta$, V_{oc} and J_{sc} over the exposure period of test cells made with N719 dye

Looking at the V_{OC} of the cells, the pattern is again very familiar. Cells exposed to UV light shows a rapid drop in V_{OC} whilst cells kept in the dark show an increase. Out of the cells exposed in the light soaker, only the cells under load show a drop in V_{OC} close to that of cells exposed to UV light. This could show how important a factor photogenerated TiO_2 holes are to the degradation of DSCs.

The photon flux, ϕ of each light source can be calculated at a particular wavelength with the following equation.

$$\phi = P_d q E \quad (5.1)$$

Where P_d is the power density at a particular wavelength, q is the elementary charge = 1.602×10^{-19} coulombs and E is the photon energy in electron volts. Photon energy can be calculated from the Planck-Einstein relationship, $E = hc/\lambda$ where E is the energy in electron volts (eV), h is the Planck constant and c the speed of light, so that $E = (1240 \text{ eV}\cdot\text{nm})/\lambda$.

At 380 nm the power density of the UV lamps is around 0.22 W m^{-2} and the light soaker lamps around 0.01 W m^{-2} . Using equation 5.1 and the Planck-Einstein equation this gives a photon flux of $4.2 \times 10^{17} \text{ m}^{-2} \text{ s}^{-1}$ for the UV lamps and $1.9 \times 10^{16} \text{ m}^{-2} \text{ s}^{-1}$ for the light soaker. In other words, the number of hole generating photons emitted at 380 nm by the UVA lamps is an order of magnitude greater from the UV lamps than it is from the light soaker. This is true for nearly all wavelengths below 390 nm. Despite this fact, the photon flux of the light soaker in the UV is still significant enough to cause some amount of photoexcitation of the TiO_2 . In light soaked cells under load, the electrons, as before, are exported to the external circuit leaving an excess of holes which could contribute to the protonation of the TiO_2 surface which is said to be the cause of the drop in V_{OC} . There is no real difference in the drop in V_{OC} between two sets of cells exposed under open circuit suggesting that electronic transport to the external circuit is an important factor in the downward shift of the conduction band. The V_{OC} of cells kept in the dark decreases initially which could be due to the temperature dependency of the back reaction rate constant, which has been shown to increase at elevated temperatures [4]. The V_{OC} then increases and has been observed before in cells subjected to elevated temperatures but kept in the dark [5]. An explanation has been offered that the increase in V_{OC} is caused by an increase of electrolyte species

adsorbed onto the TiO₂ surface. The V_{OC} then starts to decline at around 2300 hours, possibly due to thermal degradation of the electrolyte.

The larger initial increase in J_{SC} seen in UV exposed cells is less severe in cells exposed in the light soaker with the rate of increase slightly higher in light-soaked cells under load. The ensuing rate of decline in J_{SC} in the light soaked cells could possibly be due to depletion in I₃⁻ concentration and it is interesting to note that the normal pattern of decay is reversed in that the rate decay in J_{SC} of cells is faster under open circuit than it is under load. This might be due to a continuing shifting of the conduction band, as evidenced by the V_{OC} decreases, which is causing increasing electron injection efficiency. This is obviously not the dominant mechanism as all cell sets show declining J_{SC} but it could be the reason why the rate of J_{SC} decrease in cells under load is slower because the relative increase in electron injection efficiency is faster when compared to cells exposed under open circuit.

The cells kept in the dark show the greatest rate of J_{SC} decrease and it is possible that this is caused by a negative shift in the conduction band, this would explain why the V_{OC} increases and the decreasing J_{SC} may be due to narrowing of the energy gap between the LUMO of the dye and the TiO₂ conduction band causing decreasing electron injection efficiency [6].

5.2 EIS Data

Figure 5.3 below shows the back reaction resistance (R_{BR}) of the cell sets over the exposure period. Similarly to the drop in V_{OC}, the drop in R_{BR} for light soaked cells under load is of a similar magnitude to the UV exposed cells which reiterates how important electronic transport to the external circuit is to cell stability. Even the small amount of UV generated by the light soaker, and even with the charge injection that must be coming from the dye under visible light, external electronic transport in cells under load is enough to cause the drop in V_{OC} and R_{BR} on a similar scale to that seen in UV exposed cells. Under open circuit, it appears that the cells exposed from the CE side are degrading faster than those exposed from the WE side. This may be because charge injection from the dye excited at around 530 nm is stabilising the cells, slowing down the V_{OC}/R_{BR} drop in forward exposed cells. In

reverse exposed cells, less dye charge injection occurs due to the filtering properties of the electrolyte.

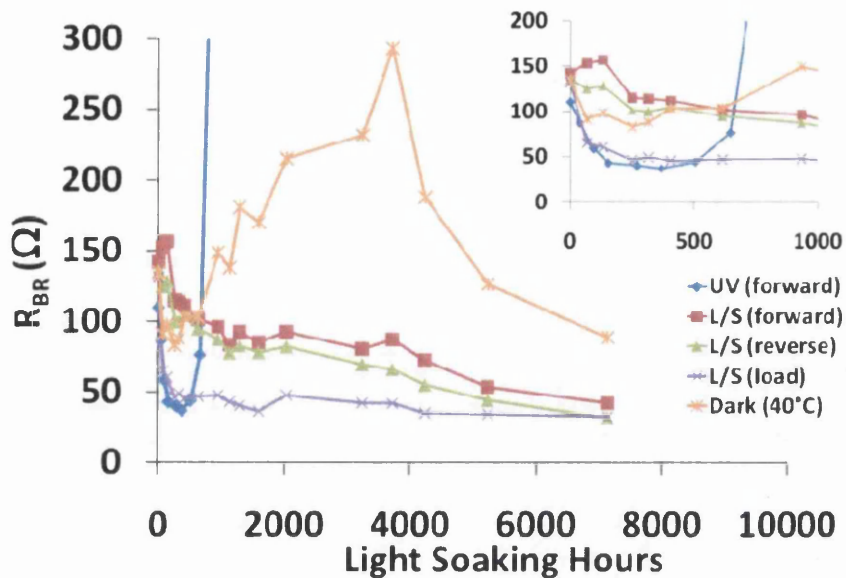


Figure 5.3 R_{BR} of cells over the exposure period

For unexposed cells, an initial decrease in R_{BR} , which may be caused by the temperature dependency of the back reaction rate constant is seen which is then followed by an increase in R_{BR} . This could again possibly be due to increased adsorption of species onto the TiO_2 film, blocking sites for the back reaction to occur (and increasing V_{OC}) after time thermal degradation may have degraded electrolyte components sufficiently for the R_{BR} and V_{OC} to begin decreasing.

5.3 Conclusion

This chapter shows how important UV light is to DSC stability. It shows that even small amounts, such as that emitted by the light soaker, are enough to cause the ageing characteristics, in cells under load, that have already been described in *chapters 3 and 4*. This chapter also shows how important electronic transport to the external circuit is to DSC stability in that electrons exported to the external circuit result in less recombination of TiO₂ electron-hole pairs, and increased rates of degradation, which occurs despite the stabilising effects of electronic injection from the dye which must be occurring under visible light soaking conditions. These conclusions lead to two recommendations.

The first is that future accelerated stability testing should always be done under load, or perhaps short circuit conditions so that electronic transport can occur to an external circuit. The first advantage of this is obvious as this would better simulate a DSC module under operating conditions. The second advantage is that the characteristic signs of cell degradation occur faster under load and so UV protection measures can be rapidly assessed.

When the manufacturer of the light soaker quotes an output of 0.9 Sun all that is meant is the power of the lamp is 900 W m⁻², as can be seen from figure 5.1, there is little spectral match to AM 1.5. The second recommendation therefore, is that accelerated ageing should be carried under a light source that is a spectral match to the solar emission spectrum with both the visible and UV components emitted at realistic power densities. The plastics and coatings industry use xenon-arc weatherometers for just this purpose.

Neither of the exposure methods presented in this work is perfect as although UV photodegradation has been shown to be the dominant degradation mechanism, the stabilising effect of charge injection from dye electrons excited at 530 nm is also an important factor.

1. Ravi Harikisun and Hans Desilvestro, Long-term stability of dye solar cells, *Solar Energy* 2011 **85**(6) 1179-1188
2. N. Kato, Y. Takeda, K. Higuchi, A. Take Cichi, E. Sudo, H Tanaka, T. Motohiro, T. Sano and T. Toyoda, Degradation analysis of dye-sensitized solar cell module after long-term stability test under outdoor working condition, *Solar Energy Materials and Solar Cells* 2009 **93**(6-7) 893-897
3. ASTM International ASTM G173-03 Standard Tables for Reference Solar Spectral Irradiances: Direct Normal and Hemispherical on 37° Tilted Surface.
4. Minna Toivola, Lauri Peltokorpi, Janne Halme and Peter Lund, Regenerative effects by temperature variations in dye-sensitized solar cells, *Solar Energy Materials and Solar Cells* 2007 **91**(18) 1733-1742
5. M. Toivola, J. Halme, L. Peltokorpi and P. Lund, Investigation of Temperature and Aging Effects in Nanostructured Dye Solar Cells Studied by Electrochemical Impedance Spectroscopy, *International Journal of Photoenergy* **2009**
6. S. Ferrere and B.A. Gregg, Large increases in photocurrents and solar conversion efficiencies by UV illumination of dye sensitized solar cells, *Journal of Physical Chemistry B* 2001 **105**(32) 7602-7605

Chapter

6.

UV Filtering of Dye-Sensitized Solar Cells

6. UV FILTERING OF DYE-SENSITIZED SOLAR CELLS

6.1 UV Filtering as Protection against UV Photodegradation

The data in chapters 3,4 and 5 have shown that UV irradiation is highly detrimental to DSC stability over a period of up to 2000 hours and that in visible light soaking experiments, it is likely that the cause of cell degradation is the small amount of UV light emitted by the light soaking lamps. One of the most obvious methods of UV protection would be to use UV filters. Three filters were obtained from Schott AG (UK), their UV-Vis %T curves can be seen in figure 6.1 below, their UV cut-offs are defined by Schott as 385 nm, 400 nm and 420 nm.

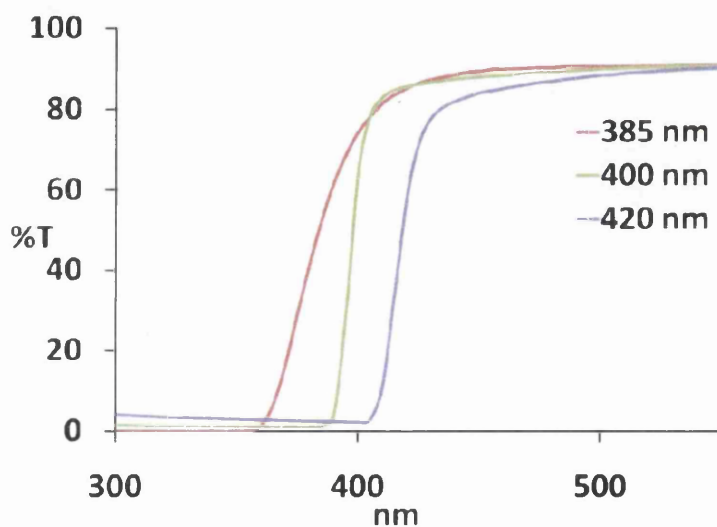


Figure 6.1 UV-Vis %T curves of the filters used in this chapter

Cells were irradiated under these filters as well as a control group with no filter. As in *chapter 3*, the most obvious feature to measure would be the change in η over time. Figure 6.2 shows the change in η over the exposure period and the first thing to notice is that all cells degrade at a similar rate but it may be that the cells filtered at 385 nm are degrading faster. The difference may not seem significant at first until the change in V_{oc} is observed. This is shown in figure 6.3.

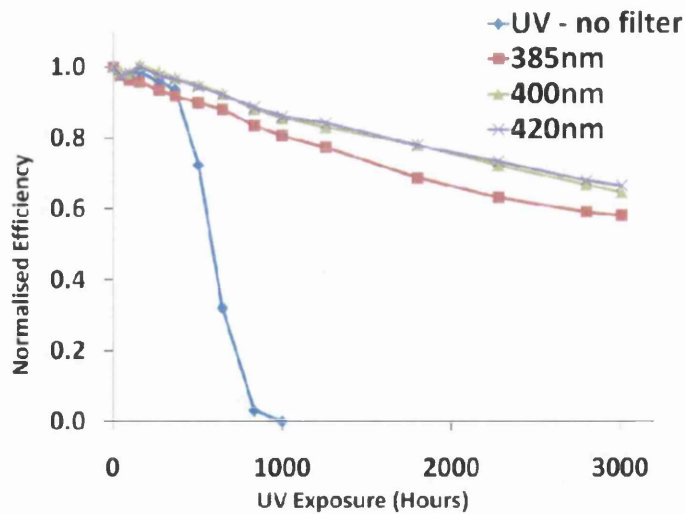


Figure 6.2 Change in η over the exposure period shown

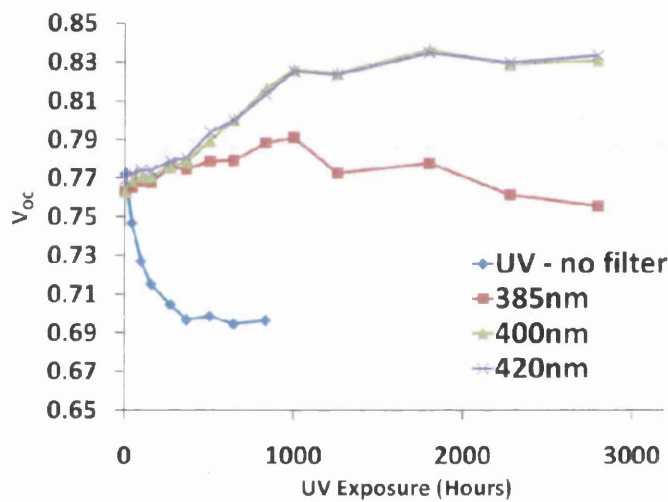


Figure 6.3 Change in V_{OC} over the exposure period shown. Measurement of cells exposed with no UV filter was stopped at around 800 hours due to cell failure

In figure 6.3 it can be seen that in all cases except the cells exposed without a filter the V_{OC} initially increases. This is very typical of cells kept in the dark and makes sense as cells filtered at 420 nm from a UV lamp with a maximum emission at around 360 nm are effectively in the dark. At 3000 hours exposure, the cells filtered at 400 nm and 420 nm are still behaving as though they have been kept in the dark (compare to shown data in figure 5.2), at least as far as the increase in V_{OC} is concerned, but at 1000 hours exposure the cells

filtered at 385 nm begin to see a decrease in V_{OC} , a clear sign of the onset of UV photodegradation. Figures 6.2 and 6.3 suggest two things. The first is that UV filtering can extend the life of a DSC by preventing UV photodegradation. The second is that filtering is required at a level above 385 nm but no more than 400 nm. There appears to be no evidence that increasing the level of filtering from 400 nm to 420 nm has any benefit in terms of DSC UV stability.

Figure 6.4 shows the change in R_{BR} over the exposure period. Cells filtered at 400 nm and 420 nm show an increase in R_{BR} which is typical of cells kept in the dark. Cells filtered at 385 nm show neither the initial decrease in R_{BR} which is typical of cells exposed to UV light nor the increase which is typical of cells kept in the dark suggesting that the cell is absorbing some UV light but not enough to cause the changes which are typical of UV exposed cells. All three sets of filtered cells start see a reduction in R_{BR} at around 2800 hours this is unlikely to be caused by photodegradation, at least in the case of those cells filtered at 400 nm and 420 nm, and may be caused by some other element such as heat or O_2/H_2O ingress.

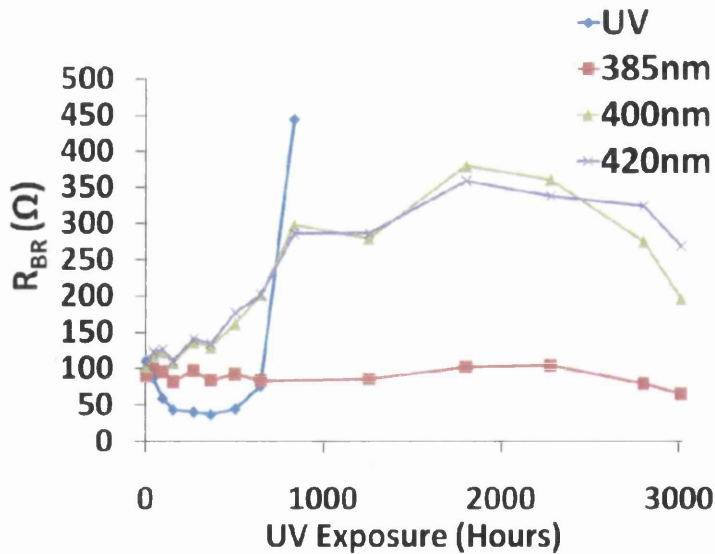


Figure 6.4 Change in R_{BR} of filtered cells over the exposure period shown

This chapter has so far shown how UV filtering can increase DSC stability. However, DSCs still convert photons at less than 400 nm into photocurrent and so cutting off light at 400 nm will result in less photons reaching the device, leading to lower photocurrents and lower % η . Work therefore was needed to quantify the effects of UV filtering upon DSC performance and % η . For this experiment, four *polymer* filters were chosen, with varying UV cut-off wavelengths that were being considered for use as CE materials for a flexible DSC based on a steel substrate. Furthermore as the filter was cutting off light in the UV part of the spectrum it was thought that the further into the red that the dye absorbed the less detrimental the UV cut off would be to cell efficiency, so four dyes were chosen which have differing photocurrent action spectra.

6.2.1 The Dyes

The dyes are all ruthenium based dyes and all were obtained from Dyesol. Figure 6.5 below shows the chemical structure of the dyes. The dyes used were:

1. **N3** which Dyesol say is the baseline dye for DSC, it has chemical formula:
 $\text{RuL}_2(\text{NCS})_2$ (L=2,2'-bipyridyl-4,4'-dicarboxylic acid)
2. **N719** is a modification of the N3 dye (it is in fact a tetrabutylammonium salt of the N3 dye) to increase cell voltage. It is the most common high performance dye. Chemical formula: $[\text{RuL}_2(\text{NCS})_2]:2\text{TBA}$ (L=2,2'-bipyridyl-4,4'-dicarboxylic acid; TBA=tetra-n-butylammonium)
3. **Z907** is a hydrophobic dye with chemical formula: $\text{RuLL}'(\text{NCS})_2$ (L=2,2'-bipyridyl-4,4'-dicarboxylic acid; L'=4,4'-dinonyl-2,2'-bipyridine)
4. **N749** also known as 'black dye', is designed for the widest range spectral sensitisation up to wavelengths beyond 800nm. It has chemical formula:
 $[\text{RuL}(\text{NCS})_3]:3\text{TBA}$ (L=2,2':6',2''-terpyridyl-4,4',4''-tricarboxylic acid; TBA=tetra-n-butylammonium)

5.

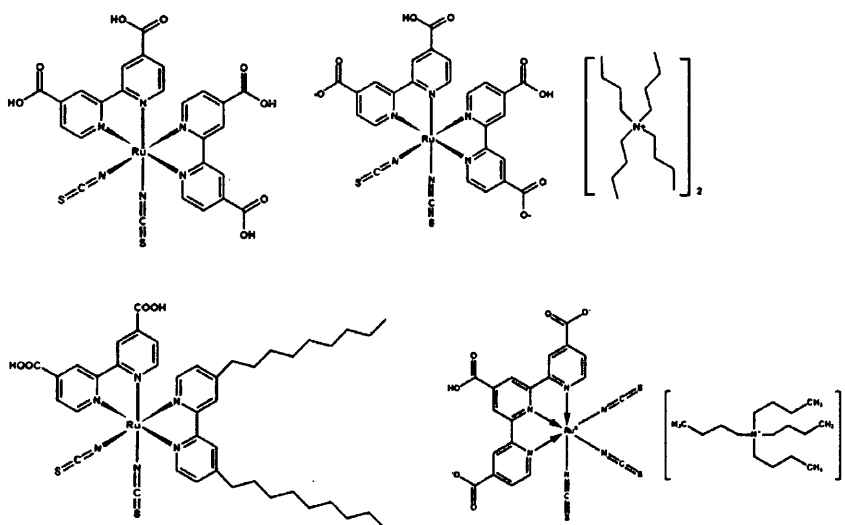


Figure 6.5 Structures of the dyes used in this chapter. Clockwise from top-left: N3, N719, N749 and Z907

Figure 6.6 below shows the IPCE plots of cells made with the four dyes. Five cells were made with each dye. In each case there were two outliers (in terms of efficiency) and so the IPCE plots here are the *median* IPCE of the three “good” cells of each dye. Cells made with N719 and N3 dye show the highest overall quantum efficiency (QE) with very similar IPCE spectra. The broadest spectrum dye was the N749 dye. Cells made with N749 show activity to just over 800 nm with a quantum efficiency that doesn’t reach above 20% at any wavelength. This may be because the electrolyte used is a specific electrolyte for N3 and N719 cells and might not give good performance with other dyes. It was necessary to keep the electrolyte the same in each case in order to rule out any effects due to the absorption characteristics of the electrolyte when looking at the cells in the reverse cell set up. The narrowest spectrum dye was the Z907. The IPCE of Z907 cells only just passed 30% at an absorption maximum of around 540 nm; again the low IPCE of Z907 cells compared to N3/N719 based cells might be because the electrolyte is not entirely suitable for use with Z907 dye.

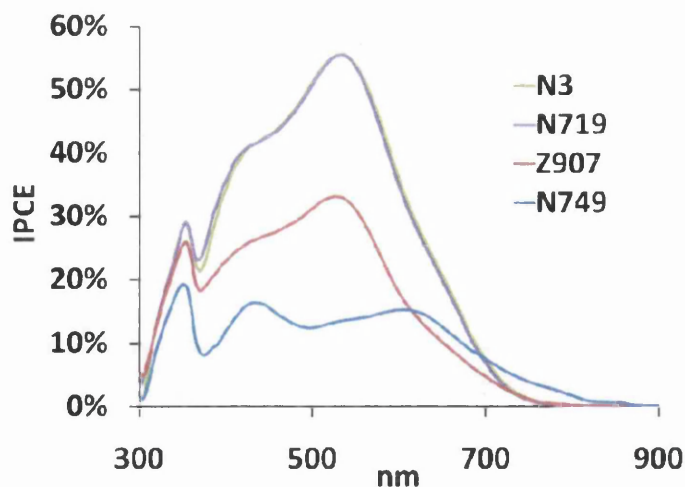


Figure 6.6 IPCE plots of the cells made with the four dyes used in this chapter. Despite having an overall lower IPCE, it can be seen that N749 dye extends its absorption further toward the NIR region than the other three dyes

Figure 6.7 shows the *median* IV curves of the cells and Table 6.1, the *mean* parameters of the cells. In contrast to their respective IPCE plots the N3 and N719 based cells have different IV curves. It might be expected looking at the IPCE plots that cells made with the N3 and N719 dyes will behave similarly. When looking at the IV curves and cell parameters however it is clear that cells made with N719 dye perform better. Both dyes have very similar current densities but N719 cells have an increased V_{OC} compared with N3 cells. This results in N719 dyed cells having a higher maximum power point, and since $\% \eta \propto P_{max}$, an increased efficiency compared to cells made with N3 dye.

Figure 6.7 also shows the IV curves of the cells made with the Z907 and the N749 dyes. As would be expected when looking at their respective IPCE plots, these cells do not perform as well as the N3 and N719 dyed cells. They have lower V_{OC} , J_{SC} , P_{max} and therefore lower $\% \eta$.

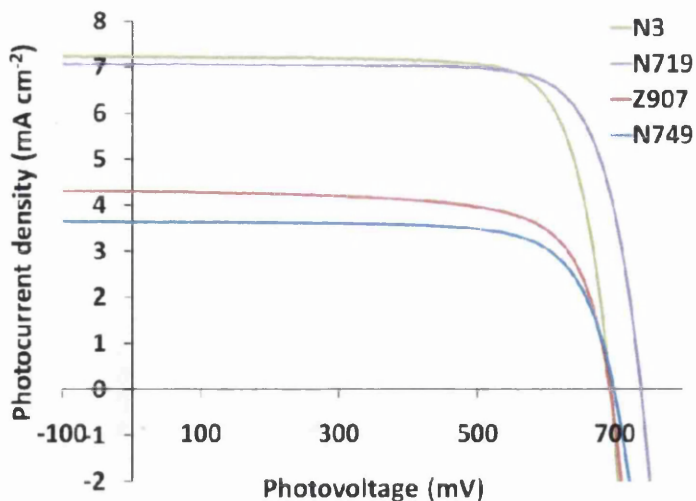


Figure 6.7 Median IV curves of cells made with the four dyes used in this chapter

Table 6.1 Mean properties of cells made with the four dyes used in this chapter

| | V_{oc} (V) | J_{sc} (mA cm^{-2}) | Fill Factor | $\% \eta$ |
|------|-----------------------|-------------------------------------|---------------------|--------------------|
| N3 | 0.702 (± 0.009) | 7.25 (± 0.02) | 0.76 (± 0.02) | 3.9 (± 0.08) |
| N719 | 0.731 (± 0.005) | 7.15 (± 0.09) | 0.77 (± 0.02) | 4.0 (± 0.02) |
| Z907 | 0.682 (± 0.007) | 4.21 (± 0.15) | 0.73 (± 0.02) | 2.1 (± 0.10) |
| N749 | 0.685 (± 0.016) | 3.83 (± 0.31) | 0.74 (± 0.01) | 1.9 (± 0.09) |

6.2.2 The Filters

Four filters were chosen, all based on PET films, to give a range of UV cut-offs. The filters were:

1. **Melinex ST505** is a PET film available from DuPont Teijin Films
2. **BASF HP** is Melinex ST505 coated with a UV absorbing lacquer obtained from BASF
3. **Kimoto B4** is an experimental film supplied by Kimoto, Japan (this film has transmission properties close to the “ideal” values – see chapter 8)

4. Spring Yellow

is a yellow PET filter obtained from Lee Filters. It was coated with BASF HP lacquer (20 μm) to reduce its original UV transmittance (around 40% at 340 nm)

A summary of their spectral properties can be seen in Table 6.2 below. The last column of the table is entitled "UV cut-off". This term will be used extensively in this chapter and it is important to clarify what this means. UV cut-off refers to the steepest part of the UV-Vis %T curve where %T \approx 50%. As the instrument was scanning with a resolution of 5 nm, these values have been rounded to the nearest 5 nm. The %T curves of the filters are shown in figure 6.8 below.

Table 6.2 Important spectral properties of the filters used in this chapter

| | <u>Mean %T</u> (500-800 nm) | <u>λ where</u> <u>%T < 50% (nm)</u> | <u>λ where</u> <u>%T < 1% (nm)</u> | <u>UV 'cut-off'</u> |
|---------------|--------------------------------|--|---|---------------------|
| Melinex | 88.2 | 320 | 306 | 320 |
| BASF HP | 90.2 | 384 | 317 | 385 |
| Kimoto | 87.4 | 422 | 404 | 420 |
| Spring Yellow | 87.2 | 484 | 466 | 485 |

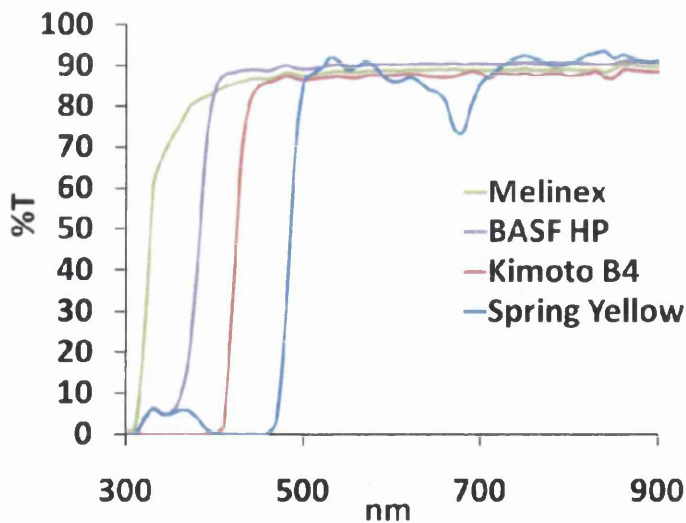


Figure 6.8 %T curves of the filters used in this chapter

Figure 6.9 shows the IPCEs of cells made with the four dyes. The solid black line represents the IPCE of the unfiltered cell with the dashed black lines showing the effect of filtering upon the IPCE. These are overlain with the %T spectra of the polymer filters (coloured lines). Figure 6.10 shows the IV curves of the cells both unfiltered and with the filters used in this chapter.

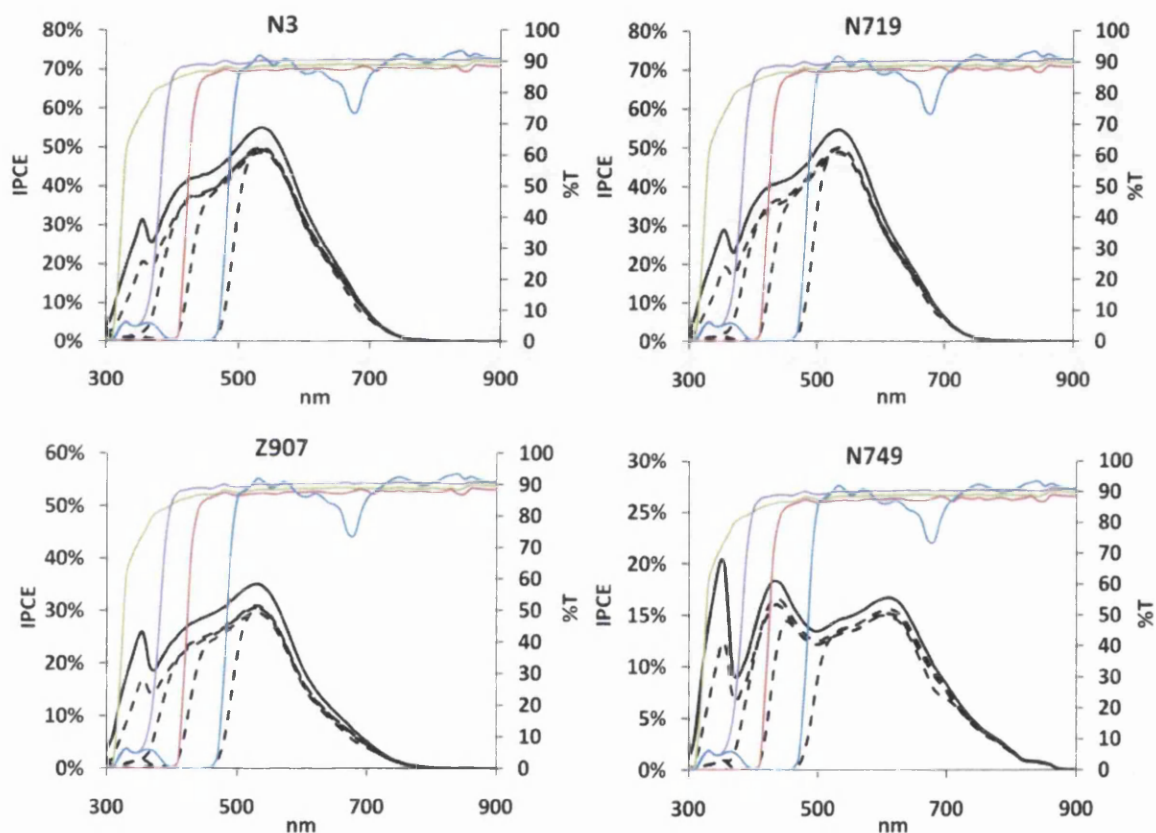


Figure 6.9 The effect of filtering upon the IPCEs (dotted black lines) of the cells made with the four dyes (N3, N719, Z907 and N749), overlain with the %T of the filters (solid coloured lines – see figure 6.8 for legend). The solid black line represents the IPCE of the cell with no filtering – N.B. the scale of the IPCE axis is different in each case

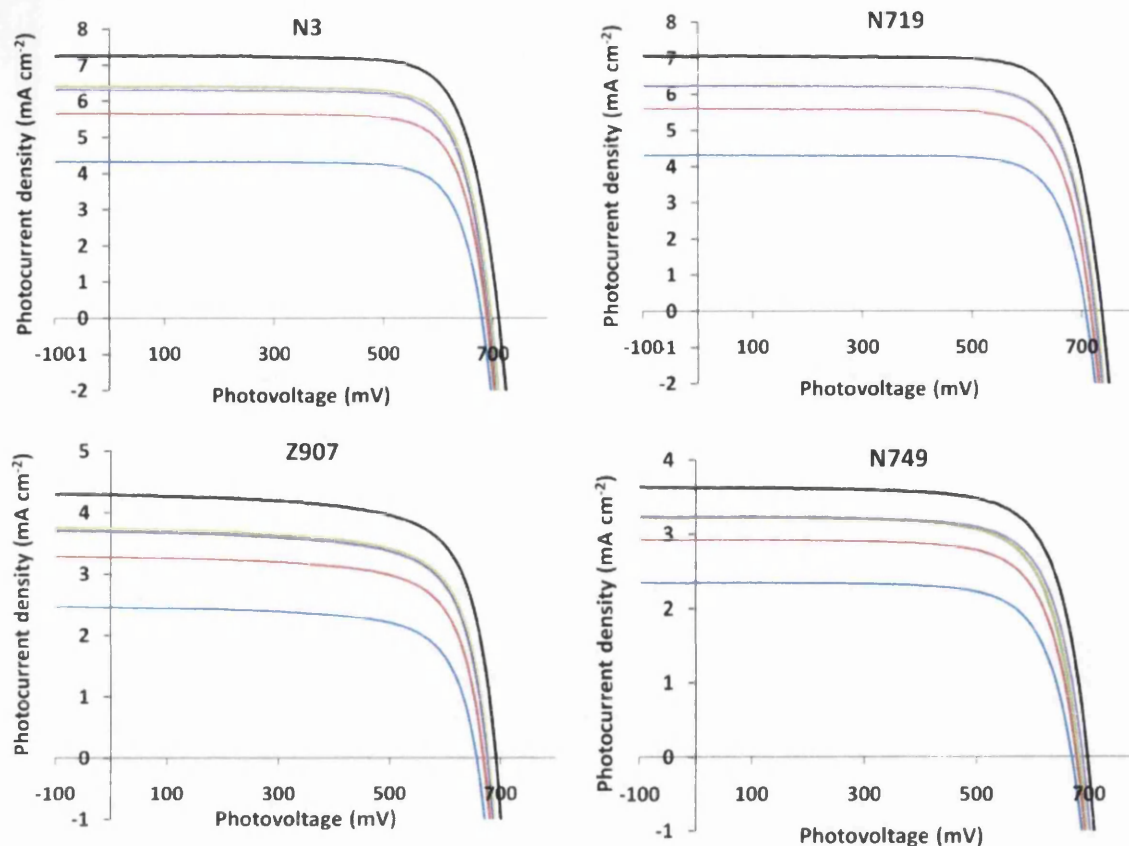


Figure 6.10 IV curves of cells made with the four dyes, both unfiltered (black line) and filtered (coloured lines – see figure 6.7 for legend)

6.3.1 Filtering of Cells Made with N719 Dye

Looking at the IPCE data in figure 6.9, it is immediately obvious how filtering affects the IPCEs of the cells in that the IPCE is cut-off at the same wavelength as the cut-off of the filter. In all cases where a filter is used, the maximum IPCE value is the same whilst the magnitude of the maximum IPCE is slightly higher in the unfiltered cells. The reason for this is clear when looking at the %T curves in that all of them have a %T of around 90% at 540 nm and so ignoring the effects of the UV cut-off, usage of a filter will immediately reduce the number of photons reaching the photoelectrode, reducing photocurrents (figure 6.10) and therefore reducing efficiencies.

Table 6.3 shows the important cell parameters for N719 dyed cells gained from the IV measurements.

Table 6.3 Mean cell parameters of N719 cells, filtered and unfiltered

| | $\frac{V_{OC}}{(V)}$ | $\frac{J_{SC}}{(mA\ cm^{-2})}$ | $\frac{Fill\ Factor}{\% \eta}$ | $\frac{\% Loss\ cf.}{unfiltered}$ | $\frac{\% Loss\ cf.}{Melinex}$ |
|------------------------------|--------------------------|--------------------------------|--------------------------------|-----------------------------------|--------------------------------|
| N719-Unfiltered | 0.731 (± 0.006) | 7.15 (± 0.09) | 0.77 (± 0.007) | 4.01 (± 0.02) | N/A |
| N719-Melinex Filtered | 0.718 (± 0.006) | 6.33 (± 0.09) | 0.77 (± 0.004) | 3.5 (± 0.01) | 12.7 |
| N719-BASF HP Filtered | 0.720 (± 0.004) | 6.27 (± 0.05) | 0.77 (± 0.009) | 3.47 (± 0.01) | 13.5 |
| N719-Kimoto Filtered | 0.709 (± 0.007) | 5.66 (± 0.08) | 0.77 (± 0.004) | 3.09 (± 0.01) | 22.9 |
| N719-Yellow Filtered | 0.698 (± 0.008) | 4.35 (± 0.06) | 0.77 (± 0.003) | 2.34 (± 0.005) | 33.1 |

Figures 6.9, 6.10 and Table 6.3 all show clearly how filtering affects cell performance. The IPCE curves in figure 6.9 show how the filters block out photons at their respective UV cut off wavelengths resulting in virtually zero IPCE at wavelengths beyond the cut-off. Looking at the IV curves and cell parameters in Figure 6.10 and Table 6.3, it is clear that there is a significant decrease in J_{SC} of the cell as the UV cut off of the filters shifts towards the blue end of the spectrum. The open circuit voltage V_{OC} decreases also, but on a smaller scale compared to the J_{SC} . It seems obvious why there is a decrease in J_{SC} as the photocurrent is dependent on the incident photon flux and wavelength. The photon flux and wavelength are clearly altered by the filters as can be seen in the %T spectra of the filters and the IPCEs of the filtered cells. It seemed puzzling at first why the V_{OC} would decrease with increased filtering but the energy of the Fermi level and therefore the V_{OC} are dependent on incident light intensity. It has been shown [1] that the photovoltage, qU_{photo} , of an ideal DSC is proportional to the log of the incident photon flux (I_0), which is shown in equation (6.1) below where k_B is the Boltzmann constant, T is the temperature, η_{lh} and η_{inj} are respectively the light harvesting and the electron injection efficiencies and τ_0 is the conduction band electron lifetime determined from the back reaction kinetics.

$$qU_{photo} = k_B T \ln \left[\frac{\eta_{lh} \eta_{inj}}{n_{c,eq} d} \right] + k_B T \ln \tau_0 + k_B T \ln I_0 \quad (6.1)$$

The relationship is confirmed in figure 6.11 where the V_{OC} of all the cells used in this chapter are plotted against the log of incident light intensity, which was measured in $W m^{-2}$ and obtained by placing the filter over a silicon reference cell when the lamp was set at 1.000 Sun ($1000 W m^{-2}$).

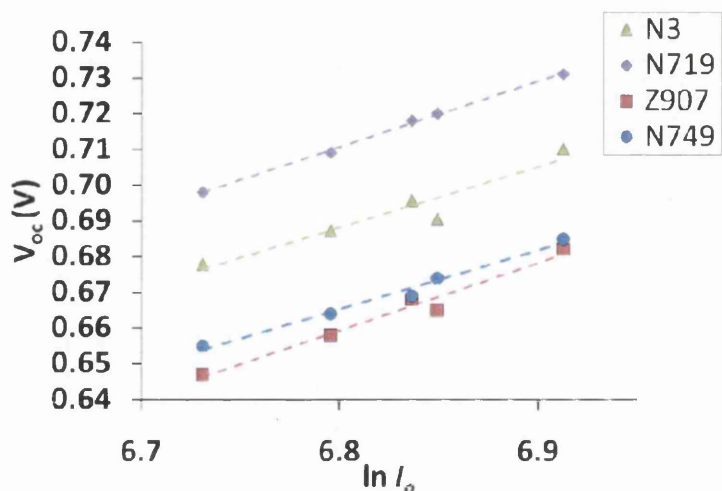


Figure 6.11 Mean V_{OC} vs. $\ln I_0$ for all cells used in this chapter

The $\% \eta$ losses due to filtering can be seen in the last two columns of Table 6.3. The efficiency loss due to using a Melinex PET filter could be taken as a base level and ignored as in a flexible DSC, the filtering effects of PET would be intrinsic to the device module if it is used as the top electrode in reverse illuminated devices. In that case, $\% \eta$ losses due to filtering at 385 nm (PET coated with BASF HP lacquer) only represent a 0.9% relative loss in efficiency. It has already been shown in *chapter 6* that filtering at 385 nm can significantly increase the lifetime of cells subjected to UV irradiation. It was also shown in section 6.1 that filtering at 400 nm would probably be required and that there seems to be no advantage of filtering with a cut-off above 400 nm. Unfortunately there were no polymer filters available with a 400 nm cut-off at the time of testing but despite that, as a cut-off of 420 nm gave a relative $\%$ loss of 11.7% *cf.* Melinex, it can be safely estimated that filtering at 400 nm would give relative losses in $\% \eta$ of less than 10%, meaning that in practice a cell of say $\% \eta = 8.0$ with a flexible PET electrode, should be expected to have $\% \eta$ of no less than 7.2 % if the PET encompassed a filter with a UV cut-off of 400 nm.

6.3.2 Filtering of Cells Made with N3 Dye

The results of N3 cell performance are very similar to the cells made with N719 dye. This is to be expected as these two dyes are very similar. One important parameter is that in all cases the V_{OC} of cells made with N719 are higher than those made with N3. This is due to the tetrabutylammonium salt, and has been attributed to the influence of dye protonation upon the energetics of the TiO_2 conduction band. The less protonated N719 dye (compared to N3) results in a more negative conduction band edge, and therefore a higher open circuit voltage [2]. Table 6.4 shows the important cell parameters for N3 dyed cells gained from the IV measurements.

Table 6.4 Mean cell parameters of N3 cells, filtered and unfiltered

| | V_{OC} (V) | J_{SC} ($mA\ cm^{-2}$) | Fill Factor | $\% \eta$ | <u>% Loss cf.</u> <u>unfiltered</u> | <u>% Loss cf.</u> <u>Melindex</u> |
|-----------------------------|--------------------------|-------------------------------|-------------------------|------------------------|--|--------------------------------------|
| N3 -Unfiltered | 0.702 (± 0.009) | 7.25 (± 0.02) | 0.77 (± 0.018) | 3.86 (± 0.02) | N/A | N/A |
| N3-Melindex Filtered | 0.688 (± 0.009) | 6.42 (± 0.02) | 0.77 (± 0.012) | 3.38 (± 0.02) | 12.4 | N/A |
| N3-BASF HP Filtered | 0.683 (± 0.009) | 6.38 (± 0.07) | 0.77 (± 0.012) | 3.35 (± 0.02) | 13.2 | 0.9 |
| N3-Kimoto Filtered | 0.679 (± 0.010) | 5.73 (± 0.07) | 0.77 (± 0.010) | 3.00 (± 0.02) | 22.3 | 11.2 |
| N3-Yellow Filtered | 0.668 (± 0.011) | 4.39 (± 0.06) | 0.77 (± 0.007) | 2.27 (± 0.02) | 41.2 | 32.8 |

6.3.3 Filtering of Cells Made with Z907 Dye

The progressive red shift of the UV-cut-off of the filters has similar effects to those that are observed in the N3 and N719 dyes. The main difference between cells made with the Z907 and those made with N3/N719 dyes is that the Z907 cells are affected slightly more by filtering, especially when compared to the unfiltered cells and at higher UV cut-offs. This could be explained when looking at Figure 6.6 as the IPCE of the Z907 has a much narrower action spectrum when compared to the other dyes. UV filtering causes a greater proportion

of useful photons to be blocked from the cell when compared to cells made with dyes with broader IPCE spectra.

Table 6.5 Mean cell parameters of Z907 cells, filtered and unfiltered

| | V_{oc} (V) | J_{sc} (mA cm ⁻²) | Fill Factor | % η | % Loss cf. unfiltered | % Loss cf. Melinex |
|------------------------------|--------------------------|------------------------------------|-------------------------|------------------------|--------------------------|-----------------------|
| Z907-Unfiltered | 0.682 (± 0.007) | 4.21 (± 0.15) | 0.73 (± 0.018) | 2.09 (± 0.09) | N/A | N/A |
| Z907-Melinex Filtered | 0.668 (± 0.006) | 3.68 (± 0.13) | 0.72 (± 0.018) | 1.78 (± 0.09) | 14.8 | N/A |
| Z907-BASF HP Filtered | 0.665 (± 0.007) | 3.62 (± 0.14) | 0.72 (± 0.019) | 1.74 (± 0.09) | 16.7 | 2.2 |
| Z907-Kimoto Filtered | 0.658 (± 0.008) | 3.21 (± 0.13) | 0.72 (± 0.018) | 1.53 (± 0.09) | 26.8 | 14.0 |
| Z907-Yellow Filtered | 0.647 (± 0.007) | 2.41 (± 0.10) | 0.72 (± 0.019) | 1.12 (± 0.09) | 46.4 | 37.1 |

6.3.4 Filtering of Cells Made with N749 Dye

The results (table 6.6) show similar patterns to the three previously used dyes. There are two exceptions however. The first is that the efficiency losses due to filtering are less severe in the N749 cell than in cells made with the other dyes. This is almost certainly because of the broader absorption spectrum of the dye. The second is that cells filtered with the BASF lacquered PET have a higher efficiency than those filtered with ordinary PET, despite the higher UV cut-off of the BASF lacquered sample. This may also be a factor of the broader absorption spectrum of N749 but combined with the anti-reflection properties of the lacquer. Figure 6.8 and table 6.2 show that Melinex coated with BASF HP lacquer has a higher %T than the Melinex itself. This must be due to some anti-reflection properties caused by differences in the refractive indices of the PET and of the polyurethane in the BASF HP lacquer. This leads to the question: Why does this increase in % η only manifest itself in cells made with N749 dye and not with the cells made with the other dyes?

The answer could be that as the UV cut-off of the filter becomes less important with the broadening spectrum of the dye then other factors, such as a small increase in transmitted light through the filter may have an effect. A slight increase in light transmission would

obviously cause a slight increase in cell efficiency. This is not observed in cells made with other dyes as the decrease in efficiency due to the UV cut-off far outweighs any antireflection benefits caused by the lacquer.

Table 6.6 Mean cell parameters of N749 cells, filtered and unfiltered

| | V_{oc} (V) | J_{sc} (mA cm ⁻²) | P_{max} (mW) | Fill Factor | % η | % Loss cf. unfiltered | % Loss cf. Melinex |
|------------------------------|--------------------|------------------------------------|-------------------|-------------------|------------------|--------------------------|-----------------------|
| N749-Unfiltered | 0.685 (± 0.016) | 3.83 (± 0.31) | 1.74 (± 0.09) | 0.74 (± 0.006) | 1.93 (± 0.10) | N/A | N/A |
| N749-Melinex Filtered | 0.669 (± 0.016) | 3.41 (± 0.29) | 1.51 (± 0.09) | 0.74 (± 0.005) | 1.68 (± 0.10) | 13.0 | N/A |
| N749-BASF HP Filtered | 0.674 (± 0.016) | 3.45 (± 0.33) | 1.54 (± 0.11) | 0.74 (± 0.04) | 1.71 (± 0.13) | 11.4 | -1.8 |
| N749-Kimoto Filtered | 0.664 (± 0.016) | 3.13 (± 0.30) | 1.38 (± 0.01) | 0.74 (± 0.005) | 1.53 (± 0.11) | 20.7 | 8.9 |
| N749-Yellow Filtered | 0.655 (± 0.016) | 2.51 (± 0.24) | 1.09 (± 0.08) | 0.74 (± 0.004) | 1.21 (± 0.09) | 37.3 | 28.0 |

6.3.5 Forward Illumination Summary

Figure 6.12 shows a summary of the results shown so far in *chapter 6.3* with regards to the efficiency losses (and increases) caused by the differing levels of filtering . For a discussion of the results see the conclusions discussed *in section 6.5*.

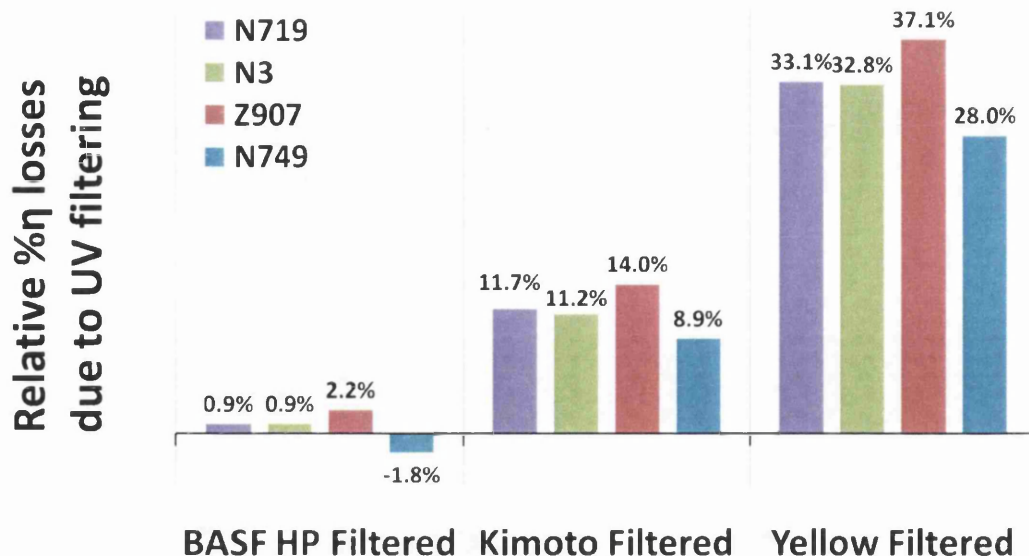


Figure 6.12

Relative % η losses in forward illuminated, filtered cells compared to % η of Melinex(PET) filtered cells

6.4 The Effect of Filtering on Cell Performance – Reverse Illumination

Figure 6.13 shows the IPCE data of cells made with the four dyes, measured with reverse illumination. Figure 6.14 shows the IV curves of the cells, illuminated in reverse, both unfiltered and with the filters used in this chapter. Table 6.7 shows the mean cell parameters of the cells made with the four different dyes.

Looking generally at all the data presented in figures 6.13, 6.14 and table 6.7, it can be seen that in all cases the effect of reverse illumination is similar to that seen when a filter is used in forward illumination. The shape of the IPCE is modified by the spectral properties of the electrolyte, the V_{OC} is only slightly affected but the J_{SC} is considerably reduced thereby reducing overall % η . The electrolyte could in fact be regarded as a filter analogous to the polymer filters in the way its spectral characteristics alter cell parameters. The filtering effect of the electrolyte can be seen in figure 6.15 below where the IPCE of a cell made with N719 dye is shown overlain with the transmission spectrum of the CE-CE cell

described in chapter 4. The dotted black line shows the IPCE of the same cell, illuminated in reverse.

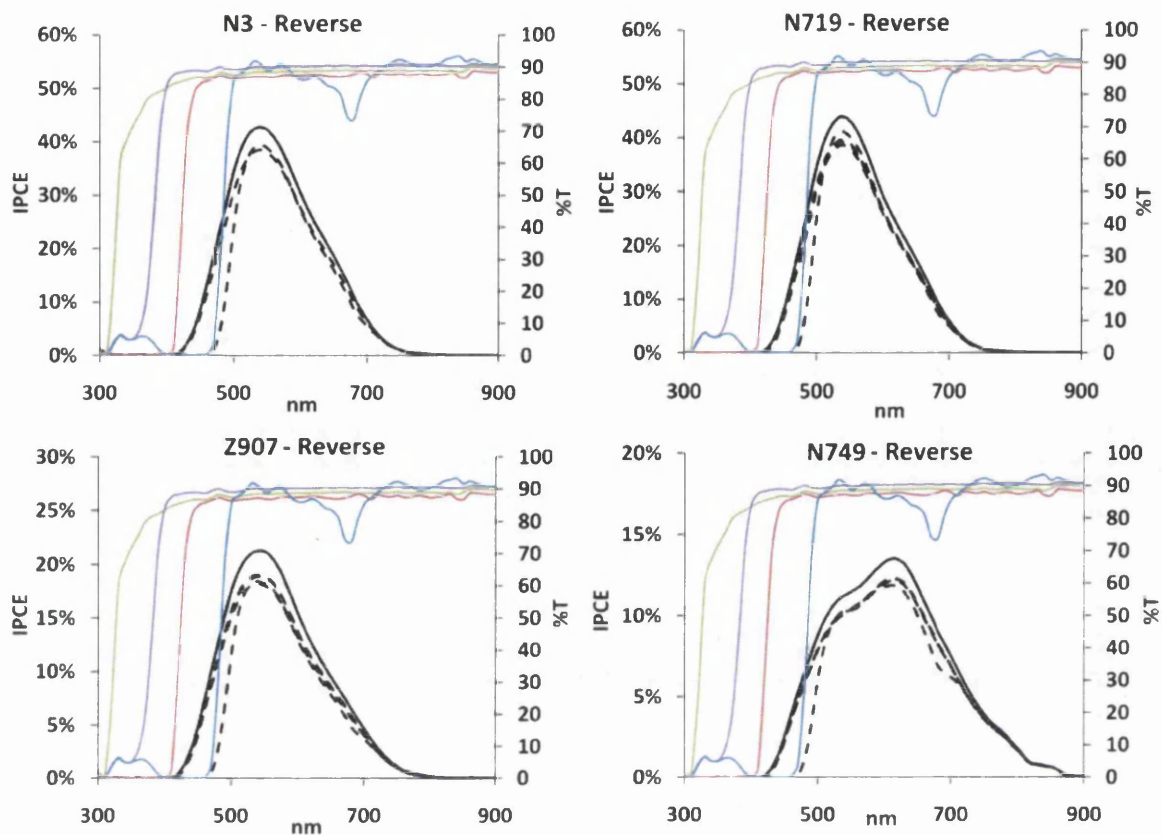


Figure 6.13 The effect of filtering upon the IPCEs (dotted black lines) of reverse illuminated cells made with the four dyes (N3, N719, Z907 and N749), overlain with the %T of the filters (solid coloured lines – see figure 6.8 for legend). The solid black line represents the IPCE of the cell with no filtering – N.B. the scale of the IPCE axis is different in each case

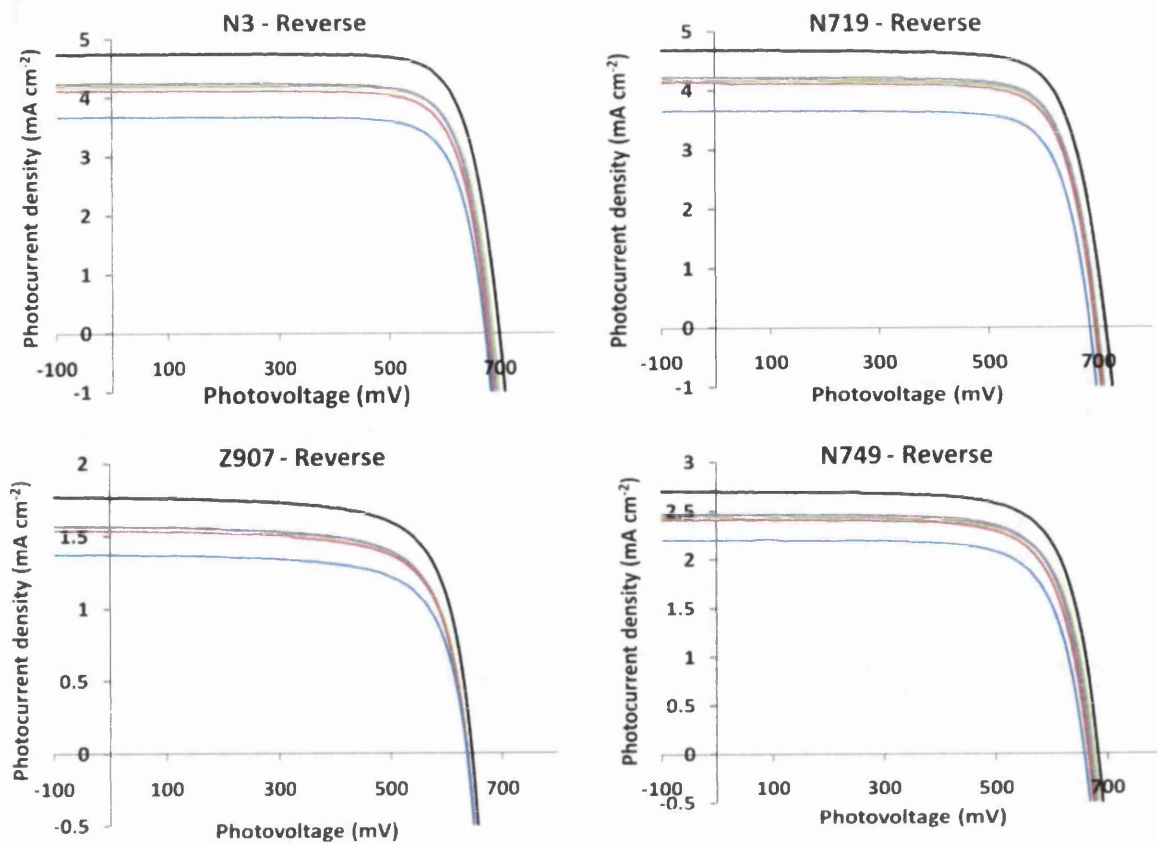


Figure 6.14 IV curves of cells made with the four dyes, both unfiltered (black line) and filtered (coloured lines – see figure 6.7 for legend) and measured in reverse illumination

Table 6.7 Mean cell parameters of reverse illuminated cells, filtered and unfiltered

| | V_{oc} (V) | J_{sc} (mA cm ⁻²) | Fill Factor | % η | % Loss cf. unfiltered | % Loss cf. Melinex |
|------------------------------|--------------------|------------------------------------|-------------------|------------------|--------------------------|-----------------------|
| N719-Unfiltered | 0.721 (± 0.008) | 4.62 (± 0.13) | 0.77 (± 0.007) | 2.56 (± 0.08) | N/A | N/A |
| N719-Melinex Filtered | 0.707 (± 0.010) | 4.12 (± 0.10) | 0.77 (± 0.005) | 2.25 (± 0.07) | 12.1 | N/A |
| N719-BASF HP Filtered | 0.706 (± 0.011) | 4.17 (± 0.11) | 0.78 (± 0.005) | 2.28 (± 0.07) | 10.9 | -1.3 |
| N719-Kimoto Filtered | 0.702 (± 0.010) | 4.07 (± 0.10) | 0.77 (± 0.006) | 2.2 (± 0.07) | 14.1 | 2.2 |
| N719-Yellow Filtered | 0.695 (± 0.013) | 3.58 (± 0.11) | 0.78 (± 0.004) | 1.93 (± 0.06) | 24.6 | 14.2 |
| N3-Unfiltered | 0.688 (± 0.011) | 4.66 (± 0.20) | 0.78 (± 0.010) | 2.49 (± 0.12) | N/A | N/A |
| N3-Melinex Filtered | 0.675 (± 0.012) | 4.15 (± 0.17) | 0.78 (± 0.007) | 2.19 (± 0.11) | 12.0 | N/A |
| N3-BASF HP Filtered | 0.672 (± 0.011) | 4.2 (± 0.17) | 0.78 (± 0.006) | 2.20 (± 0.11) | 11.6 | -0.5 |
| N3-Kimoto Filtered | 0.67 (± 0.007) | 4.08 (± 0.17) | 0.78 (± 0.007) | 2.13 (± 0.09) | 14.5 | 2.7 |
| N3-Yellow Filtered | 0.664 (± 0.009) | 3.61 (± 0.15) | 0.78 (± 0.004) | 1.87 (± 0.09) | 24.9 | 14.6 |
| Z907-Unfiltered | 0.66 (± 0.004) | 2.04 (± 0.20) | 0.73 (± 0.034) | 0.98 (± 0.14) | N/A | N/A |
| Z907-Melinex Filtered | 0.649 (± 0.005) | 1.79 (± 0.18) | 0.72 (± 0.034) | 0.83 (± 0.11) | 15.3 | N/A |
| Z907-BASF HP Filtered | 0.647 (± 0.004) | 1.79 (± 0.17) | 0.71 (± 0.034) | 0.83 (± 0.10) | 15.3 | 0.0 |
| Z907-Kimoto Filtered | 0.644 (± 0.002) | 1.74 (± 0.15) | 0.71 (± 0.036) | 0.8 (± 0.09) | 18.4 | 3.6 |
| Z907-Yellow Filtered | 0.641 (± 0.005) | 1.55 (± 0.13) | 0.71 (± 0.035) | 0.71 (± 0.08) | 27.6 | 14.5 |
| N749-Unfiltered | 0.674 (± 0.015) | 2.83 (± 0.45) | 0.74 (± 0.006) | 1.41 (± 0.20) | N/A | N/A |
| N749-Melinex Filtered | 0.657 (± 0.015) | 2.54 (± 0.39) | 0.72 (± 0.048) | 1.24 (± 0.17) | 12.1 | N/A |
| N749-BASF HP Filtered | 0.658 (± 0.017) | 2.58 (± 0.41) | 0.74 (± 0.004) | 1.25 (± 0.17) | 11.3 | -0.8 |
| N749-Kimoto Filtered | 0.654 (± 0.016) | 2.52 (± 0.41) | 0.74 (± 0.003) | 1.21 (± 0.17) | 14.2 | 2.4 |
| N749-Yellow Filtered | 0.647 (± 0.015) | 2.28 (± 0.36) | 0.74 (± 0.005) | 1.09 (± 0.15) | 22.7 | 12.1 |

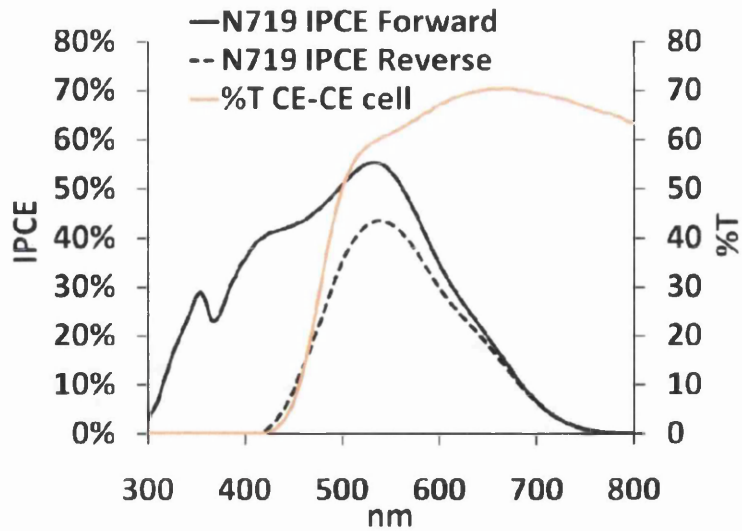


Figure 6.15 IPCE of a N719 cells in both forward and reverse illumination, overlain with the %T spectrum of a CE-CE cell

Looking at the IPCE spectra (figure 6.13) of the reverse illuminated cells it appears that the IPCEs fit within the %T curves of the first three filters (Melinex, BASF HP and Kimoto). It would therefore be expected that these filters would all cause a similar drop in efficiency due to the 10% drop in light transmission from 450 – 900nm but no further losses due to the red shifting of their UV cut-offs. Indeed looking at the IV curves of the cells filtered with these three filters it can be seen that the photocurrent is only slightly reduced in each case. This is contrasted by cells illuminated in the forward direction (figure 6.10) where there is a significant difference in photocurrent between the BASF HP filtered cells and the Kimoto filtered cells. In the reverse illuminated cells however there is still a drop in V_{OC} due to decreasing light intensity which means that the Kimoto filtered cells have a lower efficiency compared to the Melinex and BASF HP filtered cells.

Perhaps the greatest contrast between the forward and reverse measurements is that in reverse illuminated cells, the anti-reflection properties of the filters are more prominent. It can be seen that even though the BASF HP filter has a higher UV cut-off than the Melinex filter, the anti-reflection properties outweigh the UV cut-off properties and efficiencies actually increase in all cases except for the cells made with Z907 which retains the same $\% \eta$.

The anti-reflection properties of the flexible polymer electrode could be an important factor in future module design as more sophisticated anti-reflection layers and embossment techniques can significantly improve light transmission through a polymer film.

The only filter that intersects the IPCEs of the cells is the spring yellow filter and cells measured with this filter show a much greater drop in photocurrent and efficiency compared to cells measured with the other filters. Even though a proportion of the action spectrum of the dyes is filtered out by the electrolyte the broadness of their IPCE spectrum is still important. As with the forward illuminated cells, the dye that suffers least from filtering is the dye with the broadest action spectrum, i.e. N749. The results for reverse illumination filtering are summarised in figure 6.16 below.

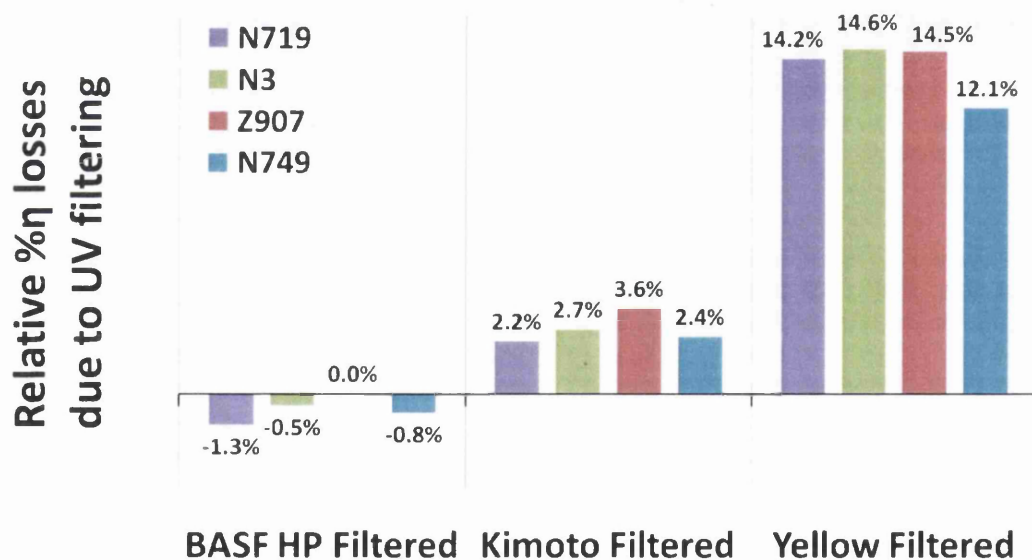


Figure 6.16

Relative %η losses in reverse illuminated, filtered cells compared to %η of Melinex (PET) filtered cells

It has already been established that the mechanism of cell failure, at least in the accelerated tests described in this thesis, is likely to be the direct photoexcitation of the TiO_2 semiconductor leading to photo-oxidation of the electrolyte and depletion of I_3^- . This chapter has shown that filtering can reduce the onset of UV photodegradation. It has been shown that for long term stability, filtering will be required above 385 nm but perhaps at no more than 400 nm. Despite the results presented here, there might still be a need for some filtering above 400 nm as rutile titania is still photoactive to around 412 nm. However, this is probably not necessary as rutile titania is generally considered not to be as photoactive as anatase due to a higher rate of electron-hole recombination which is attributed to rutile's lower capacity to adsorb oxygen onto its surface [3].

In a solar cell with a transparent polymer electrode manufactured from PET, the losses in light transmission and ultimately $\% \eta$ will be intrinsic to that device. It is therefore possible to use the $\% \eta$ values obtained with the Melinex filter as a baseline to compare the other filtering values to. Figures 6.12 and 6.16 summarise the relative losses in $\% \eta$ when using the UV cut off filters compared to the $\% \eta$ of the cells with the Melinex filter.

It has already been shown in this chapter that filtering above 400 nm gives no extra benefits in terms of cell stability at least in the timescale of the experiments conducted. So it can safely be assumed that for forward illuminated cells the right amount of filtering required for long term stability will give relative losses in $\% \eta$ of much less than 10% compared to losses caused by the PET and in reverse illuminated cells, the relative losses should be no more than 3% compared to the losses caused by PET. In fact if a broad action dye such as N749 were optimised and more sophisticated anti-reflection technologies were employed there may even be an increase in efficiency when using a PET based UV filter.

This is good news for those working on the industrialisation of metal based DSCs as in a reverse cell set up, which will be necessary if the WE is deposited on the metal, filtering at 400 nm, which has been shown to give adequate protection against UV degradation, will not affect the $\% \eta$ in a detrimental manner. When used with anti-reflection technology, polymer based filters could actually improve efficiency. However, those who are working

on reverse illuminated DSCs should be looking towards developing clear electrolytes as the current I^-/I_3^- redox couple can reduce $\% \eta$ by up to around 35%.

The results shown in this chapter also show that the spectral response of the DSC is important when considering UV filtering. It has been shown that the narrower the action spectrum of the dye, the more it is affected by UV filtering. Synthesis of new dyes with broader action spectra reaching further toward the NIR region will be essential for DSC development in general as well as being important when considering UV screening.

6.6 References

1. Anders Hagfeldt and Laurence Peter (2010). Characterisation and Modeling of Dye-Sensitised Solar Cells: A Toolbox Approach. Dye-Sensitized Solar Cells K. Kalyanasundaram. Lausanne, EPFL Press.
2. Md. K. Nazeeruddin, S. M. Zakeeruddin, R. Humphry-Baker, M. Jirousek, P. Liska, N. Vlachopoulos, V. Shklover, Christian- H. Fischer and M. Grätzel, Acid-Base Equilibria of (2,2'-Bipyridyl-4,4'-dicarboxylic acid)ruthenium(II) Complexes and the Effect of Protonation on Charge-Transfer Sensitization of Nanocrystalline Titania, *Inorganic Chemistry* 1999 **38**(26) 6298-6305
3. Marye Anne Fox and Maria T. Dulay, Heterogeneous photocatalysis, *Chemical Reviews* 1993 **93**(1) 341-357

Chapter

7.

Electrolyte Regeneration and Photocurrent Recovery in UV Photodegraded Dye- Sensitized Solar Cells.

7. ELECTROLYTE REGENERATION AND PHOTOCURRENT RECOVERY IN UV PHOTODEGRADED DYE-SENSITIZED SOLAR CELLS.

It has been found during the course of this work that severely UV degraded DSCs start to make a slow recovery when they are removed from UV exposure and put in the dark. Figure 7.1 shows the IV curves of a typical cell from the work described in *chapter 3*. This particular cell was exposed under load until it failed at around 400 hours total UV exposure. It was then left in the dark for around 2500 hours before making further IV measurements. The cell in question showed the drop in V_{OC} and a collapse in photocurrent which is typical of severely UV degraded DSCs, yet after being left in the dark the photocurrent is almost restored to original conditions. The V_{OC} and fill factor do not recover completely however, meaning that the “recovered” cell has $\% \eta = 2.5$ compared with its original $\% \eta = 3.8$; nevertheless, 2.5% efficiency is considerably better than 0.2% which is the $\% \eta$ of the cell after just 400 hours exposure under electrical load. The fact that the cell can recover in this way supports the photodegradation/recovery equilibrium hypothesis discussed in *chapter 4* (figure 4.5).

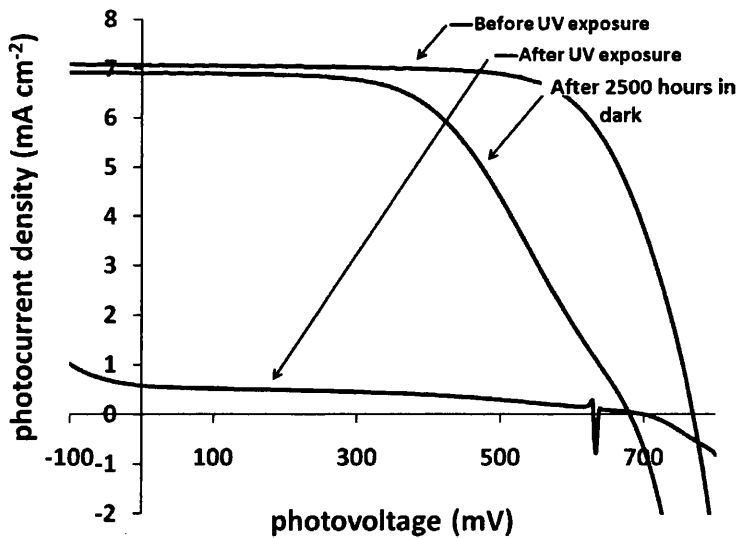


Figure 7.1 IV curves of a typical photodegraded DSC cell before UV exposure, after UV exposure and after being left in the dark for 2500 hours

During the experiments described in *chapter 4* on the photodegradation of larger area test cells, it was discovered that applying a reverse bias of around +1.2 V to an *undyed* cell restores the colouration of the bleached electrolyte. Figure 7.2 shows two still images from a video taken of the colour restoration occurring whilst conducting a cyclic voltammetry (CV) experiment on the cell. The experiment cycled the voltage from 0 V to +1.4 V in a two electrode set-up. It can clearly be seen that the yellow colour associated with electrolyte is much darker after the CV cycle indicating the regeneration of I_3^- .



Figure 7.2 Still images taken from an undyed cell undergoing a cyclic voltammetry cycle. Left is the cell at 0 V before cycling. Right is the cell at +1.3 V at the end of the first cycle

It was thought that if the photobleached electrolyte can be regenerated in an undyed cell then it may be possible to regenerate it in normal DSCs, and as it was shown in *chapters 3, 4, and 5* that the cell's ultimate failure arises from a loss of I_3^- , it might be possible to restore the cell to a working condition. Figure 7.3 shows the IV curves of a typical DSC before UV exposure, after UV exposure and after regeneration treatment. It can be seen that the cell undergoes a partial recovery of photocurrent upon regeneration but virtually no recovery of open circuit voltage, suggesting that there has been an irreversible change to the electrolyte composition or possibly a permanent change to the TiO_2 surface.

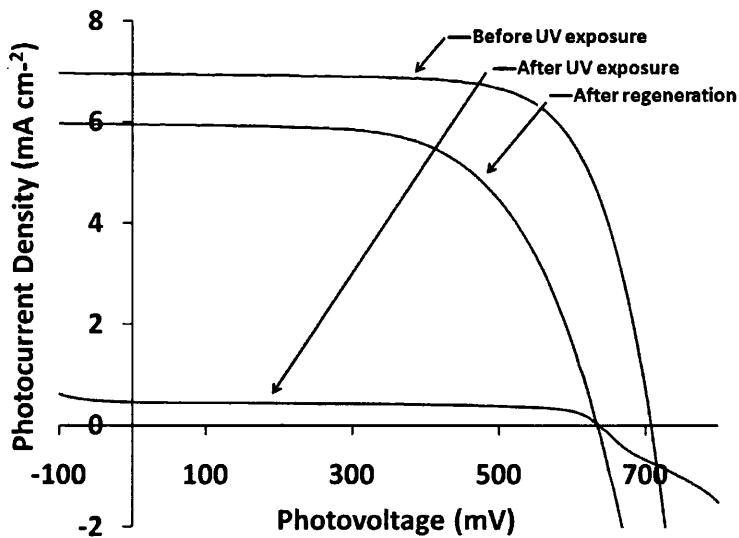


Figure 7.3 *IV curves of a typical DSC before UV exposure, after UV exposure and after regeneration treatment which consists of applying a positive bias, scanning from 0 V to + 1.4 V*

Figure 7.4 shows a typical cyclic voltammogram of a cell that has been irradiated for around 600 hours, and subsequently failed, undergoing the electrolyte regeneration process. The diffusion limited current seen from around 0.4 V to around 1.1 V is followed by an increase in current indicative of the degraded electrolyte undergoing reduction. The hysteresis of the second scan and subsequent scans, which follow an identical path, suggests that the first polarisation is responsible for the regeneration of the electrolyte.

It has been found that ramping up the voltage from 0 V to + 1.4 V, as in a CV experiment, seems to be more effective at restoring the cell properties than by simply applying the polarising voltage. It has also been found that the sooner the regeneration treatment is applied, the closer the cell properties are restored to original values. This leads to the possibility that by refining this treatment (in terms of the polarisation time, magnitude and its frequency of application) that the regeneration of the devices could be more effectively controlled. This is an attractive solution to restoring device performance since it could be periodically applied (for example at night) to maintain cell longevity.

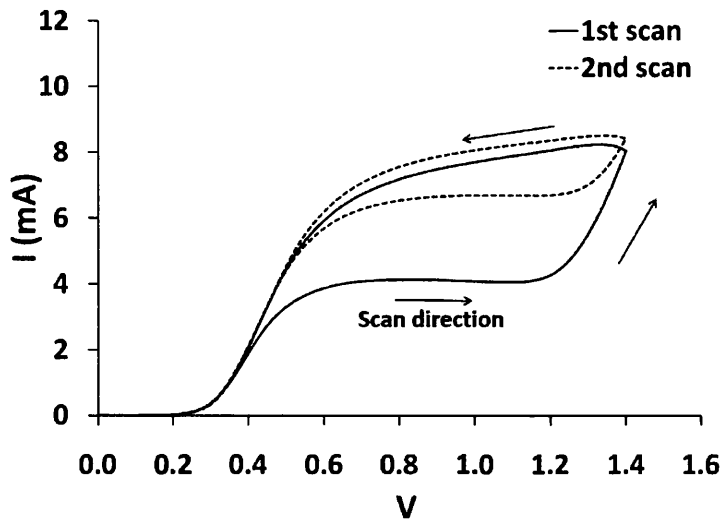


Figure 7.4 Cyclic voltammogram of UV degraded cell undergoing regeneration. The hysteresis of the 2nd scan shows the regeneration is non-reversible at least in the time scale of the experiment

7.2 Period Electrolyte Regeneration

7.2.1 Case Studies of Individual Cells

Figure 7.5 shows the change in efficiency over time of two individual cells, R1 and R2, both exposed to UV irradiation under load. In figure 7.5 it can be seen that both cells undergo UV exposure for 287 hours, both cells are subsequently given regeneration treatment. R1 is held at 1.3V for 60 seconds whilst R2 undergoes a CV cycle from 0 V to + 1.4 V, both cells make a partial recovery in efficiency and then both cells are placed in the light soaking cabinet. The regeneration seems to be short lived as after just 55 hours light soaking their efficiencies drop back down to a level only slightly above the their efficiencies after UV exposure. However, after being placed under load in the light soaking cabinet the cells start to recover more permanently. In particular, cell R2 seems to make a significant recovery. The fact that the cells recover once put in the light soaker shows once again how critical UV exposure is to DSC stability.

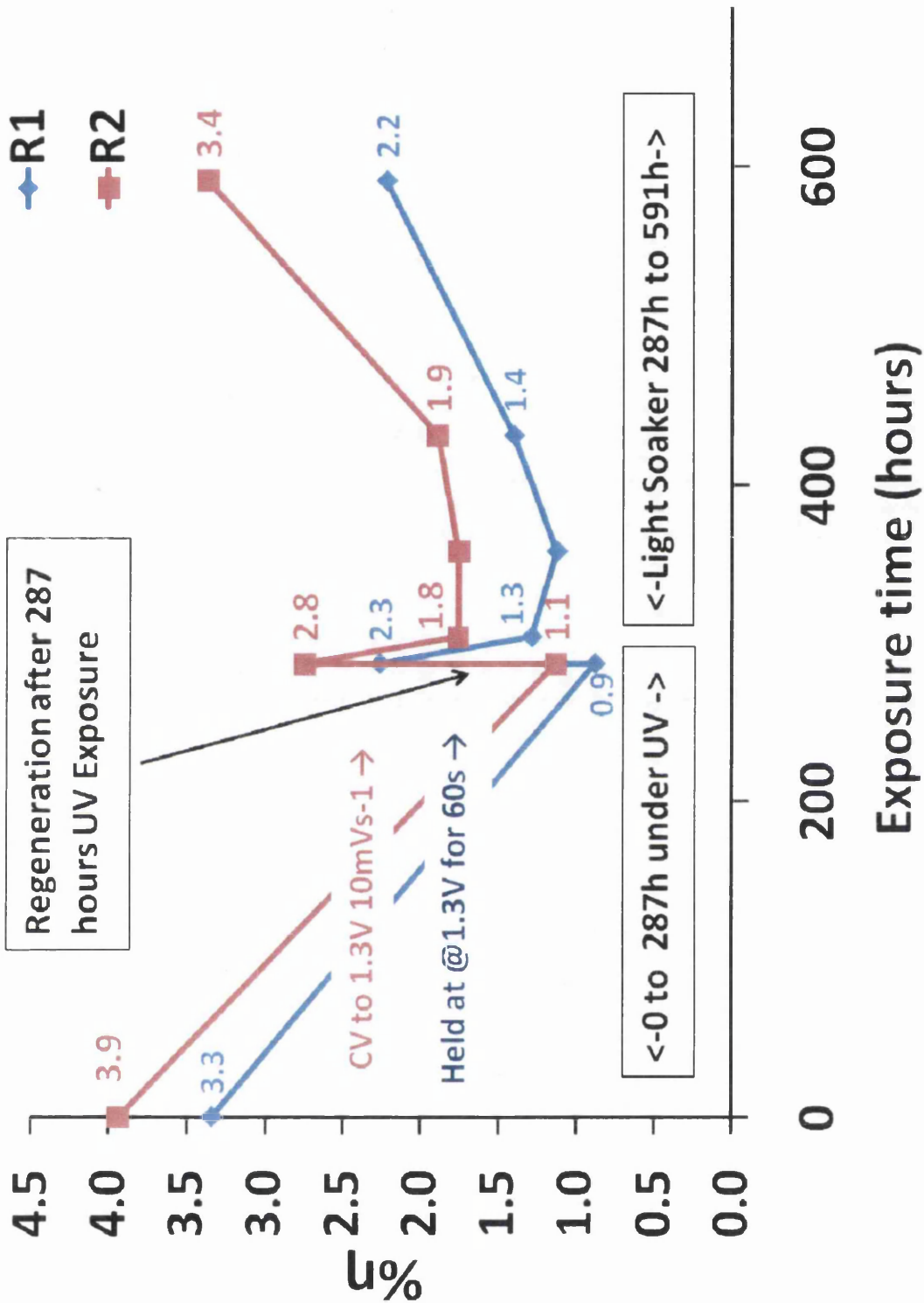


Figure 7.5 Changing η of two cells throughout UV exposure, regeneration treatment and then visible light soaking

Figure 7.6 shows the changing $\% \eta$ of another cell. This time, the cell was subjected to constant UV illumination under load and periodically treated with a CV ramping cycle at 20 mV s^{-1} to 1.4 V. It can be seen that after treatment, the cell makes a partial recovery but this seems to be short lived as the $\% \eta$ drops again quite quickly. Both the $\% \eta$ before recovery treatment and the $\% \eta$ after recovery treatment continue to decline throughout the exposure period which suggests that the periodic cell regeneration does not, at least in this case, extend cell lifetime. Nonetheless, after around 600 hours exposure, when looking at the $\% \eta$ values before treatment, the rate of degradation decreases and seems to plateau. If this is the case then it means that the periodic regeneration has prevented total cell failure even though it hasn't prevented UV degradation and the decline in $\% \eta$.

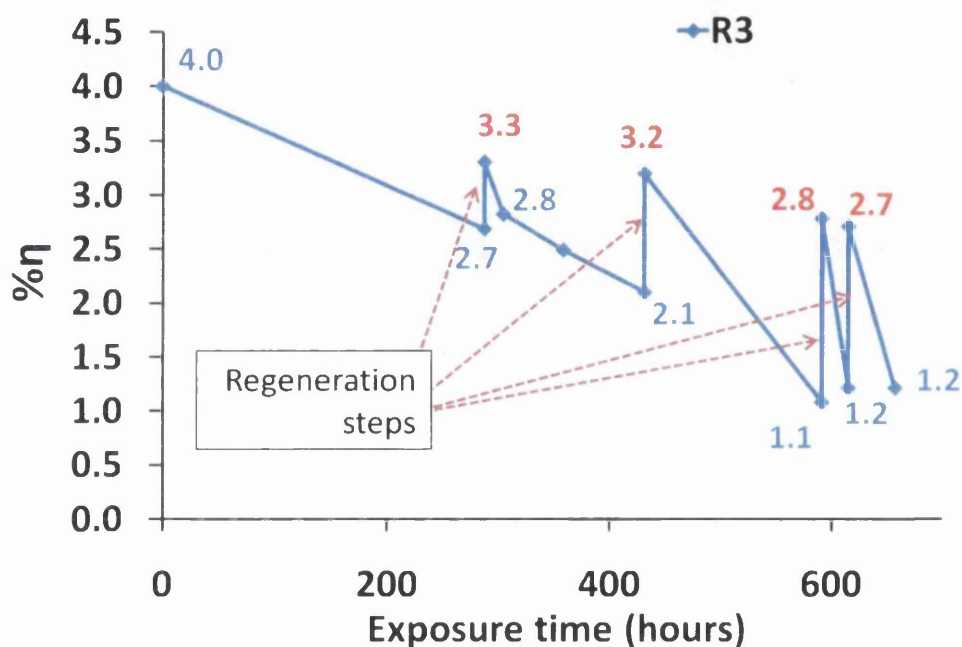


Figure 7.6 Changing $\% \eta$ of one cell throughout UV exposure and periodic regeneration treatment. The blue values represent the $\% \eta$ before regeneration the red values represent the $\% \eta$ after regeneration.

7.2.2 Systematic Study of Periodic Cell Regeneration

Two groups of cells were irradiated by UV light under open circuit conditions for the exposure period shown in figure 7.7 below. One set of cells were periodically regenerated the others were not. Figure 7.7 shows the mean $\% \eta$, J_{SC} and V_{OC} of the cells, the plots only include data before cell regeneration has taken place and *do not* include the values after regeneration. Looking at the V_{OC} , which so far has been identified as an important marker of UV degradation in DSCs, there appears to be no difference between the two groups of cells. Looking at J_{SC} and $\% \eta$ however, it can be seen that periodic regeneration seems to prevent the total failure of the cells by conserving a minimum amount of charge carriers within the electrolyte and maintaining a photocurrent density of around 2.5 mA cm^{-2} .

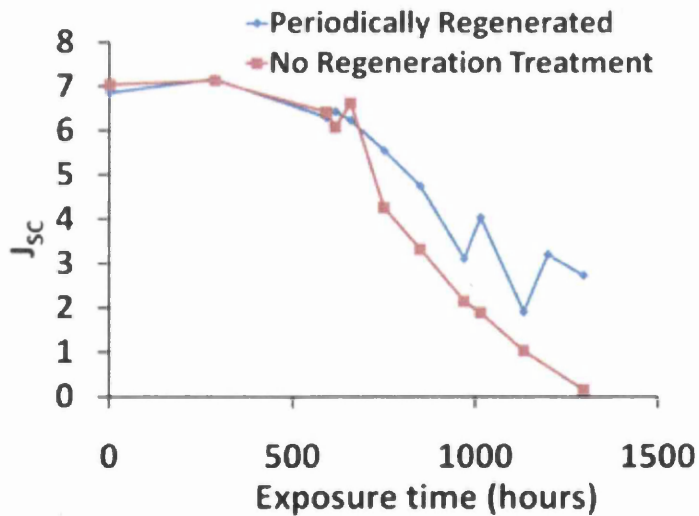
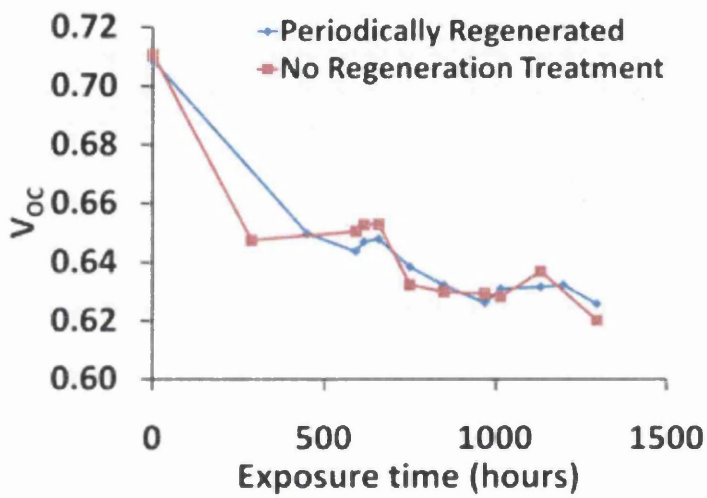
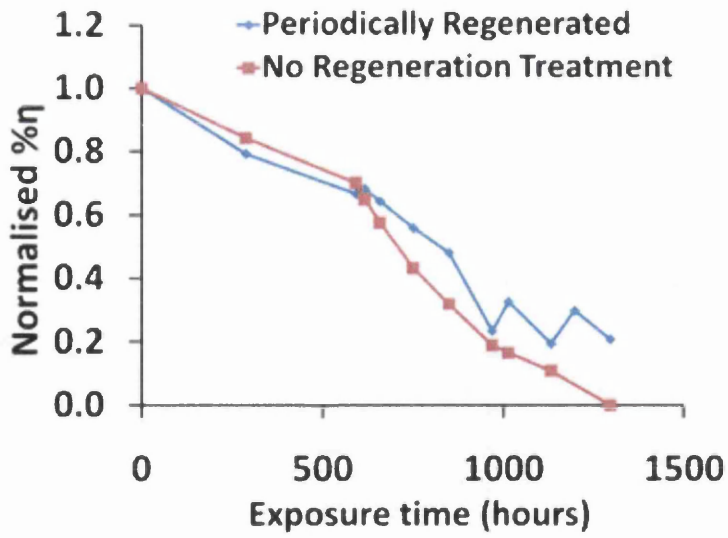


Figure 7.7 Mean %η, J_{SC}, V_{OC} of cells irradiated by UV light. One set were regenerated periodically, the other set were not

Although the power of the UV lamps has been shown to be reasonable with respect to AM 1.5, the constant UV illumination received by the cells means that the cells are being tested for stability under accelerated conditions. The amount of UV radiation received by the cells per hour is far greater than the average that would be received by the cells, even in high insolation areas. It was thought that if the cells were exposed under less severe conditions, then the regeneration treatment may be more effective. It has been shown that cell degradation is impeded somewhat when cells are exposed to UV light in reverse illumination due to the UV filtering effects of the electrolyte. It was thought it might be possible that periodic regeneration may be more effective in reverse exposed cells due to the net decrease in UV light received by the TiO_2 when cells are irradiated this way. As in figure 7.7, cells were irradiated, this time from the CE side and periodic regeneration was applied. Figure 7.8 shows the mean $\% \eta$, J_{SC} , and V_{OC} , over the exposure period of cells irradiated from the CE side. Looking at figure 7.8 it is clear that there is no difference in the long term stability of the regenerated and non-regenerated cells.

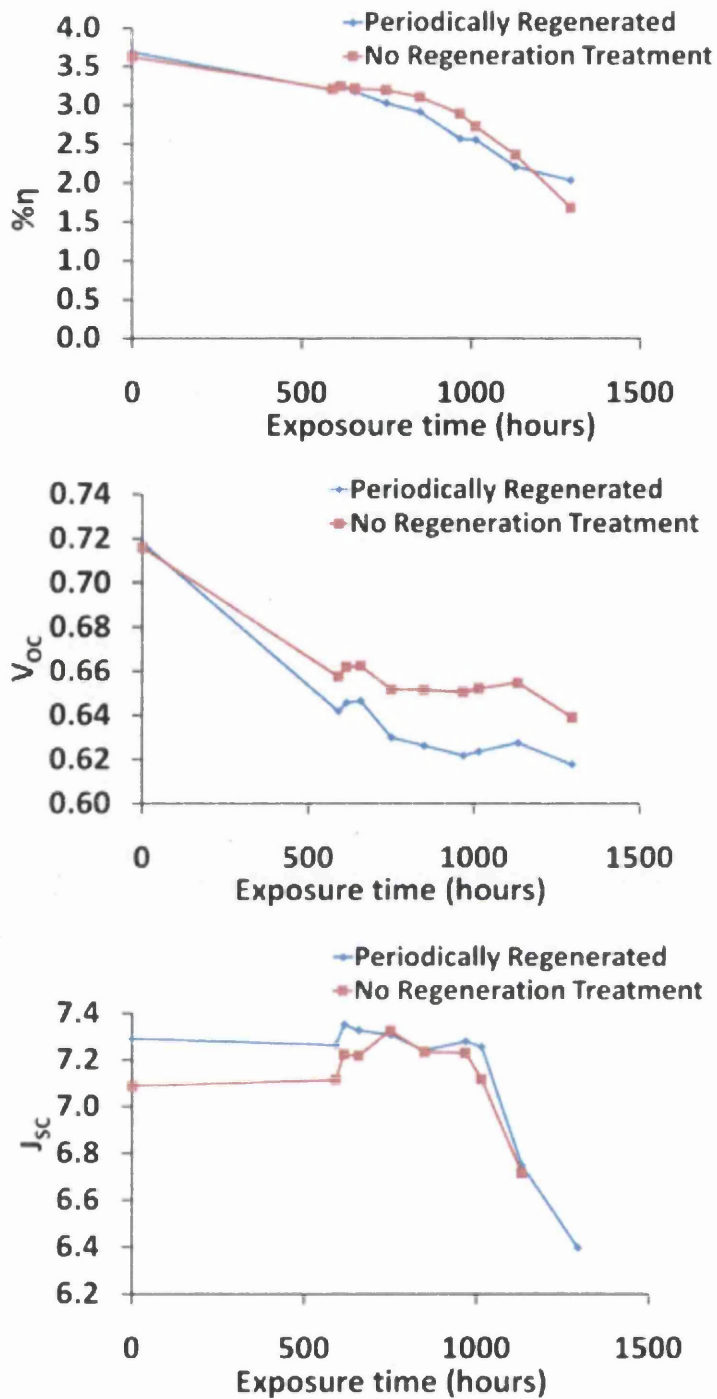


Figure 7.9 Mean $\% \eta$, J_{sc} , V_{oc} of cells irradiated from the CE side by UV light. One set were regenerated periodically, the other set were not

From the experiments conducted so far, it appears that periodic cell regeneration cannot prevent the inevitable photodegradation of DSCs irradiated by UV lamps. It appears that the equilibrium discussed in chapter 4.1.2 (and shown in figure 7.11 below) can be temporarily pushed to the left hand side *via* reverse polarising the cell but it seems that the I_3^- that is regenerated as a result, is soon re-consumed. Nonetheless, the exposure conditions are accelerated and the cells do not receive the same recovery period as operating cells would overnight. A more suitable experiment might involve irradiating the cells for 8 hours and then following a regeneration treatment, left in the dark for 16 hours. This might give the cells a chance to recover before the photocatalysed consumption of I_3^- is allowed to continue once again.

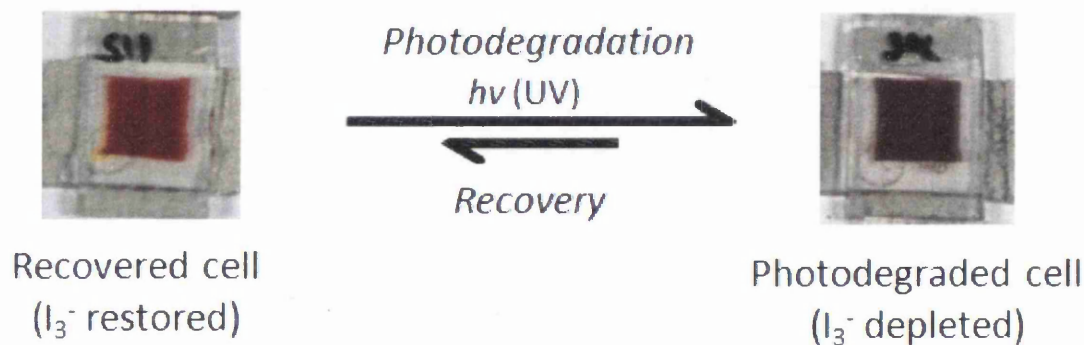


Figure 7.10 Photodegradation/recovery equilibrium of DSC test cells under UV irradiation

It is clear that the regeneration treatment cannot prevent photodegradation of the cells but if the J_{SC} data shown in figure 7.8 is replotted, this time with the post-regeneration treatment values included (figure 7.11), it can be seen how cells subjected to periodic regeneration might maintain a higher average maximum power output over a given UV exposure period compared to those that do not receive the treatment.

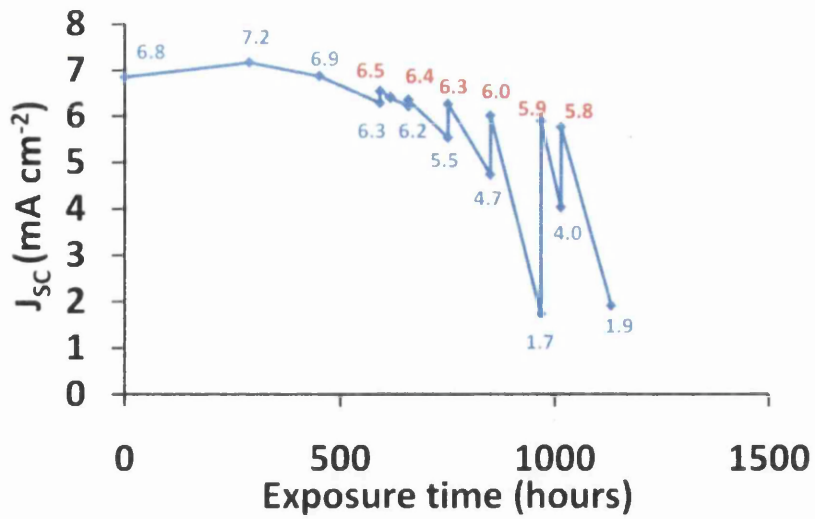


Figure 7.11 J_{sc} of cells irradiated by UV light and periodically regenerated. The blue values represent the J_{sc} before regeneration the red values represent the J_{sc} after regeneration.

This does warrant further investigation. Ideally this would involve measuring the maximum power output during operation to ascertain whether the periodically regenerated cells have a higher average maximum power output during the exposure period and allowing longer recovery times after exposure and regeneration.

Chapter

8.

UV Photodegradation of Polymer Films intended for use as Counter Electrode Materials in Flexible Dye- Sensitized Solar Cells

8. UV PHOTODEGRADATION OF POLYMER FILMS INTENDED FOR USE AS COUNTER ELECTRODE MATERIALS IN FLEXIBLE DYE-SENSITIZED SOLAR CELLS

In a flexible, metal based DSC, the counter electrode is most likely to be a polymer film coated with a TCO. This polymer film will perform many more functions than just carrying current, and acting as a substrate for the Pt catalysed reactions at the CE surface. The polymer film will form part of the encapsulation layer to keep the VOCs of the electrolyte from escaping and act as a barrier to prevent atmospheric oxygen and water ingress. The importance of UV filtering has been discussed extensively in this thesis and so the polymer film will need to provide UV filtering in order to assure long term stability. The polymer film itself will be susceptible to direct photodegradation and therefore one of the challenges to ensure durability in flexible DSCs ultimately relates to the stability of the transparent CE material. Polymer films are known to be susceptible to photodegradation by UV light, leading to the loss of mechanical and optical properties, resulting in embrittlement and O₂ and moisture ingress. This would ultimately lead to loss in efficiencies and cell module failure.

Because of its multi-functional role, the polymer film will henceforth be referred to as the “topsheet” as this will form the part of the module that is uppermost and therefore will be the part of the module that faces the Sun. Other desirable properties of the topsheet include anti-reflection, easy or self cleaning and impact protection.

8.2 The Topsheet as a UV Filter

It has already been shown in *section 6* that, in terms of DSC stability, there seems to be no extra benefit of filtering above 400 nm, at least in the time period of the experiments described there. The work described in this was carried out before the work in *chapter 6* was started and at that time it was thought that filtering may be needed at 410 nm due to the band gap of rutile TiO₂ being 3.02 eV meaning that it is theoretically photoactive at $\lambda < 410$ nm. Anatase TiO₂ on the other hand has a band gap of 3.18 eV so is photoactive at $\lambda < 390$ nm.

The photocatalytic activity of TiO_2 arises from the creation of an electron-hole pair which forms when a TiO_2 electron absorbs a photon. Oxygen and water molecules adsorbed to the TiO_2 particle surface form oxygen radicals (reduced by the electron) and hydroxyl radicals (oxidised by the hole). These radicals attack organic compounds in the vicinity leading to degradation. Despite being excited by lower energy photons than anatase molecules, rutile molecules are not as photoactive because rutile has a lower surface area than anatase meaning less water/oxygen adsorption and so fewer radicals are created [1]. In addition to this, the heat treatment used to sinter the TiO_2 means that the TiO_2 film should consist almost entirely of anatase. Despite this, at the time these experiment were started, Dyesol believed that small rutile impurities may be present or that anatase trap states may be present with lower band gaps that will excite at higher λ , because of this they set a requirement of $< 1\%T$ at $\lambda < 410 \text{ nm}$.

8.2.1 The UV Cut-Off

It is thought that the topsheet of the DSC module will be a PET film such as Melinex which is manufactured by DuPont Teijin Films. These films offer good flexibility and scratch resistance, but as it can be seen in Figure 8.1 below in the transmission spectrum of Melinex ST505 that these films do not screen UV light above 315 nm. Two methods of improving the UV screening properties were thought possible. One method was to coat the PET film with a UV screening clearcoat; another was to co-laminate another film onto the PET. Alternatively a supplier could be sought that could manufacture unique films just for this project. The ultimate aim of this part of the project at the time was to achieve a UV cut-off of around 410 nm.

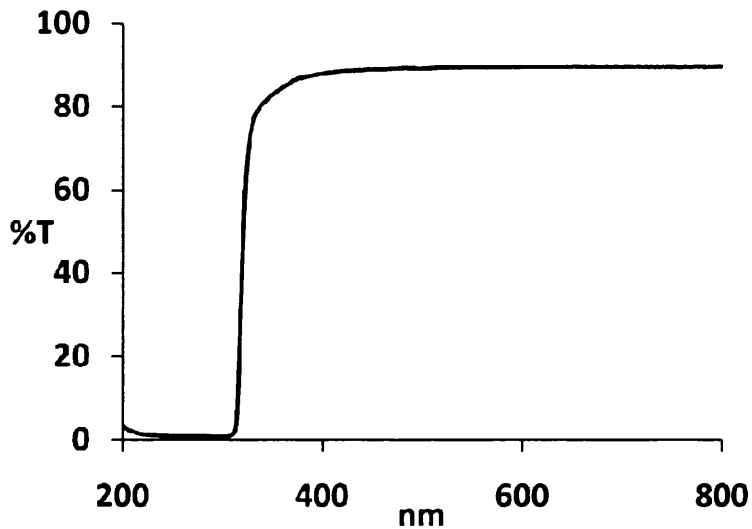


Figure 8.1 UV-Vis %T spectrum of Melinex ST505

8.2.1.1 Original Samples

The original samples in this part of the project consisted of Melinex ST505 (PET) coated with various UV absorbing polyurethane clearcoat lacquers (BASF LP, BASF HP and Beck). A last sample was included: Icosolar® T 2823 from Isovolta which is a co-laminate of a PVF and PET film with added UV absorbers (UVAs). The samples will be explained in more detail in *section 8.3*.

Figure 8.2 shows the transmission curves of the original samples, the figure contains a %T curve for an “ideal” curve where %T < 1 (at $\lambda < 410$ nm). It is clear that none of the samples could offer the level of screening that was required by Dyesol at the time.

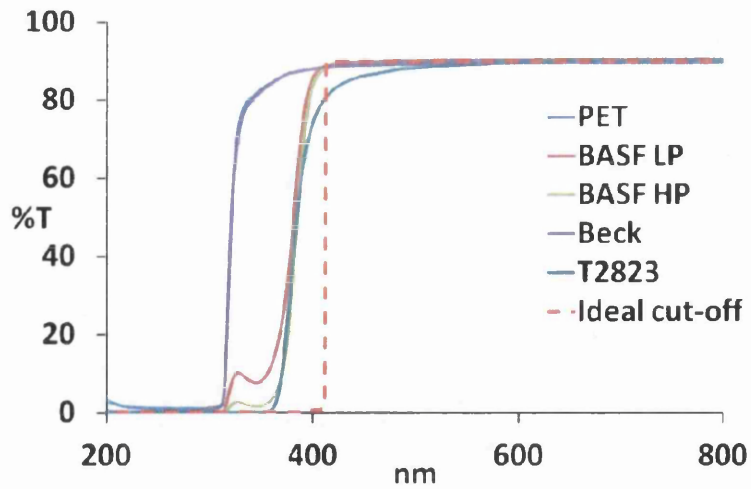


Figure 8.2 The transmission curves of the original samples tested

Figure 8.3 shows the transmission curves of some of the samples coated with Bayer UV cured polyurethane lacquers. Although they do offer some UV screening, the UV cut-off, even coated at 60 μm , is not as good as that of the BASF lacquers which are coated at 20 μm .

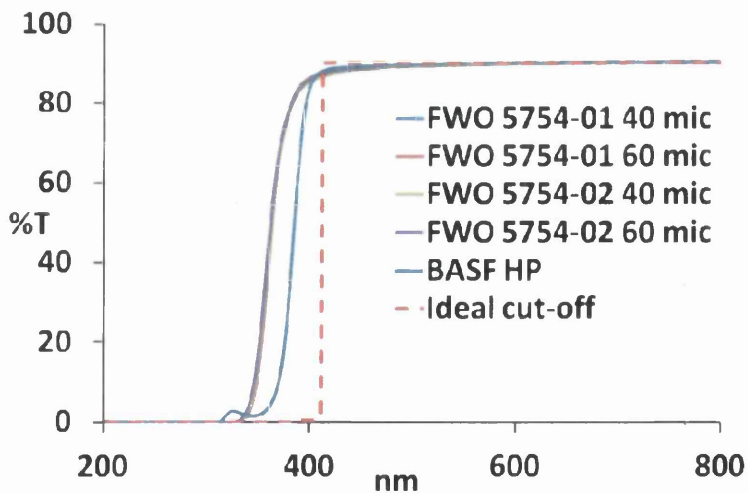


Figure 8.3 The transmission curves of the samples coated with the UV cured Bayer lacquers

8.2.1.2 The use of Additional UV Absorbers – Tinuvin 477

A sample of Tinuvin 477 was obtained BASF. Tinuvin 477 is a high performance organic UV absorber with a high UV cut-off so it was decided to see if the filtering performance of the BASF HP lacquer could be improved by additions of Tinuvin 477. Figure 8.4 shows the transmission curves of lacquers made with these additions. Increasing additions improve the UV cut and cause it to red-shift but even at a 10% addition, Tinuvin 477 does not give the level of UV screening required to completely remove TiO₂ band gap photons. However, Tinuvin 477 does improve the UV cut-off of BASF HP at a 2% addition. *Chapter 6* showed that UV screening needs to occur between 385 nm and 400 nm to ensure long term stability and as BASF HP cuts off at 385 nm, any improvement on this can only increase cell lifetime.

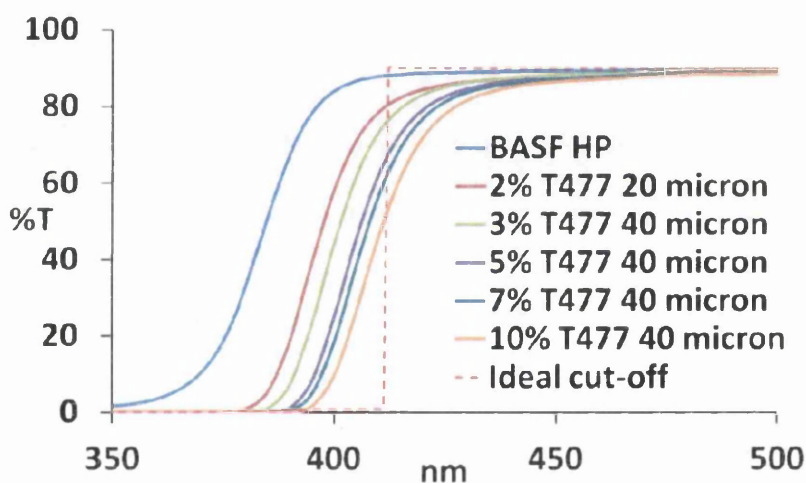


Figure 8.4 %T curves of samples with Tinuvin 477 additions

8.2.1.3 Inorganic and Yellow Pigments

Some TiO₂ UV absorber dispersions were obtained from Sachtleben (RM200 and RM400), these were tested to see if they could give the required level of UV screening. The dispersions were added to BASF HP at varying concentrations between 1% and 5% by

weight. Their %T curves spectra are shown below in figure 8.5. It is clear that a higher concentration than 5% would be needed to achieve the level of UV filtering required. It is also clear however that increasing the concentration of the TiO₂ dispersions would also result in a large loss of light transmission above 400 nm. The effect of this on cell efficiency would be too great and therefore these dispersions are unsuitable for use as UV protection for DSCs.

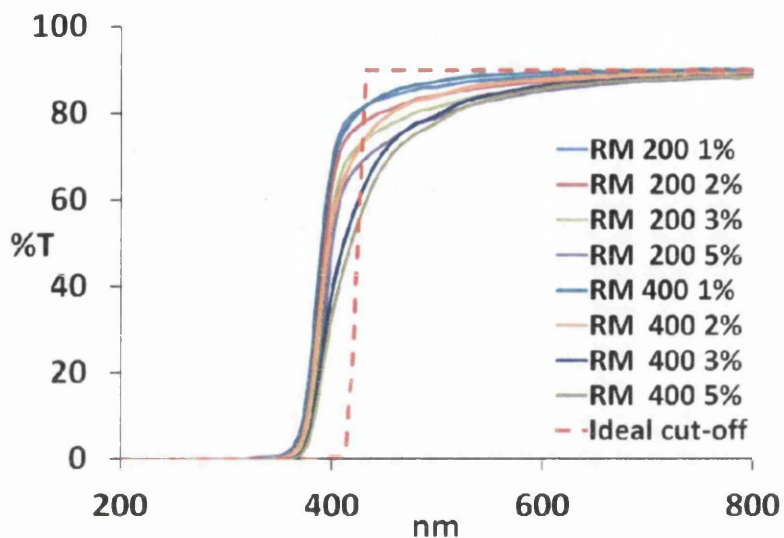


Figure 8.5 %T curves if samples with Sachtleben TiO₂ dispersion additions

Some iron oxide pigment dispersions were obtained from AMPS Ltd as FeO pigments are often used as UV absorber in wood lacquers. The dispersion was added to the BASF HP lacquer in the quantities shown in Figure 8.6. Similarly to the TiO₂ dispersions, it appears that the level of UV filtering required can be achieved but with the loss of a great deal of visible light. The effect this would have on cell efficiency means that these pigments would not be suitable either.

Finally it was decided to try some yellow organic pigment as it was thought that a yellow pigment would absorb blue light and may give the cut-off required. Two yellow pigments from BASF were added in the proportions shown. The pigments were 2P26-M158 (Y1), and 90-A105 (Y2). The transmission curves can be seen in Figure 8.7. In a similar way to TiO₂

and FeO pigments it appears that increased UV protection comes with a decrease in visible light transmission. These yellow pigments would not be suitable for UV protection of DSCs.

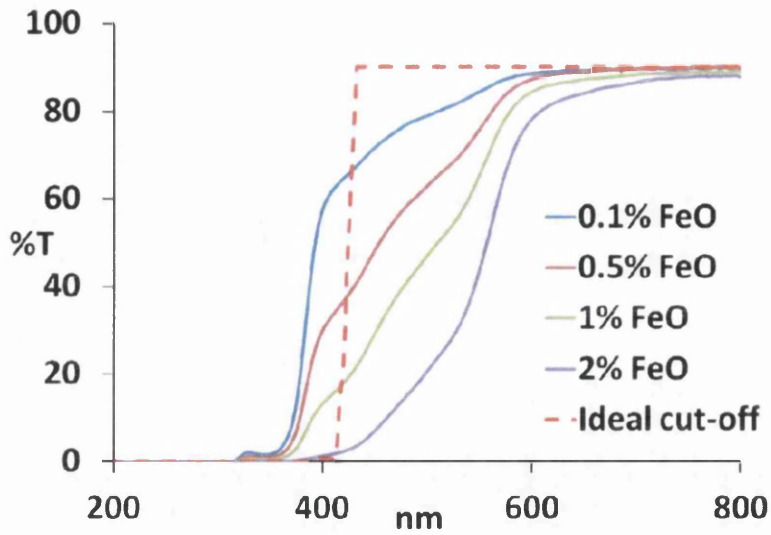


Figure 8.6 %T curves of samples with FeO dispersion additions in BASF HP lacquer

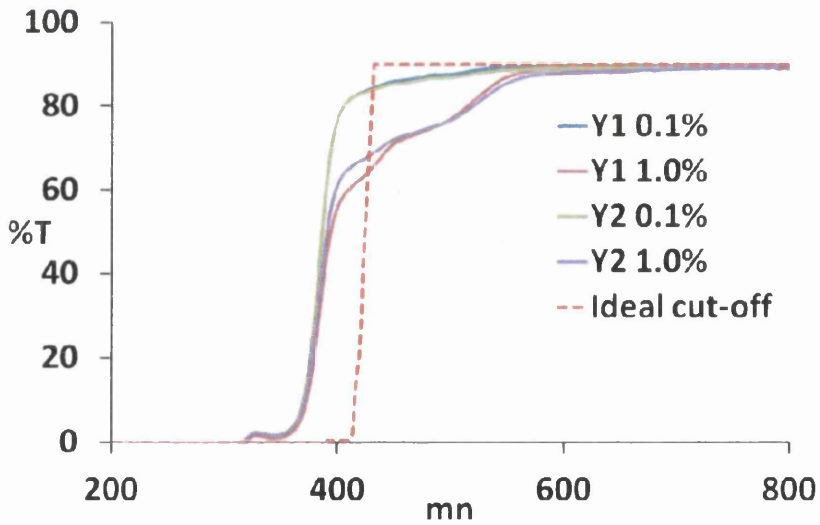


Figure 8.7 %T curves of samples with yellow pigment additions in BASF HP lacquer

8.2.1.4 Kimoto Films

Kimoto, a Japanese film converter, had been contacted and they sent samples to be evaluated. They have many films in development which may provide a solution to the UV screening problem. The films %T curves are shown in Figure 8.8 below. The films have sharp UV cut-offs that fit the “ideal curve” almost completely. These films have not however been tested for long term stability as this would break the terms and conditions of the non-disclosure agreement which Tata Steel had with Kimoto. The Kimoto films have a slight yellow discoloration so whether the UV filtering is caused by organic UV absorbers or some other pigment is unclear.

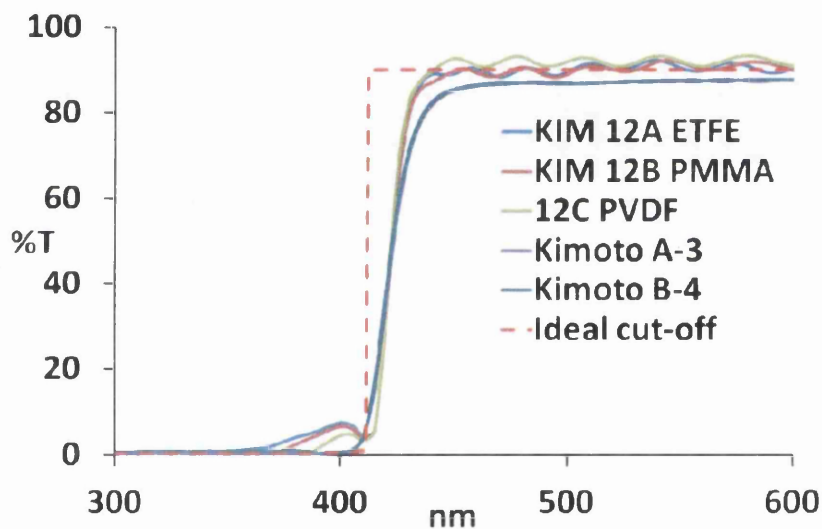


Figure 8.8 %T curves of the Kimoto films

8.2.1.5 UV Absorbers in a UV Cured Adhesive

Whilst looking at ways to laminate and adhere two sheets of PET together it was thought that it might be possible to disperse some UV absorbers in an adhesive to give UV filtering. Two adhesives were sourced. Devcon Tru Bond 18401 is a UV activated pressure-sensitive

adhesive. Devcon Tru Bond 18210 is a UV cured adhesive. Tinuvin 477 was added to the adhesive in the proportions shown in Figure 8.9 below. The adhesion of both adhesives was found to be satisfactory even at 30% (by weight) UVA addition and this almost gives the level of filtering required. After a few weeks however the UVAs were found to have leached out of the adhesive and the adhesion had been compromised. This method of creating a UV filter is promising but would require more work finding the right combination of adhesive and UV absorber.

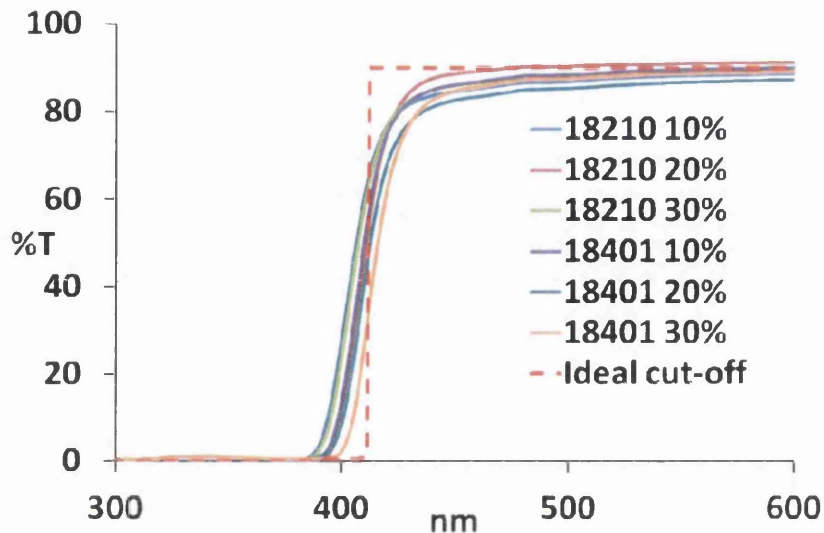


Figure 8.9 %T curves of films colaminated with UVA doped adhesives (the percentages show the amount of Tinuvin 477 added by weight to the adhesive)

8.2.1.6 UV Filtering by the Electrolyte

The ultimate aim of this project is to produce flexible DSCs on a metal substrate and because of this the cells must work in a reverse illumination set up. At the time the experiments in this section were being carried it was hoped that the electrolyte may offer some UV protection to the cell. This has since been shown not to be the case. Chapters 3, 4 and 5 show that cells do degrade more slowly when they are reverse illuminated with UV light but still eventually fail nonetheless.

The electrolyte has its own spectral properties and fits well inside the ideal %T curve as figure 8.10 shows. Figure 8.10 shows the %T spectra of a model cell made with TCO-coated and platinised glass, but no TiO_2 photoanode. When filled with electrolyte and measured with UV-Vis the cell gives an impression of what the photoanode might “see” in a reverse set up by characterising the %T properties of the TCO, platinum and the electrolyte combined.

Despite the fact that it has already been shown that the electrolyte offers only limited UV protection, it still would have been wrong to rely on the electrolyte for UV protection for a number of reasons. Firstly the electrolyte that is represented in figure 8.10 may not have the same spectral characteristics as the electrolyte that ends in up in the first generation product. For example, the iodine content may be reduced, the layer of electrolyte may be less than that represented in figure 8.10 or a transparent electrolyte may even be developed. In addition to this, a flexible cell under tension/compression will not have a uniform layer of electrolyte. All these reason could decrease the level of filtering provided by the electrolyte.

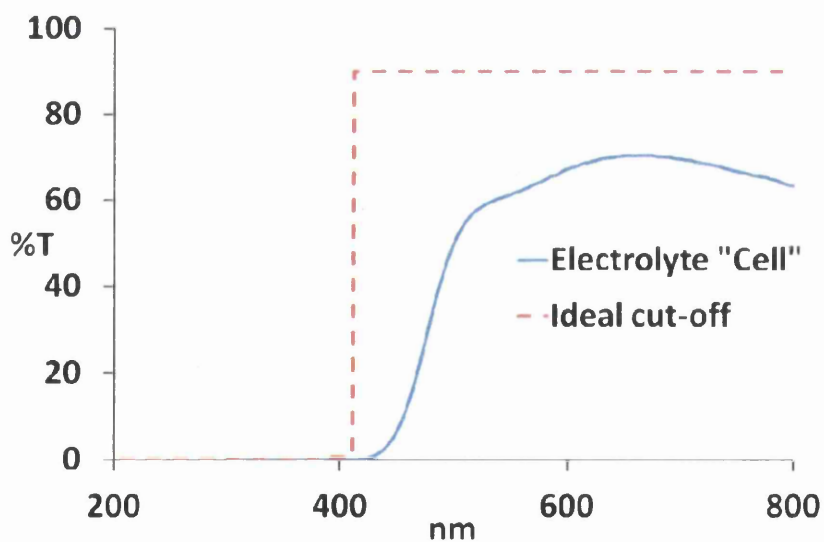


Figure 8.10 *UV-Vis spectra of the electrolyte “cell”, a device made with two platinised TCO glass “electrodes”, sealed and backfilled with electrolyte. There is no TiO_2 present in these devices meaning that the %T spectrum should give an impression of the light that should reach the photoanode in a normal DSC device.*

8.3 UV Stability of the Topsheet

The polymer films that will form the substrate for the counter electrode will be themselves susceptible to UV photodegradation. It is important therefore to be able characterise the photodegradation of these films and to assess UV protection measures. The following sections will address both these issues.

8.3.1 UV Protection with Polyurethane Clearcoat Lacquers

Three polyurethane two-pack (2k) clearcoats were obtained. Two from BASF, one designated low performance (BASF LP) and one designated high performance (BASF HP). The third clearcoat was from Beckers (Beck). The %T spectra of the lacquers coated onto Melinex ST505 can be seen in figure 8.2 above. It can be seen that whilst BASF HP and LP offer good UV screening the Beckers lacquer offered no UV screening at all compared to ordinary PET. Neither of the BASF lacquers offers the protection specified by the “ideal curve”.

Some free films of the BASF lacquers were made by coating onto a Teflon baking sheet and carefully removing the film when cured. Figure 8.11 below shows the transmission spectra of both the BASF lacquers as free films. The spectra are what one would expect to see in that they are very similar to those of the Melinex ST505 coated with the lacquers. It can also be seen that the BASF HP is has slightly better UV absorbers than the BASF LP as it has a lower %T in the region of 350 - 250 nm. This is shown perhaps more convincingly in figure 8.12 which shows that BASF HP has a larger UV absorbance, particularly in the region of 230 nm.

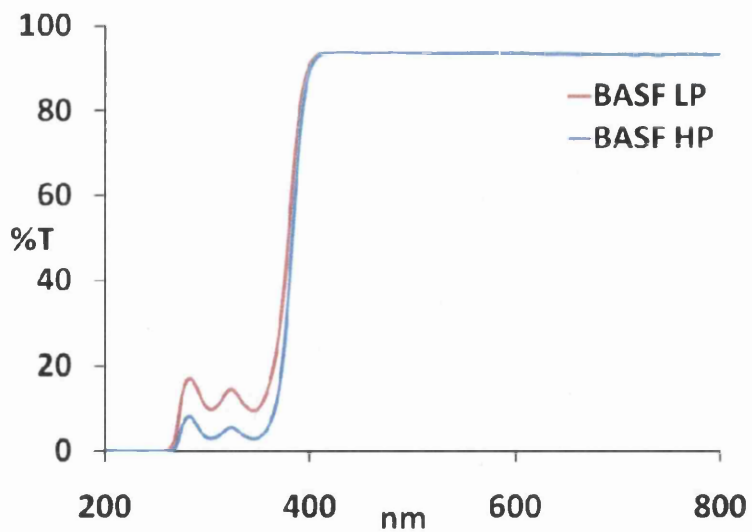


Figure 8.11 UV-Vis %T spectra of the BASF lacquers as free-films, i.e. they have been coated at 20 μm on a Teflon baking sheet and carefully removed for UV-Vis sample preparation.

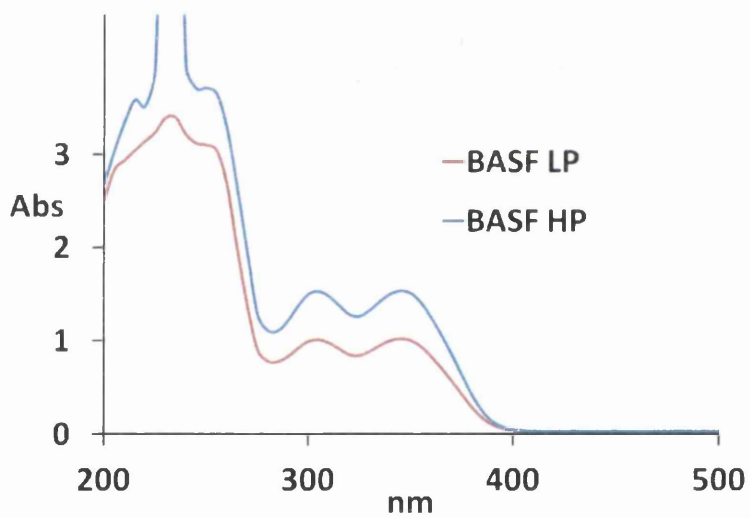


Figure 8.12 Absorbance spectra of the BASF lacquers as free-films

8.3.2 Colaminates and other Films

For the initial weathering experiments, three films were obtained, these were:

- 1) Norton® ETFE from St Gobain: an ethylene tetrafluoroethylene (ETFE) film
- 2) Icosolar® T 2754 from Isovolta: an ETFE film coated with inorganic SiO_x on one side
- 3) Icosolar® T 2823 from Isovolta: a co-laminate of a polyvinyl fluoride (PVF) and PET film coated on one side with a primer

Films 1) and 2) were laminated onto Melinex ST505 film using an ordinary office laminator and then sealing the edges with epoxy resin. This was not an ideal method as air and water would inevitably be trapped between the films. A solution was needed to get the tests running and this was found to be the best alternative at the time. If research continues into using co-laminates then perhaps a better method would be to use a clear EVA adhesive in combination with a heated roller/laminator, if this was used then it might be possible that PET films might need to be surface treated. Film 3) is bought from Isovolta already co-laminated. If this was used for PV module encapsulation then no other treatments would be needed.

Figure 8.13 shows the UV-Vis %T spectra of the films. Only one of the laminates (Icosolar® T 2823) offered substantial additional UV screening. The other films could have probably been disregarded from the start, however they were subjected to the same accelerated weathering conditions as the other samples and the results will be presented below.

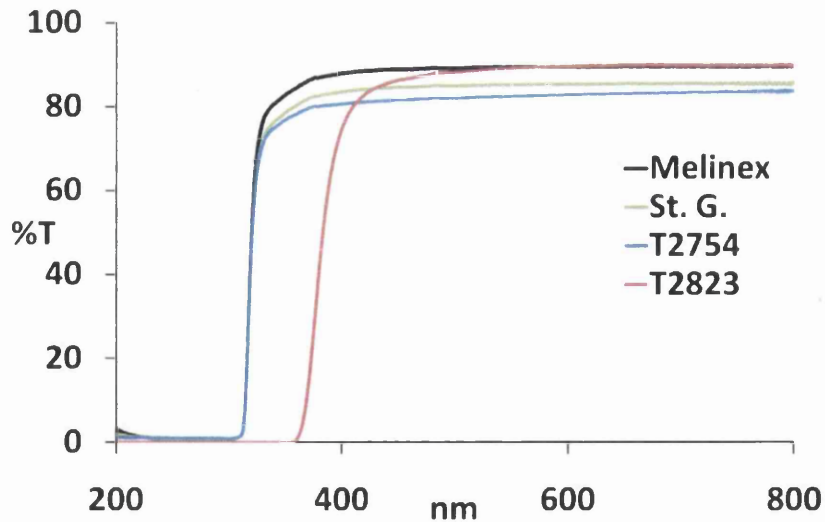


Figure 8.13 UV-Vis %T spectra of the films and colaminates

8.3.3 Accelerated Weathering of Polyurethane Clearcoats and Colaminated Films

Accelerated weathering was carried out in QUV cabinets that comply with the international standard ISO 4892. They were operated on an alternate 8 hour light cycle to 4 hours moisture cycle continuously and samples were tested approximately every 250 hours. The levels of degradation were measured using the change in UV-Vis and FTIR spectroscopy and through observation.

8.3.3.1 Photodegradation Observed with UV-Vis Spectroscopy

Melinex ST505 (PET) film shows a large absorbance from 200 nm to 315 nm. It can be observed overtime that, due to QUV weathering, this absorbance decreases (Figure 8.14) resulting in an observed change in the %T spectra (Figure 8.15). Figure 8.15 shows that over time photodegradation causes a decrease in the amount of UV light transmitted whilst appearing to increase the amount of visible light. This might be considered somewhat

beneficial were it not for the fact that over the course of 2562 hours QUV exposure the Melinex became hazed and embrittled and by 2500 hours was far too mechanically weak to continue testing. The reduction in absorbance is probably due to consumption or breakdown of the UV absorbers over the exposure period.

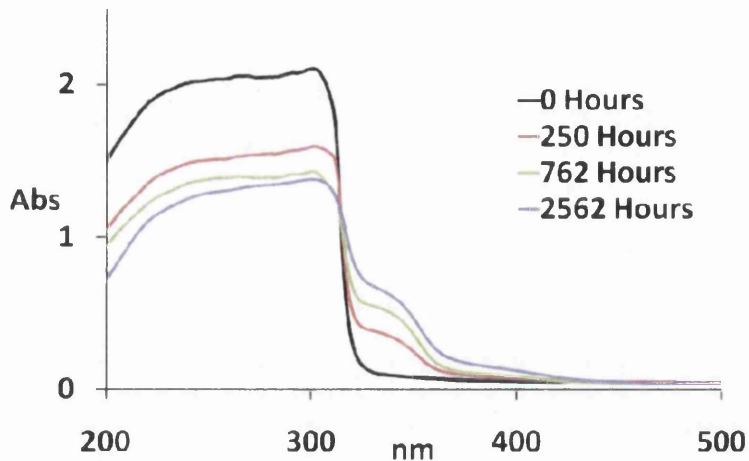


Figure 8.14 Decrease in UV-Vis Abs (200 nm to 300 nm) of Melinex ST505 exposed to QUV over 2562 hours

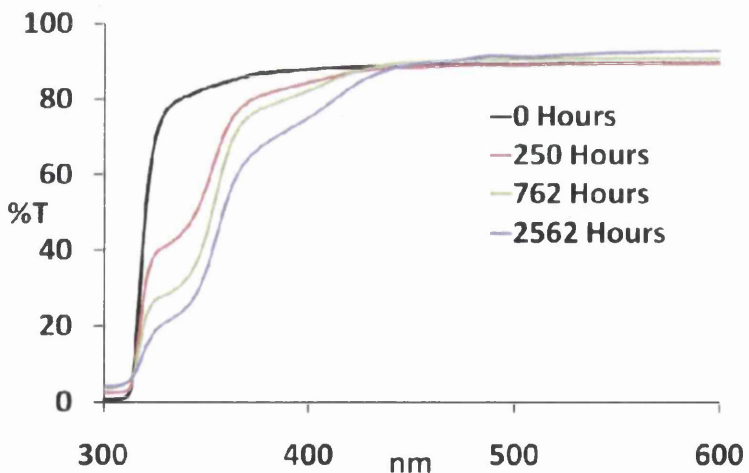


Figure 8.15 Changes to the UV-Vis %T spectra of Melinex ST505 exposed to QUV over 2562 hours

Figures 8.14 and 8.15 suggest that it might be possible to get an idea of the amount of photodegradation occurring in a sample by looking at the change in its UV-Vis spectra over time. This is correlated with physical evidence such as yellowing embrittlement and hazing.

Figures 8.16 summarises the changes in the UV-Vis %T spectra of the samples described in sections 8.3.1 and 8.3.2 over the time periods shown.

Correlation with physical evidence and FTIR spectroscopy shows that the best performing films show the least change in their %T spectra. UV-Vis %T spectra can therefore give a good indication of the extent of photodegradation.

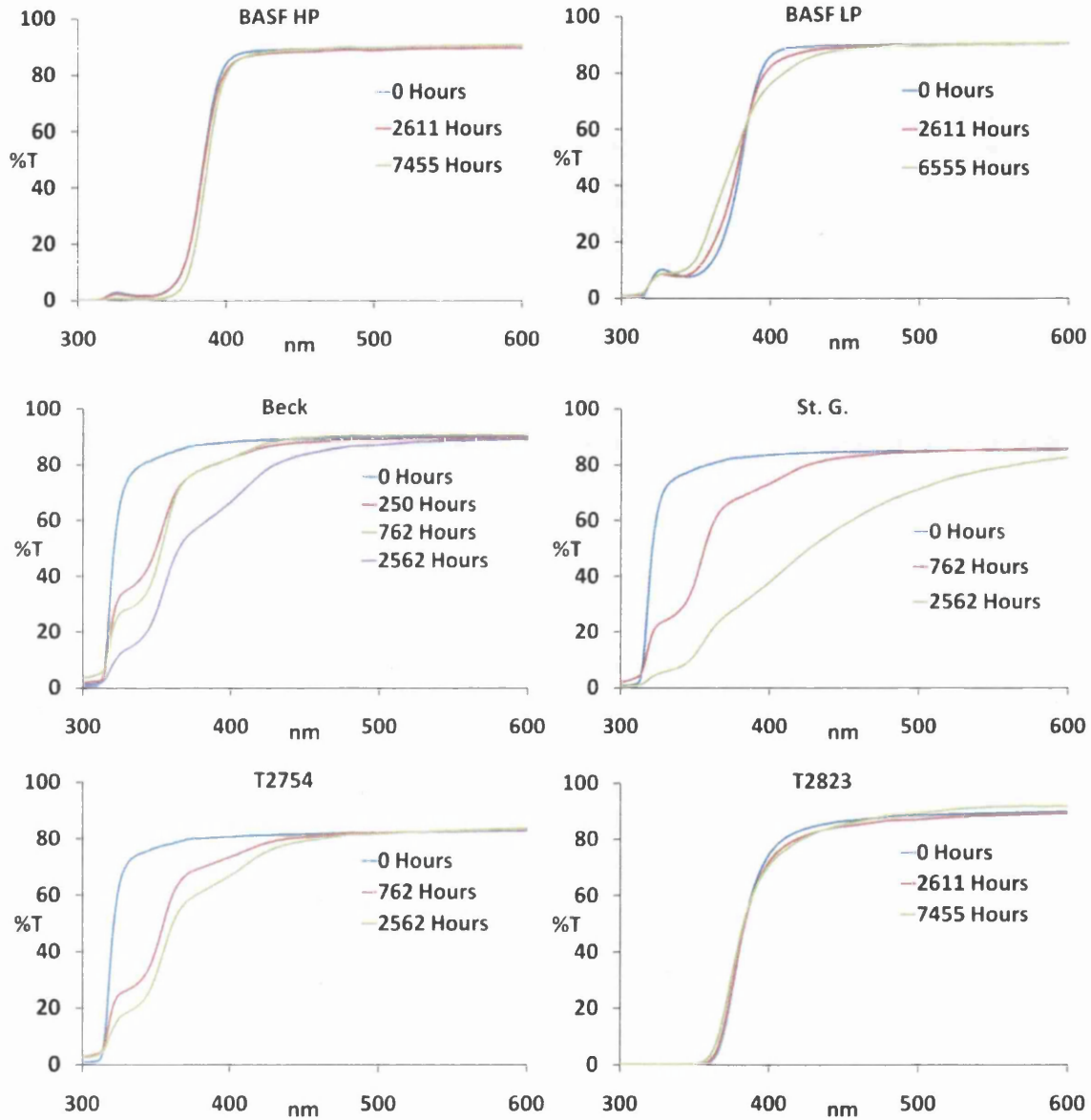


Figure 8.16 UV-Vis %T spectra of samples described in sections 8.3.1 and 8.3.2 over the exposure periods shown – NB. time period is different in the case of each sample

8.3.3.2 Quantifying Photodegradation using UV-Vis - The Yellowness Index

It has been shown [2] that photodegradation of PET films causes a yellowing which leads to an increase in absorbance in the region of 400 nm (Figure 8.17). It was also shown in [2] that this photodegradation could be quantified by measuring the increase in absorbance at 400 nm. The increase in absorbance is caused by quinone and diquinone formed during photodegradation [3]. Figure 8.18 shows the relative increase in absorbance at 400 nm of all the original samples.

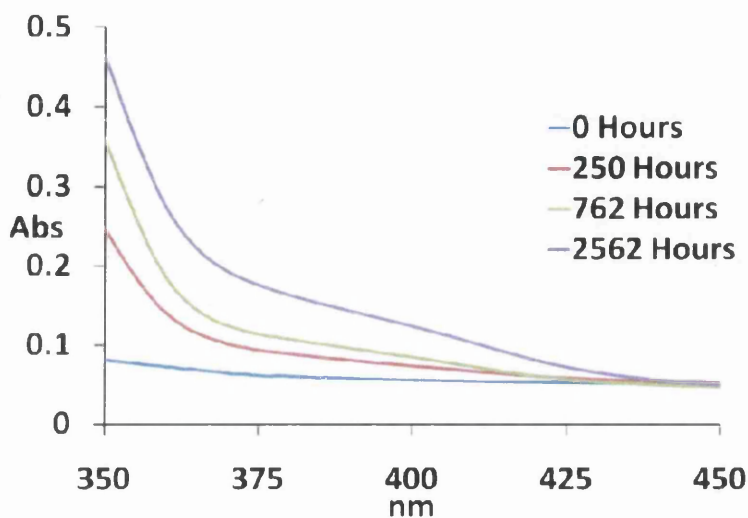


Figure 8.17 The increase in absorbance in the region of 400 nm due to UV exposure of uncoated PET (Melinex ST505) over the exposure period shown

Figure 8.18 clearly shows that BASF HP, BASF LP and T2833 have outperformed the other samples even though they have endured almost three times the amount of QUV exposure. T2754 and St.G. have a larger increase in absorbance at 400 nm than uncoated Melinex, and therefore appear to have suffered more from photodegradation. This is because T2754 and St.G. offer no protection from photodegradation whatsoever and in effect, when these films are laminated onto Melinex ST505 and irradiated, there is double the amount of material undergoing photodegradation and therefore one would expect a greater increase in Abs at 400 nm when compared to uncoated Melinex ST505.

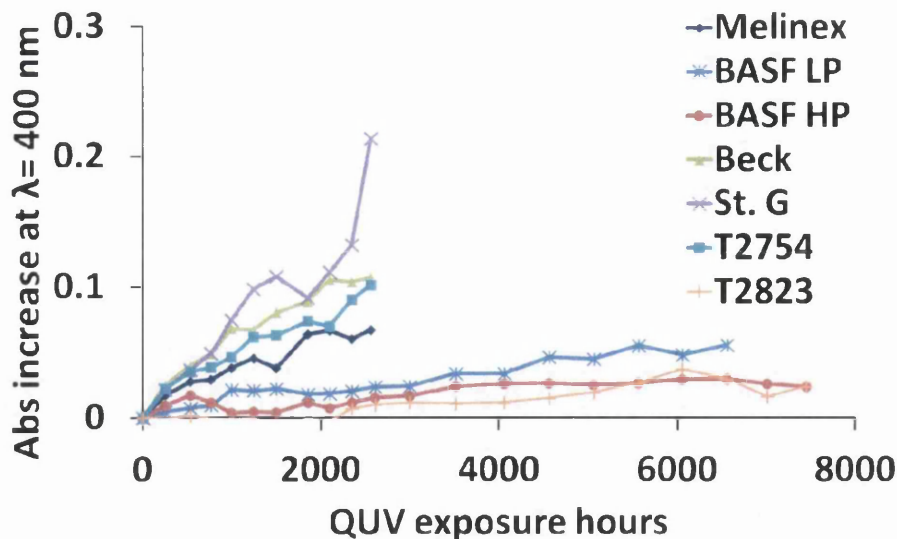


Figure 8.18 Increase in absorbance at 400 nm of the samples shown. Irradiation of some samples was stopped at 2562 hours due to the poor physical condition of the samples

The Melinex coated with the Beckers lacquer also has an increased Abs at 400 nm compared to uncoated Melinex. This is, at first, puzzling as the Beckers lacquer is supposed to be a UV-screening automotive topcoat. This evidence plus the that seen in figure 8.2, which shows no additional UV protection offered by the lacquer, strongly suggests that the author was either given the wrong formulation by Beckers or that the right formulation was given but without any UV absorbers. If this is true then what is seen in Figure 8.18, where the Beckers coated film appears to degrade more than the uncoated film, is in effect the photodegradation of a polymer film coated with another polymer film, with no additional UV protection. This would mean a greater mass of polymer undergoing photodegradation than just the uncoated film by itself which would therefore give an increase in absorbance at 400 nm compared to that given by the uncoated film.

8.3.4 FTIR spectroscopy

When PET is exposed to UV light and in the presence of oxygen (in air), it undergoes a number of photo-oxidative reactions which eventually lead to the formation of carboxyl end-groups (Figure 8.19) [4]. Because of this, it would be expected that the FTIR spectra of

PET should see an increase in the carbonyl peak at 1720cm^{-1} and peak broadening at 4000cm^{-1} to 2500cm^{-1} due to the presence of hydroxyl groups.

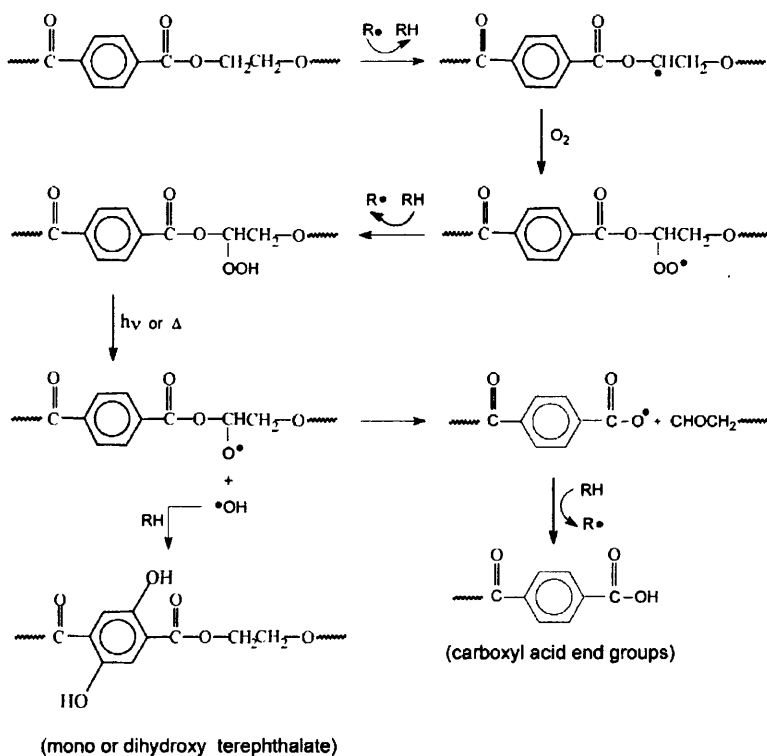


Figure 8.19 Photo-oxidative reactions undergone by PET during UV exposure leading to carboxyl and hydroxyl end-groups [4].

All samples were analysed with an FTIR spectrophotometer at 250 – 500 hour intervals. Figure 8.20 below shows how the spectrum of Melinex ST505 changes over time. It can be seen that the peaks seen from 4000cm^{-1} to 2500cm^{-1} broaden over time. Unfortunately the films are too thick for a through transmission measurement and the IR absorbance at 1720cm^{-1} is too strong to see any change in the carbonyl peak at 1720cm^{-1} .

As FTIR gives information on the fundamental chemistry of the substance being analysed, it is to be expected that the spectra of unstable samples should change after UV irradiation due to photodegradation changing their chemistry. Those samples which are more stable under UV light should see little change in their spectra. Indeed this was the case seen when looking at the FTIR spectra shown in figure 8.21 below. The samples which show the least

yellowing when measured with UV-Vis are also the samples that show the least changes to their FTIR spectra.

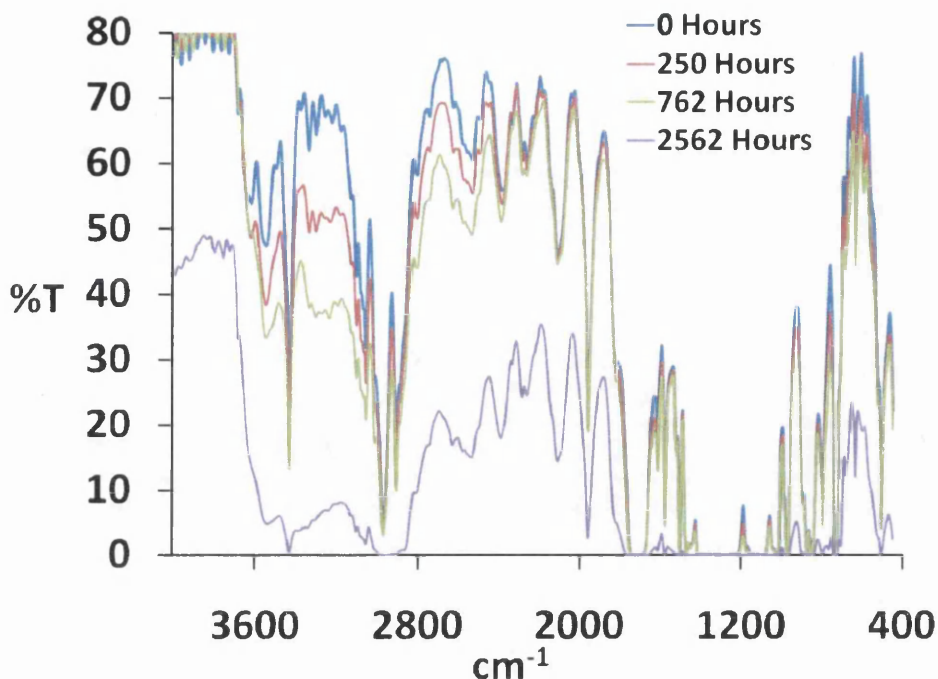


Figure 8.20 Overlaid FTIR spectra of Melinex ST505 taken over the exposure period during QUV accelerated weathering

Some the samples in this trial have already been ruled out of being used as a DSC topsheet material due to the evidence already seen from UV-Vis spectroscopy which is backed up here in figure 8.21. The samples which have shown the greatest physical damage due to irradiation are also the samples whose FTIR spectra has experienced the most peak broadening in the region of 4000 – 2500cm⁻¹. Two of the samples stand out in that they suffer very little from peak broadening in this region, these are also the samples which appear to have suffered no physical affects from irradiation. The samples are: Melinex ST505 coated with BASF HP and the Icosolar T2823 film.

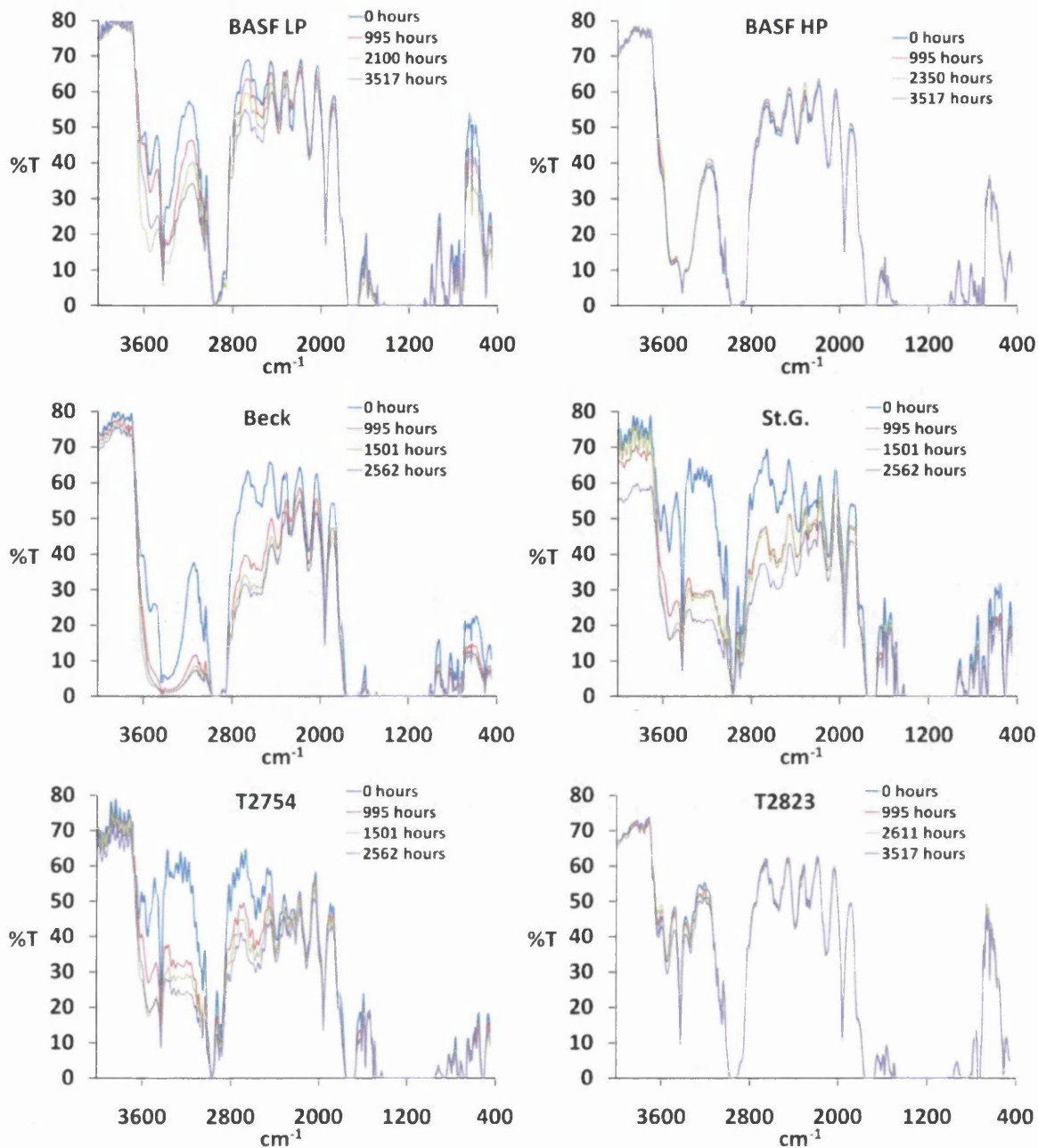


Figure 8.21 Changes to the FTIR spectra of samples undergoing QUV accelerated weathering over the exposure periods shown

The above results show the FTIR spectra taken at around 0 - 3500 hours QUV weathering. The best films were actually irradiated further until around 8000 hours. Figure 8.22 below compares the best films from 0 hours to the time shown.

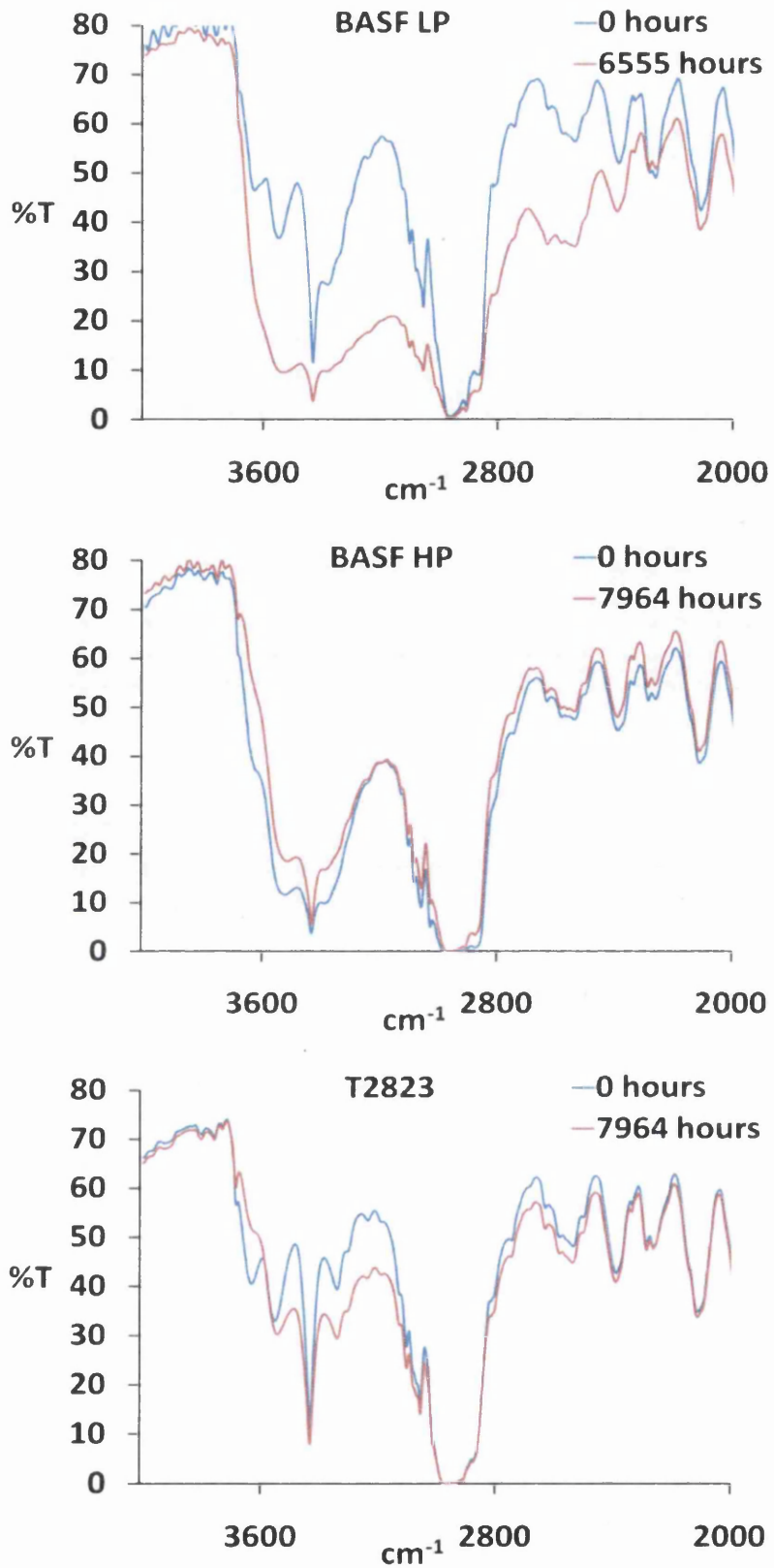


Figure 8.22 Changes to the FTIR spectra (4000 cm^{-1} to 2000 cm^{-1}) of the best performing samples over the QUV exposure periods shown

Figure 8.22 shows that the FTIR spectra of the BASF LP samples had, by 6555 Hours QUV weathering, suffered peak broadening similar to that seen in the worst performing samples. This suggests that the BASF LP sample had undergone significant photodegradation. This was backed up by physical evidence as by 6555 hours the samples were heavily embrittled and mechanically weak. Strangely the FTIR spectra of the BASF HP show a slight narrowing of the broad band centred around 3430cm^{-1} . This band is probably due to N-H stretching in the polyurethane lacquer. The reduction of this peak could be due to degradation of the polyurethane topcoat instead of the PET film as degradation of PET would cause the peak broadening seen in Figure 8.20. Looking at the T2823 sample, peak broadening is observed suggesting a degree of photodegradation although not as severe as that seen in the BASF LP sample. One feature of note is the complete disappearance of the band at 3633cm^{-1} . This maybe an O-H stretching a band and its disappearance was at first puzzling. When looking back at the data however, the intensity of this band increases and decreases over time. Bands at around 3630cm^{-1} are consistent with hydrogen bonded water molecules, so the size of the band could be due to how wet the sample is when tested. The QUV process has both a wet and dry cycle. It may be possible that when the measurements were taken when the sample was on a just after a wet cycle the band at 3633cm^{-1} may have been larger and when the measurement was taken after or during a dry cycle the band 3633cm^{-1} at may have been smaller. Unfortunately there is no way of telling from the data which cycle the sample was on when the measurements were taken.

8.3.5 ATR-FTIR Spectroscopy

After around 2500 hours into the QUV accelerated weathering testing an ATR reflectance accessory became available for the FTIR spectrophotometer. ATR spectra were taken of un-irradiated reference samples from this chapter, of samples that ceased being irradiated at 2562 hours QUV and of the samples that continued to be irradiated after 2562 hours. Only having two values, i.e. irradiated and not irradiated for the samples that were stopped at 2562 hours QUV, a pattern is at first hard to see. For this reason each sample shall be analysed individually.

8.3.5.1 Uncoated Melinex ST505 (PET)

In figure 8.20 (the FTIR %T spectrum of Melinex ST505) it can be seen that absorption bands in the fingerprint region of the spectrum are far too strong to be able to get any detail, this is in part, due to the fact that the films are too thick to take through film %T measurements. ATR-FTIR being a reflectance technique only analyses the surface of a sample and so the strength of the absorption bands is not determined by sample thickness. Figure 8.23 shows the ATR spectra of Melinex ST505 which hasn't been exposed to UV irradiation. Table 8.1 outlines some of the absorption bands in the fingerprint region.

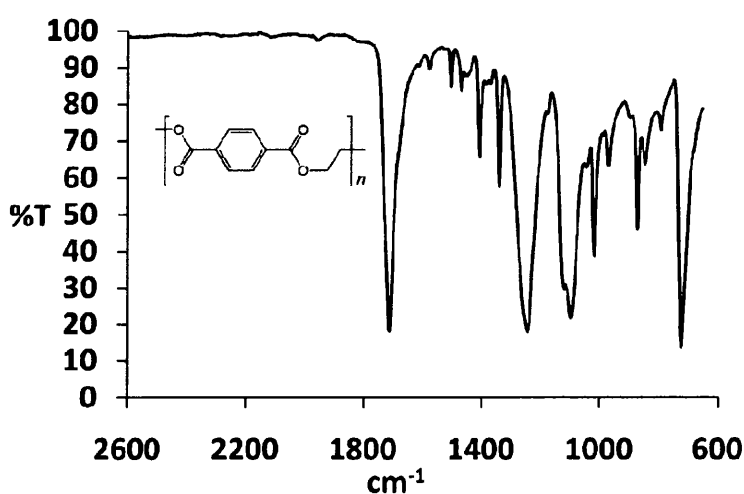


Figure 8.23 ATR-FTIR spectrum of unexposed Melinex ST505 showing close up of the fingerprint region, a PET monomer is shown inset

Figure 8.24 shows the ATR spectra of the unirradiated Melinex overlain with that of the same sample that has received 2562 hours total QUV exposure. Like the through film measurements there is peak broadening observed in the region, 4000 – 2500cm⁻¹. Looking at the finger print region, all the peaks have reduced in intensity; this is in contrast to some photodegradation studies which use the increase in the carbonyl peak at around 1720cm⁻¹ to quantify photodegradation. There are however studies that have returned similar results to those seen in Figure 8.24 when ATR-FTIR is used to observe photodegradation of PET [5]. Of the most noticeable changes between the spectra, is the decrease in absorbance at the positions close to major PET absorbance bands (Table 8.1). The C=O stretch at about 1720 cm⁻¹; the ring in plane deformation at 1410 cm⁻¹; the -CH₂- wagging at 1340 cm⁻¹; the ring and ester modes at 1300–1000 cm⁻¹; and the ring C-H + C=O out of plane bending at 724

cm^{-1} all reduce in size after the film has been irradiated. The decreases in the absorption bands in the fingerprint region for the PET functional groups strongly suggest there is a large breakdown in the chemical structure of the polymer through processes such as chain scission. The peak broadening at around 3000cm^{-1} suggests that high concentrations of carboxylic acids are being formed from the breakdown products.

Table 8.1 **The absorption bands of PET in the fingerprint region**

| Wavenumber (cm^{-1}) | Corresponding PET band |
|---------------------------------|--|
| 1716 | C=O stretch |
| 1410 | Ring in-plane deformation of benzene ring |
| 1342 | CH_2 wagging (<i>trans</i>) |
| 1246 | Ring-ester in-plane mode |
| 1122 | Ring-ester in-plane mode |
| 1099 | Symmetric glycol C–O stretch (<i>gauche</i>) |
| 1019 | Ring C–H in-plane deformation |
| 975 | O- CH_2 stretch |
| 724 | Ring C–H + C=O out-of-plane deformation |

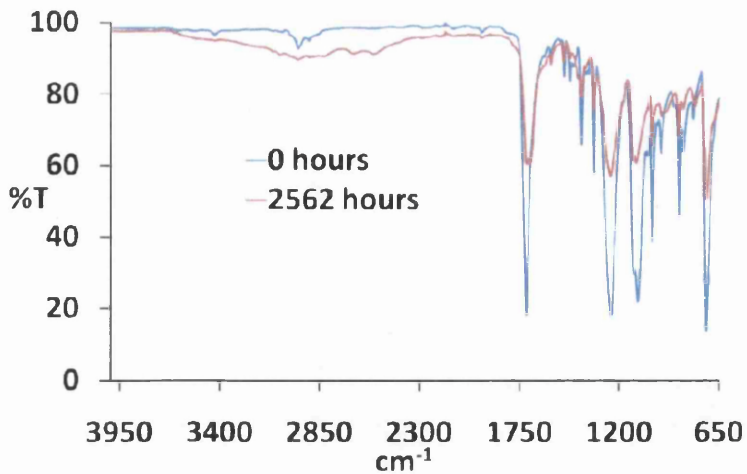


Figure 8.24 Overlain spectra of Melinex ST505, unirradiated (blue) and after 2563 hours QUV (red)

8.3.5.2 ATR spectra of BASF LP and BASF HP Lacquers at 3517 Hours QUV

Figures 8.25 and Figures 8.26 show the overlain spectra of BASF LP and BASF HP respectively. Unlike the spectra of the Melinex which is typical of PET. The reflectance spectra for these two samples are typical of that of polyurethane. This shows that ATR-FTIR only collects the IR spectra of the surface of the film.

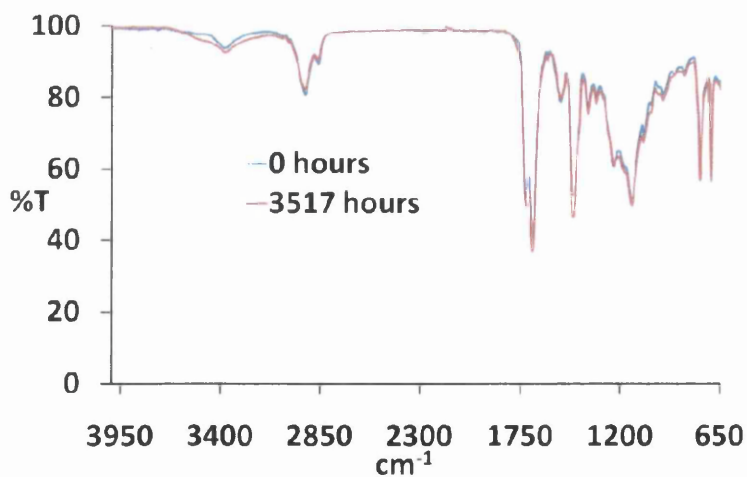


Figure 8.25 FTIR-ATR spectra of BASF LP at 0 hours (blue) and 3517 hours irradiation (red)

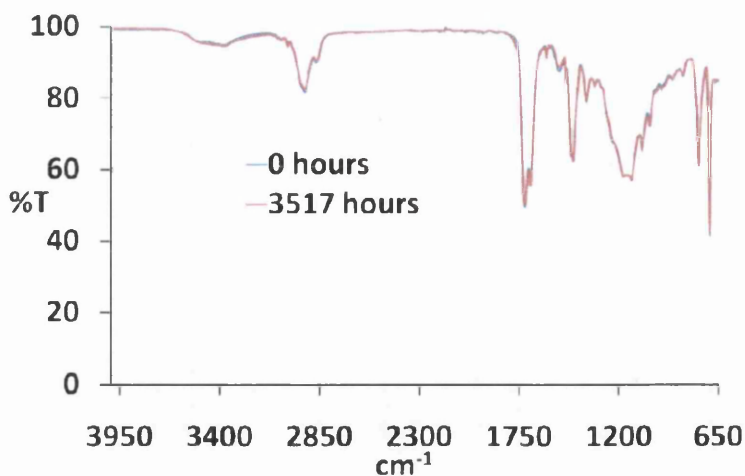


Figure 8.26 FTIR-ATR spectra of BASF HP at 0 hours (blue) and 3517 hours irradiation (red)

The main features of the above spectra are: a N-H stretch at 3370cm^{-1} , a C-H₂ asymmetric stretch at 2940cm^{-1} , C-H₂ stretching at 2870cm^{-1} , a C=O stretch at 1725cm^{-1} , a vibrational band at 1691cm^{-1} which is characteristic of the NH-(C=O)-NH of polyurethane and a C-H stretch at 1460cm^{-1} . The broad band between 1300cm^{-1} and 1100cm^{-1} could be due to an ester linkage. The peak at 760cm^{-1} could be due to C-H rocking and the band at 702cm^{-1} could be due to a styrenated polyol.

It has been shown [6] that when polyurethane degrades, there are band reductions at 1680cm^{-1} and 1720cm^{-1} and that there should be reductions of both 1460cm^{-1} and 1230cm^{-1} vibrational bands. The study also shows that photodegradation of polyurethane causes the appearance of broader N-H bands at 3370cm^{-1} . Looking at figures 8.25 and 8.26 it is quite clear that there are no signs of major degradation of the polyurethane lacquer by 3517 hours total QUV exposure, although there is a slight broadening of the N-H peak in the BASF LP. This suggests that both the BASF LP and the BASF HP lacquers are extremely stable to UV photodegradation with the BASF high performance lacquer living up to its name and being the higher performing lacquer.

Further irradiation of these samples was undertaken and the ATR spectra were measured. Figure 8.27 shows the overlain spectra of the BASF LP sample at 0 hours and 6053 hours QUV. Figure 8.28 shows the overlain spectra of BASF HP at 0 hours and 7964 hours QUV.

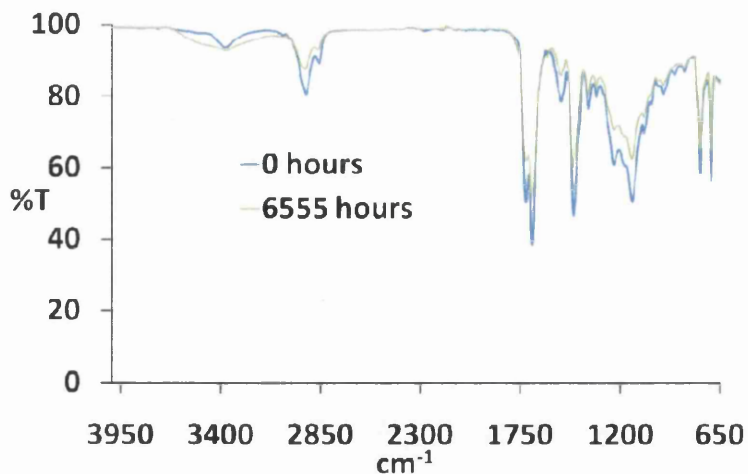


Figure 8.27 FTIR-ATR spectra of BASF LP at 0 hours (blue) and 6053 hours irradiation (green)

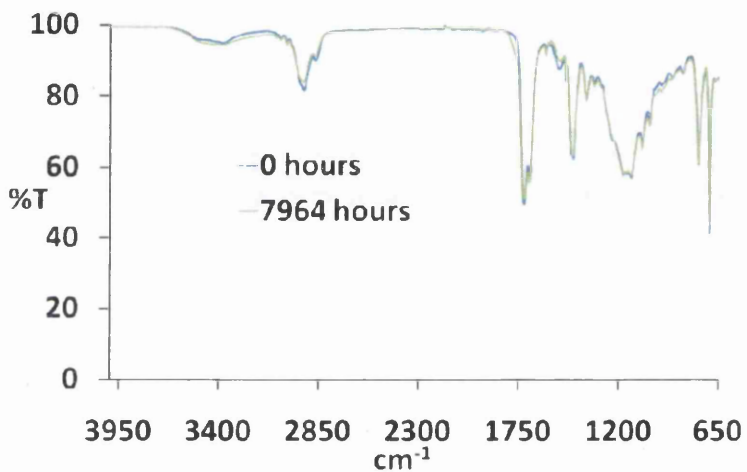


Figure 8.28 FTIR-ATR spectra of BASF HP at 0 hours (blue) and 7964 hours irradiation (green)

When looking at Figure 8.27 it is clear that the BASF LP sample has undergone photodegradation. The reduction in the bands show in [6] have clearly taken place along with broadening of the peak at 3370cm^{-1} . In Figure 8.28 there is little reduction of the bands in the fingerprint region, a very small reduction of the C-H₂ bands at around 2900cm^{-1} and a very slight broadening at around 3370cm^{-1} . This strongly suggests that the BASF HP lacquer is extremely stable under QUV accelerated weathering conditions.

8.3.5.3 ATR spectra of Melinex (PET) Coated with the Beckers Lacquer

Figure 8.29 shows the overlain spectra of the Melinex coated with the Becker Lacquer, before irradiation and after 2562 hours irradiation. These spectra show changes due to photodegradation which match those found in [6]. Figure 8.29 shows that this sample has undergone considerable photodegradation compared to the BASF lacquers, especially when considering the exposure period.

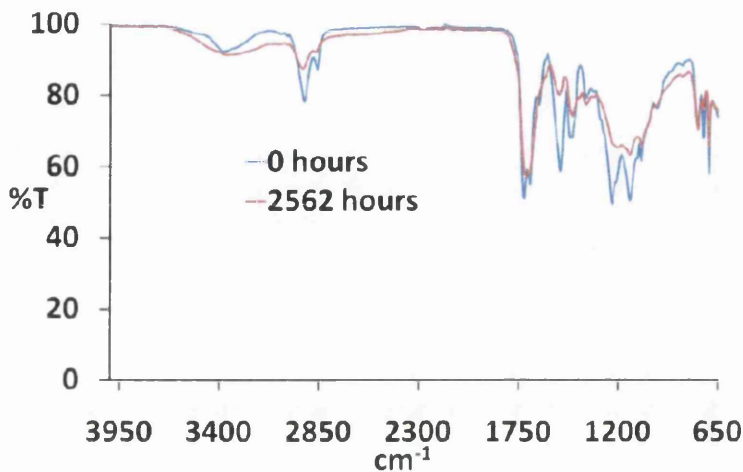


Figure 8.29 ATR spectra of Melinex coated with the Beckers lacquer at 0 hours and 2562 hours QUV exposure

8.3.5.4 ATR spectra of T2754 and St Gobain Co-laminates

The Icosolar film T2754 and the St. Gobain film are both ETFE films. Figure 8.30 shows the ATR spectra of the Icosolar film T2754 laminated to the Melinex. Figure 8.31 shows the ATR spectra of the St. Gobain film (St. G) laminated to the Melinex. As ATR is a reflectance measurement all that is seen is the spectra of the ETFE film. The main absorption bands to take note of are: the weak band due to the CH₂ asymmetric stretching vibration at 2976 cm⁻¹, and the sharp band at 1454 cm⁻¹ representing the CH deformation. The strong bands in the region 1000–1300 cm⁻¹ are characteristics of CF₂ groups. Except for some small peak broadening around 3000 cm⁻¹ and the evolution of a carbonyl peak at 1720 cm⁻¹, there appears to be little sign of photodegradation when looking at the fingerprint region. This is because ETFE does not absorb very well in the UV region (figure 8.32), so UV photons

cannot cause much damage to its polymeric structure. So whilst not being susceptible to UV damage, ETFE offers no protection to the underlying PET. Thus the evidence of photodegradation seen in the T2754/Melinex and the St. G/Melinex co-laminates must be purely caused by degradation of the underlying PET. The increased degradation seen in these samples when compared to ordinary PET is probably due therefore to air and moisture being trapped between the laminates this could increase the rate of photodegradation and give the result of the ETFE/PET co-laminates having an increased yellowness index compared to uncoated PET.

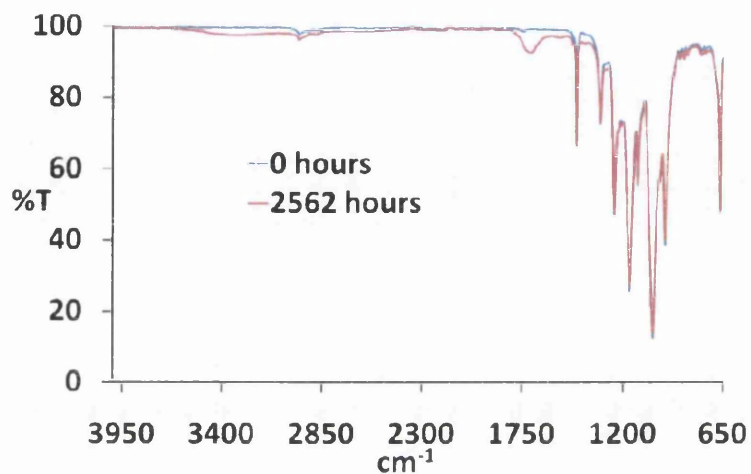


Figure 8.30 ATR spectra of T2754/Melinex co-laminate at 0 hours and at 2562 hours QUV exposure

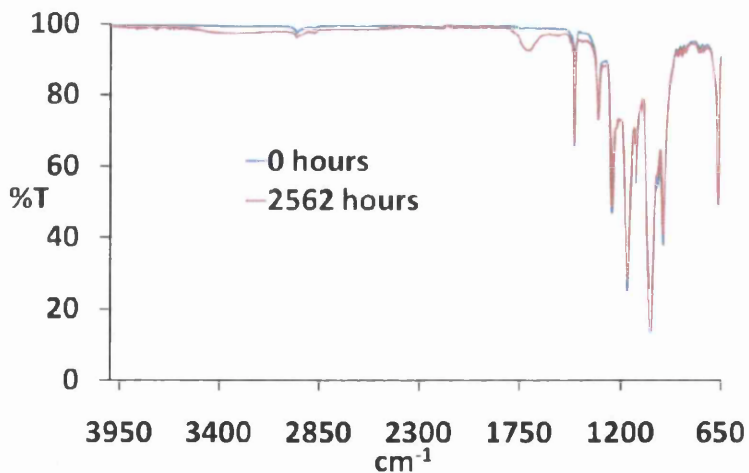


Figure 8.31 ATR spectra of St Gobain/Melinex co-laminate at 0 hours and at 2562 hours QUV exposure

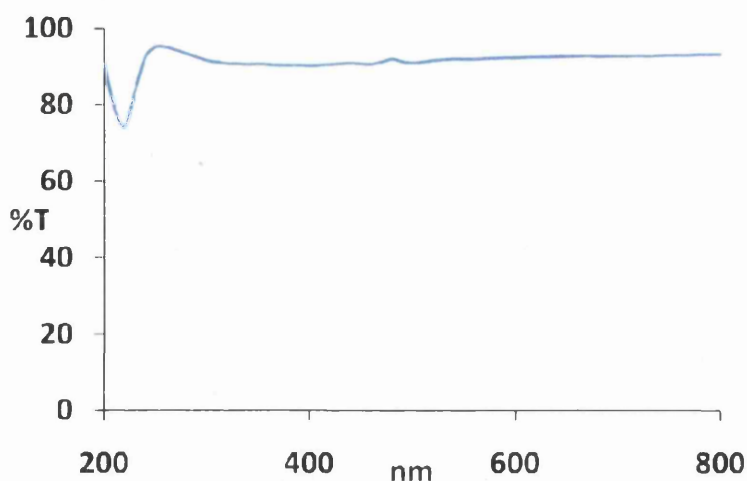


Figure 8.32 UV-VIS spectra of T2754 (ETFE film only) showing very little absorbance in the UV

8.3.5.5 ATR spectra of Icosolar T2823

Icosolar's T2823 film is a co-laminate of PET and PVF. ATR spectra of the front sheet (PVF) show a C-H stretch at 2934cm^{-1} . The two broad peaks between 1000cm^{-1} and 1100cm^{-1} are due to the C-F stretch. The peak at 825cm^{-1} is due to CH_2 rocking. At 3517 hours QUV (figure 8.33), T2823 appears to undergo little photodegradation if looking at the fingerprint region and there is no sign of any peak broadening around 3000cm^{-1} which has been seen in other polymer films. The only sign of degradation is a small increase in the carbonyl peak at 1725cm^{-1} . When the T2823 sample is subjected to further QUV, a slight increase is seen in the bands in the fingerprint region as well as a slight increase in the band around 2950cm^{-1} . This is inconsistent with the degradation seen in the other samples in this section whereby chain scission reduces the intensity of the bands in the fingerprint region. Oreski and Wallner [7] have shown that thermal degradation produces the appearance of a broad band between 1700cm^{-1} and 1500cm^{-1} . This is not observed in the T2823 sample. The only sign of degradation in the ATR spectra of T2823 is the appearance of the carbonyl peak at 1740cm^{-1} , indeed this peak increases in Abs from 0.0101 (at 3517 hours) to 0.0162 (at 7964 hours) showing that there is some continuing degradation occurring.

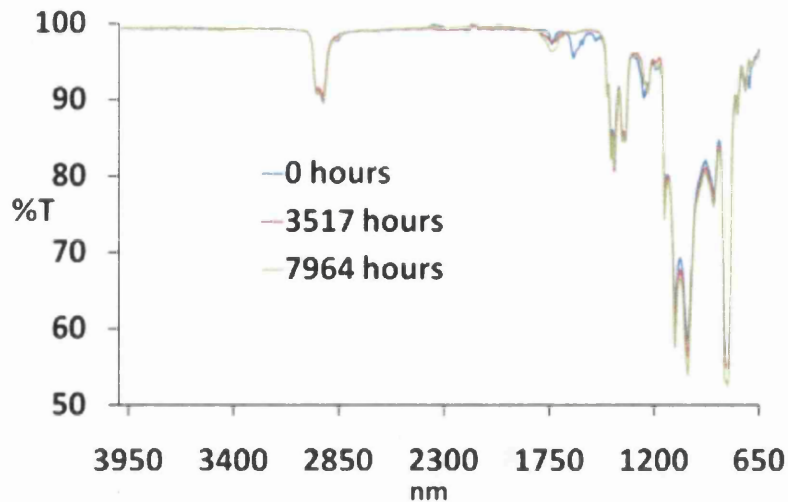


Figure 8.33 ATR spectra of T2823 film at 0 hours (blue), 3517 hours (red) and 7964 hours (green).

8.4 Conclusions of Work on Original Film Samples

Of the samples tested so far, two stand out as being candidates for DSC module encapsulation. These are: PET coated with BASF HP and the Icosolar T2823 film. These two samples have been shown to be exceptionally stable under UV irradiation with all three achieving around 8000 hours of QUV and showing only small signs of photodegradation. Mechanically, the BASF HP sample is showing slight signs of embrittlement and the T2823 still appears mechanically sound. It is worth pointing out that the grade of Melinex used, ST505, is for indoor applications meaning that both BASF lacquers have been very effective in protecting the underlying PET, however the BASF LP lacquer did not perform as well as the BASF HP lacquer and the sample was withdrawn from QUV testing due to mechanical failure at around 6500 hours.

The advantages of using the T2823 film over the BASF HP sample is that it is a complete film that would not need any further treatment. Current collectors could be printed onto the underside (PET) and the film could then be applied directly to the module. The major disadvantage is that T2823 is expensive. PET coated with the BASF HP would be much cheaper and has the added advantage that the lacquer can post applied to individual

modules. This could offer a true encapsulation in that the lacquer would not just coat the upper surface, but encapsulate around the module edge.

8.5 UV Cured Lacquers from Bayer

Samples of Melinex ST505 were sent to Bayer Materials Science in Germany to be coated with their UV cured “Desmolux” polyurethane clearcoat. The samples sent back were coated with two experimental variations of the Desmolux coated at 20 μm , 40 μm and 60 μm . One of the variations is designated FWO 5754-01 and the other designated FWO 5754-02. The only difference between the two is that FWO 5754-02 contains an isocyanate urethane acrylate. This additive is used to affect NCO cross linking in shadow areas. Shadow areas are a problem when radiation curing of three dimensional parts. Radiation curing is a ‘line of sight’ technique and so there may be areas of the part which may be in shadow with respect to the radiation source. Urethane acrylates containing reactive NCO groups can give crosslinking in geometrically unfavourable areas.

8.5.1 Action of the Lacquers

No free films were obtained as the samples were coated in Germany but the transmission spectra of the coated films can give some insight into the action of the lacquer. The %T curves of the Bayer lacquer is shown above in figure 8.3 and it is clear that the Bayer lacquer, even at 60 μm does not offer as much UV screening as the BASF HP lacquer, having a ‘cut off point’ further into the UV region.

Figure 8.3 shows that the UV screening of the Bayer lacquers is not as effective compared to the BASF HP lacquer. It should not be however, ruled out immediately as it would be beneficial to see how the Bayer-lacquered films behave upon irradiation compared to the BASF lacquered films.

8.5.2 Yellowness Index of the Bayer Lacquers

Figure 8.34 shows the increases in absorbance at 400 nm of the samples of PET coated with the Bayer UV cured lacquers. It is quite clear that the lacquered PET films have performed better than the unmodified PET. Figure 8.34 also shows there is a marked difference between the FWO-5754-01 and the FWO-5754-02 samples, with the “-02” samples all performing better. This is probably due to the NCO cross linking agent present in the “-02” formulation promoting greater cross-linking and increasing UV photodegradation resistance. The best performing samples are the FWO-5754-02 samples coated at 40 μm and 60 μm and it would be helpful if these were compared to the BASF lacquers. Figure 8.35 shows FWO-5754-01 (40 μm) and FWO-5754-02 (40 μm and 60 μm) compared to the BASF lacquers.

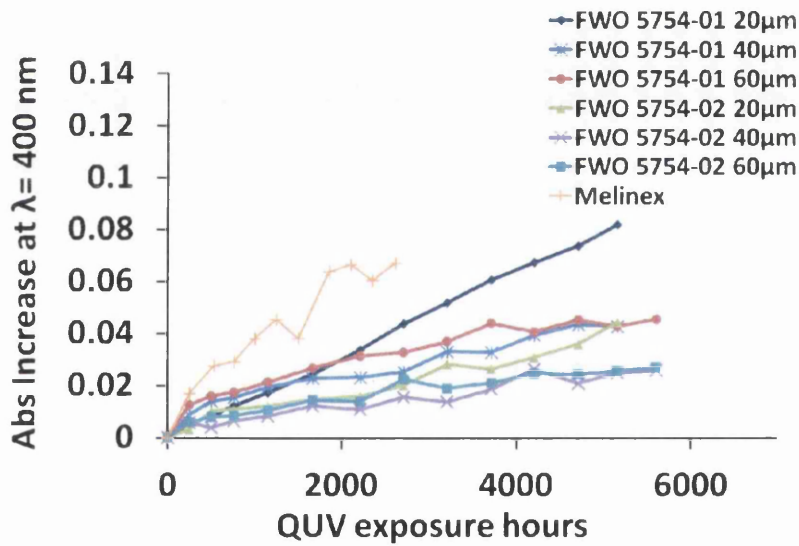
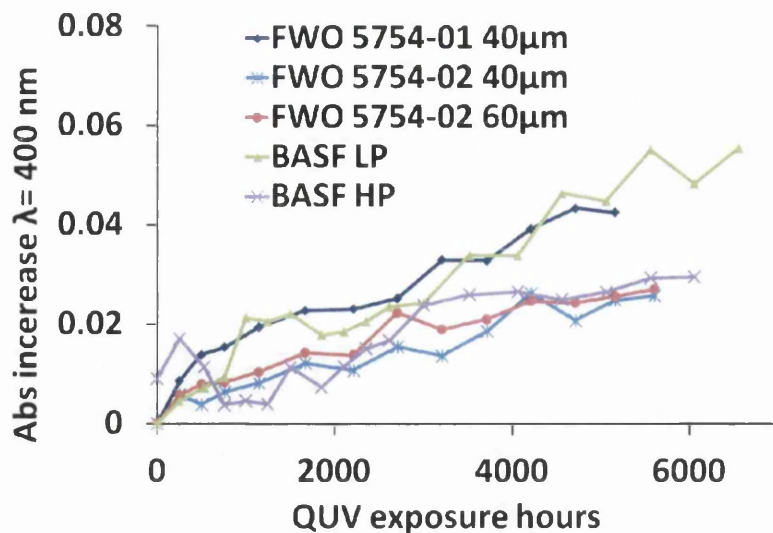


Figure 8.34 Increase in abs at 400 nm of the Bayer lacquered samples



8.35 The best performing Bayer lacquers compared to the BASF lacquers

Figure 8.35 above shows that the FWO 5754-01 (40 μm) has a comparable performance to that of the BASF LP lacquer and that the FWO 5754-02 (both 40 μm and 60 μm) have a comparable performance to the BASF HP. It should be noted however that the BASF lacquers were coated at 20 μm and that a thicker coating of the Bayer lacquer is needed to match its performance. It should also be noted that whilst the Bayer lacquer match the BASF lacquers in performance, it is only with respect to protecting the PET film from photodegradation. It has already been seen in this section that the UV cut-off properties of the Bayer lacquers cannot match that of the BASF lacquers.

8.5.3 FTIR Spectroscopy

Figure 8.36 shows the overlain spectra of samples FWO 5754-01 and FWO 5754-02, the latter containing the NCO cross-linking additive, both coated at 20 μm. The spectra are very alike except some obvious peak broadening. One point in which the spectra are different is the peak at 2265cm^{-1} which is much larger for FWO 5754-02 than for FWO 5754-01. This peak is associated with isocyanate groups and so the absorbance of FWO 5754-02 at 2265cm^{-1} is greater due to the addition of the NCO cross-linking additive.

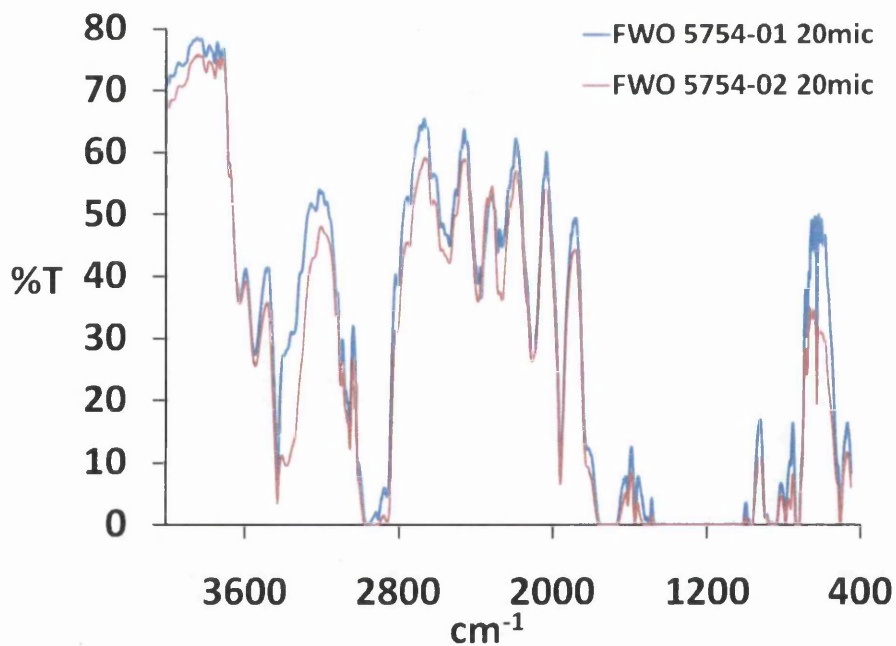


Figure 8.36 FTIR spectra of samples FWO 5754-01 (blue) and FWO 5754-02 (red)

Figure 8.37 and figure 8.38 show the FTIR absorbance spectra of FWO 5754-01 and FWO 5745-02 respectively, both coated at 20 μm , from 0 hours to 5105 hours QUV. It could be argued that the level of peak broadening in the “-02” sample is less than that seen in the “-01” this would be consistent with evidence seen from the yellowness index and further suggests that the NCO cross linking agent in the -02 formulation gives a significant improvement in performance. The pattern seen in the difference in degrees of peak broadening between the -01 and the -02 formulation is repeated at the heavier coating weights. The degree of peak broadening is lessened somewhat in both formulations as the higher coating weights give increased protection against UV photodegradation.

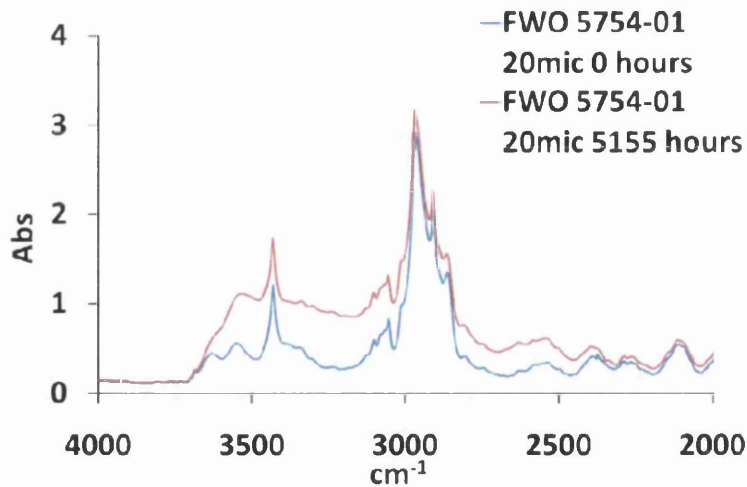


Figure 8.37 FTIR absorbance spectra of FWO 5754-01 (20 μm) from 0 hours to 5105 hours QUV

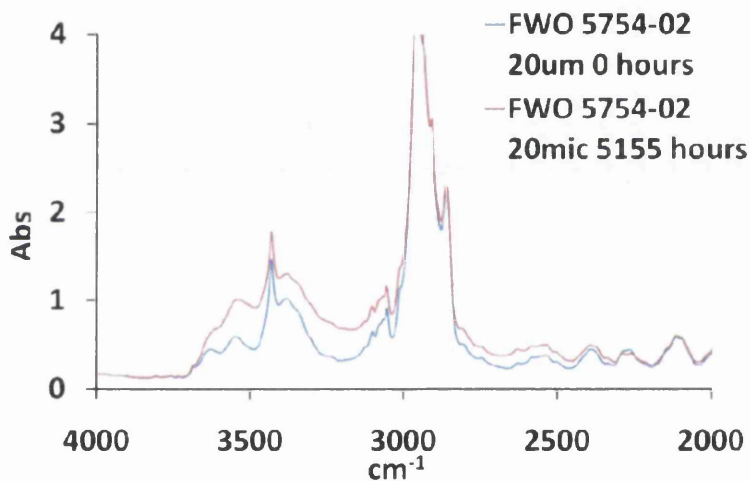


Figure 8.38 FTIR absorbance spectra of FWO 5754-02 (20 μm) from 0 hours to 5105 hours QUV

8.5.4 Disappearance of the NCO Cross Linker Peak at 2265cm^{-1}

Figure 8.39 shows the spectra of FWO 5754-02 at 0 hours and 250 hours QUV and it can be seen that there is a shortening of the isocyanate peak at 2265cm^{-1} . This is due to free NCO groups present in the coating after UV curing. According to Bayer, these free NCO groups then react with moisture to give further crosslinking. This means that that the NCO additive transforms the UV cured coating into a dual cure coating, whereby the initial cure is

initiated through UV irradiation and photoinitiators. A second curing step then occurs when the NCO groups react with moisture to initiate curing in shadow areas. The change in the spectra seen in figure 8.39 is representative of all 5754-02 samples.

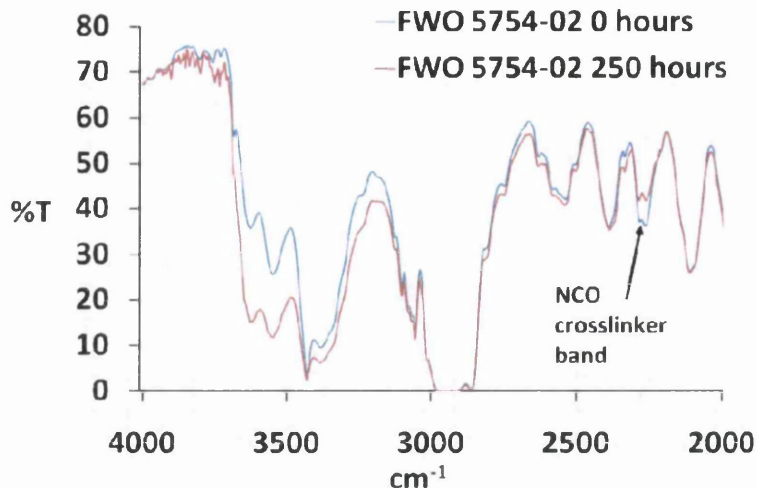


Figure 8.39 Spectra of FWO 5754-02 (20 μm) from 0 hours to 250 hours QUV showing the reduction of the NCO peak

8.5.5 ATR Spectroscopy of Bayer UV Cured Lacquers

Figure 8.40 shows the ATR spectra of FWO 5754-01 (20 μm) at 0 hours, 3709 hours and 5105 hours QUV. There is some peak broadening around the area of the N-H stretch at 3360 cm^{-1} from 0 to 3709 hours with the band then decreasing in intensity at 5105 hours. There are decreases in all the major bands in the fingerprint region which is typical of the photodegradation seen in polyurethane topcoats. Figure 8.41 shows the ATR spectra of FWO 5754-02 (20 μm) at 0 hours, 3709 hours and 5105 hours. The pattern is the same as above and there seems to be no difference in performance between the -01 and -02 coatings. This is in contrast to the evidence seen in UV-Vis and %T FTIR measurements where there is a clear difference in performance between the -01 and -02 formulations. This may be because the extent of photodegradation of these two samples may be similar at the surface of the coating where the ATR takes its measurement but in the whole film, where the UV-Vis and FTIR through %T measurements are taken, PET with the -02 formulation outperforms the PET with the -01 formulation. All the other Bayer samples

show a similar pattern of photodegradation in their ATR spectra with respect to their formulation and coating weight.

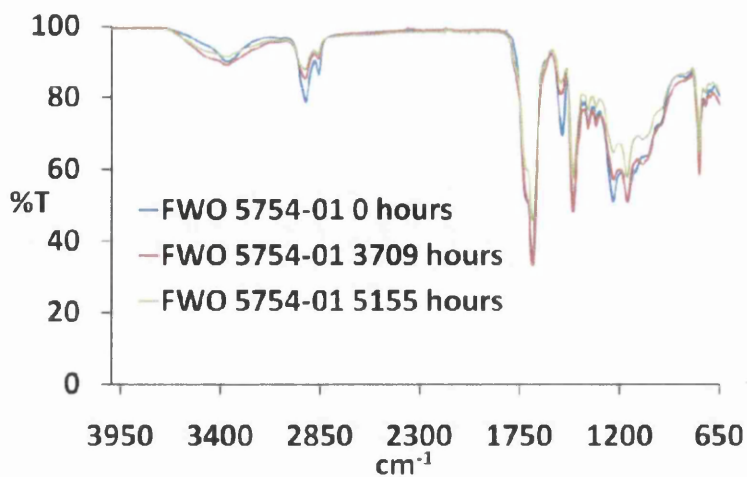


Figure 8.40 Spectra of FWO 5754-01 (20 μm) at 0 hours, 3709 hours and 5105 hours QUV

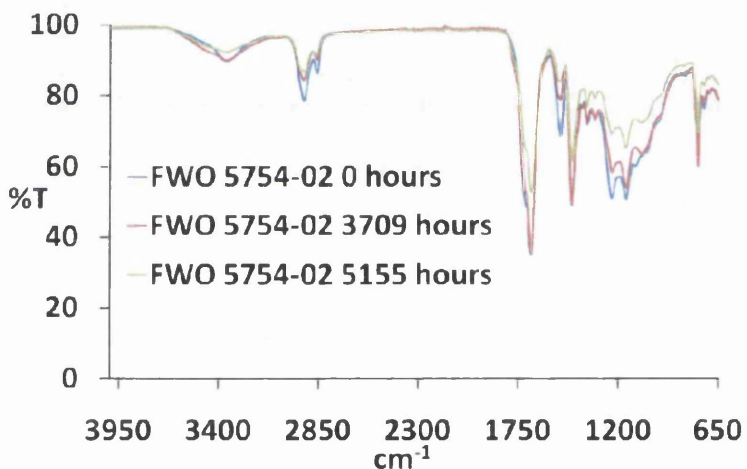


Figure 8.41 Spectra of FWO 5754-01 (20 μm) at 0 hours, 3709 hours and 5105 hours QUV

8.5.6 Conclusions to Work on Bayer UV Cured Clearcoats

Looking at the UV-Vis (yellowness index) data it could be argued that the Bayer formulation, FWO 5754-01 performs comparatively to BASF LP lacquer and that the formulation, FWO 5754-02 performs comparatively to the BASF HP lacquer. When looking at FTIR spectra however it appears that both Bayer formulations (at 5105 hours) have undergone a degree of photodegradation similar to that of the BASF LP lacquer at 6053

hours. It is only when looking at the ATR spectra of BASF HP at 0 and 7964 hours (figure 8.28) that it can be seen how stable the BASF HP coating is. The ATR spectra hardly changes despite the sample being subject almost 8000 hours QUV. Mechanically the Bayer formulation samples became embrittled much faster than the BASF samples.

Overall the Bayer formulations do very well at protecting the PET from photodegradation, however their performance cannot match that of the BASF HP lacquer. There is also the problem of the position of their UV cut which cannot match that of the BASF HP lacquer and so even though UV cured coatings could vastly increase the throughput of a coil coated DSC module the Bayer formulations cannot be considered as candidates.

8.6 PET vs. PEN as the Topsheet Material

Figures 8.42 shows the UV-Vis Absorbance spectra of PET and PEN and from these spectra, some predictions about the films' respective behaviours upon exposure to UV irradiation can be made. It is at first difficult to say which film absorbs more strongly in the UV as although PET absorbs at double the intensity of PEN, PEN absorbs a wider range of photons between 200 nm and 400 nm. However, given that PET absorbs more intensely of higher energy photons it is likely that PET might be more susceptible to UV photodegradation given similar exposure conditions.

Figure 8.43 shows the emission spectra of a QUV-A lamp such as those used in this project. The QUV-A lamps emit light from around 300 nm to 400 nm with a λ max emission at around 340 nm. If this is then compared to the Abs spectra of PET and PEN, it is clear that although the PET absorbs highly from 300 nm to 320 nm, it would be the PEN which will absorb the majority of the energy emitted by the QUV-A lamps and therefore would be expected to show a greater degree of photodegradation.

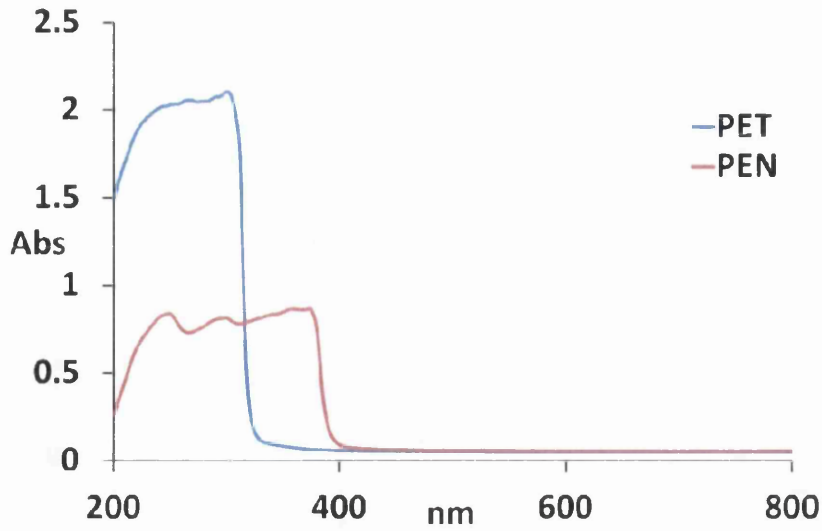
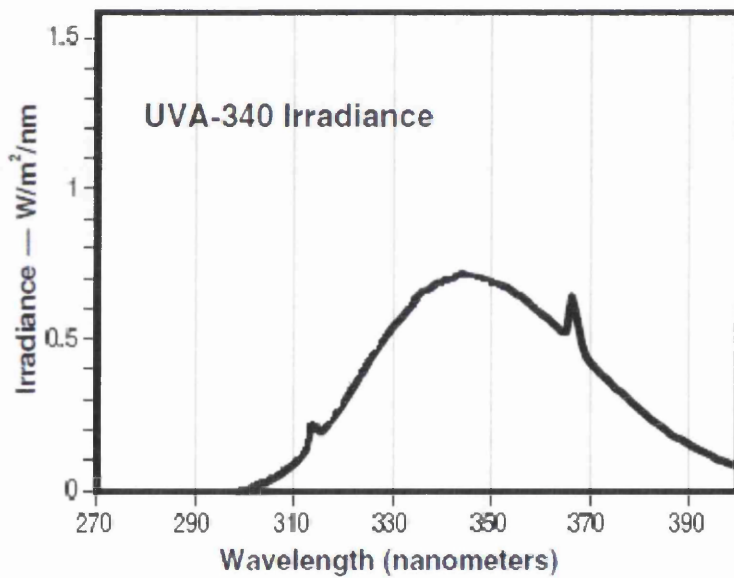


Figure 8.42 Overlain Abs spectra of PET and PEN



8.43 Emission spectra of a typical QUV-A lamp

8.6.1 PET vs. PEN – Yellowness Index

Much like PET, when PEN undergoes photodegradation a yellowing effect is observed. This is thought to be caused by the production of 2-naphthanoic acid. Schiers and Gardette have used this previously to compare rates of photodegradation in PET and PEN films [8]. Figure

8.44 shows the increasing yellowness index of PEN and of PET over the QUV exposure period. It is clear from this that PEN is showing a greater degree of photodegradation (in terms of the increase in Abs at 400 nm) compared to that of PET.

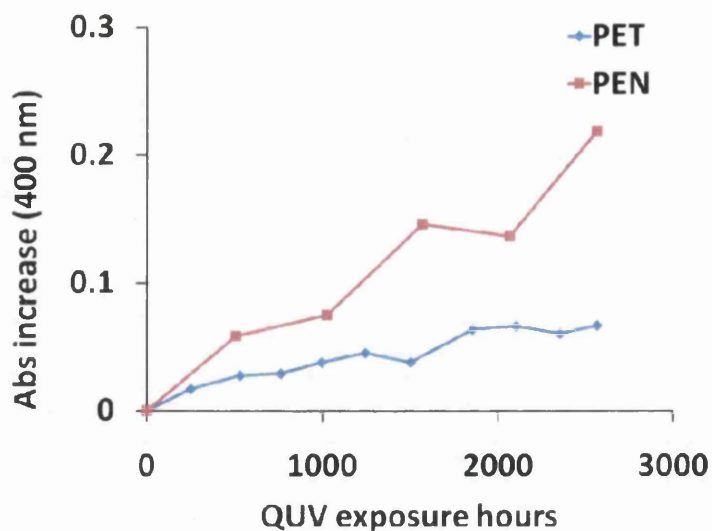


Figure 8.44 Yellowness index of both PET and PEN exposed to QUV-A

8.6.2 FTIR and ATR Analysis of PEN

The Infra Red spectra of the PET and PEN share some common features. However the exact wavenumber of the bands are often shifted due to the effect of the different chemical environment of the polymers. Figure 8.45 shows the structures of PET and PEN for reference. Figure 8.46 shows the %T spectra of PEN and PET film and figure 8.47 shows a close-up of the fingerprint region of the ATR spectra of the films. One thing to notice is that the presence of the naphthalene group in PEN shifts certain absorbances *cf.* PET. In PET, the band at 3431cm^{-1} is an overtone of the stretching vibration of the C=O bond. In the case of PEN this overtone is shifted by -15 wavenumbers to 3416cm^{-1} (Figure 4.43). PEN shows a strong band at 1580cm^{-1} whereas in PET it occurs at 1600cm^{-1} and is much weaker. The ring in-plane deformation seen in PET at 1410cm^{-1} is absent from PEN due to the presence of the naphthalene group. The ring-ester in plane-mode at 1246cm^{-1} is the same for both PET and PEN; however the band at 1122cm^{-1} , also ring-ester in plane-mode for PET, becomes a doublet, or possibly even a triplet for PEN. At 1020cm^{-1} , there occurs for PET, a band due to

a Ring C–H in-plane deformation which is absent from the spectra of PET. Lastly the ring C–H + C=O out-of-plane deformation has shifted in PEN to 762cm^{-1} from 724cm^{-1} where it occurs in PET [9].

Schiers and Gardette point out that care must be exercised in interpreting the spectral changes that occur in polyester films after irradiation since some of these originated from conformational and crystallinity changes as a result of the temperature of irradiation. For example, in PET the absorption at 974cm^{-1} has been attributed to the *trans* form of PET since rotation around the ethylene glycol linkages presents the possibility of two conformational isomers. The peak at 974cm^{-1} has been found to decrease with progressive UV exposure reflecting a conversion from the *trans* isomer to the *gauche* [8].

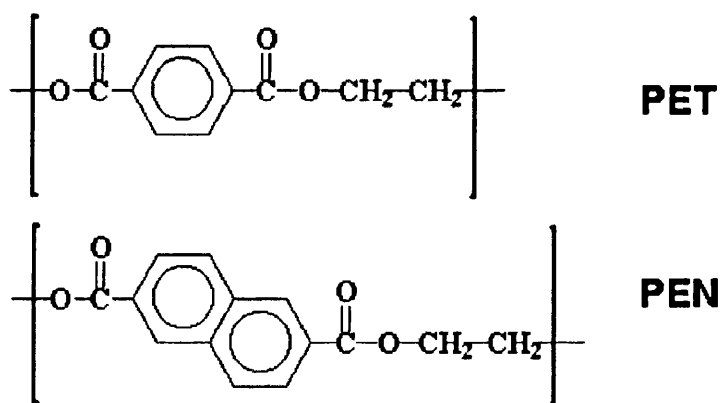


Figure 8.45 the molecular structures of PET and PEN monomers

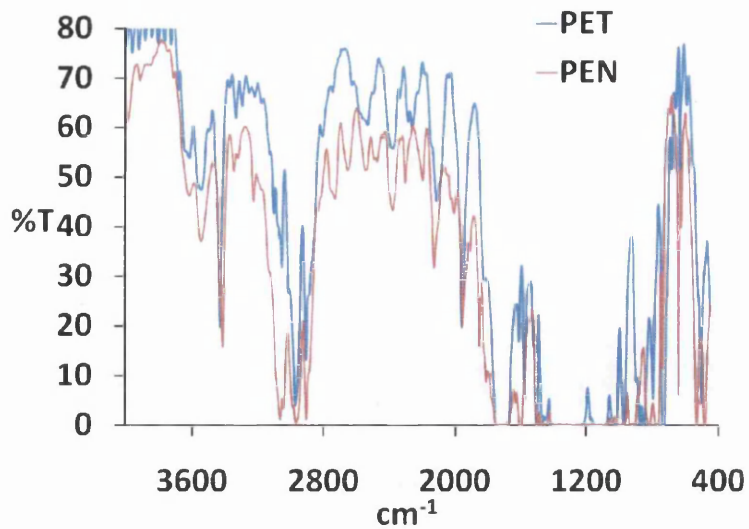


Figure 8.46 FTIR %T spectra of PET and PEN films

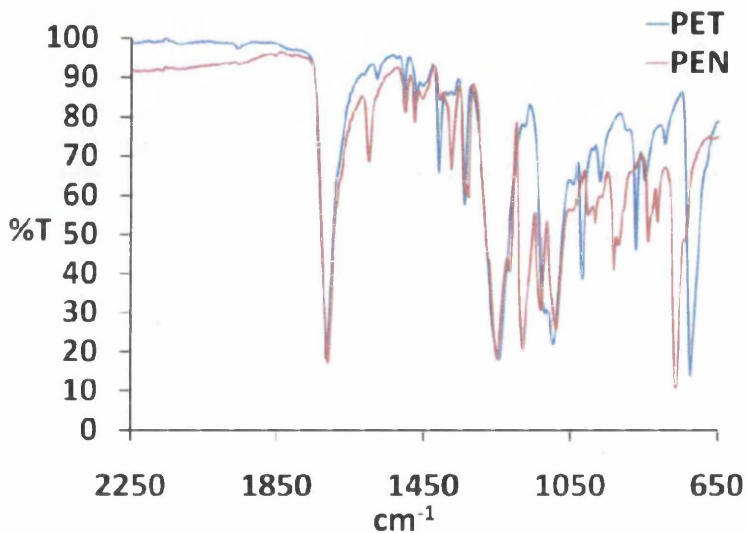


Figure 8.47 Close-up in the fingerprint region of the ATR spectra of PET and PEN films

8.6.3 Measuring Photodegradation of PEN with FTIR and ATR Spectroscopy

Figures 8.48 and 8.49 show respectively, the FTIR and ATR spectra of PEN, at 0 hours QUV and at 3065 hours QUV. The most striking observation to be made is that the through %T spectra of the PEN changes little whilst the ATR reflectance spectra displays signs of

photodegradation to a similar extent to, if not greater than, that seen in PET. This is at first could seem puzzling but an explanation could be that the photodegradation is only occurring at the surface of the film within the few microns that the ATR can penetrate. If the degradation was more severe at the surface of the film compared to that of the bulk film then it could be possible that the extreme band reduction seen in the fingerprint region of ATR spectra will be observed, whilst the through %T spectra shows little change. An explanation for this may be due to PEN's optical properties (figure 8.42), in that PEN absorbs most of the light emitted by the QUV-A lamp. It could therefore be possible that the surface of the PEN film absorbs all the UV light, undergoing photodegradation, whilst filtering out the UV light from the bulk of the film.

If this hypothesis were correct then at fist it may seem strange that photodegradation is observed using with UV-Vis measurements as these are also through %T measurements. The difference must be that the UV-Vis measurements, especially regarding the yellowness index, are measuring the increase in absorbance due to the creation of a few by-products (mainly naphthanoic acids in the case of PEN) with similar λ max values, and due to the Beer-Lambert law ($A = \epsilon cl$) the absorbance of the film at or around these λ max values is directly proportional to the concentration of these by-products. On the other hand, the FTIR measurements are measuring vibrational-rotational energy change in a large complex polymer molecule and so small changes in end groups and limited chain scission, when looking at the bulk film, may not have much of an effect on the spectrum before and after the sample has been subjected to QUV. This is despite the fact that ATR-FTR shows significant degradation at the surface of the film.

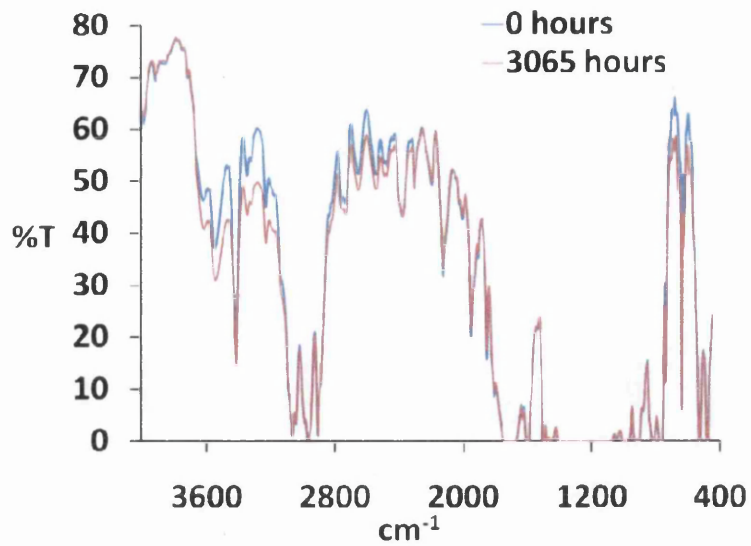


Figure 8.48 The FTIR spectra of PEN at 0 hours and at 3065 hours QUV

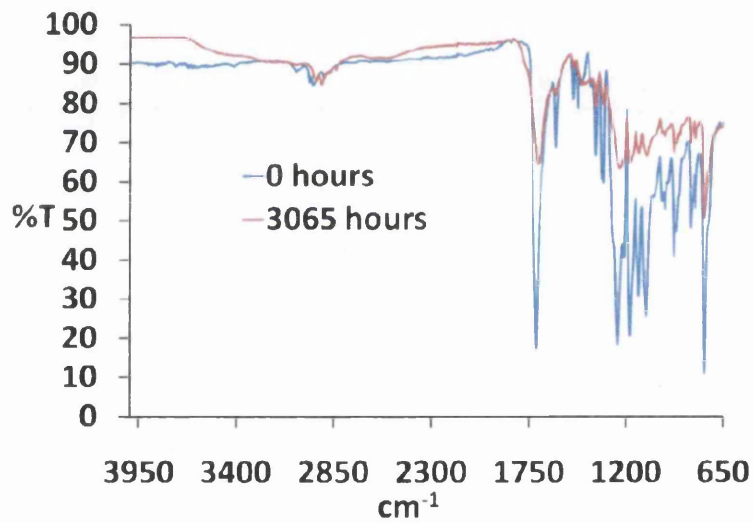


Figure 8.49 The ATR spectra of PEN at 0 hours and at 3065 hours QUV

8.6.4 PEN vs. PET – Conclusion

If comparing PEN to PET, the UV-Vis evidence suggests that PET is more stable to UV light. This makes sense as PEN absorbs a greater proportion of the UV spectrum than PET. It

would be interesting however to see what the results would be under UV-B lamps as the emission spectra would be blue shifted compared to UV-A lamps and therefore PET might absorb a greater proportion of the radiation being emitted. FTIR Evidence at first may seem inconclusive as it appears that the surface of the film exposed to UV light experiences a great degree of photodegradation whilst the bulk film shows little sign. CO₂ evolution data does indicate that PEN is far more photoactive than PET under UV-A lamps, but again this could be due to surface photodegradation rather than photodegradation in the bulk film.

8.7 The Effect of Coating Weight on the Efficacy of the Lacquer

Figure 8.50 shows the increases in the Yellowness Index (the absorbance at 400 nm) of the samples shown. The samples are sheets of PEN coated with either BASF LP or HP and coated at 20 μm 40 μm and 60 μm . It is quite obvious that when the coating thickness is increased then the protection from photodegradation is also increased. This can be explained simply by the fact that the thicker the coating, the more of it the photon has to travel through and the more likely that that photon will be prevented from reaching the substrate by a UVA molecule. The case is not quite so clear for PET (Figure 8.51) but the patterns are the same in that generally a heavier coating weight gives more protection against photodegradation.

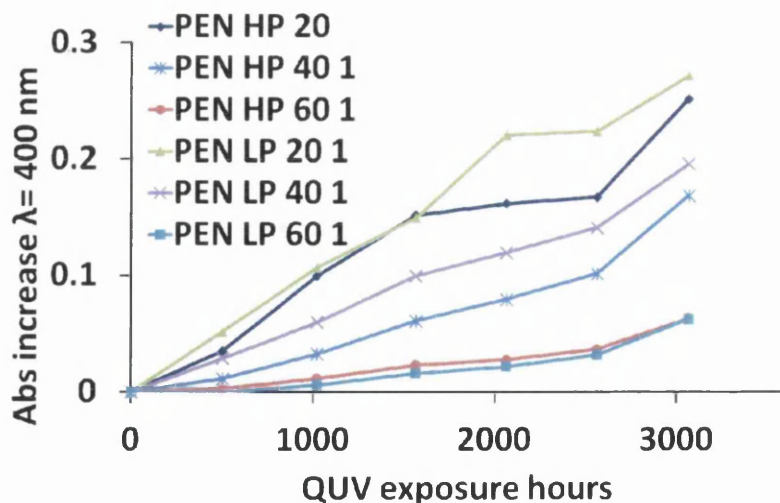


Figure 8.50 The increases in the Yellowness Index (abs at 400 nm) of the samples shown

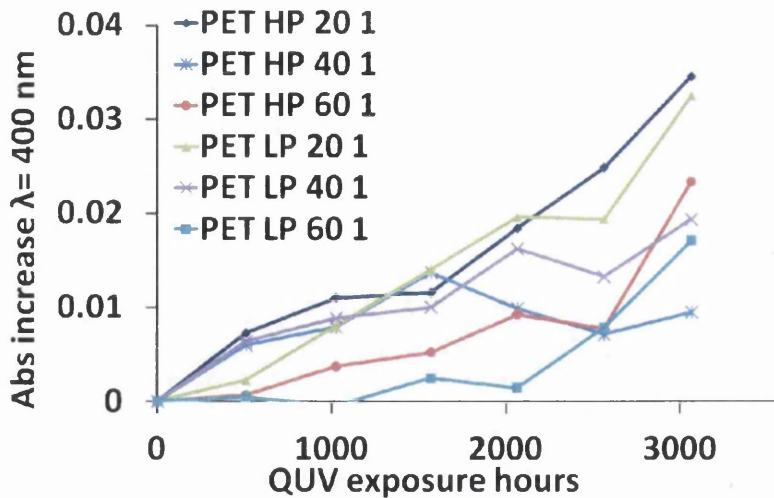


Figure 8.51 The increases in the Yellowness Index (abs at 400 nm) of the samples shown

8.8 The Effect of Increasing Additives on the Coating Performance

BASF HP and BASF LP lacquers were doped with varying levels of Tinuvin 400 UV absorber and Tinuvin 5100 HALS. Figure 8.52 shows the cumulative increase of the Yellowness Index of the samples shown. It is clear from Figure 8.52 that increasing the amount of HALS in the coating has very little effect on performance whereas increasing the levels of UVAs, increases the performance of the coating. This may be because HALS are radical scavengers which neutralise photo-oxidation products that catalyse further degradation. If there are already enough HALS in the coating to do the job in the first place then adding more will have little effect. Increasing the levels of UVA will mean, due to the Beer-Lambert Law, that more UV light will be absorbed. Why then does BASF not just put more UVAs in their coatings to make them more UV stable? The answer must be that BASF have to weigh up their cost to performance ratio as UVAs are expensive. Another reason is that in general the more additives there are in a coating, the harder it is to cure and this can lead to problems such as poor adhesion. The pattern seen in the BASF HP coating is almost identical to that seen in Figure 8.52 for the BASF LP coating.

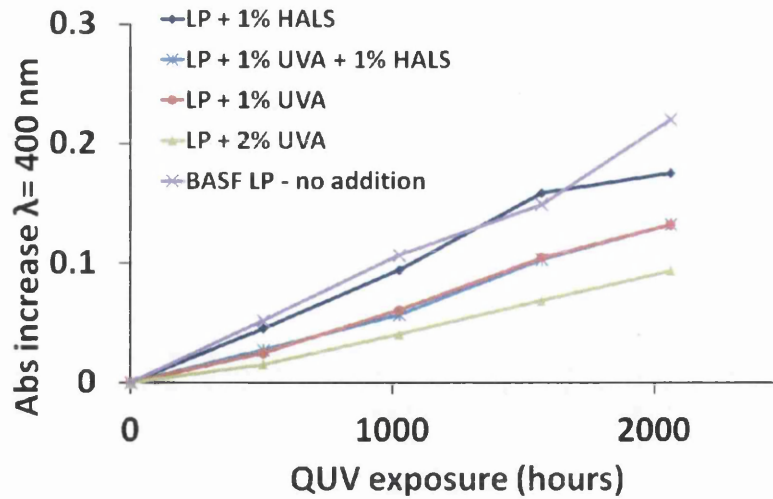


Figure 8.52 Increase of the Yellowness Index of the samples shown

8.9 Curing of the BASF lacquers

A visit was undertaken to Tata Steel's PV Accelerator facility at Shotton, the main purpose of which was to understand the curing rates of the BASF lacquers and to see if they could be cured quickly using a belt furnace equipped with IR lamps. The assessment of the level of cure is carried out using a solvent rub technique that conforms to the ASTM D5402-06 standard. Tables 8.2 and 8.3 below show the number of MEK double rubs needed to cause coating failure or breakthrough of the BASF LP and BASF HP lacquers respectively. As the lacquers are polyurethanes the testing standards of Colorcoat Prisma® were used. Prisma is considered cured if the number of double rubs is greater than 100 although this is a minimum value and ideally should be greater than 150.

Table 8.2 Number of MEK double rubs needed to cause coating failure or breakthrough of the BASF LP lacquer. Tata Steel Colours would consider a polyurethane coating cured if it could withstand 100 double rubs, although > 150 double rubs is the desired result.

| BASF LP | Cure Time | | | | | | Touch dry |
|----------------|-----------|---------|---------|---------|---------|---------|-----------|
| Cure Temp (°C) | 5 mins | 10 mins | 15 mins | 20 mins | 25 mins | 30 mins | |
| 60°C | 1 | 2 | 2 | 3 | 10 | 30 | 15 mins |
| 80°C | 20 | 38 | 38 | 40 | 50 | 100 | 5 mins |
| 100°C | 45 | 40 | 70 | 150 | 230 | 400 | 5 mins |
| 120°C | 100 | 130 | 280 | 350 | 500 | | 5 mins |
| 140°C | 300 | 360 | 500 | | | | 5 mins |

Table 8.3 Number of MEK double rubs needed to cause coating failure or breakthrough of the BASF HP lacquer

| BASF HP | Cure Time | | | | | | Touch dry |
|----------------|-----------|---------|---------|---------|---------|---------|-----------|
| Cure Temp (°C) | 5 mins | 10 mins | 15 mins | 20 mins | 25 mins | 30 mins | |
| 60°C | 3 | 10 | 18 | 30 | 50 | 100 | 15 mins |
| 80°C | 20 | 55 | 95 | 160 | 200 | 320 | 5 mins |
| 100°C | 120 | 130 | 350 | | | | 5 mins |
| 120°C | 160 | 300 | 500 | | | | 5 mins |
| 140°C | 3 mins | 5 mins | | | | | 3 mins |

PET film will wrinkle at about 150°C so this is the processing temperature limit. Table 8.2 shows that the minimum needed to fully cure the BASF LP is 100°C for 20 minutes. 100°C may be too high for the components of the cell to withstand and 20 minutes is far too long to be involved in any kind of coil coating process. To fully cure the BASF HP (Table 8.3), 80°C for 20 minutes is needed. These cure times are also far too slow for coil coating, however 80°C will be within the temperature limits of the cell components as this is the temperature a roof could reach in full summer sunlight.

As the polyurethane is a 2-pack system which relies on the presence of a catalyst to form crosslinkages, it should continue to cure even when taken away from the heat source. Table 8.3 shows that the BASF HP was dry to the touch after 5 mins at 80°C, this could mean that it might be possible to cure the coating enough to enable manual handling and then further cure may be achieved by setting aside the finished module for a number of hours until it is fully cured. Table 8.4 shows the results of a trial where the BASF HP lacquer was cured at

80°C for varying amounts of time. The samples were subject to solvent rub tests immediately after leaving the oven, and then 24 and 48 hours after leaving the curing oven.

Table 8.4 Number of MEK double rubs needed to cause failure of the BASF HP lacquer after curing and then being left for the times shown

| Oven time | Wait time | | |
|-----------|-----------|----------|----------|
| | 0 hours | 24 hours | 48 hours |
| 5 mins | 20 | 105 | 280 |
| 10 mins | 55 | 170 | 350 |
| 15 mins | 95 | 280 | |
| 20 mins | 160 | 320 | |

Table 8.4 shows that it would be possible to lacquer a module and then ‘cure’ the lacquer at 80°C for just 5 minutes so that manual handling would be possible. A full cure would then be achieved if the module was left for 48 hours after coating. This is a positive result for module production as the module will not be subject to high temperatures for a long period of time.

8.9.1 Spray Coating and Curing the Lacquers on the PV Accelerator Pilot Line

All coatings in this section were applied with a wire wound bar but it is likely that any coatings used on the pilot line at Shotton will be spray-coated. For this reason it was decided that the lacquers should be applied with a spray gun to get an idea of what coating thicknesses were achievable. The spray gun used is shown in Figure 8.53. There are three adjustment knobs on the spray gun and changing any of the settings can have a large impact on coating thickness. Operator technique is also highly important to the quality and thickness of the coating and getting consistent coatings takes some considerable practice on behalf of the operator. After some practice the author was able to get a consistent coating so that one pass of the gun would give a 20 µm dry film thickness. When the consistency of coating thickness had been achieved, samples of steel strip that had been laminated with PET were sprayed and cured in the belt furnace on the pilot line at Shotton.

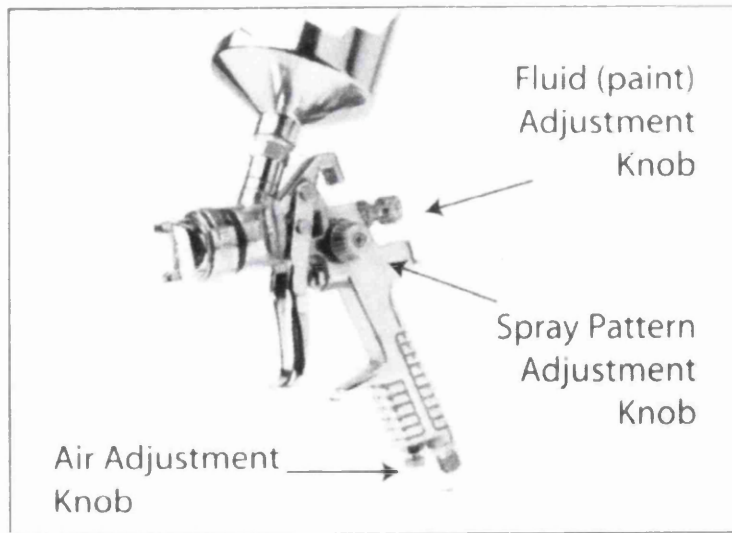


Figure 8.53 The spray gun used in the coating trial

The pilot line at Shotton has a Hengli Belt Furnace fitted with IR lamps. It is known from the BASF TDS that the lacquers can be cured quickly using IR radiation so it was decided to run a trial to see if the spray coated panels mentioned above could be cured using the belt furnace. In this trial all sections of the furnace were set to 80°C. Thermocouples were put through the furnace to get a heating profile and the panels were put onto the belt and the cure was measured by the solvent rub test. Figure 8.54 below shows the heating profile of the first trial where the belt speed was set to 0.8m/min (the slowest setting allowed). This meant the sample was above 80°C for almost 7 minutes. Two samples were put through the furnace, one at 20 µm and one at 40 µm. Both samples were completely cured, in fact the lacquer could not be removed even after over 500 double MEK rubs. After the success of the first trial it was decided to double the speed of the belt to 1.6m/min, the heating profile is shown in Figure 8.55 below

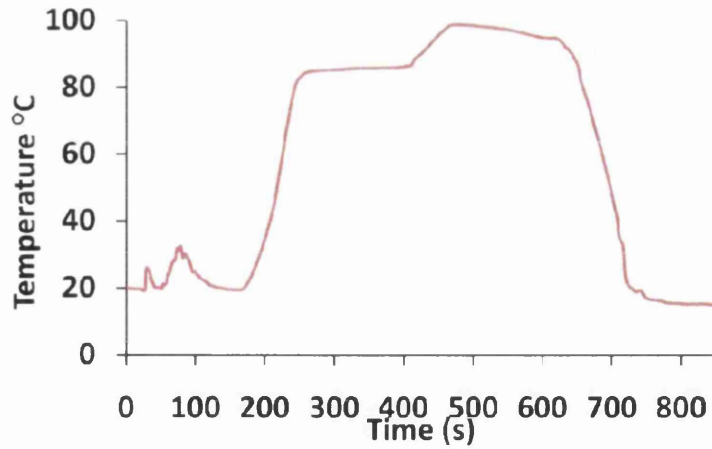


Figure 8.54 The heating profile of the belt furnace was at 0.8m/min

Figure 8.55 shows that the samples didn't get up to 80°C during the heating process and was only above 60°C for around 2.6 minutes. With the information given in the thermal cure trial it was not expected that the sample would even be 'touch dry' when they exited the belt furnace, yet the samples were fully cured, again the lacquers could not be removed even after 500 MEK double rubs. This means that the curing process can be vastly accelerated using the IR lamps in the belt furnace. There were no more belt furnace curing trials after this as there was not enough time.

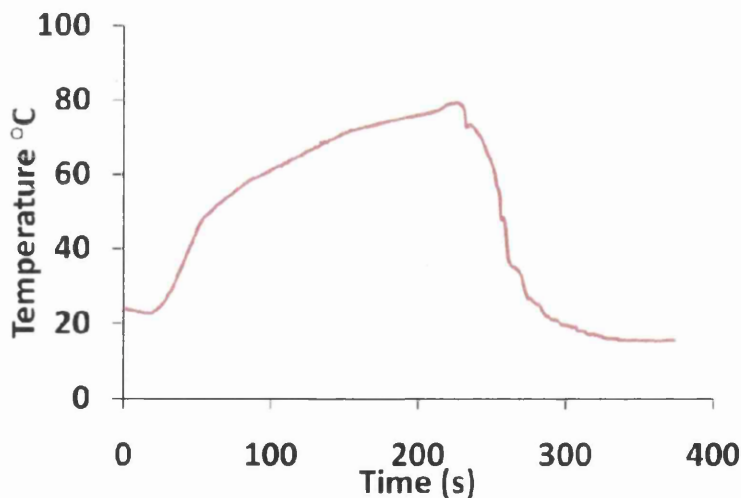


Figure 8.55 The heating profile of the belt furnace was at 1.6m/min

A flexible DSC built upon a metal substrate will almost certainly have a polymer-film counter electrode and it has been shown in this section that polymer films are susceptible to photodegradation by UV light. UV stabilised polymer films are commercially available but are expensive and could add a considerable amount to the cost per watt produced by the module. It has also been shown in this section that it is possible to match the performance of one of these commercial films by simply coating a cheaper “indoor grade” film with a clear UV absorbing lacquer. With more research into suitable coatings this has the potential to bring down the cost per m² and therefore the cost per watt produced, of the complete module.

Whilst it would be ideal to have a fast cured coating, such as a UV cured coating to enable roll to roll processing, the UV cured coatings in this section could not match up to the performance of the BASF 2-k coatings, that is not to say however, that they will never match up to them but this is an issue for coating formulation scientists and is beyond the scope of this work.

Some formulation work has been carried out and it has been shown that increasing levels of UVAs and increasing coating weights can increase UV protection performance. This however will inevitably affect cost and possibly the mechanical properties of the coating. Again these issues need to be weighed up on a cost/performance basis by formulation scientists.

Hopefully, one of the greater benefits of the work carried out for this section will be the identification of simple methods to detect photodegradation in clear polymer films. If new films become available in the future then it may be possible to identify relatively quickly, their UV stability by using the methods described.

8.11. References

1. M.A. Fox and M.T. Dulay, Heterogeneous photocatalysis, *Chemical Reviews* 1993 **93**(1) 341-357
2. G.J.M. Fechine, M.S. Rabello and R.M. Souto-Maior, The effect of ultraviolet stabilizers on the photodegradation of poly(ethylene terephthalate), *Polymer Degradation and Stability* 2002 **75**(1) 153-159
3. M. Edge, N.S. Allen, R. Wiles, W. McDonald and S.V. Mortlock, Identification of luminescent species contributing to the yellowing of poly (ethylene terephthalate) on degradation, *Polymer*, 1995 **36**(2) 227-234
4. G.J.M. Fechine, M.S. Rabello, R.M. Souto Maior and L.H. Catalani, Surface characterization of photodegraded poly(ethylene terephthalate). The effect of ultraviolet absorbers, *Polymer*, 2004 **45**(7) 2303-2308
5. Z. Zhu and M.J. Kelley, IR spectroscopic investigation of the effect of deep UV irradiation on PET films, *Polymer*, 2005 **46**(20) 8883-8891
6. X.F. Yang, C. Vang, D.E. Tallman, G.P. Bierwagen, S.G. Croll and S. Rohlik Weathering degradation of a polyurethane coating, *Polymer Degradation and Stability*, 2001 **74**(2) 341-351
7. G. Oreski and G.M. Wallner, Aging mechanisms of polymeric films for PV encapsulation, *Solar Energy*, 2005 **79**(6) 612-617
8. J. Scheirs and J-L. Gardette, Photo-oxidation and photolysis of poly(ethylene naphthalate) *Polymer Degradation and Stability*, 1997 **56**(3) 339-350
9. C. Lechat, A. Bunsell, P. Davies and A. Piant Mechanical behaviour of polyethylene terephthalate & polyethylene naphthalate fibres under cyclic loading, *Journal of Materials Science*, 2006 **41**(6) 1745-1756

Chapter

9.

Conclusions and Future Work

9. CONCLUSIONS AND FUTURE WORK

Although the UV photodegradation of DSCs has been alluded to in past literature and mechanisms have been proposed, no particular mechanism has been proven. From the outset, it was never the aim of this project to characterize UV photodegradation in the way it has been presented in this thesis. However, there was a need to look at subtle changes to DSC properties as they were undergoing UV exposure, so that these changes could be used to quickly assess the effectiveness of UV protection measures.

During this initial study, aspects of the photodegradation of DSCs, particularly the fact that they degrade faster when placed under electrical load, gave insights into the mechanism of UV photodegradation of DSCs which required further investigation. A systematic characterization of the UV photodegradation of DSCs was carried out and aspects mentioned in the literature were confirmed. These include the drop in V_{OC} , the initial increase in J_{SC} and the apparent bleaching of the electrolyte. Even the eventual reduction in J_{SC} has been reported before but this has not been linked with the large increase in recombination resistance which in this work is observed concurrently. These two observations point to a removal of charge carriers from the electrolyte and along with the photobleaching observed, shows that it is the I_3^- that is being removed. Something which is not mentioned in the literature however is the fact that cells fail considerably faster when irradiated under an electrical load. This seems to suggest that the main mechanism for cell degradation is by reaction with photogenerated holes, as under load, electrons in the TiO_2 conduction band will be exported to the external circuit lowering the rate of electron-hole recombination and so increasing the rate of degradation. This is the mechanism proposed but it does not explain what has happened to the I_3^- . One hypothesis is that the iodine has been oxidized to I_3^+ , IO_3^- or perhaps IO_4^- and it is recommended that any future work would start by trying to find these oxidation states in the degraded electrolyte.

The role of TiO_2 in the photodegradation of DSCs is further implicated by the fact that the electrolyte does not appear to degrade when UV illuminated in the absence of TiO_2 . The fact that the electrolyte degrades faster in a cell where there is no dye could also point to the importance of photogenerated holes as electronic injection from the dye appears to be a stabilising mechanism in that it may increase hole recombination by increasing the

population of electrons in the TiO₂ conduction band. It is possible however that the dye is just blocking active sites in the semiconductor surface and slowing photoreactions with the electrolyte.

Another aim of the characterization study was to try to identify degradation processes that are associated with UV exposure so that these may be separated out from other degradative mechanisms. To certain extent this was not achieved as although test cells degraded more slowly under visible light soaking, the degradation characteristics were similar to those observed in cells under UV exposure, albeit at much reduced rate. It is also likely that the degradation characteristics observed under visible light soaking were due to the small amount of UV light emitted by the light soaker. One way of achieving a separation of UV and visible light mechanisms would have been the use of varying cut off filters on visible light soaked cells so that only visible light would reach the cell. If this study were to be conducted then it would be recommended that this be carried out under a lamp emitting 1 Sun power and with a good spectral match to that of AM 1.5, furthermore the cells should be placed on a cooling table to rule out the effects of elevated temperatures.

Despite not fully being able to reconcile the degradation caused by direct excitation of TiO₂ from degradation that might be caused by visible light alone, it was shown that the light soaking cabinet emits very little light in the UV spectrum compared to the emission spectrum given by AM 1.5. This presents a potential problem as arguably the most common test for DSC durability is visible light soaking, yet neither of the two leading suppliers of light soaking units emit significantly from 300 nm to 400 nm. Having shown how detrimental UV light is to the DSC, it is therefore the author's opinion that visible light soaking tests at ambient temperatures do not stress the cells enough to conduct comparative stability studies in a time frame suitable for commercial/industrial R & D. It is therefore recommended that a standard be set for light soaking tests and that the standard output should be as close a spectral match to AM 1.5 as possible including the appropriate emissions in the UV spectrum.

It has been shown that a very effective way of stopping UV degradation is simply by use of a UV filter. It was shown that filtering is likely needed above 385 nm but probably no more than 400 nm. A question that might be asked therefore is: Why bother carrying out this work if all you have to do to prevent photodegradation is use a UV filter? The answer to

this was presented in *chapter 6*. UV filtering is an easy solution but it is far from ideal as photons which otherwise might have been converted into current are blocked. This will obviously lower photocurrents but it was also shown that this lowers the photovoltage as well because the quasi-Fermi level and therefore the V_{OC} are dependent on incident light intensity. Future work to try and resolve this issue will require a two-pronged approach. Firstly, photons in the red and NIR region need to be captured more effectively. This can be achieved either by extending dye absorption spectra into the red/NIR or by co-sensitization. The second approach would be to investigate the use of light down-converters that absorb UV light and re-emit visible photons so that some of the UV photon energy can be utilised and not just dissipated thermally as with standard organic UV absorbers.

The apparent recovery of photodegraded DSCs was investigated and it was shown that the depleted electrolyte can be restored somewhat by application of a reverse bias. This could have implications for long term stability. The periodic application of the recovery treatment does not appear to prevent degradation however, and at least at this stage, cells could not be restored to their original conditions. This is especially evident when looking at the V_{OC} , which doesn't recover suggesting that UV exposure might cause a permanent change to the electrolyte or to the surface of the TiO_2 . Nonetheless, cells which had undergone a periodic regeneration did appear to retain a higher overall photocurrent throughout their lifetimes meaning that whilst not preventing degradation, the regeneration treatment could result in a greater power output for the cell over its lifetime than those cells that do not undergo regeneration. It is recommended therefore that investigations into cell regeneration continue. For example looking at less severe exposure periods and more frequent application of regeneration treatments.

Finally an investigation was conducted on the photostability of clear polymer films intended for use as counter electrode materials for DSC modules. It was shown that a number of spectroscopic methods can be used to easily identify the extent of photodegradation in these films when they are exposed to QUV accelerated weathering. It was shown that the photostability films can be vastly improved by application of inexpensive, UV absorbing clearcoat lacquers.

If there is only one recommendation to come from this work, it is the need for standardized testing for DSC test cells, especially light soaking tests which should have a spectral match to that of AM 1.5. In the tests conducted for this thesis, UV photodegradation causing consumption of I_3^- seems to be a dominant failure mechanism and evidence suggests that this occurs via a reaction with a UV photogenerated hole. If a simulation of sunlight is required then neither UV exposure nor visible light soaking can achieve this alone. For effective accelerated stability testing the whole UV-VIS-NIR spectrum needs to be considered. As such it is suggested that the ideal 'weathering' system be adapted from that used in the paint industry with xenon arc weathering being the most suitable because of its close spectral match to AM 1.5.